RICE UNIVERSITY

Manipulation of Carbon Nanostructures for

Multifunctional Composite Materials

by

Jay Rostrata Lomeda

A THESIS SUBMITTED
IN PARTIAL FULFILLMENTOF THE
REQUIREMENTS FOR THE DEGREE

Doctor of Philosophy

APPROVED, THESIS COMMITTEE:

James M. Tour,
Chao Professor of Chemistry, Professor of Mechanical Engineering & Materials Science, and Professor of Computer Science

Matteo Pasquali,
Professor of Chemical and Biomolecular Engineering

Robert H. Hauge,
Distinguished Faculty Fellow of Chemistry

HOUSTON, TEXAS

AUGUST 2010

Abstract

Manipulation of Carbon Nanostructures for Multifunctional Composite Materials

by

Jay R. Lomeda

Composite fibers comprised of 5:95 wt ratio of ultra-short single walled carbon nanotubes (US-SWCNT):polyacrylonitrile (PAN) were spun using a dry-jet wet-spinning method followed by oxidative stabilization at 285 °C. The as-spun and stabilized composite fibers exhibited a 50 and 40 % increase, respectively, in modulus when compared to neat PAN.

The vacuum pressure impregnation (VPI) method was employed to reinforce SWCNT fibers. SWCNT fibers were impregnated with polyamic acid (PAA) solution at 100 psi followed by thermal imidization to obtain fibers reinforced with polyimide (PI). The tensile strength was increased form 68 to 215 MPa for SWCNT fibers after VPI and imidization.

Surfactant-wrapped chemically converted graphene (CCG) sheets obtained from the hydrazine reduction of GO were functionalized by treatment with aryl diazonium salts. The functionalized nanosheets disperse readily in polar aprotic solvents. A one-pot method has also been developed for reducing GO and simultaneously functionalizing it

with alkyl and aryl groups. The alkyl functionalized reduced GO shows higher solubility in organic solvents when compared to GO.

Graphene-filled PI composite films were prepared bu solution blending of GO and PAA, casting the mixture and imidizing the films bu heating up to 400 °C resulting in composite films that exhibit up to a ~75 % increase in modulus and low moisture uptake. At 2 wt % loading GO, the composite films exhibit a conductivity of 1.25 x 10^{-5} S/cm. The layer-by-layer (LbL) assembly technique was also employed in the fabrication of thin film composites of CCG and PI. The assembly was driven by the acid-base interaction between the aniline moieties on functionalized CCG and the carboxyl groups of the PAA.

A simple fluid-phase processing method to obtain single to few layers of graphene without the aid of sonication has been developed. Graphene is spontaneously exfoliated from graphite and dissolved at isotropic concentrations as high as ~1000 ppm in chlorosulfonic acid. The dissolution mechanism in superacids is protonation and electrostatic repulsion. The utility of this simple exfoliation process is further extended to diazonium functionalization of graphene allowing access to edge-functionalized graphenes with a minimal disruption of the graphitic network on the basal plane.

Alpha, Beta, Gamma

Acknowledgments

I thank Professor James Tour for giving me the opportunity to be a member of your excellent research group and for further extending your guidance in areas that are outside the grasps of academic life. My sincere thanks also go to Professor Matteo Pasquali and Dr. Robert Hauge, both my informal co-advisers and members of my thesis committee, I truly appreciate your support and insight throughout my term at Rice University in most of the projects that I have worked on. And more importantly, I will be forever grateful to the three of you for giving me a second chance.

I also would like to express my gratitude to the people who have been very influential in my development as a researcher and as a person sharing the pains and joys of graduate school journey. Among them are: Wen-Fang Hwang, Kazufumi Kobashi, Dustin James, Christopher Hamilton, Noe Alvarez, Dmitry Kosynkin, Hua Fan, Richard Booker, Colin Young, Shin-ichiro Kohama, Ashley Leonard, Amanda Higginbotham, Bo Chen, Natnael Behabtu and Zhengzong Sun. It has been a very fruitful 4 or 5 years for me because of your support, influence and camaraderie.

Lastly, I would like to thank Aniway Lomeda, a very smart, loving woman to whom I owe so much.

Table of Contents

Introduction 1

Carbon Nanotubes 2

Graphene 5

Functionalization of Graphene Sheets 7

References 9

1 Ultra-Short Single Walled Carbon Nanotube/Polyacrylonitrile Composite Fiber as Carbon Fiber Precursor 17

1.1 Introduction 17

1.2 Results and Discussion 23

1.3 Experimental Section 35

1.3.1 Preparation of PAN and US-SWCNT/PAN in DMSO 35

1.3.2 Fiber Spinning and Stabilization 36

1.3.3 Characterization 36

1.4 Conclusion 37

1.5 Experimental Contribution 37

References 37

2 Vacuum Pressure Impregnation of Acid-Spun Single-Walled Carbon Nanotube Fibers with Polyimide 40

2.1 Introduction 40

2.2. Results and Discussion 43

2.3 Experimental Section 57

2.3.1 Materials 57

2.3.2 Spinning of SWCNT fibers and SWCNT fibers

	having 10 wt % f-SWCNT	57
	2.3.3 Characterization	57
	2.3.4 Vacuum Pressure Impregnation (VPI) Procedure	58
	2.3.5 Imidization Procedure	58
	2.4 Conclusion	59
	2.5 Experimental Contribution	59
	References	60
3	Diazonium Functionalization of Surfactant Wrapped Chemically Converted Graphene Sheets	63
	3.1 Introduction	63
	3.2 Results and Discussion	65
	3.3 Experimental Section	76
	3.3.1 Graphite Oxide	76
	3.3.2 Diazonium Functionalization	76
	3.4 Conclusion	77
	3.5. Experimental Contribution	78
	References	78
4	Reductive Alkylation of Graphite Oxide	81
	4.1 Introduction	81
	4.2 Results and Discussion	82
	4.3 Experimental Section	99
	4.3.1 General Procedure for the Synthesis of Alkylated CCG	99
	4.3.2 Characterization	100
	4.4 Conclusion	102
	4.5 Experimental Contribution	102

References 102

5 Thermally Converted Graphene-Polyimide Composite Films 105

5.1 Introduction 105

5.2 Results and Discussion 107

5.3 Experimental Section 120

5.3.1 Materials 120

5.3.2 Solvent Blending 120

5.3.3 Film Casting 121

5.3.4 Characterization 121

5.4 Conclusion 122

5.5 Experimental Contribution 122

References 123

6 Graphene Dispersion at High Concentrations in Chlorosulfonic Acid 127

6.1 Introduction 127

6.2 Results and Discussion 129

6.3 Experimental Section 140

6.3.1 General Procedure for Preparation of Dispersions 140

6.3.2 Characterization 141

6.3.3 Fabrication and Testing of Thin Films 142

6.4 Conclusion 143

6.5 Experimental Contribution 144

References 144

7 Layer-by-Layer Assembly of Chemically Converted Graphene-

Polyimide Composite Films 148

7.1 Introduction 148

7.2 Results and Discussion 149

7.3 Experimental Section 162

7.3.1 Materials 162

7.3.2 LbL Assembly 163

7.3.3 Thermal Imidization 164

7.3.4 Characterization 164

7.4 Conclusion 165

7.5 Experimental Contribution 165

References 165

8 Edge Selective Functionalization for Low Resistivity of Soluble Graphene 169

8.1 Introduction 169

8.2 Results and Discussion 171

8.2.1 Protocol for Chemical Assisted Exfoliation 171

8.2.2 Functionality and Quality of Graphene Films 173

8.2.3 Edge Selectivity of Functional Groups 179

8.2.4 Electrical Properties 180

8.2.5 Morphologhy of CEG 181

8.3 Experimental Section 183

8.3.1 Thermal Expansion of Acid Intercalated Graphite 183

8.3.2 Functionalization of Thermally Expanded Graphite in Chlorosulfonic Acid 183

8.3.3 Exfoliation of Graphene from Functionalized Graphite in DMF 183

8.3.4 Characterization 183

8.4 Conclusion 183

8.5 Experimental Contribution 184

References 184

List of Figures and Schemes

Figure 1.	Graphene as the parent material of carbon nanostructures: (a) wrapped into 0D fullerene, (b) rolled up into 1D nanotube (b) and (c) stacked into 3D graphite.	2
Figure 2.	Possible vectors for general carbon nanotubes including zigzag, armchair, and chiral nanotubes. The encircled dots are for metallic nanotubes and the single dots are for semiconducting nanotubes.	4
Figure 3.	(a) An armchair (5,5) nanotube, (b) a zigzag (9,0) nanotube and (c) a chiral (10,5) nanotube.	4
Figure 4.	Structural model for GO.	7
Figure 1.1.	General scheme for fabrication of carbon fiber using PAN precursor.	18
Figure 1.2.	General scheme for fabrication of carbon fiber using pitch precursor (a) istropic pitch and (b) mesophase pitch.	19
Figure 1.3.	Scheme for carbon fiber processing using PAN precursor.	20
Figure 1.4.	Structural changes occurring in PAN fibers during (a) stabilization and (b) carbonization.	21
Figure 1.5.	(a) Model of US-SWCNT and (b) structure of PAN	24
Figure 1.6.	Optical micrographs of US-SWCNTs dispersion in (a) DMSO, (b) 99:1 DMSO:triethylamine, and (c) 99:1 DMSO:triethanolamine	24
Scheme 1.1.	Spinning and processing of carbon fiber using US-SWCNT/PAN precursor	25
Figure 1.7.	Experimental set-up for the stabilization of fibers	27

Figure 1.8. FT-IR spectra of (a) PAN, (b) PAN stabilized at 285 °C for 5 h, (c) PAN stavilized at 285 °C for 10 h, (d) US-SWCNT/PAN stabilized at 285 °C for 5 h, (e) US-SWCNT/PAN stabilized at 285 °C for 10 h. 28

Figure 1.9. SEM images of as-spun PAN fiber (a) fracture point after tensile test and (b) along the fiber axis. 30

Figure 1.10. SEM images of as-spun US-SWCNT/PAN fiber (a) fracture point after tensile test and (b) along the fiber axis 31

Figure 1.11. SEM images of stabilized PAN fiber at the fracture point after tensile test. 32

Figure 1.12. SEM images of stabilized US_SWCNT/PAN fiber at the fracture point after tensile test. 33

Figure 1.13. Scheme for mounting of fiber specimens for tensile test. 36

Figure 2.1. SEM images of the dry spinning process of CNT array. 41

Figure 2.2. (a) Photograph of spinning apparatus for SWCNTs in 102 % H_2SO_4. (b) Fibers being extruded from a glass spinneret and (c) a spool of SWCNT fiber coagulated in water. 42

Figure 2.3. Concept for VPI of SWCNT fiber. 43

Figure 2.4. Photographs of wettability testing of PAA solution conducted on (a) the SWCNT fiber or (b) the f-SWCNT fiber. 44

Figure 2.5. Diagram for the VPI processing of SWCNT fibers 45

Figure 2.6. SEM images of (a) neat SWCNT fiber spun from 102 % H_2SO_4, (b) morphology of a cross section of the fiber prepared by pulling apart the fiber. 47

Figure 2.7. SEM images of (a) SWCNT fiber impregnated with PAA, (b) morphology of a cross section of the fiber prepared by pulling apart the fiber 48

Figure 2.8. SEM images of (a) SWCNT fiber impregnated with PI, (b) morphology of a cross section of the fiber prepared by pulling apart the fiber 49

Figure 2.9. SEM images of (a) neat f-SWCNT fibers spun from 102 % H_2SO_4, (b) morphology of a cross section of the fiber prepared by pulling apart the fiber 50

Figure 2.10. SEM images of (a) f-SWCNT fiber impregnated with PAA, (b) morphology of a cross section of the fiber prepared by pulling apart the fiber 51

Figure 2.11. SEM images of (a) SWCNT fiber impregnated with PI, (b) morphology of a cross section of the fiber prepared by pulling apart the fiber 52

Figure 2.12. Representative ATR-IR spectrum of PI-SWCNT and PI-f-SWCNT fibers showing the imide peaks at 1772 cm^{-1} (C=O imide peak) and 1380 cm^{-1} (C-N imide peak). 54

Figure 2.13. Core-level C1s spectra of (a) PAA-SWCNT fibers, (b) PI-SWCNT fibers, (c) PAA-f-SWCNT fibers and (d) PI-f-SWCNT fibers. 55

Figure 2.14. Quartz stand for the drying and imidization process 59

Figure 3.1. Scheme for the preparation of stable aqueous dispersions of CCG by (1) oxidation of graphite to GO, (2) stabilization of GO sheets by electrostatic repulsion, and (3) hydrazine reduction to convert GO to CCG. 64

Scheme 3.1. Starting with SDBS-wrapped GO, reduction and functionalization of intermediate SDBS-wrapped CCG with diazonium salts. 66

Figure 3.2. Cryo-TEM iamge of S-CCG and a crystal of ice situated beside thte graphene sheet. 66

Figure 3.3. Core-level C1s XPS spectra of GO and CCG showing significant loss of C-O (286 eV) and C=O (287 eV) groups after reduction. 68

Figure 3.4. XPS survey scan of (a) GO; (b) CCG; (c) **1b** showing Cl 2p peak at ~ 200 eV; and (d) **4b** showing Br 3d peak at 70 eV. 68

Figure 3.5. Raman spectra of (a) GO; (b) S-CCG; (c) **1b** abd (d) **1b** after heating under Ar to 850 °C. 70

Figure 3.6. ATR-IR spectra of (a) GO; (b) S-CCG; and (c) f-CCG **2b**. 71

Figure 3.7. Photographs of supernatant solutions obtained from DMF dispersions of (a) CCG and (b) **4b**; (c) **1b**; (d) **2b**; (e) **3b** after centrifugation for 15 min at 3200 rpm. 72

Figure 3.8. Atomic force micrographs by height of f-CCG **2b** spin coated from DMF dispersions onto a freshly cleaved mica surface showing single f-CCG sheets accompanied by bilayer to several layers. 73

Figure 3.9. Section analysis of **2b** showing height ranges from 1.8 to 2.2 nm. 74

Figure 3.10. TGA thermograms of (a) CCG, (b) **2b**, (c) **3b**, (d) **1b** and (e) GO. 75

Figure 4.1. Scheme for reductive alkylation of SWCNT in Li/NH_3. 82

Figure 4.2. The supernatant chloroform solution after centrifugation of (a) GO, (b) CCG, (c) **1** and (d) **2**. 83

Figure 4.3. Raman spectrum of GO with D:G ratio of 1.9:1. 84

Figure 4.4. Raman spectrum of CCG with D:G ratio of 1.4:1. 85

Figure 4.5. Raman spectrum of f-CCG **1** with D:G ratio of 1.7:1. 86

Figure 4.6. ATR-FTIR spectra of (a) GO, (b) f-CCG **3** treated with 10 %

	HCl and (c) f-CCG **3** treated with 0.1 N NaOH.	88
Figure 4.7.	Solution 500 MHz ^{1}H NMR spectrum of **1** in $CDCl_3$.	89
Figure 4.8.	^{1}H-^{13}C Cross polarization magic angle spinning (CPMAS) spectrum of **2**.	90
Figure 4.9.	^{1}H-^{13}C CPMAS NMR spectrum of **2** after insertion of a 50-μs dephasing interval between cross polarization and FID acquisition resulting in sever attenuation of the methylene signal at δ 29 ppm.	91
Figure 4.10.	Direct ^{13}C pulse magic angle spinning (MAS) spectrum of **2**.	92
Figure 4.11.	Core-level C1s XPS spectrum of GO.	93
Figure 4.12.	Core-level C1s XPS spectrum of CCG.	94
Figure 4.13.	Core-level C1s spectrum of **3**.	94
Figure 4.14.	TGA thermograms of CCG, GO, **1**, and **2**.	95
Figure 4.15.	AFM micrograph of f-CCG **2** on a freshly cleaved mica surface.	97
Figure 4.16.	AFM micrograph of **1** in height mode consisting of several layers and exhibiting folding of sheets; average height: 1.8 – 3 nm.	98
Figure 4.17.	AFM micrograph of **2** in amplitude mode; height range: 2 – 3.5 nm.	99
Scheme 5.1.	Conversion of GO and PAA into TCG-PI composite film.	108
Figure 5.2.	Optical micrographs of GO-PAA mixtures after degassing, (a) 2 wt % GO and (b) 1 wt % GO.	109
Figure 5.3.	Optical micrographs of (a) **PI-0**; (b) **PI-1**; (c) **PI-2**; and (d) **PI-3** after imidization at 400 °C.	110
Figure 5.4.	*I-V* curves of composite films with different GO concentrations.	110
Figure 5.5.	ATR-IR spectra of **PI-0** and **PI-3** at different stages of thermal imidization.	112

Figure 5.6. ATR-IR spectra of **PI-0**, **PI-1**, **PI-2** and **PI-3**. 112

Figure 5.6. XPS C1s spectra of **PI-0**: (a) after vacuum drying at 80 °C for 24 h; (b) after thermal imidization at 400 °C; and **PI-3**: (c) after vacuum drying at 80 °C for 24 h; (d) after thermal imidization at 400 °C. 114

Figure 5.7. Wide angle XRD patterns of (a) **PI-0**; (b) **PI-1**; (c) **PI-2** and (d) **PI-3**. 115

Figure 5.8. DSC thermogram of **PI-0** and **PI-3** showing the GO transition for GO filled samples. 116

Figure 5.9. SEM images taken from the fracture surfaces of imidized film samples subjected to tensile tests: (a) **PI-0**; (b) **PI-1**; (c) **PI-2** and (d) **PI-3**. 119

Figure 6.1. Proposed model for the swelling of SWCNT bundle in oleum. 128

Figure 6.2. Photographs of different graphene dispersions in $ClSO_3H$ with a starting concentrationof 25 mg/mL. 129

Figure 6.3. (a) UV-vis absorption spectra of the top phase from the vials after centrifugation. (b) Optical absorbance divided by the cell length as a function of different concentrations. 130

Figure 6.4. Effect of the initial dispersion concentration on the isotropic concentration. To calculate the top phase concentration, the initial dispersion was first centrifuged at 5000 rpm for 12 h. 131

Figure 6.5. Qualitative comparison between graphite dissolution into different solvents showing graphite in vials with a Teflon-coated stir bar to promote dissolution. 132

Figure 6.6. Comparison of acid-induced shifts in the liquid-phase Raman G-peak for graphite dispersed in the same mixtures of $ClSO_3H$ in H_2SO_4. 133

Figure 6.7. Solid-state Raman spectra of the initial graphite dry powder and the graphite quenched from the acid dispersion. 134

Figure 6.8. XPS from the dry material obtained upon quenching the isotropic phase from a centrifuged vial. 134

Figure 6.9. HR-TEM images of few-layer graphene deposited from a $ClSO_3H$ solution. 136

Figure 6.10. Cryogenic-temperature transmission electron microscopy (cryo-TEM) images of graphene flakes dispersed in $ClSO_3H$. A graphene flake (a) is shown nearby the TEM lacey carbon edge at very low imaging conditions (< 10 electrons/A^2), (b) the contrast between the graphene and acid is heightened nearby the graphene edges as acid is preferentially etched at these sites. In a large flake (c), a number of wrinkles, folds, and flat edges can be seen. 138

Figure 6.11. 80 % transparent (at 550 nm) film made by vacuum filtration of a 10 ppm isotropic Graphoil dispersion in chlorosulfonic acid. The measured sheet resistance was 1000 Ω/□. 139

Scheme 7.1. Reductionof nitrophenyl-functionalized-CCG (**1**) to aniline f-CCG (**2**) using elemental sulfur. 142

Figure 7.1. ATR-IR spectra (a) **1**, (b) **2**, and (c) core-level N1s spectra of **1** showing the NO_2 peak at 406 eV and after reduction to **2** (blue) indicating the reduction to NH_2 (400 eV). 152

Figure 7.2. XPS survey scans on Si substrate after (a) piranha treatment, (b) APTES assembly, (c) PAA deposition, and (d) f-CCG (**2**) deposition. 154

Figure 7.3. Raman spectrum of 40-bilayer film taken using 633 nm laser. 156

Figure 7.4. Core-level C1s spectrum of 40-bilayer film. 157

Figure 7.5. AFM micrographs of (a) APTES treated glass slide (phase mode), (b) in-plane morphology of 40-bilayer LbL assembled films and (c) section analysis of the 40-bilayer film. 159

Figure 7.6. SEM micrographs of 40-bilayer film (a) in-plane structure showing rough morphology and (b) cross-section image. 161

Scheme 7.2. Scheme for LbL deposition using PAA and f-CCG. 164

Scheme 8.1. Production of chemically-assisted exfoliated graphene (CEG). 171

Figure 8.1. Simulated CEG structure. The inset shows the expanded graphite control supernatant and the CEG supernatant after both had been treated with sonication and centrifugation in DMF. 172

Figure 8.2. High resolution XPS analysis of CEG. (a) C1s peak and (b) Br3d peak. 174

Figure 8.3. SAED of (a) a single layer of CEG, (b) two layers of CEG with a slight twist angle between the layers. 176

Figure 8.4. HRTEM of the edges of various samples. (a) eight-layer CEG; (b) six-layer CEG; (c) three-layer CEG; (d) single-layer CEG; (e) simulated four-layer CEG edge (inset is the FFT) overlaid on an HRTEM. 177

Figure 8.5. (a) Raman spectrum of the expanded graphite before functionalization; (b) Raman spectrum of CEG after functionalization. 178

Figure 8.6. EFTEM of CEG flakes: (a) zero loss image, (b) C mapping (K edge at 284 eV), and (c) Br mapping (M_{45} edge at 69 eV).

Figure 8.7. SEM image of CEG flake atop a lacey carbon grid. 180

Figure 8.8. AFM of CEG on mica. (a) The edge of the image is 4 μm and the vertical distance marked id 1.7 nm; (b) the edge of the image is 2.5 μm and the vertical distance is 1.4 nm. 182

List of Tables

Table 1.1.	Properties of Different High Performance Carbon Fibers.	22
Table 1.2.	Summary of Fiber Tensile Properties of SWCNT/PAN.	34
Table 2.1.	Summary of Tensile Strength Properties of SWCNT Fibers Before and After VPI.	46
Table 2.2.	Summary of Conductivity Measurements on Fibers Subjected To VPI.	53
Table 5.1.	Summary of the Mechanical Properties of Composite Films PI-0 to PI-3 after Imidization.	118
Table 5.2.	Results of the Moisture Absorption Test Based on ASTM D-5229.	120
Table 8.1.	Solubility and Sheet Resistance Comparison of Graphene Materials.	181

List of Symbols and Abbreviations

Å	angstrom
AFM	atomic force microscopy
AIBN	azobisisobutyronitrile
ATR-IR	attenuated total-reflectance infrared
a.u.	arbitrary units
°C	degrees Celsius
CCG	chemically converted graphene
$CHCl_3$	chloroform
CH_2Cl_2	dichloromethane
CH_3CN	acetonitrile
$ClSO_3H$	chlorosulfonic acid
cm	centimeter(s)
cm^{-1}	inverse centimeter(s)
CNT	carbon nanotubes
CVD	chemical vapor deposition
d	day(s)
δ	chemical shift in parts per million
D/G	diamondoid to graphitic peak
DMA	dynamic mechanical analysis
DMF	*N*,*N*-dimethylformamide
DMSO	dimethylsulfoxide
DSC	differential scanning calorimetry
equiv	equivalent
ESEM	environmental scanning electron microscope
EtOH	ethanol

eV	electron volt
f-CCG	functionalized chemically converted graphene
f-SWCNT	functionalized single-walled carbon nanotube
FTIR	Fourier transform infrared
g	gram(s)
GO	graphene oxide
GPa	gigapascal(s)
h	hour(s)
H_2	hydrogen
H_2O_2	hydrogen peroxide
H_2SO_4	sulfuric acid
HCl	hydrochloric acid
HDPE	high density polyethylene
HF	hydrofluoric acid
HiPco	high-pressure carbon monoxide
HNO_3	nitric acid
H_2O	water
Hz	Hertz
K	Kelvin
KBr	potassium bromide
$KClO_3$	potassium chlorate
K_2CO_3	potassium carbonate
$KMnO_4$	potassium permanganate
KOH	potassium hydroxide
λ	wavelength
L	liter(s)
μ	micro

m	meter(s)
M	moles per liter
MeOH	methanol
meq	milliequivalent
min	minute(s)
mol	mole(s)
MPa	megapascal(s)
MW	molecular weight
N_2	nitrogen
N_2H_4	hydrazine
NaCl	sodium chloride
$NaHCO_3$	sodium bicarbonate
$NaNO_2$	sodium nitrite
NaOH	sodium hydroxide
NH_4Cl	ammonium chloride
NH_4OH	ammonium hydroxide
nm	nanometer
NMP	*N*-methyl-2-pyrrolidone
NMR	nuclear magnetic resonance
Ω	ohm
PAA	polyamic acid
PAN	polyacrylonitrile
PI	polyimide
ppm	parts per million (spectral)
psi	pounds per square inch
p-SWCNT	purified single-walled carbon nanotube
PTFE	poly(tetrafluoroethylene)

s	second(s); singlet (spectral)
S	Siemens
S-CCG	surfactant-wrapped chemically converted graphene
SDBS	sodium dodecylbenzenesulfonate
SEM	scanning electron microscope
SO_3	sulfur trioxide
SWCNT	single-walled carbon nanotube
TEM	transmission electron microscope
TGA	thermogravimetric analysis
THF	tetrahydrofuran
US-SWCNT	ultra-short single-walled carbon nanotube
UV-vis	ultraviolet-visble
VDW	van der Waals
VPI	vacuum pressure impregnation
W	Watts
wt %	weight percent
XPS	x-ray photoelectron spectroscopy
XRD	x-ray diffraction

Thesis Summary

This thesis describes the manipulation of carbon nanomaterials specifically single-walled carbon nanotubes (SWCNTs), graphene and graphene derivatives namely graphene oxide (GO) and chemically converted graphene (CCG).

Chapter 1 describes the use of oxidized SWCNT as a nanofiller for spinning fibers comprised of ultra-short SWCNTs (US-SWCNTs) and polyacrylonitrile (PAN). At 5 wt% loading of US-SWCNTs the reinforcement in modulus of PAN is observed to be at 50 %. Chapter 2 presents a processing technique for a hybrid fiber comprised of SWCNTs and polyimide (PI). The acid spun SWCNT fibers were subjected to vacuum pressure impregnation (VPI) using a PI precursor followed by thermal imidization resulting in the enhancement of tensile strength of SWCNT fiber.

Chapter 3 extends the utility of the aryl diazonium functionalization protocols developed for carbon nanotubes (CNTs) and graphite to surfactant-wrapped CCG. The resulting functionalized CCG (f-CCG) sheets exhibit better solubility in polar aprotic solvents compared to CCG. Chapter 4 presents work that converts GO to CCG under Birch reduction conditions. Upon treatment with alkyl or aryl iodides the CCG sheets are functionalized with alkyl or aryl moieties thereby increasing solubility in non-polar organic solvents.

Chapter 5 presents work on the incorporation of GO sheets in a PI matrix resulting in a conductive composite film with low moisture absorption. The GO is transformed to thermally converted graphene (TCG) concomitantly during imidization.

The incorporation of TCG in the PI matrix also resulted in significant reinforcement in the mechanical properties of the resulting composite films.

Chapter 6 explores a fluid phase processing technique to spontaneously exfoliate graphene from graphite in chlorosulfonic acid ($ClSO_3H$) without the aid of ultrasound. The exfoliation is facilitated by the protonation of graphene sheets, resulting in the disruption of van der Waals interaction between the graphene sheets. The dispersions have concentrations as high as ~ 1000 ppm.

Chapter 7 is an extension of the work described in Chapter 3 for use in composites fabrication. The f-CCG sheets and PAA were employed in fabricating thin composite films using layer-by-layer assembly technique. The assembly is governed by the acid-base interaction between the aniline moieties in f-CCG and the carboxylic acid groups in PAA.

Chapter 8 discusses the edge-selective functionalization of graphene dispersed in $ClSO_3H$ via in-situ generation of aryl diazonium salt. The resulting functionalized grapehene sheets exhibited better solubility in DMF and have minimal defects on the basal planes thereby preserving the desirable characteristics arising from the sp^2 honeycomb lattice.

Introduction

The discovery of fullerenes by Smalley, Curl and Kroto in 1985[1] can be considered the catalyst that paved the way for the unification of the different facets of physical sciences into nanotechnology. Fullerene, the third allotrope of carbon, in addition to graphite and diamond, renewed interest in carbon-based materials. A decade after the intensive research in fullerenes began, results produced by that work caused researchers to expand their curiosity to 1D carbon nanotubes (CNTs) that possess interesting electronic, thermal and mechanical properties.[2] Currently, the focus has shifted to graphene; the pace of the research draws parallels with research on CNTs since the former often exhibits similar or superior properties to the latter. Graphene is a 2-dimensional one-atom-thick network of sp^2 carbons arranged in a perfect crystalline lattice.[3] Earlier studies on monatomic thick graphene sheets predicted that it was too unstable to exist in its free state[4-6] until the first isolation in 2004 by Novoselov.[3] Graphene has been used to describe carbon nanostructures such as the 0D fullerenes, 1D CNTs and 3D graphite (Figure 1)[7,8] but ironically it is the last system to be studied experimentally.

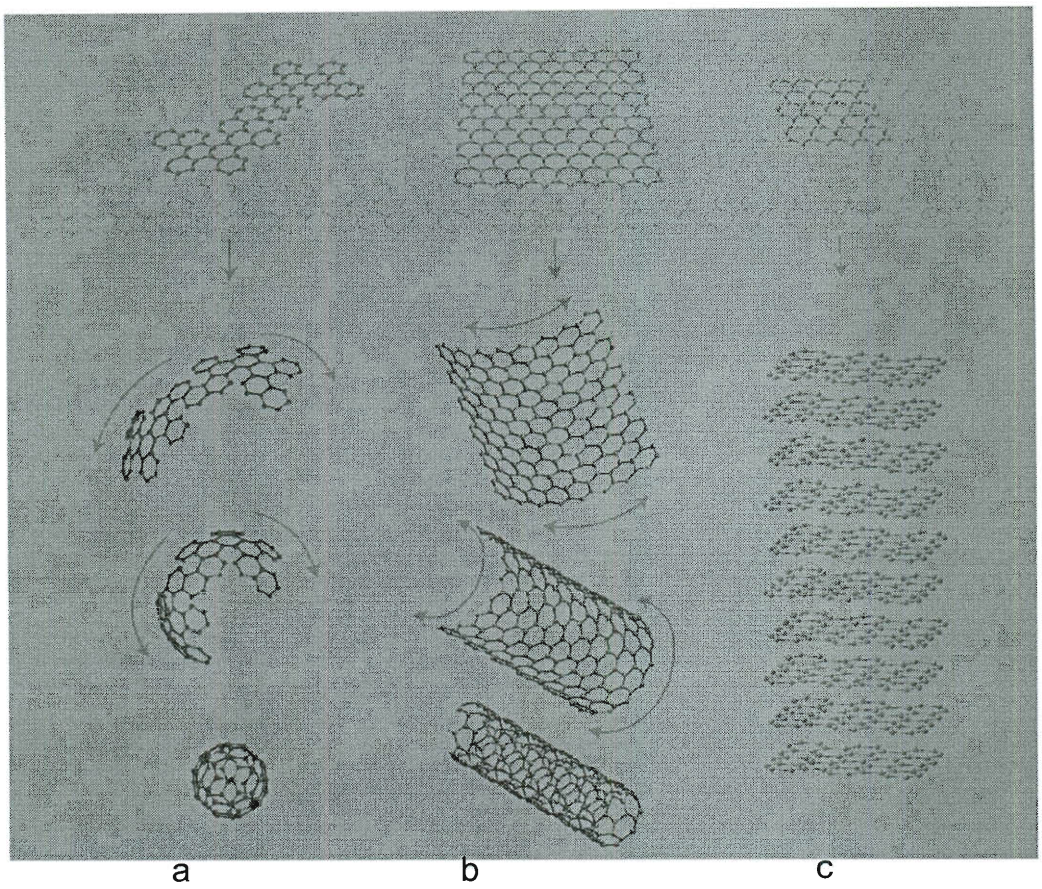

Figure 1. Graphene as the parent material of carbon nanostructures: (a) wrapped up into 0D fullerene, (b) rolled up into 1D nanotube and (c) stacked into 3D graphite.[8]

Carbon Nanotubes

Individual single-walled carbon nanotubes (SWCNTs) possess remarkable mechanical (tensile strength ~37 GPa, Young's modulus ~1.25 TPa),[9-11] electrical (electrical resistivity 0.1 m.cm)[12-14] and thermal (thermal conductivity ~ 3000 W/m.K)[15-16] properties that equal or surpass those of other benchmark materials such as steel, copper, diamond and high performance polymeric fibers.[2,17-18] In addition, the density of CNTs (~1.3 g/cm^3) is lower than that in commercial carbon fibers (1.8 – 1.9 g/cm3).[16]

This excellent combination of properties is the main driving force for the interest in the fabrication of macroscopic articles such as fibers and films using SWCNTs. The key application envisioned for SWCNT fibers include thermal management systems, electrical conduits and structural reinforcements for military and aerospace vehicles.

Carbon nanotubes can be considered to be a sheet of graphene rolled into a cylindrical structure (Figure 2).[19] If only one graphene cylinder exists, the nanotubes are termed single-walled carbon nanotubes (SWCNTs); several concentric cylinders are referred to as multi-walled carbon nanotubes (MWCNTs). A sheet of graphene can be rolled up in a number of ways and the nomenclature of carbon nanotubes is given by an integer pair (n,m) which refers to the tube's chiral vector. For example, a (10,10) tube denotes a graphene sheet that is rolled by going ten cells in the a_1 direction and ten cells in the a_2 direction. The chiral vector also defines SWNT chirality and electronic properties. The vectors (n,0) and (0,m) denote zigzag nanotubes and the vectors (n,n) denote armchair nanotubes. Both the armchair and zigzag nanotubes have a mirror plane and are therefore achiral; all other vectors (n,m) correspond to chiral nanotubes (Figure 3).[20]

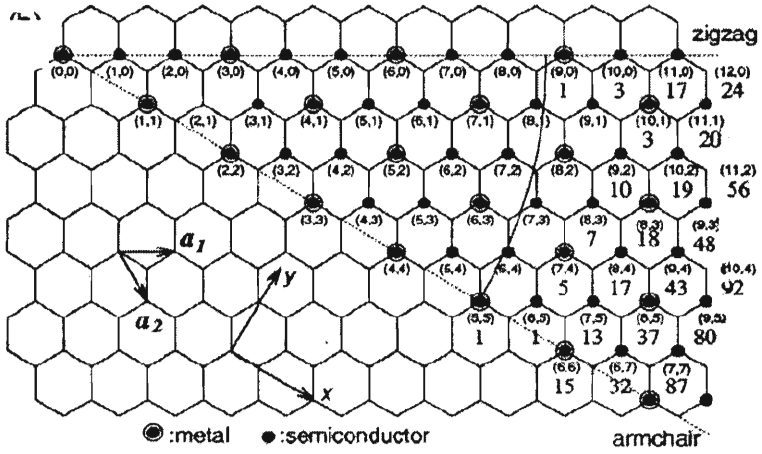

Figure 2. Possible vectors for general carbon nanotubes including zigzag, armchair, and chiral nanotubes. The encircled dots are for metallic nanotubes and the single dots are for semiconducting nanotubes.[19]

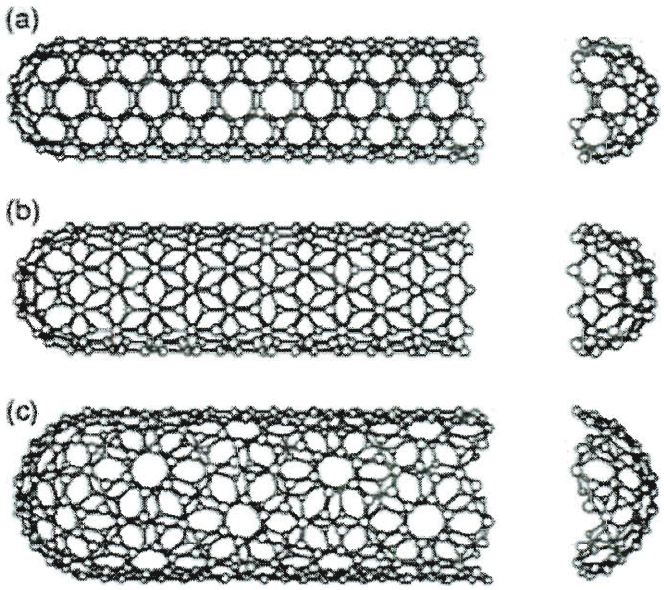

Figure 3. (a) An armchair (5,5) nanotube, (b) a zigzag (9,0) nanotubes and (c) a chiral (10,5).[20]

The discovery of MWCNTs produced using arc-discharge technique[21] began a flurry of interest in synthesis of CNTs. This discovery was followed by the production of high quality MWCNT growth by arc discharge in gram quantities[22] and later on by the production of SWCNT.[23] Further developments also led to the HiPco process based on the decomposition of CO by iron clusters formed from thermal decomposition of iron pentacarbonyl.[24] This process has high yield (>70%) and can run continuously with a production rate of 1g/h. In addition to arc-discharge,[22] and the high yielding CVD technique, laser vaporization[25] is also capable of producing CNTs.

Neat macroscopic fibers have been spun from CNTs and some processes have the promise of scalability. Spinning techniques such as fluid phase processing[26-29] and dry spinning by drawing from nanotubes arrays or "forests"[17,30-31] have resulted in fibers with properties that rival those of existing commercial fibers.[32] Incorporation of CNTs into polymeric fibers is another approach being explored to take advantage of the interesting mechanical properties of CNTs.[33-36]

Graphene

The isolation of graphene in 2004 by Novoselov[3] involved micromechanical cleavage of highly ordered pyrolytic graphite (HOPG) using adhesive tape. The ensuing characterizations performed on the 2D crystal showed that it has a Young's modulus of ~1100 GPa,[37] fracture strength ~ 125 GPa,[37] electron mobility of up to 200,000 $cm^2/V•s$,[38] thermal conductivity of ~ 5000 $W/m•K$[39] and surface area of 2630 m^2/g.[40]

The ballistic electron transport is comparable to the length scales reported for SWCNTs.[7,8]

Graphene obtained from the micromechanical cleavage affords crystalline single sheets and is central to many fundamental studies involving graphene. However, it is likely that this route would be very difficult to scale-up and allow access to bulk quantities. One alternative method to obtain graphene sheets is by liquid phase exfoliation of graphite with the aid of ultrasound in organic solvents.[41-43] Graphene has also been dispersed in aqueous solutions by sonication and stabilization using surfactants.[44] In addition, chemical vapor deposition (CVD) techniques have been shown to be a viable technique to grow thin and highly crystalline graphitic layers atop catalysts.[45-47] Epitaxial growth by annealing SiC at temperatures as high as 2000 °C is a promising method for producing graphene that is deposited directly on the SiC wafer.[48] Both CVD and epitaxial growth will likely be among the dominant growth methods for future high performance graphene electronics.

For bulk applications however, such as fabrication of nanocomposites, the abovementioned methods fall short in giving access to large quantities of graphene. One of the most practical approaches to circumvent the low yield is by employing harsh oxidation chemistry that dates back more than 150 years.[49-51] The oxidation of graphite to GO allows for a high yielding route to exfoliated carbon nanosheets. The GO sheets disperse readily in water due to the presence of hydrophilic oxygen groups on the basal planes and edges,[52-54] although there may be variations depending on which oxidation method is used.[55] While the graphitic nature of the resulting nanosheets is highly compromised by the oxidation, leading to a loss of conductivity, reduction by chemical,[56] thermal,[57-58] or electrochemical[59] methods results in partial recovery of the graphitic

character. The partial restoration of the graphitic network can be determined by the conductivity of the films when these nanosheets are deposited on different substrates,[60] by powder X-Ray diffraction data,[61] and by electron diffraction pattern data.[62]

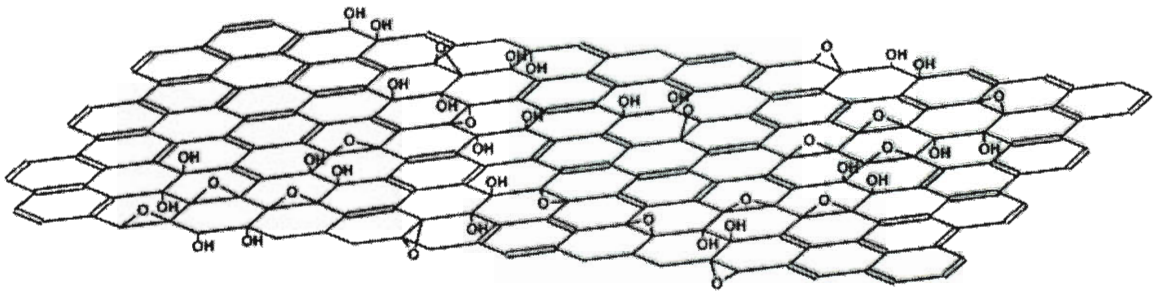

Fig. 3. Structural model for GO.[64]

Dispersion of graphene sheets and their derivatives, in polymers and ceramic precursors has been shown to enhance mechanical properties and impart electrical conductivity[62-64] and reduce flammability.[65-67]

Functionalization of Graphene Sheets

The chemistry of fullerenes[68] and CNTs[69,71-75] has been well-developed, turning these carbon nanostructures into useful building blocks and fillers. Similar chemical methods have been employed on graphite and its derivatives as well.[76-82] Similar to SWCNTs, carrying out functionalization of graphene sheets would improve solubility in solvents and improve interfacial adhesion in matrices.[83] In contrast to graphite-polymer composites, exfoliated graphene sheets dispersed in matrices would allow better load transfer at lower volume fractions.

Functionalized graphene sheets obtained from rapid thermal expansion of GO have been shown to yield individual sheets that disperse readily in a variety of solvents.[57-58] Furthermore, derivatization of GO via the oxygen groups[84-88] have rendered the initially hydrophilic sheets hydrophobic. However, to take advantage of the desirable thermal and electrical conductivities of graphene, reduction has to be employed. Hydrazine has been the reducing agent of choice employed in partially restoring the graphitic network leading to chemically converted graphene (CCG).[89-93] Hydroquinone and HI have also been shown to be efficient in deoxygenating the oxidized graphitic network.[53] With the restoration of the aromatic network, it is then possible to employ the same reaction chemistry used in bulk graphite and CNTs. The major advantage to going through GO route in order to make graphene is the access to large quantities of single to few layer sheets.

For graphene sheets to be effective reinforcing agents in matrices, functionalization is essential. Not only will functional groups improve solubility during bulk processing, tailoring the functionality would also allow for better interfacial adhesion. While GO sheets are stable in aqueous solutions, the CCG is still the preferred material since it resembles the pristine graphene obtained from mechanical exfoliation. CCG has been stabilized in solvents such as water by taking advantage of surfactants or polymers to physically prevent close contact of the graphene sheets. Without these precautions, the CCG sheets would likewise end up restacking to turbostratic graphite.[52-53,94]

References

1. Kroto, H. W.; Heath, J. R.; O'Brien, S. C.; Curl, R. F.; Smalley, R. E. *Nature* **1985,** *318*, 162.
2. Baughman, R. H.; Zakhidov, A. A.; de Heer, W. A. *Science* **2002,** *297*, 787.
3. Novoselov, K. S.; A, K.; Geim, A. K.; Morozov, S. V.; Jiang, D.; Zhang, Y.; Dubonos, S. V.; Grigorieva, I. V.; Firsov, A. A. *Science* **2004,** *306*, 666.
4. Slonczewski, J. C.; Weiss, P. R. *Phys. Rev.* **1958,** *109*, 272.
5. Venables, J. A.; Spiller, G. D. T.; Hanbucken, M. *Rep. Prog. Phys.* **1984,** *47*, 399-459.
6. Evans, J. W.; Thiel, P. A.; Bartelt, M. C. *Surface Sci. Rep.* **2006,** *61*, 1-128.
7. Charlier, J.-C.; Eklund, P. C.; Zhu, J.; Ferrari, A. C. *Carbon Nanotubes: Advanced Topics in the Synthesis, Structure, Properties and Applications*. Springer: Berlin, 2008.
8. Geim, A. K.; Novoselov, K. S. *Nature Mater.* **2007,** *6*, 183-191.
9. Krishnan, A.; Dujardin, E.; Ebbesen, T. W.; Yianilos, P. N.; Treacy, M. M. J. *Phy.l Rev. B* **1998,** *58*, 14013.
10. Walters, D. A.; Ericson, L. M.; Casavant, M. J.; Liu, J.; Colbert, D. T.; Smith, K. A.; Smalley, R. E. *App. Phys. Lett.* **1999,** *74*, 3803-3805.
11. Yu, M. F.; Files, B. S.; Arepalli, S.; Ruoff, R. S. *Phys. Rev. Lett.* **2000,** *84*, 5552.
12. Thess, A.; Lee, R.; Nikolaev, P.; Dai, H.; Petit, P.; Robert, J.; Xu, C.; Lee, Y. H.; Kim, S. G.; Rinzler, A. G.; Colbert, D. T.; Scuseria, G. E.; Tomanek, D.; Fischer, J. E.; Smalley, R. E. *Science* **1996,** *273*, 483-487.
13. Tans, S. J.; Devoret, M. H.; Dai, H.; Thess, A.; Smalley, R. E.; Geerligs, L. J.; Dekker, C. *Nature* **1997,** *386*, 474.

14. McEuen, P. L.; Fuhrer, M. S.; Hongkun, P. *IEEE Trans. Nanotechnol.* **2002,** *1*, 78-85.

15. Hone, J.; Whitney, M.; Piskoti, C.; Zettl, A. *Phys. Rev. B* **1999,** *59*, R2514.

16. Che, J.; Cagin, T.; Goddard, W. A., *Nanotechnology* **2000,** *11*, 65.

17. Li, Y.; Kinloch, I. A.; Windle, A. H., *Science* **2004,** *304*, 276.

18. Baughman, R. H.; Zakhidov, A. A.; de Heer, W. A. *Science* **2002,** *297*, 787-792.

19. Dresselhaus, M. S.; Avouris, P., *Introduction to Carbon Materials. Carbon Nanotubes: Synthesis, Structure, Properties and Applications.* Springer-Verlag: Berlin, 2001.

20. Dresselhaus, M. S.; Dresselhaus, G.; Saito, R. *Carbon* **1995,** *33*, 883-891.

21. Iijima, S., *Nature* **1991,** *354*, 56.

22. Ebbesen, T. W.; Ajayan, P. M. *Nature* **1992,** *358*, 220-222.

23. Bethune, D. S.; Klang, C. H.; de Vries, M. S.; Gorman, G.; Savoy, R.; Vazquez, J.; Beyers, R. *Nature* **1993,** *363*, 605-607.

24. Nikolaev, P.; Bronikowski, M. J.; Bradley, R. K.; Rohmund, F.; Colbert, D. T.; Smith, K. A.; Smalley, R. E. *Chem. Phys. Lett.* **1999,** *313*, 91-97.

25. Eklund, P. C.; Pradhan, B. K.; Kim, U. J.; Xiong, Q.; Fischer, J. E.; Friedman, A. D.; Holloway, B. C.; Jordan, K.; Smith, M. W. *Nano Lett.* **2002,** *2*, 561-566.

26. Miaudet, P.; Badaire, S.; Maugey, M.; Derre, A.; Pichot, V.; Launois, P.; Poulin, P.; Zakri, C. *Nano Lett.* **2005,** *5*, 2212-2215.

27. Ericson, L. M.; Fan, H.; Peng, H.; Davis, V. A.; Zhou, W.; Sulpizio, J.; Wang, Y.; Booker, R.; Vavro, J.; Guthy, C.; Parra-Vasquez, A. N. G.; Kim, M.; Ramesh, S.; Saini, R. K.; Kittrell, C.; Lavin, G.; Schmidt, H. K.; Adams, W. W.; Billups, W.

E.; Pasquali, M.; Hwang, W. F.; Hauge, R. H.; Fischer, J. E.; Smalley, R. E. *Science* **2004,** *305*, 1447.

28. Davis, V. A.; Ericson, L. M.; Parra-Vasquez, A. N. G.; Fan, H.; Wang, Y.; Prieto, V.; Longoria, J. A.; Ramesh, S.; Saini, R. K.; Kittrell, C.; Billups, W. E.; Adams, W. W.; Hauge, R. H.; Smalley, R. E.; Pasquali, M. *Macromolecules* **2004,** *37*, 154.

29. Ramesh, S.; Ericson, L. M.; Davis, V. A.; Saini, R. K.; Kittrell, C.; Pasquali, M.; Billups, W. E.; Adams, W. W.; Hauge, R. H.; Smalley, R. E. *J. Phys. Chem. B* **2004,** 108, 8794.

30. Zhang, M.; Atkinson, K.; Baughman, R. H. *Science* **2005,** *306*, 1358.

31. Zhang, X.; Li, Q.; Holesinger, T. G.; Arendt, P. N.; Huang, J.; Kirven, P. D.; Clapp, T. G.; DePaula, R. F.; Liao, X.; Zhao, Y.; Zheng, L.; Peterson, D. E.; Zhu, Y. *Adv. Mater.* **2007,** *19*, 4198-4201.

32. Davis, V. A. *Phase Behavior and Rheology of Single-Walled Carbon Nanotubes (SWNTs) in Superacids with Application to Fiber Spinning.* PhD Thesis, Rice University, 2006.

33. Andrews, R.; Jacques, D.; Rao, A. M.; Rantell, T.; Derbyshire, F.; Chen, Y.; Chen, J.; Haddon, R. C. *Appl. Phys. Lett.* **1999,** *75*, 1329.

34. Quin, D.; Dickey, E. C.; Andrews, R.; Rantell, T. *Appl. Phys. Lett.* **2000,** *76*, 20.

35. Kumar, S.; Doshi, H.; Srinivasrao, M.; Park, J. O.; Schiraldi, D. A. *Polymer* **2002,** *43*, 1701.

36. Kumar, S.; Dang, T. D.; Arnold, F. E.; Bhattacharyya, A. R.; Min, B. G.; Zhang, X.; Vaia, R. A.; Park, C.; Adams, W. W.; Hauge, R. H.; Smalley, R. E.; Ramesh, S.; Willis, P. A. *Macromolecules* **2002,** *35*, 9039-9043.

37. Lee, C.; Wei, X. D.; Kysar, J. W.; Hone, J. *Science* **2008,** *321*, 385-388.

38. Bolotin, K. I.; Sikes, K. J.; Jiang, Z.; Klima, M.; Fudenberg, G.; Hone, J.; Kim, P.; Stormer, H. L. *Solid State Commun.* **2008,** *146*, 351.

39. Balandin, A. A.; Ghosh, S.; Bao, W. Z.; Calizo, I.; Teweldebrhan, D.; Miao, F.; Lau, C. N. *Nano Letters* **2008,** *8*, 902-907.

40. Stoller, M. D.; Park, S.; Zhu, Y.; An, J.; Ruoff, R. S., Graphene-Based Ultracapacitors. *Nano Lett.* **2008,** *8*, 3498-3502.

41. Hernandez, Y.; Nicolosi, V.; Lotya, M.; Blighe, F. M.; Sun, Z.; De, S.; McGovern, I. T.; Holland, B.; Byrne, M.; Gun'Ko, Y. K.; Boland, J. J.; Niraj, P.; Duesberg, G.; Krishnamurthy, S.; Goodhue, R.; Hutchinson, J.; Scardaci, V.; Ferrari, A. C.; Coleman, J. N. *Nature Nanotechnol.* **2008,** *3*, 563.

42. Blake, P.; Brimicombe, P. D.; Nair, R. R.; Booth, T. J.; Jiang, D.; Schedin, F.; Ponomarenko, L. A.; Morozov, S. V.; Gleeson, H. F.; Hill, E. W.; Geim, A. K.; Novoselov, K. S. *Nano Lett.* **2008,** *8*, 1704-1708.

43. Hamilton, C. E.; Lomeda, J. R.; Sun, Z.; Tour, J. M.; Barron, A. R. *Nano Lett.* **2009**. *ASAP*

44. Lotya, M.; Hernandez, Y.; King, P. J.; Smith, R. J.; Nicolosi, V.; Karlsson, L. S.; Blighe, F. M.; De, S.; Wang, Z.; McGovern, I. T.; Duesberg, G. S.; Coleman, J. N. *J. Am. Chem. Soc.* **2009,** *131*, 3611.

45. Reina, A.; Jia, X.; Ho, J.; Nezich, D.; Son, H.; Bulovic, V.; Dresselhaus, M. S.; Kong, J. *Nano Lett.* **2008,** *9*, 30-35.

46. Kim, K. S.; Zhao, Y.; Jang, H.; Lee, S. Y.; Kim, J. M.; Kim, K. S.; Ahn, J.-H.; Kim, P.; Choi, J.-Y.; Hong, B. H. *Nature* **2009,** *457*, 706-710.

47. Obraztsov, A. N. *Nature Nanotechnol.* **2009,** *4*, 212-213.

48. Berger, C.; Song, Z. M.; Li, X. B.; Wu, X. S.; Brown, N.; Naud, C.; Mayou, D.; Li, T. B.; Hass, J.; Marchenkov, A. N.; Conrad, E. H.; First, P. N.; de Heer, W. A. *Science* **2006,** *312*, 1191.

49. Brodie, B. *Ann. Chim. Phys.* **1855,** *45*, 351.

50. Hummers, W.; Offeman, R. E. *J. Am. Chem. Soc.* **1958,** *80*, 1339.

51. Staudenmaier, L. *Ber. Dtsch. Chem. Ges.* **1898,** *31*, 1481.

52. Lerf, A.; He, H.; Forster, M.; Klinowski, J. *J. Phys. Chem. B* **1998,** *102*, 4477-4482.

53. He, H. Y.; Riedl, T.; Lerf, A.; Klinowski, J. *J. Phys. Chem. B* **1996,** *100*, 19954.

54. Szabo, T.; Berkesi, O.; Forgo, P.; Josepovits, K.; Sanakis, Y.; Petridis, D.; Dekany, I. *Chem. Mater.* **2006,** *18*, 2740-2749.

55. Boehm, H. P.; Scholtz, W., *Z. Anorg. Allg. Chem.* **1965,** *335*, 74.

56. Stankovich, S.; Dikin, D. A.; Piner, R.; Kohlhaas, K. M.; Kleinhammes, A.; Jia, Y.; Wu, Y.; Nguyen, S. T.; Ruoff, R. S. *Carbon* **2007,** *45*, 1558.

57. McAllister, M. J.; Li, J.-L.; Adamson, D. H.; Schniepp, H. C.; Abdala, A. A.; Liu, J.; Herrera-Alonso, M.; Milius, D. L.; Car, R.; Prud'homme, R. K.; Aksay, I. A. *Chem. Mater.* **2007,** *19*, 4396-4404.

58. Schniepp, H. C.; Li, J. L.; McAllister, M. J.; Sai, H.; Herrera-Alonso, M.; Adamson, D. H.; Prud'homme, R. K.; Car, R.; Saville, D. A.; Aksay, I. A., *J. Phys. Chem. B* **2006,** *110*, 8535.

59. Voloshin, A. G.; Kolesnikova, I. P., *Elektrokhimiya* **1980,** *16*, 270.

60. Gilje, S.; Han, S.; Wang, M.; Wang, K. L.; Kaner, R. B., *Nano Lett.* **2007,** *7*, 3394.

61. Bourlinos, A. B.; Gournis, D.; Petridis, D.; Szabo, T.; Szeri, A.; Dekany, I., *Langmuir* **2003,** *19*, 6050.

62. Stankovich, S.; Dikin, D. A.; Dommett, G. H. B.; Kohlhaas, K. M.; Zimney, E. J.; Stach, E. J.; Piner, R. D.; Nguyen, S. T.; Ruoff, R. S., *Nature* **2006,** *442*, 282-286.

63. He, H.; Klinowski, J.; Forster, M.; Lerf, A., *Chem. Phys. Lett.* **1998,** *287*, 53.

64. Watcharotone, S.; Dikin, D. A.; Stankovich, S.; Piner, R.; Jung, I.; Dommett, G. H. B.; Evmenenko, G.; Wu, S. E.; Chen, S. F.; Liu, C. P.; Nguyen, S. T.; Ruoff, R. S. *Nano Lett.* **2007,** *7*, 1888-1892.

65. Zhang, R.; Hu, Y.; Xu, J.; Fan, W.; Chen, Z.; Wang, Q., *Macromol. Mater. Eng.* **2004,** *289*, 355.

66. Wang, J. Q. and Han, Z. D. *In Fire and Polymers IV: Materials and Concepts for Hazard Prevention*; Wilkie, C. A. and Nelson, G. L., Eds.; American Chemical Society: Washington, DC, 2005; Vol. 922, pp 172– 184.

67. Higginbotham, A. L.; Lomeda, J. R.; Morgan, A. B.; Tour, J. M. *ACS App. Mater. Interfaces* **2009**. *ASAP*

68. Hirsch, A.; Brettreich, M. *Fullerenes, Chemistry and Reactions*. Wiley-VCH: Weinheim, 2005.

69. Tasis, D.; Tagmatarchis, N.; Bianco, A.; Prato, M. *Chem. Rev.* **2006,** *106*, 1105-1136.

70. Bahr, J. L.; Yang, J.; Kosynkin, D. V.; Bronikowski, M. J.; Smalley, R. E.; Tour, J. M. *J. Am. Chem. Soc.* **2001,** *123*, 6536.

71. Bahr, J. L.; Tour, J. M. *Chem. Mater.* **2001,** *13*, 3823.

72. Dyke, C. A.; Tour, J. M. *Nano Lett.* **2003,** *9*, 1215.

73. Dyke, C. A.; Stewart, M. P.; Maya, F.; Tour, J. M., *Synlett.* **2004**, 155.

74. Doyle, C. D.; Rocha, J. D. R.; Weisman, R. B.; Tour, J. M. *J. Am. Chem. Soc.* **2008,** *130*, 6795.

75. Price, B. K.; Tour, J. M. *J. Am. Chem. Soc.* **2006,** *128*, 12899.

76. Chakraborty, S.; Guo, W.; Hauge, R. H.; Billups, W. E. *Chem. Mater.* **2008,** *20*, 3134-3136.

77. Niyogi, S.; Bekyarova, E.; Itkis, M. E.; McWilliams, J. L.; Hamon, M. A.; Haddon, R. C. *J. Am. Chem. Soc.* **2006,** *128*, 7720.

78. Lomeda, J. R.; Doyle, C. D.; Kosynkin, D. V.; Hwang, W. F.; Tour, J. M. *J. Am. Chem. Soc.* **2008,** *130*, 16201.

79. Allongue, P.; Delamar, M.; Desbat, B.; Fagebaume, O.; Hitmi, R.; Pinson, J.; Saveant, J. M. *J. Am. Chem. Soc.* **1997,** *119*, 201.

80. Delamar, M.; Hitmi, R.; Pinson, J.; Saveant, J. M. *J. Am. Chem. Soc.* **1992,** *114*, 5883.

81. Kariuki, J. K.; McDermott, M. T. *Langmuir* **2001,** *17*, 5947.

82. Kariuki, J. K.; McDermott, M. T. *Langmuir* **1999,** *15*, 6534.

83. Mitchell, C. A.; Bahr, J. L.; Arepalli, S.; Tour, J. M.; Krishnamoorti, R. *Macromolecules* **2002,** *35*, 8825.

84. Matsuo, Y.; Nishino, Y.; Fukutsuka, T.; Sugie, Y. *Carbon* **2007,** *45*, 1384.

85. Matsuo, Y.; Fukunaga, T.; Fukutsuka, T.; Sugie, Y. *Carbon* **2004,** *42*, 2117.

86. Matsuo, Y.; Tabata, T.; Fukunaga, T.; Fukutsuka, T.; Sugie, Y. *Carbon* **2005,** *43*, 2875.

87. Niyogi, S. *J. Am. Chem. Soc.* **2006,** *128*, 7720-7721.

88. Stankovich, S.; Piner, R. D.; Nguyen, S. T.; Ruoff, R. S. *Carbon* **2006,** *44*, 3342-3347.

89. Stankovich, S.; Piner, R.; Chen, X.; Wu, N.; Nguyen, S. T.; Ruoff, R. S. *J. Mater. Chem.* **2006,** *16*, 155.

90. Dikin, D. A.; Stankovich, S.; Zimney, E. J.; Piner, R.; Dommett, G. H. B.; Evmenenko, G.; Nguyen, S. T.; Ruoff, R. S. *Nature* **2007,** *448*, 457.

91. Stankovich, S.; Dikin, D. A.; Piner, R. D.; Kohlhaas, K. A.; Kleinhammes, A.; Jia, Y.; Wu, Y.; Nguyen, S. T.; Ruoff, R. S. *Carbon* **2007,** *45*, 1558-1565.

92. Becerril, H. A.; Mao, J.; Liu, Z.; Stoltenberg, R. M.; Bao, Z.; Chen, Y. *ACS Nano* **2008,** *2*, 463.

93. Gomez-Navarro, C.; Weitz, R. T.; Bittner, A. M.; Scolari, M.; Mews, A.; Burghard, M.; Kern, K. *Nano Lett.* **2007,** *7*, 3499.

94. Lerf, A.; He, H.; Riedl, T.; Forster, M.; Klinowski, J. *Solid State Ionics* **1997**, 101.

Chapter 1

Ultra-Short Single-Walled Carbon Nanotube/Polyacrylonitrile Composite Fiber as Carbon Fiber Precursor

1.1 Introduction

In the last two decades, the carbon fiber industry saw a 12 % increase in overall growth and is estimated to hit $2.4 billion in 2014.[1] The key advantage of using a polymeric carbon composites is that its specific strength can be as high as 5 – 10 × higher than that of bulk materials. This is enabled by the small diameter fibers ranging from 5 – 15 μm, that can be obtained.[2] The limit in the diameter is dictated by processing constraints. As improved processes are developed, smaller diameter fibers will yield increased strength in the final fibers and their resulting composites.

Two precursor materials have been developed in the last 40 years for use in producing carbon fibers. One precursor is pitch, derived from petroleum or coal tar, and processed by melt spinning at temperatures as high as 350 °C, thereby making it an energy intensive process.[3] The other standard precursor for carbon fibers is polyacrylonitrile (PAN) that can be processed at lower temperatures using a variety of spinning techniques such as wet, melt, gel or dry jet wet spinning.[3] At present, PAN is the preferred precursor not only because of its good mechanical attributes but also due to

its high carbon yield of up to 50 – 60 % during stabilization and carbonization. Figure 1.1 shows the general scheme for carbon fiber processing using a PAN precursor;[4] the process is similarly employed to isotropic and mesophase pitch (Figure 1.2).[5] To achieve good mechanical properties, the key steps involved in the fabrication of carbon fibers are: (1) stabilization, (2) carbonization and (3) graphitization.[4-6] PAN fibers are stabilized at temperatures between 200 – 300 °C and subsequently carbonized to 1500 °C and then graphitization is achieved at 2700 °C.[7] A more detailed scheme has been provided by Kumar including the changes in the properties (Figures 1.3).[3] Structural changes occur during stabilization, where the linear polymers are converted to a ladder-type structure,[8] leading eventually to a honeycomb carbon-rich framework after carbonization (Figure 1.4). Electrospinning is also being explored because of its capability of achieving diameters in the range of 100 nm that are expected to have a significantly higher tensile strength.[3,9-11]

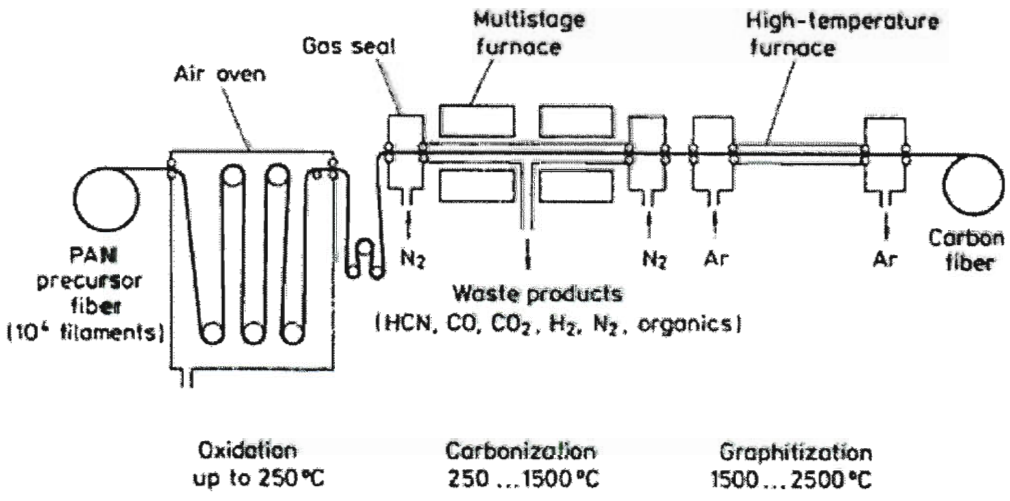

Figure 1.1. General scheme for fabrication of carbon fiber using PAN precursor.[4]

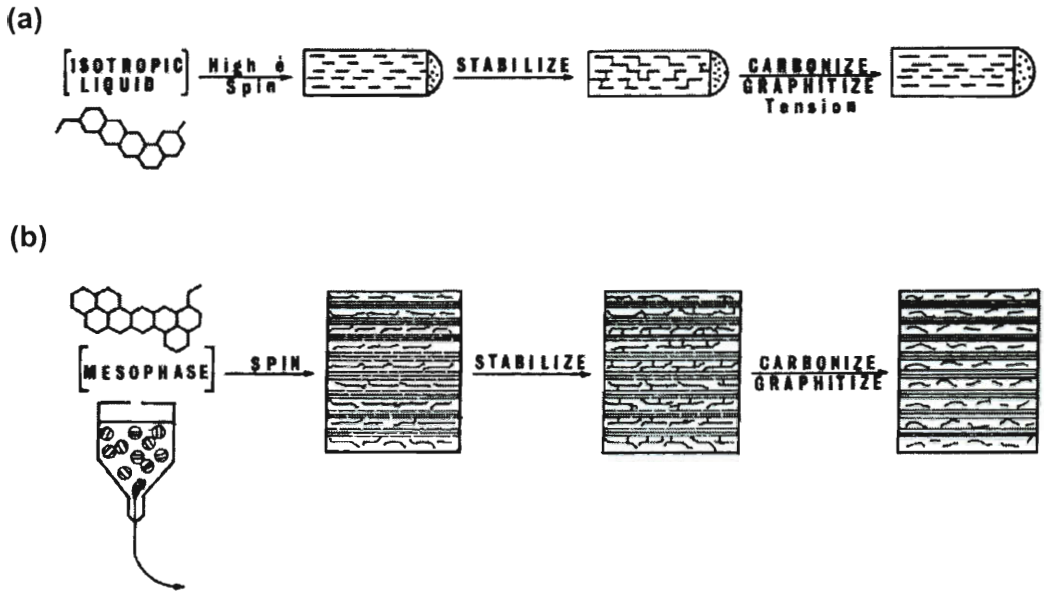

Figure 1.2. General scheme for fabrication of carbon fiber using pitch precursor (a) isotropic pitch and (b) mesophase pitch.[5]

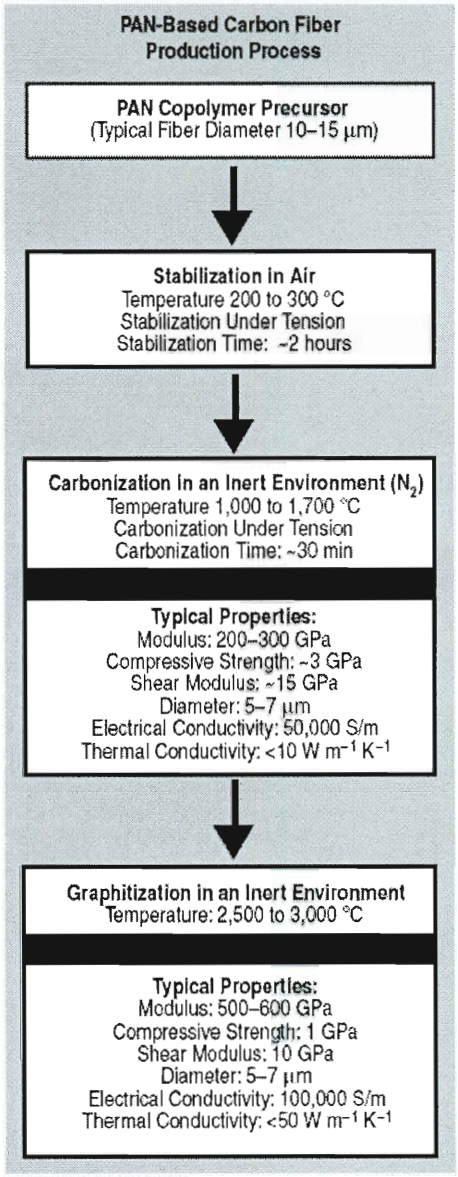

Figure. 1.3. Scheme for carbon fiber processing using PAN precursor.[3]

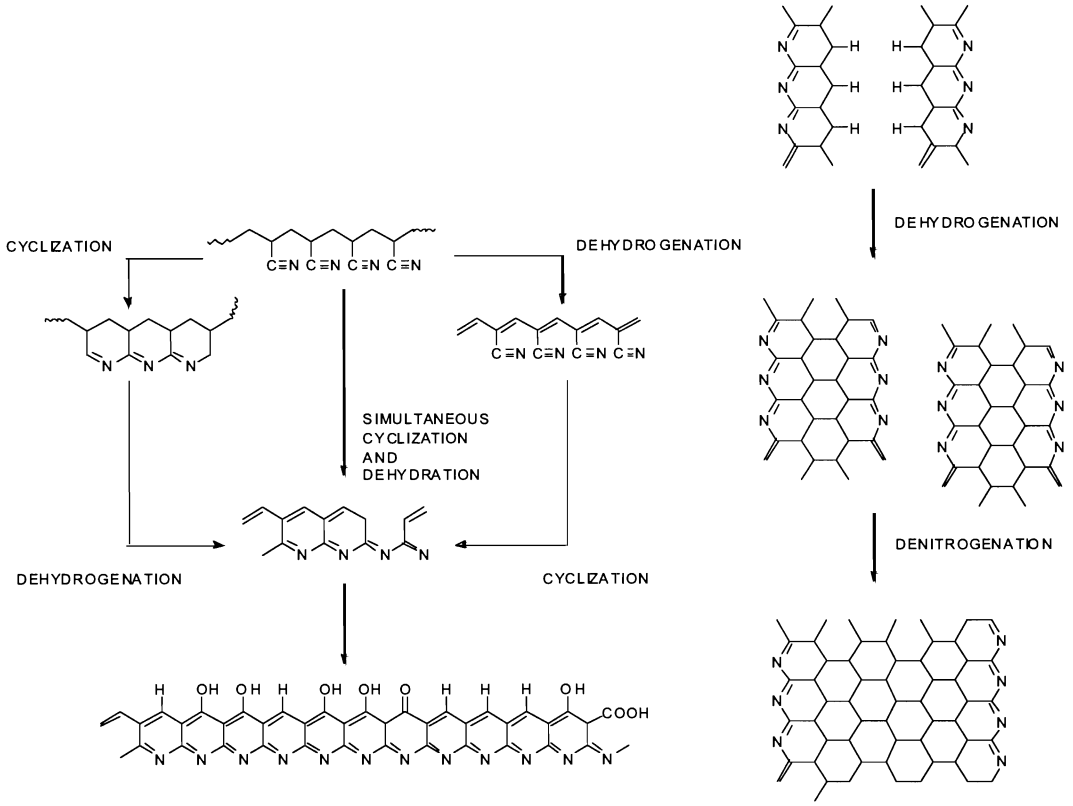

Figure 1.4. Structural changes occurring in PAN fibers during (a) stabilization and (b) carbonization.[8]

Carbon fibers typically possess a tensile strength of 3 – 7 GPa, a modulus of 200 – 500 GPa, a compressive strength of 1 – 3 GPa and a density range of 1.75 – 2 g/cm^3. The properties of various high performance carbon fibers have been summarized by Kumar (Table 1.1).[3] Typically, pitch derived carbon fiber exhibits higher modulus but lower tensile strength compared to PAN.

Table 1.1. Properties of different high performance carbon fibers.[3]

Fiber	Tensile Strength(GPa)	Tensile Modulus(GPa)	Elongation to Break (%)	Density(g/cm^3)	Thermal Conductivity (W/mK)	Electrical Conductivity (S/m)
Hexcel Magnamite® PAN-Based						
AS4	4.27	228	1.87	1.79	--	6.5×10^4
AS4C	4.34	231	1.88	1.78	--	--
IM4	4.79	276	1.74	1.78	--	--
IM8	5.58	304	1.84	1.79	--	--
PV42/850	5.76	292	1.97	1.79	--	--
Cytec Thornel® PAN-Based						
T300	3.75	231	1.4	1.76	8	5.56×10^4
T650/35	4.28	255	1.7	1.77	14	6.67×10^4
T300	3.75	231	1.4	1.76	8	5.56×10^4
Toray Torayca® PAN-Based						
T300	3.53	230	1.5	1.76	--	--
T700SC	4.90	230	2.1	1.80	--	--
M35JB	4.70	343	1.4	1.75	--	--
M50JB	4.12	475	0.9	1.88	--	--
M55J	4.02	540	0.8	1.91	--	--
M30SC	5.49	294	1.9	1.73	--	--
Cytec Thornel® pitch-based						
P-25	1.38	159	0.9	1.90	22	7.69×10^4
P-55S	1.90	379	0.5	1.90	120	1.18×10^5
P-100S	2.41	758	0.3	2.16	520	4.00×10^5
P-120S	2.41	827	0.3	2.17	640	4.55×10^5
K-800X	2.34	896	--	2.20	900-1000	$6.67 \times 10^5 - 8.33 \times 10^5$
K-1100	3.10	965	--	2.20	900-1100	$7.69 \times 10^5 - 9.09 \times 10^5$

Similar to continuous progress in polymeric fibers, but starting just in recent years, the development of carbon nanotube (CNT) fibers has seen promising results. Several spinning techniques have been reported such as fluid phase processing,[12,13] and drawing from nanotubes arrays or "forests".[14,15] Incorporation of CNTs into polymeric fibers is another approach being explored to take advantage of the interesting mechanical properties of CNTs.[16-19]

This work focuses on the use of PAN as a host matrix in the development of single wall carbon nanotube (SWCNT)/PAN composite fibers that might be good candidates for the next generation of carbon fibers. Other reports about CNT/PAN composite fibers use long purified CNTs dispersed in *N,N'*-dimethylformamide (DMF) and they were spun using a gel-spinning process that is normally employed for high density polyethylene (HDPE).[11] The approach taken in this project is to use ultra-short (US)-SWCNTs derived form oxidative treatment of purified HiPco CNTs in a mixture of oleum and HNO_3, conditions that have been shown to cut and simultaneously introduce exceedingly high ratios of oxygen functionality into the CNT structure.[20]

1.2 Results and Discussion

The spinning dope was prepared by dissolving 5:95 weight ratio of US-SWCNT:PAN in DMSO. This route circumvents the need for distillation of a solvent, such as DMF, from the dilute suspension to increase the concentration to a spinnable material, which is normally from 13 – 20 wt % dissolved solids.[21] The preparation of the dope was accomplished by dispersing US-SWCNTs (30-60 nm in length) in DMSO containing 1 wt % of triethanolamine, followed by the addition to a vacuum dried PAN polymer yielding 20 wt % of solids (Figure 1.5). The choice of solvent for dispersion of

CNTs was determined by dissolving 1.25 wt % of US-SWCNTs in DMSO, 99:1 DMSO:triethylamine and 99:1 DMSO:triethanolamine. Figure 1.6 shows the ability of triethanolamine to effectively minimize aggregation in DMSO. Triethylamine also exhibited good dispersion of US-SWCNTs, in contrast to DMSO, but is somewhat inferior compared to triethanolamine. This would be an important consideration during processing as it allows good dispersion of the US-SWCNTs and minimize stress concentration points due to the presence of large aggregates.[2]

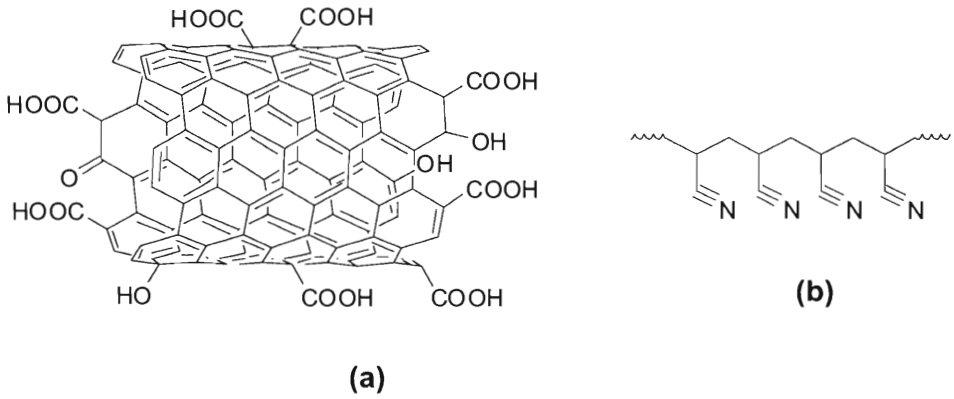

Figure 1.5. (a) Model of US-SWCNT and (b) structure of PAN

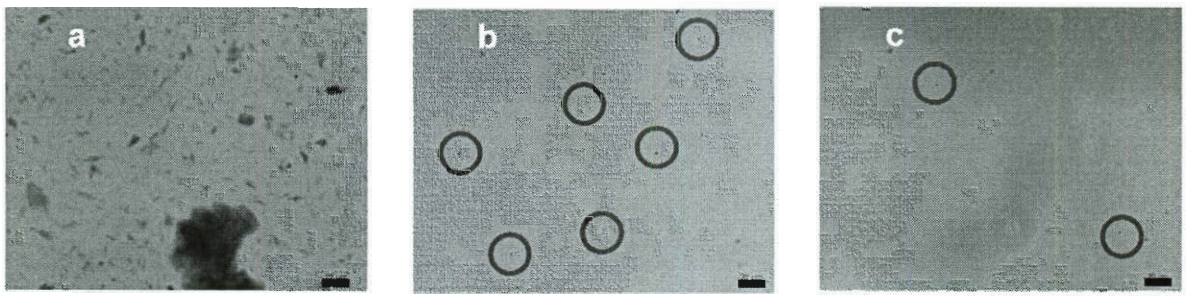

Figure 1.6. Optical micrographs of US-SWCNTs dispersion in (a) DMSO, (b) 99:1 DMSO:triethylamine, and (c) 99:1 DMSO:triethanolamine.

The viability of dry-jet wet-spinning of PAN in DMSO was evaluated and air gaps up to 30 mm are possible since instability was observed at 40 mm.[22] The spinnability of fibers depends on several parameters such as the rheology, temperature, spinneret size and shape, extrusion rate and coagulation efficiency.[22,23] The dope was spun at room temperature using a custom-built piston-driven extruder for dry-jet wet-spinning process (Scheme 1.1). The air gap was varied between 5 mm and 10 mm with an initial spin draw ratio of 10. There was little difference observed between the air gaps, therefore 5 mm was used as the air gap throughout this work.

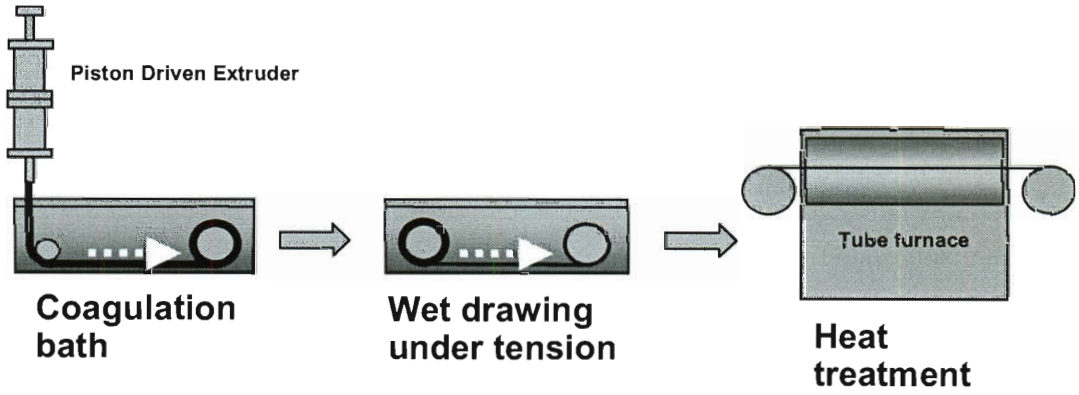

Scheme 1.1. Spinning and processing of carbon fiber using US-SWCNT/PAN precursor.

The advantage of dry-jet wet spinning over wet-spinning is that the fiber collapses upon drying with the latter process while collapse is minimized with the former process. This process then combines the high degree of jet stretch observed in dry spinning and the ability to control coagulation by selection of the proper bath. Since the process involves successive stretching and orientation up to the stabilization stage, dry-jet wet-

spinning allows for relaxation hence the orientation is minimized.[7] The choice of coagulation bath during spinning was 80:20 DMSO:H_2O (v/v). The use of pure DMSO resulted in very soft fibers due to insufficient coagulation. The presence of water facilitates the removal of DMSO and increases the polymer chain interaction.[22] The use of pure water as a coagulation bath was attempted but the solvent exchange was found to be so rapid that the PAN crystallized prematurely and resulted in fibers that could not be stretched after spinning. The optimum conditions to minimize the formation of voids and prevent rapid crystallization was to slowly decrease the concentration of DMSO while increasing the amount of water. From the initial coagulation bath of 80:20 DMSO:H_2O, the fibers were stretched to 2× their original length by doubling the velocity of the take-up roll, and stretching the fibers while immersed in a 60:40 DMSO:H_2O coagulation bath. The third round of fiber stretching was conducted in a hot water bath set at 80 °C with the fiber stretch maintained at 2×. The temperature of the bath was maintained using an immersion heater (Cole-Parmer EW-03046-22) set at the maximum setting. At this final stage, the spin draw ratios of the fibers have nominal values of 45 – 50, although a spin draw ratio of 60 can be achieved.

The stabilization of fibers was investigated by slowly heating the fibers in the air in an oven. The fibers were mounted on a quartz stand and stretch was applied by mounting a stainless 2.5 g steel weight on a bundle of fibers (Figure 1.7). The fibers were heated from room temperature at a rate 1 °C/min to 285 °C and held at 5 h or 10 h.

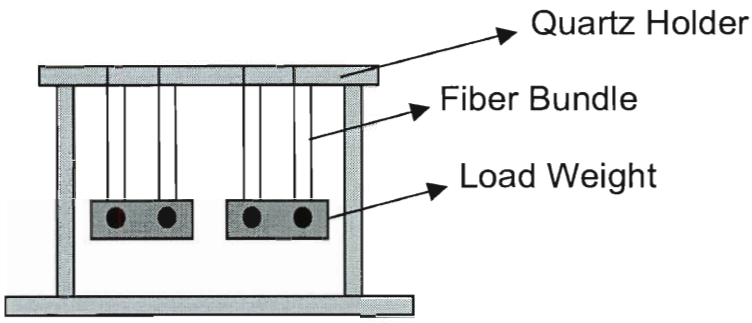

Figure 1.7. Experimental setup for the stabilization of fibers.

The resulting stabilized fibers were analyzed by FT-IR, monitoring the nitrile peak at 2240 cm^{-1}. Based on the data obtained from FT-IR analysis (Figure 1.8), the stabilization time of 5 h is not enough to completely form the ladder structures, since the nitrile peak was still evident. After 10 h of stabilization, however, the band at 2240 cm^{-1} had disappeared, signifying the conversion of the linear PAN chains to the honeycomb framework. After stabilization, the resulting fibers showed a significant decrease in tensile strength.

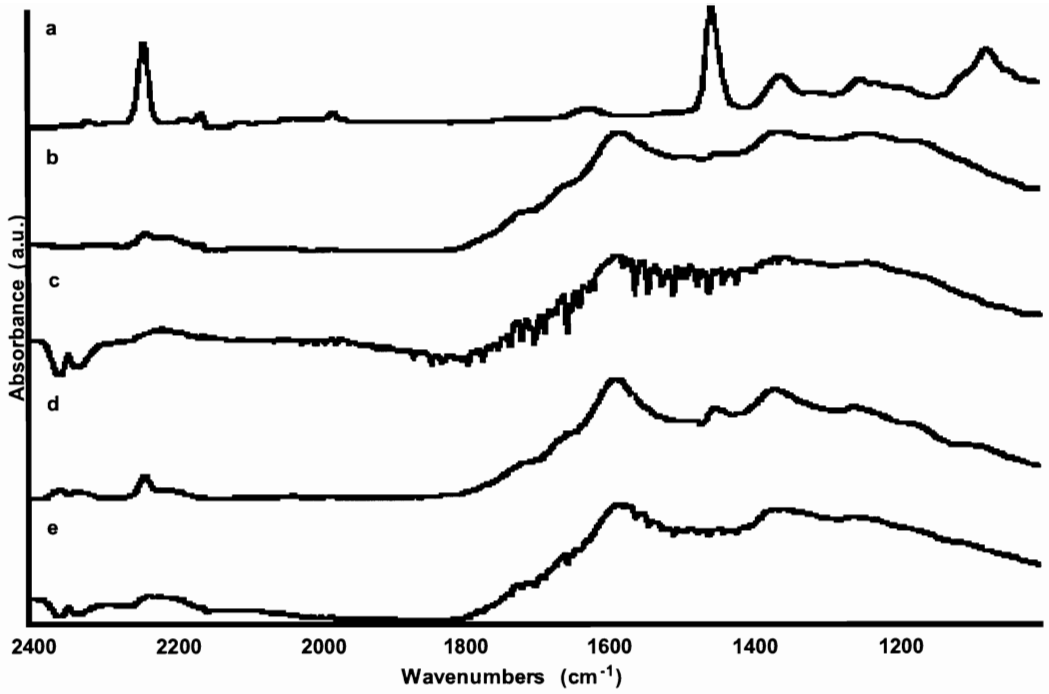

Figure 1.8. FT-IR spectra of (a) PAN, (b) PAN stabilized at 285 °C for 5 h, (c) PAN stabilized at 285 °C for 10 h, (d) US-SWCNT/PAN stabilized at 285 °C for 5 h, (e) US-SWCNT/PAN stabilized at 285 °C for 10 h. The disappearance of the nitrile peak at 2240 cm^{-1} indicates the completion of the conversion of PAN to the cyclic structure. The spectra were collected by pressing bundles of fibers onto the ATR-IR fixture.

The fracture surfaces of the fiber analyzed by SEM exhibit excellent dispersion of the US-SWCNTs in the PAN matrix. While the as-spun fibers do not show differences in morphology on the fracture surface with respect to the neat PAN fibers (Figure 1.9 and 1.10), after oxidative stabilization in air, the composite fiber show long fibrils that may be indicative of the presence of SWCNTs in the matrix (Figures 1.11 and 1.12). The fibrils are as long as 500 nm, hence they are longer than US-SWCNTs, that have a length

distribution of only 30 – 60 nm. Most likely, the US-SWCNTs, due to the high fractions of COOH in the carbon framework, are acting as a catalyst in the cyclization process of PAN similar to the action of itaconic acid.[24]

The carbonization conditions are currently being optimized towards achieving SWCNT/carbon composite fibers. With this approach, it is hoped that superior dispersion of SWCNTs in the carbon fiber matrix will be realized. Another key attribute of the process is the straightforward method of dispersing SWCNTs into the matrix without employing large volumes of solvents or additional distillation steps that would be significant issues in scaling-up the process.

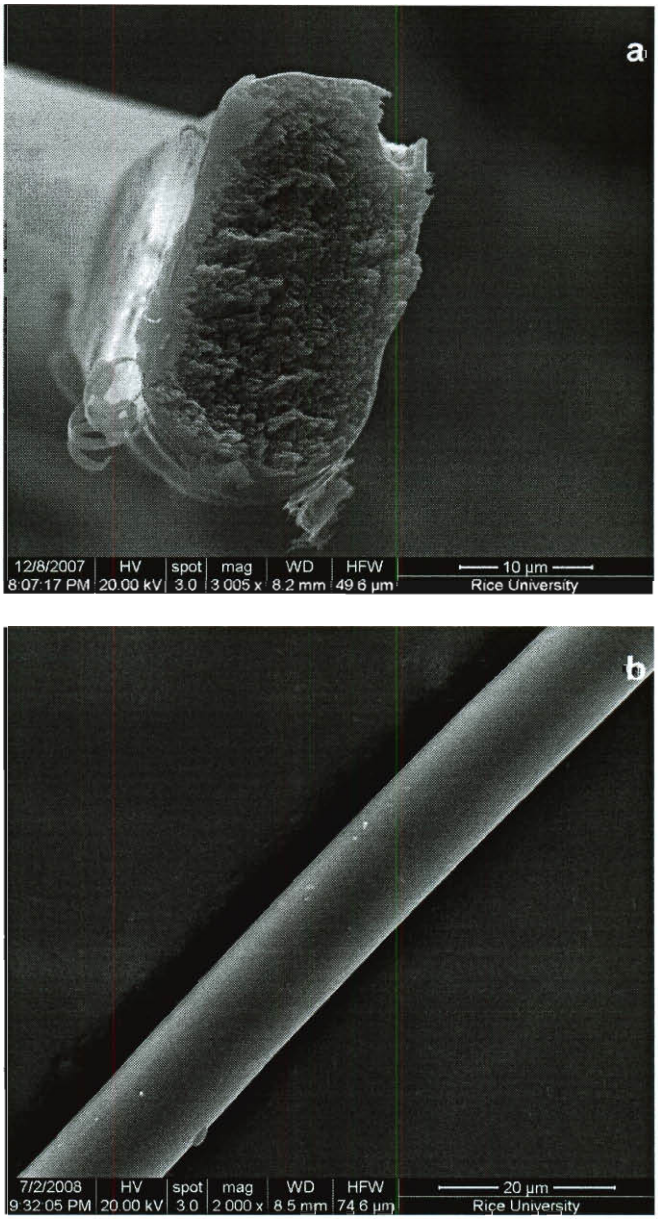

Figure 1.9. SEM images of as-spun PAN fiber (a) fracture point after tensile test and (b) along the fiber axis.

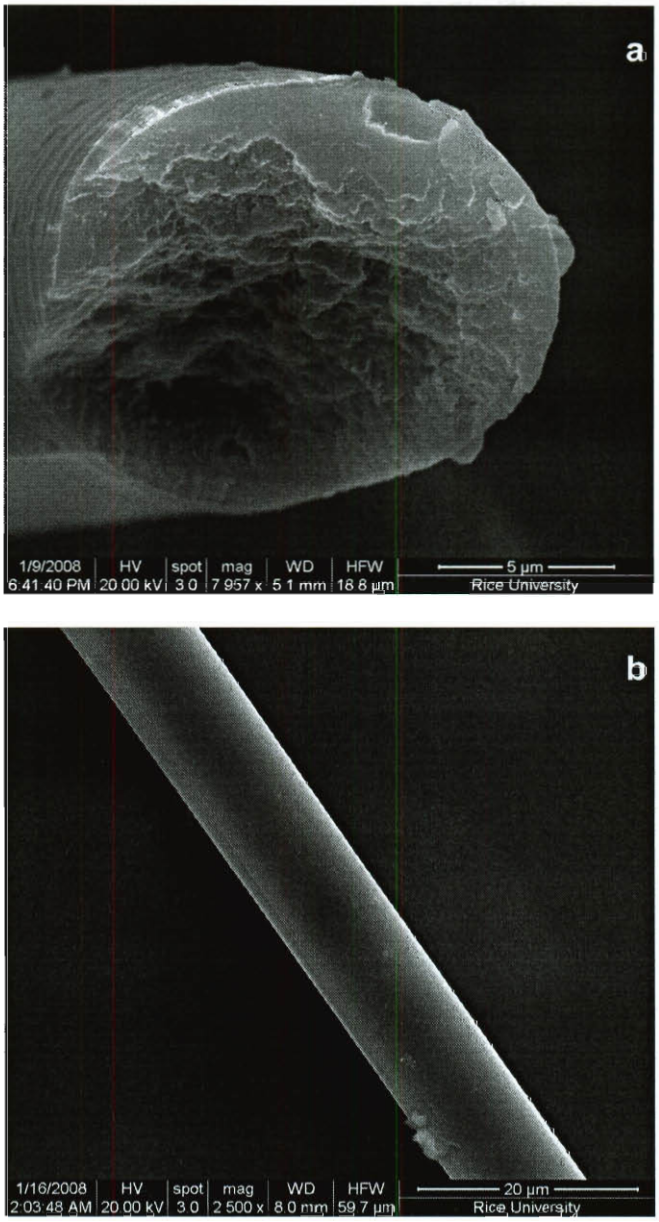

Figure 1.10. SEM images of as-spun US-SWCNT/PAN fiber (a) fracture point after tensile test and (b) along the fiber axis.

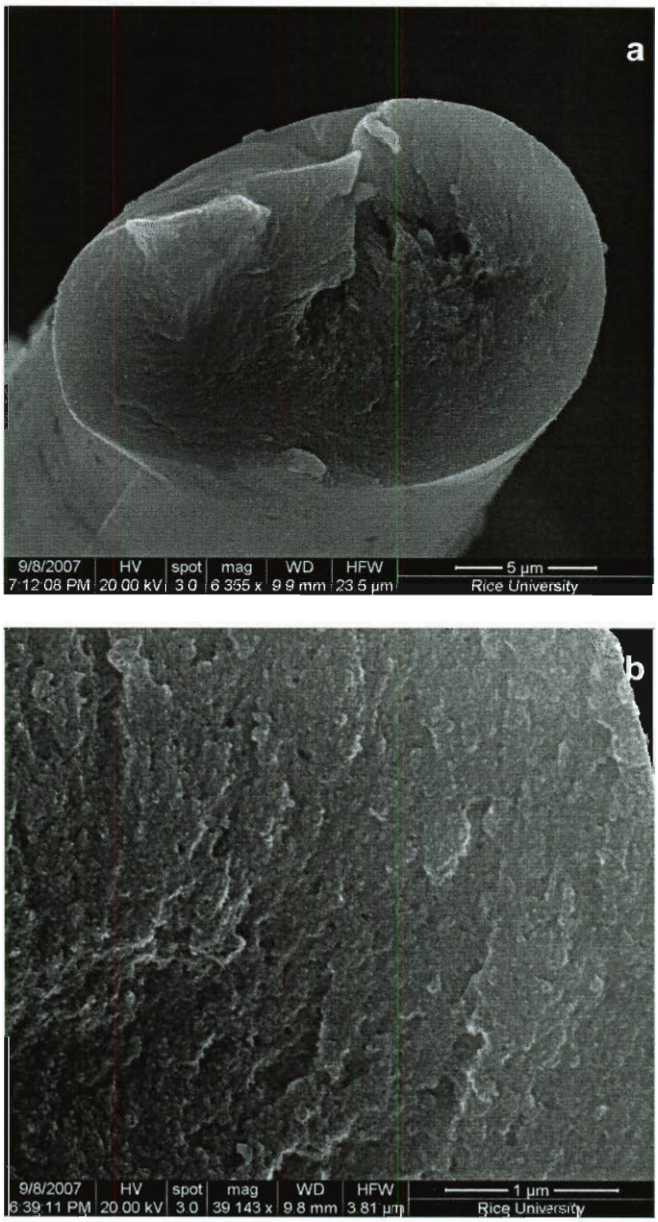

Figure 1.11. SEM images of stabilized PAN fiber at the fracture point after tensile test.

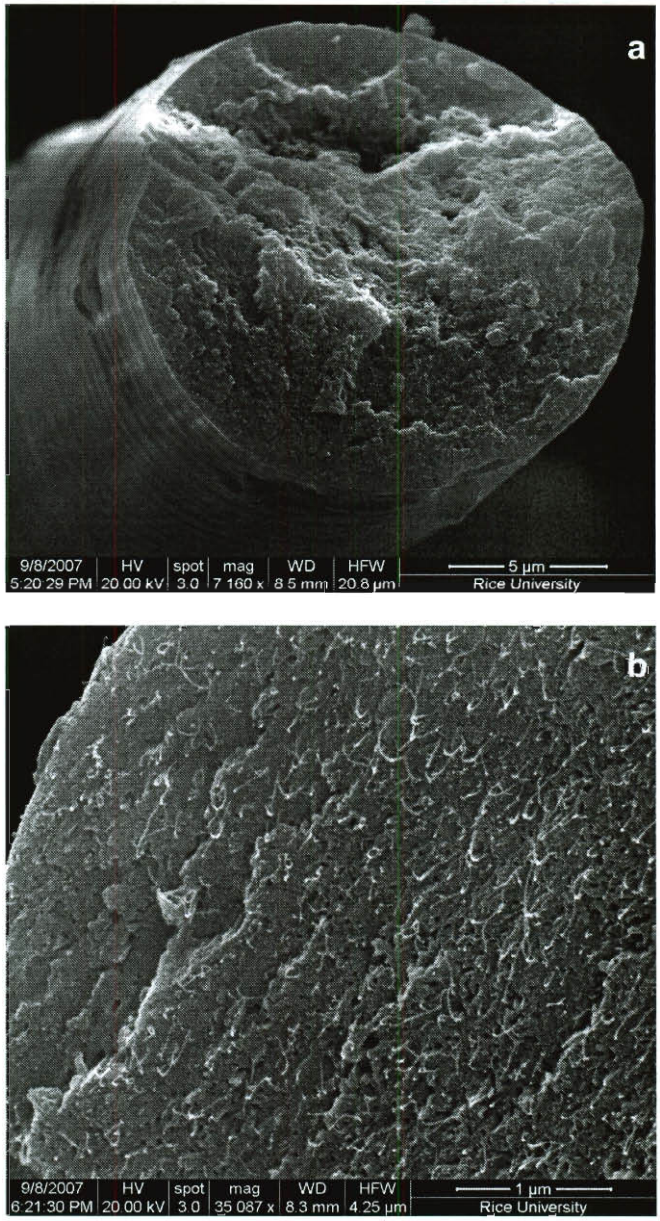

Figure 1.12. SEM images of stabilized US-SWCNT/PAN fiber at the fracture point after tensile test. Note the presence of fibrils on the surface.

The as-spun composite fibers had an increase in modulus of 50 % compared to the neat PAN fiber. The oxidized fibers also showed significant reinforcement (~ 40 %), albeit a decrease in tensile strength, which is a common during the cyclization of PAN and formation of the ladder structure (Table 1.2).

Table 1.2. Summary of Fiber Tensile Properties of SWCNT/PAN.

Fiber	Tensile Strength(MPa)	Tensile Modulus(GPa)	Elongation to Break (%)
PAN (as-spun)	500	9	11.6
US-SWCNT/PAN (as-spun)	460	13.5	11.0
PAN (stabilized at 285 °C)	114	28.9	1.83
US-SWCNT/PAN (stabilized at 285 °C)	197	41.5	2.7

While reinforcement by SWCNTs has already been shown numerous times in different matrices leading to better composites, the unique feature of this particular system is the excellent dispersion of the nanofillers, thus minimizing defect sites leading to failure of the fiber.

1.3 Experimental Section

1.3.1 Preparation of PAN and US-SWCNT/PAN in Dimethylsulfoxide (DMSO)

To obtain 20 wt % of PAN in DMSO, 5 g of PAN (M_w 150,000 g/mol, Sigma-Aldrich) was charged into a 4-neck reaction kettle equipped with a vacuum/nitrogen inlet and mechanical stirrer. The polymer was vacuum dried for 12 h at 80 °C. The polymer was allowed to cool to room temperature and DMSO (20 g) was added and the mixture was stirred at 25 rpm until the viscous spinning dope was obtained (typically within 24 h). For 5:95 US-SWCNT:PAN spinning dope, 263 mg of US-SWCNTs, prepared using the procedure reported by Chen *et al.*[20] was dispersed in 20.84 g of 99:1 DMSO:triethanolamine (Figure 1). The mixture was sonicated for 1 h at room temperature using a bath sonicator (Ultrasonic cleaner Cole-Parmer model 08849-00). The resulting dispersion was transferred to the reaction kettle with the vacuum dried PAN polymer (5 g) and mixed with a mechanical stirrer at 25 rpm for 24 h under nitrogen.

1.3.2 Fiber Spinning and Stabilization

PAN and US-SWCNT/PAN spinning dopes were spun using piston driven custom built dry-jet wet-spinning apparatus (Scheme 1). The dope is extruded using a 175 μm spinneret with a 5 mm air gap into an 80:20 v/v mixture of DMSO:H_2O coagulation bath, guided by a Teflon idle roll and collected in a 12.7 cm stainless steel drum rolling bobbin. Immediately after collecting enough fibers for characterization, the bath was replaced with 60:40 DMSO:H_2O and the spun fibers were stretched 2× the original length by mounting the end of the fiber to another 12.7 cm drum. Finally, the fibers were again stretched to 2× in hot water (~ 80 °C). Heat treatment using a Eurotherm tube furnace at

200 °C with nitrogen flow (~ 1 L/min) to facilitate quick drying of the fibers was done at 1.25× stretch. The stabilization of fibers was investigated by slowly heating the fibers in the air in an oven. The fibers were mounted on a quartz stand and stretch was applied by mounting a 2.5 g stainless steel weight on a bundle of fibers (~ 20 fibers per bundle) (Figure 2). The fibers were heated from room temperature at a rate of 1 °C/min to 285 °C and held for 5 h or 10 h. The subsequent carbonization and graphitization were not considered as part of the study here.

1.3.3 Characterization

The US-SWCNT dispersion in PAN and the fiber diameter measurements were analyzed using an optical microscope (Zeiss Axioplan-2). Raman spectroscopy was performed on a Renishaw Raman microscope using 785 nm laser. FT-IR analysis was performed using a Nicolet FT-IR fitted with attenuated total reflectance (ATR) attachment. Mechanical properties were tested using Instron 1000 with 10 lbs load cell with a crosshead speed of 1 mm/min. Individual fiber specimens were mounted on a paper frame using epoxy cement (Figure 3). The gauge length of the fibers was 25.4 mm. Fiber microstructure was analyzed using a FEI Quanta 400 ESEM.

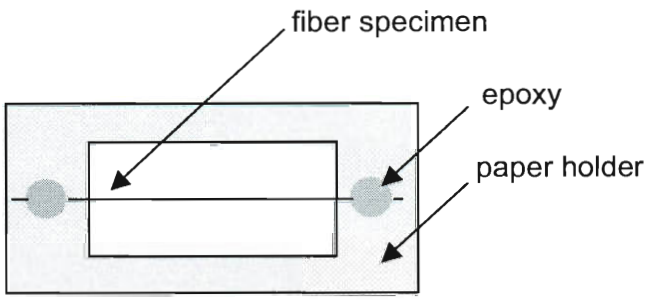

Figure 1.13. Scheme for mounting of fiber specimens for tensile test.

1.4 Conclusion

A fiber spinning process for CNT/PAN composite fibers has been developed using US-SWCNTs as reinforcing agents. The preparation of the spinning dope is straightforward and does not require high volumes of solvent because of the excellent solubility of US-SWCNTs. The as-spun fibers show an increase in modulus of 50% compared to neat PAN at 5 wt % loading of CNTs.

1.5 Experimental Contibutions

My contribution to this work is the following: preparation of US-SWCNT, US-SWCNT/PAN and spinning dope and fiber spinning. I also performed the mechanical properties characterization and microscopy. Shinichiro Kohama assisted in dope preparation and fiber spinning efforts and performed SEM imaging for fiber structure analysis. Richard Booker and Colin Christopher Young provided purified and disentangled HiPco SWCNTs.

References

1. http://www.researchandmarkets.com/reports/997638/ (accessed 09/30/2009)/
2. Chae, H. G.; Kumar, S. *Science* **2008**, *319*, 908-909.
3. Minus, M.; Kumar, S. *JOM Journal of the Minerals, Metals and Materials Society* **2005**, *57*, 52-58.
4. Baker, A. A. *Metals Forum* **1983,** *6*, 81-101.
5. Diefendorf, R. J.; Tokarsky, E. *Polym. Sci. Eng.* **1975**, *15*, 150-159.
6. Chawla, K. K. *Composite Materials: Science and Engineering*. Springer-Verlag: New York, 1998.

7. Gupta, V. B.; Kothari, V. K. *Manufactured Fiber Technology*. Chapman & Hall: London, p 664.

8. Gupta, A. K.; Paliwal, D. K.; Bajaj, P. *J. Macromolecular Sci. Rev. Macromolecular Chem. Phys.* **1991**, *C31*, 1-89.

9. Moon, S.; Farris, R. J. *Carbon* **2009**, *47*, 2829-2839.

10. Ali, A. A.; Rutledge, G. C. *J. Mater. Proc. Technol.* **2009**, *209*, 4617-4620.

11. Chae, H. G.; Minus, M. L.; Rasheed, A.; Kumar, S. *Polymer* **2007,** *48*, 3781-3789.

12. Miaudet, P.; Badaire, S.; Maugey, M.; Derre, A.; Pichot, V.; Launois, P.; Poulin, P.; Zakri, C. *Nano Lett.* **2005**, *5*, 2212-2215.

13. Ericson, L. M.; Fan, H.; Peng, H.; Davis, V. A.; Zhou, W.; Sulpizio, J.; Wang, Y.; Booker, R.; Vavro, J.; Guthy, C.; Parra-Vasquez, A. N. G.; Kim, M.; Ramesh, S.; Saini, R. K.; Kittrell, C.; Lavin, G.; Schmidt, H. K.; Adams, W. W.; Billups, W. E.; Pasquali, M.; Hwang, W. F.; Hauge, R. H.; Fischer, J. E.; Smalley, R. E. *Science* **2004,** *305*, 1447.

14. Zhang, M.; Atkinson, K. R.; Baughman, R. H. *Science* **2004**, *306*, 1358-1361.

15. Koziol, K.; Vilatela, J.; Moisala, A.; Motta, M.; Cunniff, P.; Sennett, M.; Windle, A. *Science* **2007**, *318*, 1892-1895.

16. Andrews, R.; Jacques, D.; Rao, A. M.; Rantell, T.; Derbyshire, F.; Chen, Y.; Chen, J.; Haddon, R. C. *Appl. Phys. Lett.* **1999**, *75*, 1329.

17. Quin, D.; Dickey, E. C.; Andrews, R.; Rantell, T. *Appl. Phys. Lett.* **2000**, *76*, 20.

18. Kumar, S.; Doshi, H.; Srinivasrao, M.; Park, J. O.; Schiraldi, D. A. *Polymer* **2002**, *43*, 1701.

19. Kumar, S.; Dang, T. D.; Arnold, F. E.; Bhattacharyya, A. R.; Min, B. G.; Zhang, X.; Vaia, R. A.; Park, C.; Adams, W. W.; Hauge, R. H.; Smalley, R. E.; Ramesh, S.; Willis, P. A. *Macromolecules* **2002**, *35*, 9039-9043.

20. Chen, Z.; Kobashi, K.; Rauwald, U.; Booker, R.; Fan, H.; Hwang, W.-F.; Tour, J. M. *J. Am. Chem. Soc*. **2006**, *128*, 10568-10571.

21. Sreekumar, T. V.; Liu, T.; Min, B. G.; Guo, H.; Kumar, S.; Hauge, R. H.; Smalley, R. E. *Adv. Mater*. **2004,** *16*, 58.

22. Lianjiang, T.; Huifang, C.; Ding, P.; Ning, P. **2008**, *110*, 1997-2000.

23. Rahman, M. A.; Ismail, A. F.; Mustafa, A., *Mater Sci Eng A Struct* **2007,** 448, 275.

24. Morgan, P. *Carbon Fibers and Their Composites*. CRC Press: Florida, 2005.

Chapter 2

Vacuum Pressure Impregnation of Acid-Spun Single-Walled Carbon Nanotube Fibers with Polyimide

2.1 Introduction

Individual single-walled carbon nanotubes (SWCNTs) possess remarkable mechanical,[1-3] electrical[4-6] and thermal[7,8] properties that equal or surpass those of other benchmark materials such as steel, copper, diamond and high performance polymeric fibers.[9,10] This excellent combination of properties is the main driving force for fabrication of macroscopic articles such as fibers and films using SWCNTs. The key application envisioned for SWCNT fibers include thermal management systems, electrical conduits and structural reinforcements for military and aerospace vehicles. To realize these goals, the ability to process these new materials must be developed.

Currently, two promising methods for the fabrication of neat SWCNT fibers are (1) dry spinning and (2) solution spinning. The former takes inspiration from the spinning of wool and cotton, and spinning is done from a reactor furnace containing a vertically grown CNT array.[9,11-12] The resulting fibers exhibited the highest tensile strength and modulus of any CNT fiber to date. Solution spinning takes advantage of the ability to disperse SWCNTs in highly acidic conditions[13] by sidewall protonation,[14] thereby disrupting the strong van der Waals interactions between the CNTs. Neat macroscopic fibers were successfully spun at high concentration using this protocol (up to 8 wt % in 102% H_2SO_4).[15] Fibers produced by this method have superior electrical

properties and high modulus albeit low tensile strength compared to existing commercial fibers.[16]

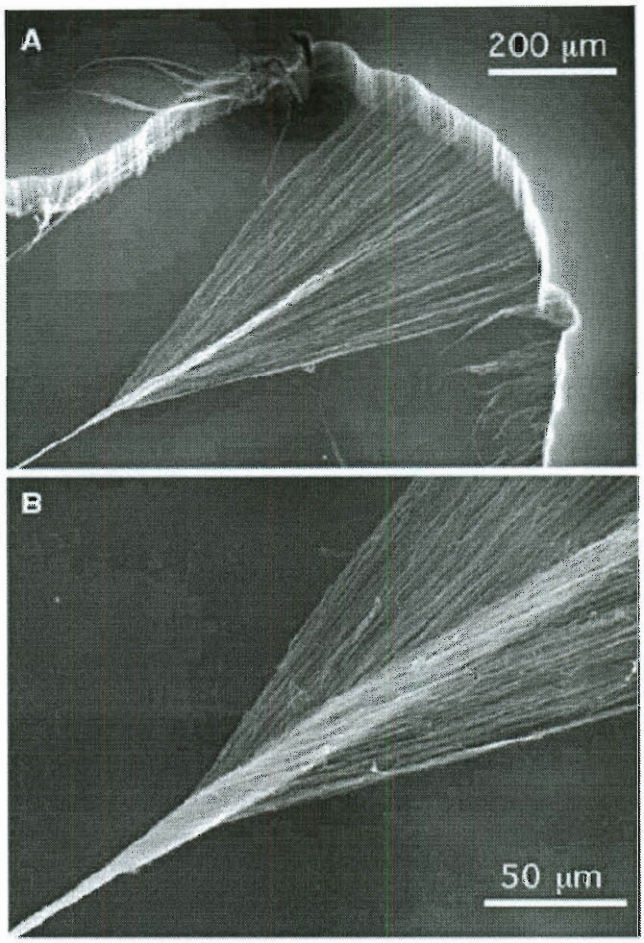

Figure 2.1. SEM images of the dry spinning process of CNT array.[11]

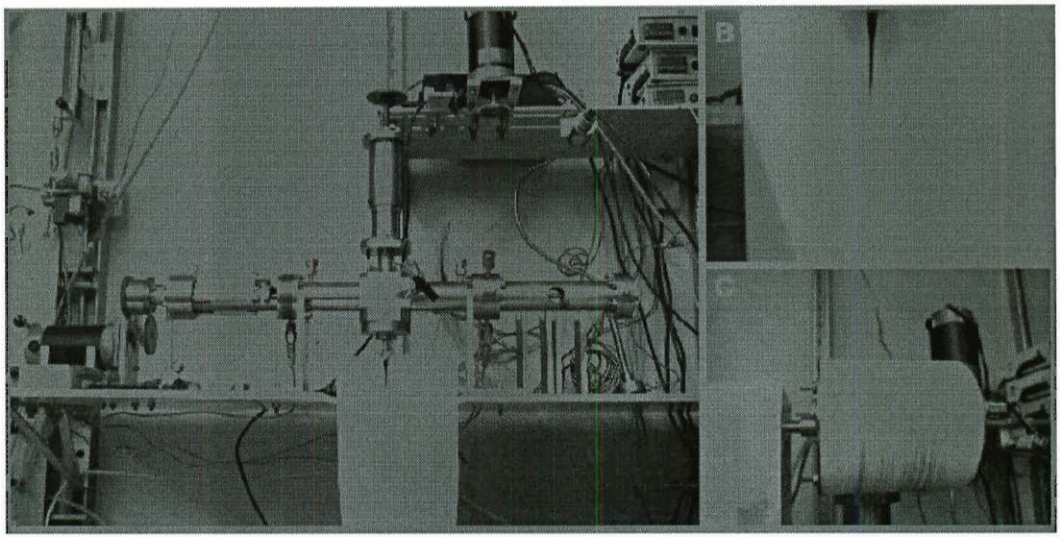

Figure 2.2. (a) Photograph of Spinning Apparatus for SWCNTs in 102 % H2SO4. (b) Fibers being extruded from a glass spinneret and (c) a spool of SWCNT coagulated in water.[15]

In this work, a protocol was developed to impart better mechanical properties to acid spun SWCNT fibers by employing the vacuum pressure impregnation (VPI) technique.[17,18] Macroscopic fibers spun using the dry-jet wet-spinning technique reported by Ericson[15] was subjected to the VPI process. The resin used was polyamic acid (PAA) that is thermally cured to polyimide (PI) using published procedures. PIs are used widely in the aerospace, automotive and electronic industry because of their excellent thermal stability, solvent and radiation resistance, and superior mechanical properties.[19] However, most PIs are not generally processible when imidized unless the polymer contains flexible backbones. However, the precursor PAA is soluble and easily processed before imidization. If the internal voids in acid-spun SWCNT fiber could be filled with PI, it is expected that the mechanical properties of the fiber will be improved.

2.2 Results and Discussion

The VPI process has been successfully employed for coating copper coils used for magnets with resins such as polyester.[18] It has also been employed to reinforce wood by impregnating articles with cross-linking agents.[17] The strength of this technique lies in its ability to fill voids and spaces with chemical agents that can impart reinforcement (Figure 2.3).

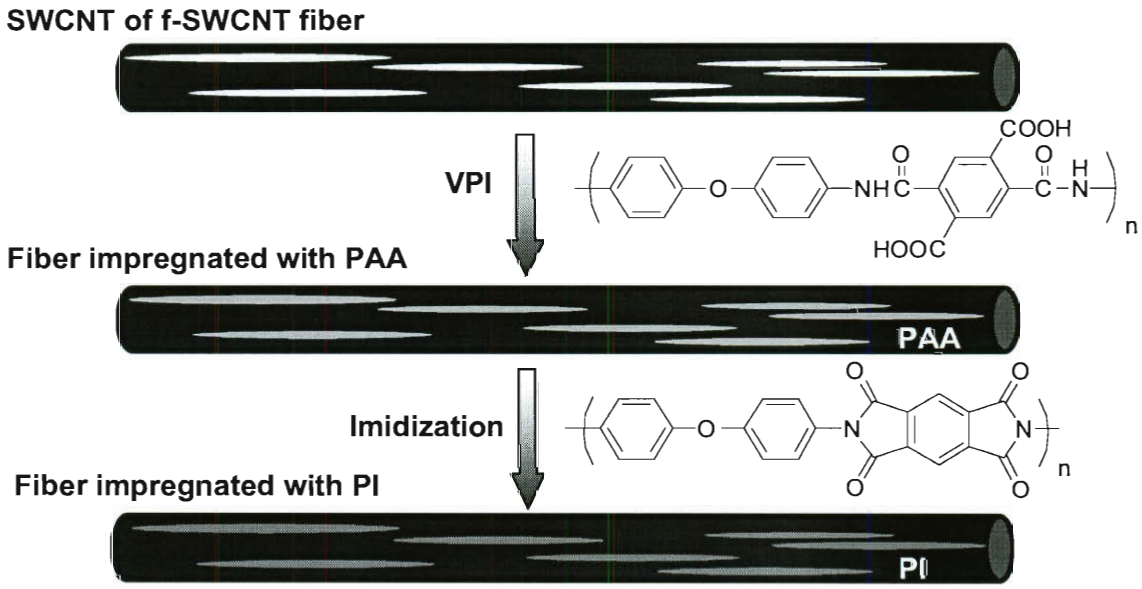

Figure 2.3. Concept for VPI of SWCNT fiber

Neat SWCNT fibers, and a batch of f-SWCNT fiber containing 10 wt % of isophthalic acid f-SWCNTs were spun and subjected to VPI. Two different fibers were made in order to assess differences in wettability of the fibers. Contact angle

measurements for SWCNT and f-SWCNT fibers in PAA solution were 54° and 48°, respectively (Figure2.4), indicating that as expected, the f-SWCNT fibers have a slightly higher PAA solution wettability than SWCNT fibers.

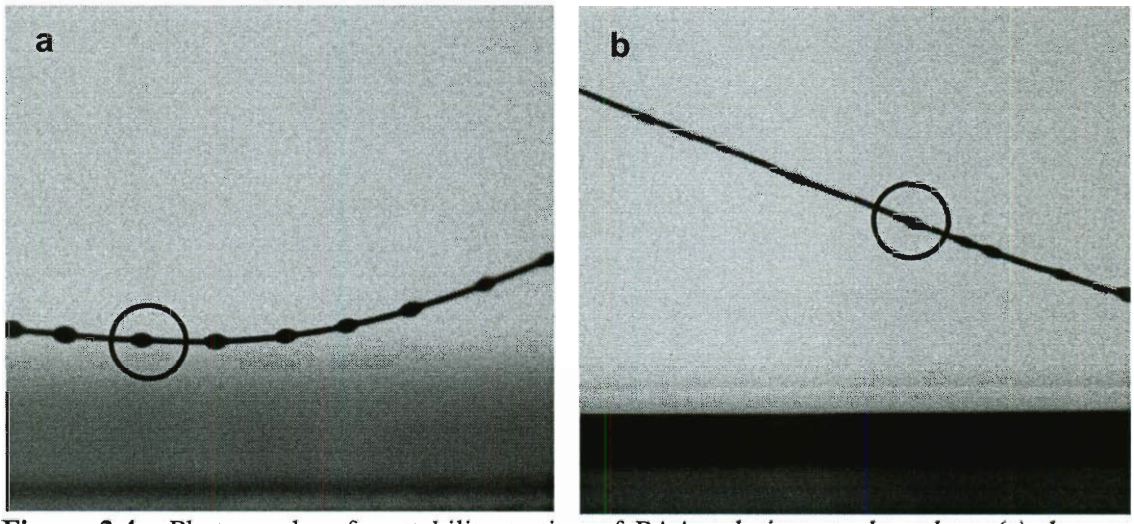

Figure 2.4. Photographs of wettability testing of PAA solution conducted on (a) the SWCNT fiber or (b) the f-SWNT fiber.

The VPI process was performed by placing the fibers mounted on a holder and the PAA solution in separate chambers as shown in Figure 2.5. After sufficient degassing of both chambers (~1.5×10^{-2} torr) the polymer solution was slowly pumped to the fiber chamber until the volume was sufficient enough to submerge the fibers. The chamber was then pressurized to 100 psi to impregnate the fibers with the resin. In order to minimize the breakage of fibers as the solution was flowing into the VPI chamber, the valves were slowly opened to control the flow rate. The impregnated fibers were then thermally cured to allow the cyclodehydration and imidization of the PAA precursor.

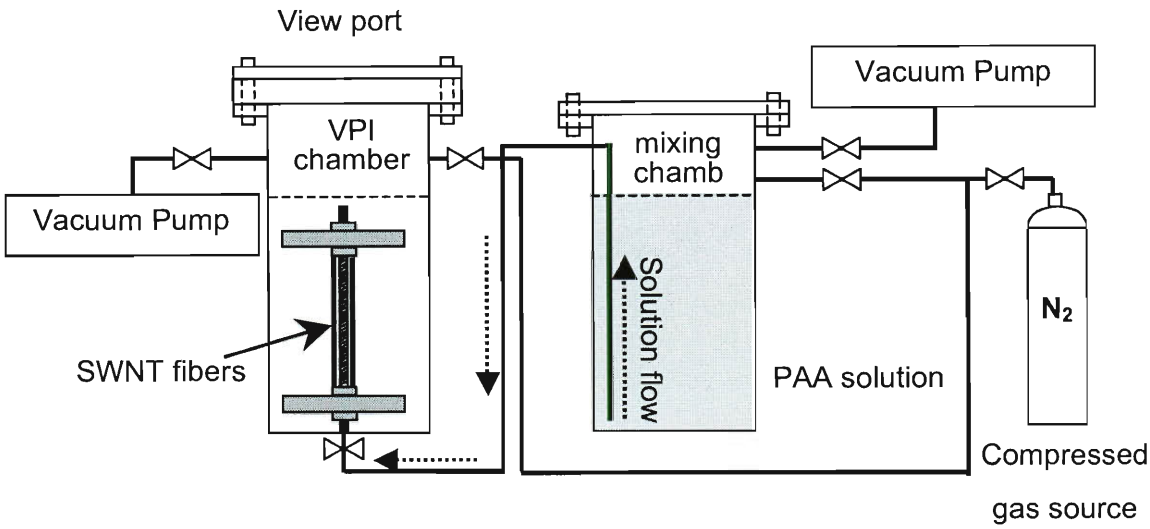

Figure 2.5. Diagram for the VPI processing of SWCNT fibers.

Mechanical properties evaluations of the resulting fibers are summarized in Table 2.1. Overall, the tensile strength increased after the fibers were subjected to VPI. The tensile strength of the SWCNT fiber was 68 MPa while that of the PAA impregnated fiber increased to 101 MPa. Moreover, it increased to 215 MPa after imidization. These results show that the SWCNT fibers were reinforced with impregnated PAA and were further strengthened after imidization. For f-SWCNT fibers, the tensile strength of the starting f-SWCNT fiber was 40 MPa while that of PAA impregnated fiber increased to 65 MPa and subsequently to 111 MPa after imidization. These results show that f-SWCNT fibers were successfully impregnated with PAA and were further reinforced after the conversion of the PAA to the PI.

Table 2.1. Summary of Tensile Strength Properties of SWCNT fibers before and after VPI.

Fiber Sample	Tensile Strength, MPa
SWCNT	68
SWCNT-PAA	101
SWCNT-PI	215
f-SWCNT	40
f-SWCNT-PAA	65
f-SWCNT-PI	111

The morphologies of the fibers were analyzed by SEM. The acid spun SWCNT fibers showed a wrinkled skin and a lamellar cross section (Figure 2.6). Figures 2.7 and 2.8 show the resulting fibers after impregnation with PAA and the thermal imidization, respectively. The f-SWCNT fibers gave similar results having very smooth skins after PAA impregnation and imidization (Figures 2.9 – 2.11).

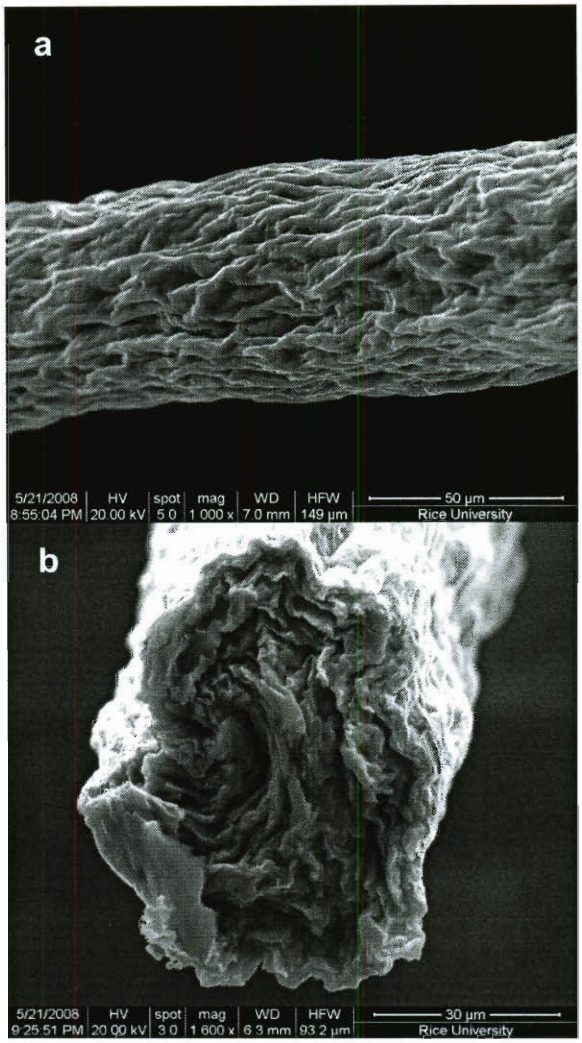

Figure 2.6. SEM Images of (a) neat SWCNT fiber spun from 102 % H_2SO_4, (b) morphology of a cross section of the fiber prepared by pulling apart the fiber.

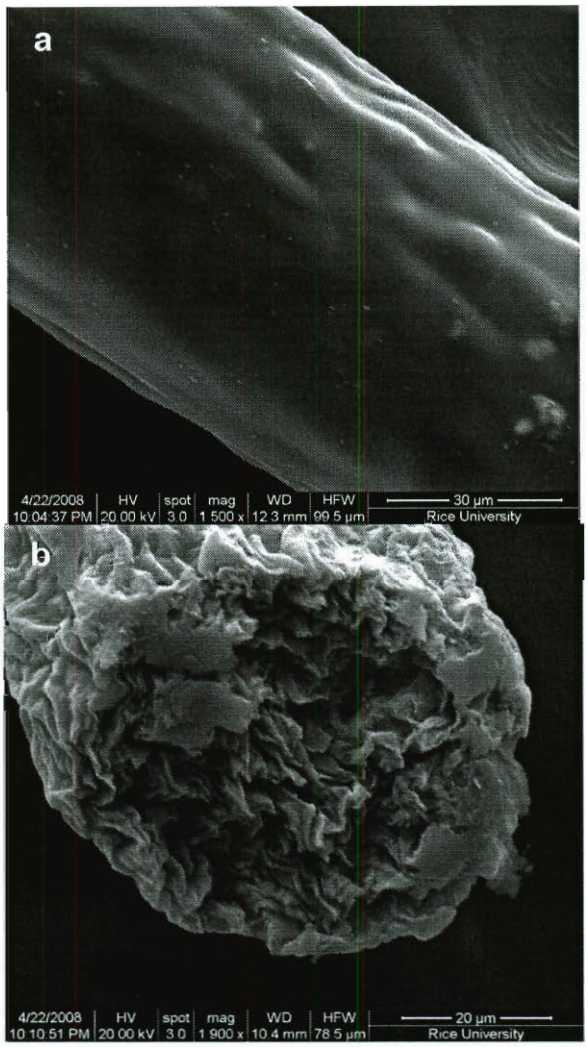

Figure 2.7. SEM Images of (a) SWCNT fiber impregnated with PAA, (b) morphology of a cross section of the fiber prepared by pulling apart the fiber.

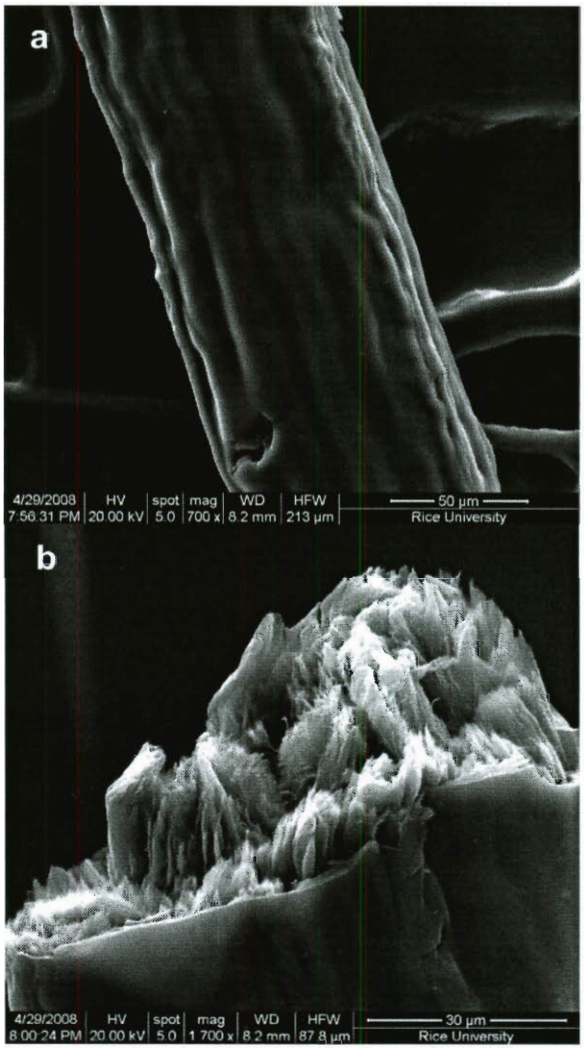

Figure 2.8. SEM Images of (a) SWCNT fiber impregnated with PI, (b) morphology of a cross section of the fiber prepared by pulling apart the fiber.

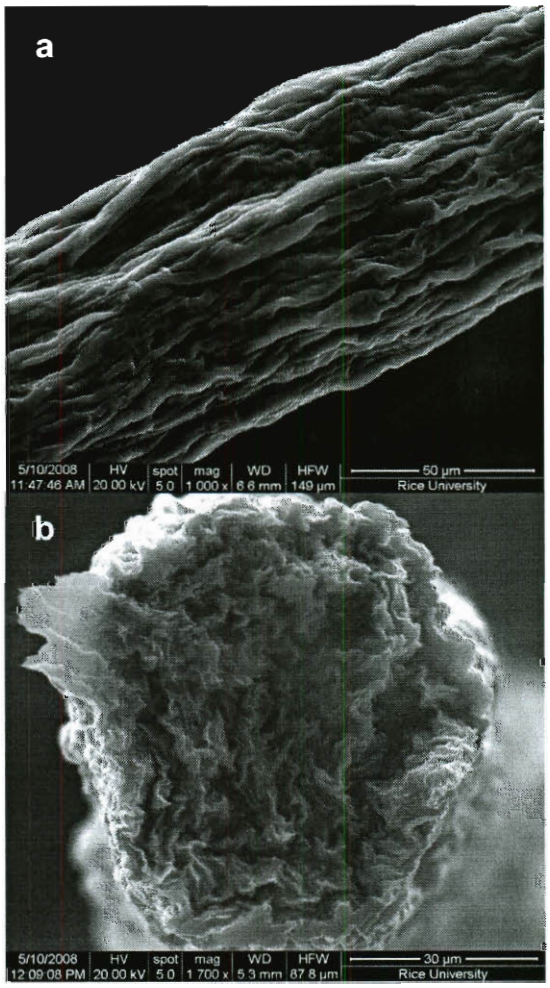

Figure 2.9. SEM Images of (a) neat f-SWCNT fiber spun from 102 % H_2SO_4, (b) morphology of a cross section of the fiber prepared by pulling apart the fiber.

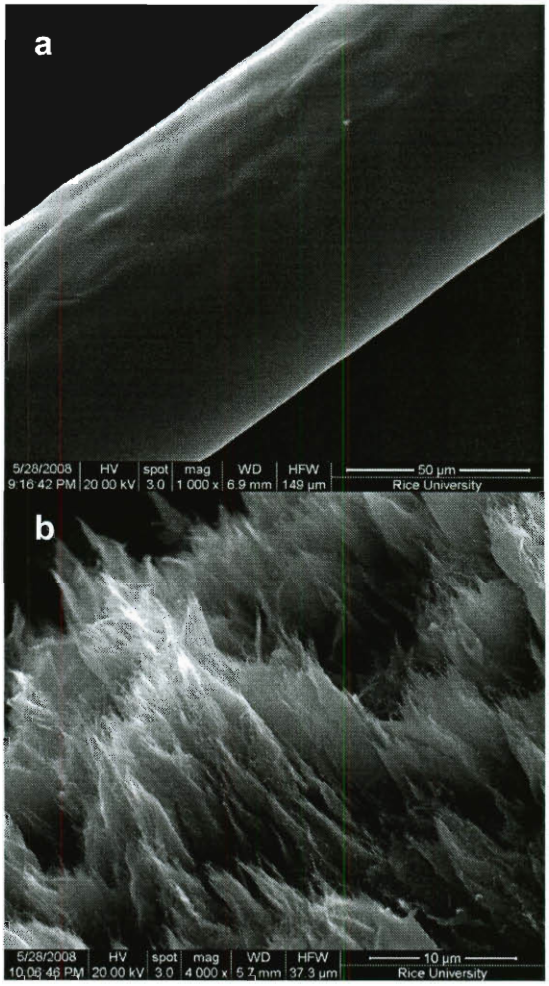

Figure 2.10. SEM Images of (a) f-SWCNT fiber impregnated with PAA, (b) morphology of a cross section of the fiber prepared by pulling apart the fiber.

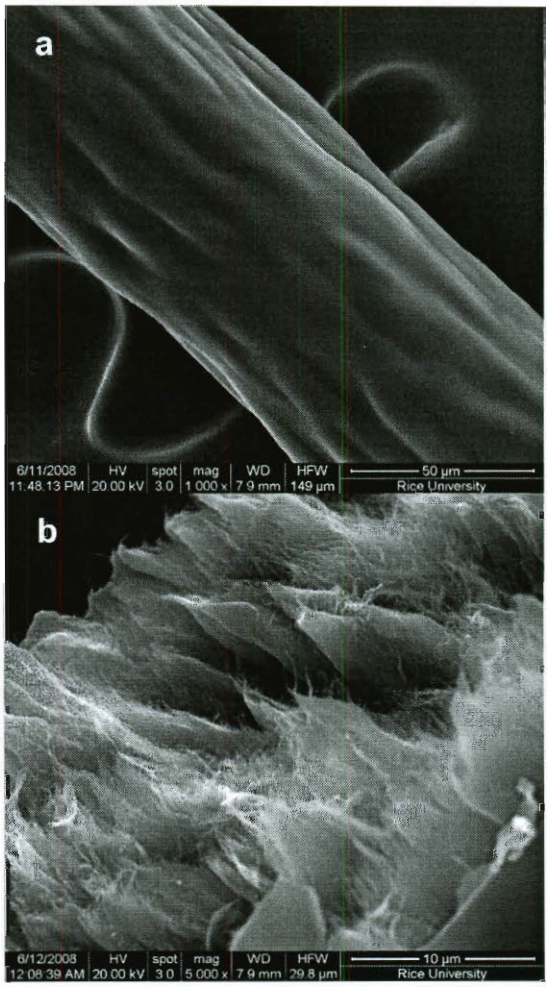

Figure 2.11. SEM Images of (a) f-SWCNT fiber impregnated with PI, (b) morphology of a cross section of the fiber prepared by pulling apart the fiber.

To assess the impregnation of PAA, conductivity measurements that can indirectly suggest impregnation of the non-conductive PI were performed on the fibers. Conductivity measurements were carried out on the neat fibers and on the samples subjected to VPI. The results are summarized in Table 2.2. The diameters used in the calculation were based on the cross section analysis of the fibers using SEM.

Conductivity of the SWCNT fiber was 2.0×10^2 S/cm. In contrast to this, the conductivity of the SWCNT fibers impregnated with PAA decreased to 1.3×10^2 S/cm. Moreover, the conductivity of fibers after imidization decreased to 0.7×10^2 S/cm. The conductivity of the f-SWCNT fiber was 5.4×10^2 S/cm and decreased in a similar manner to what was observed for the neat SWCNT fibers. The conductivity of both the f-SWCNT fibers impregnated with PAA and those impregnated with PI was 3.5×10^2 S/cm. These results suggest that PAA is impregnated into the f-SWCNT fibers and subsequently PI, leading to a decrease in conductivity.

Table 2.2. Summary of Conductivity Measurement on Fibers Subjected to VPI.[a]

Fiber Sample	**Conductivity (S/cm) ($\times 10^2$)**
SWCNT-PAA	1.3
SWCNT-PI	0.7
f-SWCNT-PAA	3.5
f-SWCNT-PI	3.5

[a] The conductivity of SWCNT fibers and f-SWCNT fibers were 2.0×10^2 S/cm and 5.4×10^2 S/cm by 2-probe method, respectively.

The presence of PI in the SWCNT and f-SWCNT fibers were further assessed spectroscopically using ATR-IR and XPS. From the IR spectrum (Figure 2.12), the imide peaks at 1772 cm^{-1} (C=O imide peak) and 1380 cm^{-1} (C-N imide) signify the successful conversion of the PAA into PI. However, the XPS spectra taken on single filament fibers do not show a strong imide peak at 288 eV. Nevertheless, the C1s profile

show a marked difference after the PAA impregnated fibers were imidized at 225 °C, largely dominated by the C=C, C-H peak at 284.8 eV and the disappearance of the peak at 289 eV (-COOH group) (Figure 2.13).

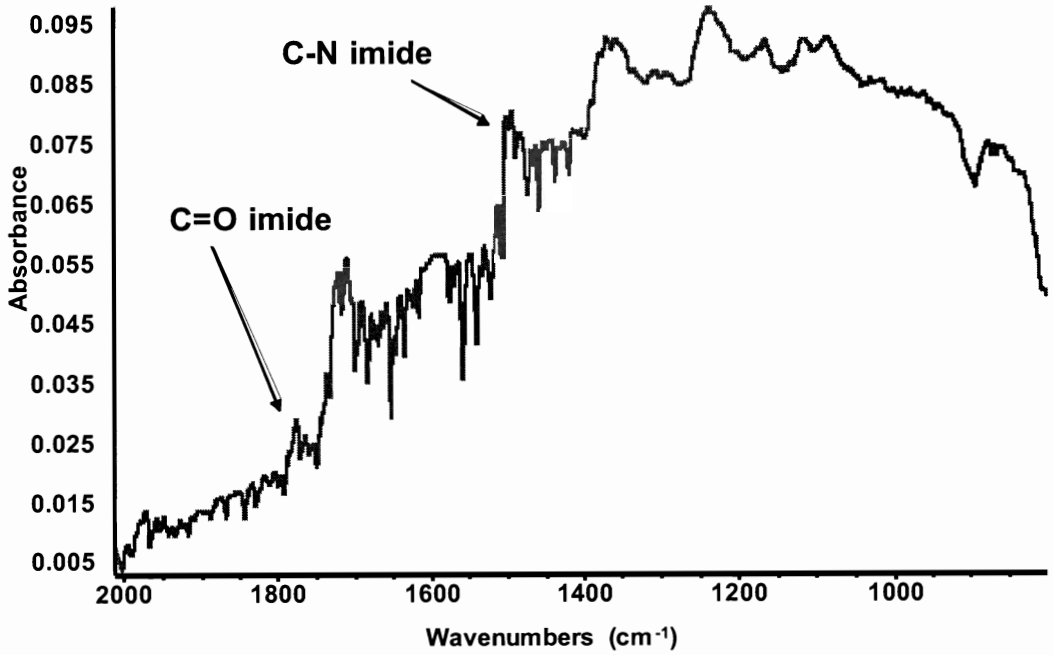

Figure 2.12. Representative ATR-IR spectrum of PI-SWCNT and PI-f-SWCNT fibers showing the imide peaks at 1772 cm^{-1} (C=O imide peak) and 1380 cm^{-1} (C-N imide).

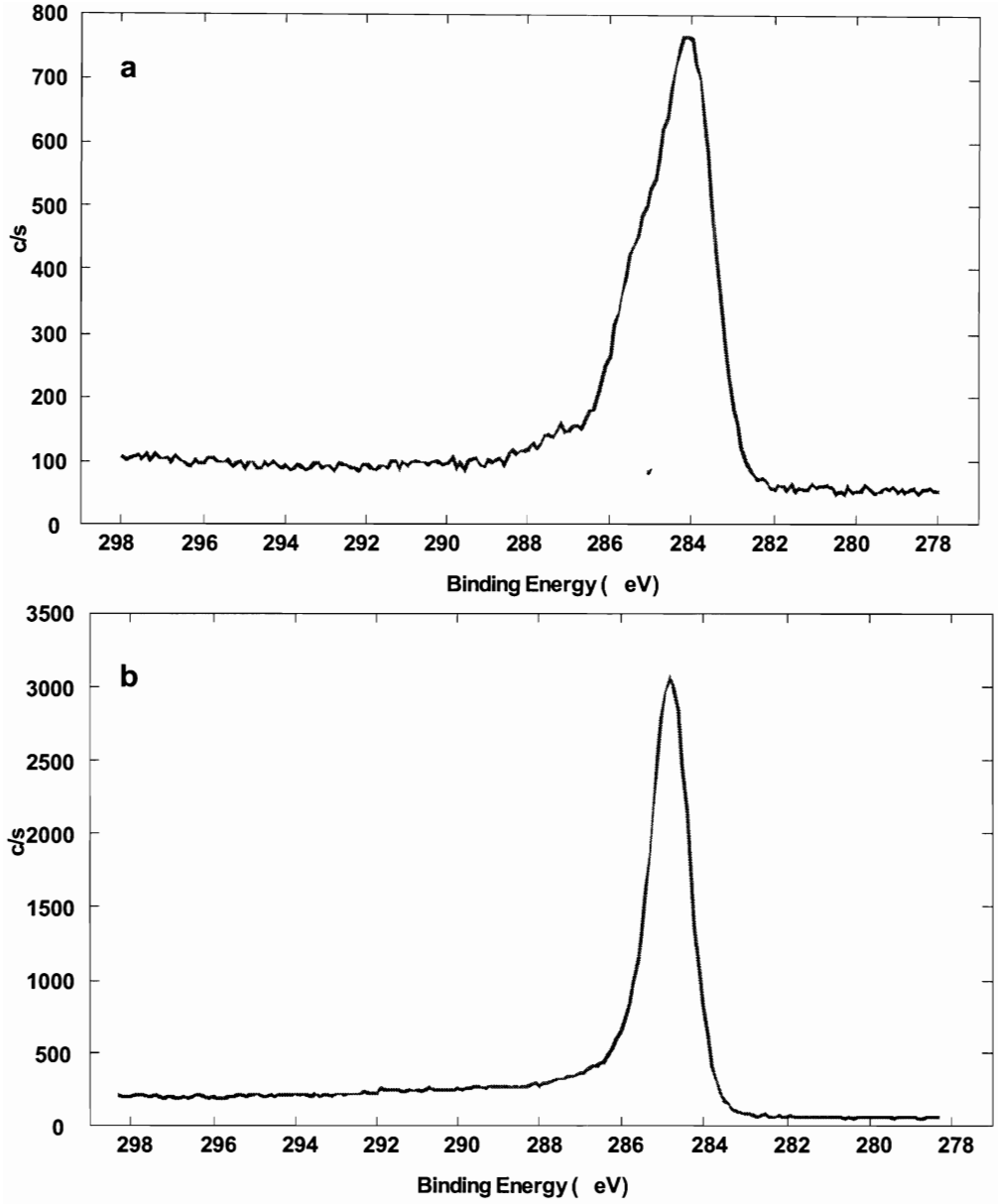
a
c/s
800
700
600
500
400
300
200
100
0
298
296
294
292
290
288
286
284
282
280
278
Binding Energy (eV)
b
c/s
3500
3000
2500
2000
1500
1000
500
0
298
296
294
292
290
288
286
284
282
280
278
Binding Energy (eV)

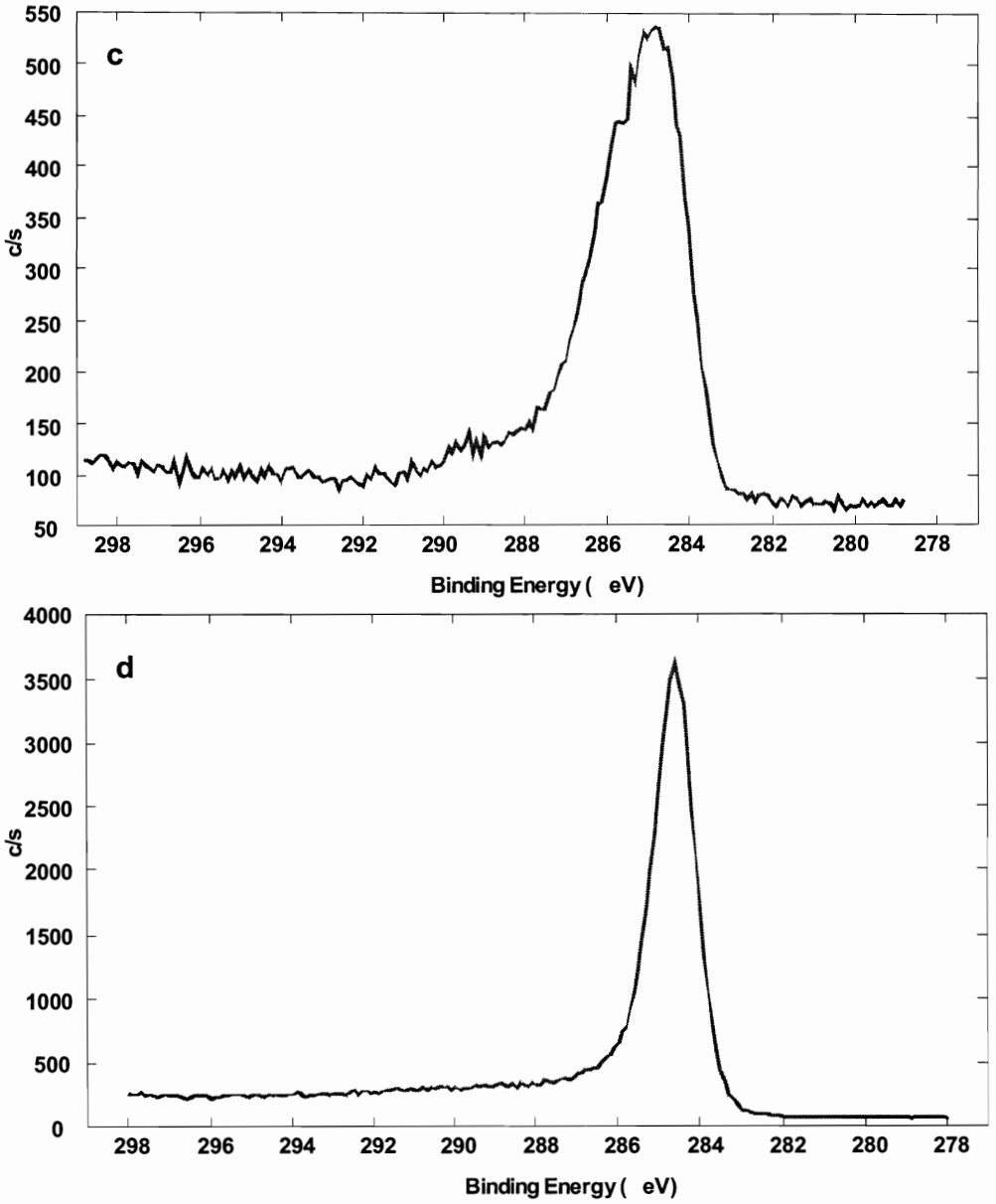

Figure 2.13. Core-level C1s spectra of (a) PAA-SWCNT fibers, (b) PI-SWCNT fibers, (c) PAA-f-SWCNT fibers and (d) PI-f-SWCNT fibers. For (a) and (c) the spectra is a combination of the peak from C=C, C-H (284.8 eV), C-O (286 eV), C-N amide (287 eV) and COOH (289 eV). For (b) and (d) the spectra is dominated by the C=C, C-H peak and the imide peak at 288 eV is not discernible.

2.3 Experimental

2.3.1 Materials

The SWCNTs used in this study were produced by high-pressure decomposition of CO (HiPco) and were purified to remove excess metal catalyst.[20-22] *N*-methyl-2-pyrrolidone (NMP) and poly(pyromellitic-co-4,4'-oxydianiline)amic acid (PAA) (15.0-16.0 wt. % NMP solution) were purchased from Aldrich, Co. Ltd. 5 wt % PAA solution in NMP (PAA solution) was prepared by diluting with additional anhydrous NMP. SWCNT functionalized with 4-aminoisophthalic acid (f-SWCNT) was prepared according to published procedures.[23]

2.3.2 Spinning of SWCNT fibers and SWCNT fibers having 10 wt % f-SWCNT

Acid-spun SWCNT fiber and acid-spun SWCNT fiber having 10 wt % f-SWCNT (f-SWCNT fiber) were prepared according to the previous procedures.[15]

2.3.3 Characterization

The morphology of the fiber was determined using a scanning electron microscope (SEM, QUANTA 400F, FEI). Samples for SEM observation were dried, sputtered with gold and observed at 20 kV. The tensile testing was done using an Instron Universal Testing Machine (MODEL 1000). The conductivity of the fibers was measured on a 4-point probe (Desert Cryogenics TT-probe 6 system) at 10^{-5} Torr. The PI-SWCNT fibers were characterized spectroscopically using Nicolet FT-IR equipped with attenuated total reflectance (ATR) attachment and X-ray photoelectron spectroscopy was done using

Phi Quantera SXM Scanning X-Ray Microprobe with a pass energy of 26.00 eV, 45 ° takeoff angle and a 100 μm beam size.

2.3.4 Vacuum Pressure Impregnation (VPI) Procedure

The VPI set-up is shown in Figure 1. SWCNT or f-SWCNT fibers were mounted on the fiber holder with epoxy. The PAA solution (5 wt % in NMP) was placed in the mixing chamber and fiber holder was placed in the VPI chamber. The VPI chamber was placed under a vacuum of 1.5×10^{-2} Torr. The PAA solution was transferred from the mixing chamber to the VPI chamber through the capillary at that pressure. After completion of the PAA solution transfer, the VPI chamber was isolated from the mixing chamber, and was pressurized with nitrogen to 100 psi for 1 h. Finally, the fiber holder was removed from the VPI chamber after releasing the pressure. After removal from the VPI chamber, the fiber holder was placed in a vacuum oven 15 Torr at 80 °C overnight to remove the NMP from the fibers.

2.3.5 Imidization procedure

The vacuum dried fibers were removed form the holder and mounted onto a quartz stand for imidization (Figure 2). Imidization was initiated under nitrogen by heating at a rate of 10 °C/min to 100 °C, holding for 1 h, then heating at the same rate to 225 °C for 1 h.

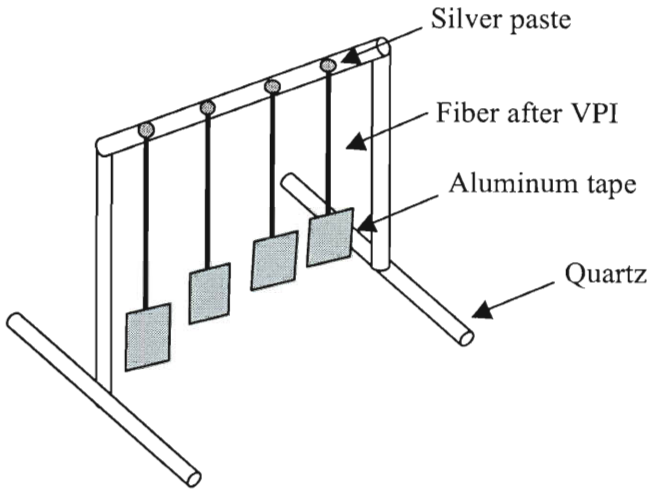

Figure 2.14. Quartz stand for the drying and imidization process

2.4 Conclusion

The reinforcement of SWCNT fibers was successfully achieved by employing the VPI method to incorporate PI into the fibers. The tensile strength of the fibers increased after impregnation with PAA when compared to the starting SWCNT fibers. Moreover, it further increased after imidization of impregnated PAA. Morphology observations and conductivity tests on fibers suggest that SWCNT and f-SWCNT fibers were impregnated with PAA and subsequently PI. This method could provide a new approach for strengthening SWCNT fibers.

2.5 Experimental Contributions

My contribution to this work is the following: fiber spinning of SWCNT fibers, execution of the VPI process. Shinichiro Kohama assisted in dope preparation and VPI

experiments and performed SEM imaging for fiber structure analysis. Jun Yao and Zhengzhong Sun tested the fibers for conductivity and Natnael Behabtu performed the contact angle measurements. Richard Booker and Colin Christopher Young provided the purified HiPco SWCNTS and performed SWCNT fiber spinning.

References

1. Krishnan, A.; Dujardin, E.; Ebbesen, T. W.; Yianilos, P. N.; Treacy, M. M. J. *Phys. Rev. B* **1998,** *58*, 14013.
2. Walters, D. A.; Ericson, L. M.; Casavant, M. J.; Liu, J.; Colbert, D. T.; Smith, K. A.; Smalley, R. E. *Appl. Phys. Lett.* **1999,** *74*, 3803-3805.
3. Yu, M. F.; Files, B. S.; Arepalli, S.; Ruoff, R. S. *Phys. Rev. Lett.* **2000,** *84*, 5552.
4. Thess, A.; Lee, R.; Nikolaev, P.; Dai, H.; Petit, P.; Robert, J.; Xu, C.; Lee, Y. H.; Kim, S. G.; Rinzler, A. G.; Colbert, D. T.; Scuseria, G. E.; Tomanek, D.; Fischer, J. E.; Smalley, R. E. *Science* **1996,** *273*, 483-487.
5. Tans, S. J.; Devoret, M. H.; Dai, H.; Thess, A.; Smalley, R. E.; Geerligs, L. J.; Dekker, C. *Nature* **1997,** *386*, 474.
6. McEuen, P. L.; Fuhrer, M. S.; Hongkun, P. *Nanotechnol. IEEE Trans.* **2002,** *1*, 78-85.
7. Hone, J.; Whitney, M.; Piskoti, C.; Zettl, A. *Phys. Rev. B* **1999,** *59*, R2514.
8. Che, J.; Cagin, T.; Goddard, W. A., *Nanotechnology* **2000,** *11*, 65.
9. Li, Y.; Kinloch, I. A.; Windle, A. H. *Science* **2004,** *304*, 276.
10. Baughman, R. H.; Zakhidov, A. A.; de Heer, W. A. *Science* **2002,** *297*, 787-792.
11. Zhang, M.; Atkinson, K.; Baughman, R. H. *Science* **2005,** *306*, 1358.

12. Zhang, X.; Li, Q.; Holesinger, T. G.; Arendt, P. N.; Huang, J.; Kirven, P. D.; Clapp, T. G.; DePaula, R. F.; Liao, X.; Zhao, Y.; Zheng, L.; Peterson, D. E.; Zhu, Y. *Adv. Mater.* **2007,** *19*, 4198-4201.

13. Davis, V. A.; Ericson, L. M.; Parra-Vasquez, A. N. G.; Fan, H.; Wang, Y.; Prieto, V.; Longoria, J. A.; Ramesh, S.; Saini, R. K.; Kittrell, C.; Billups, W. E.; Adams, W. W.; Hauge, R. H.; Smalley, R. E.; Pasquali, M. *Macromolecules* **2004,** *37*, 154.

14. Ramesh, S.; Ericson, L. M.; Davis, V. A.; Saini, R. K.; Kittrell, C.; Pasquali, M.; Billups, W. E.; Adams, W. W.; Hauge, R. H.; Smalley, R. E. *J. Phys. Chem. B* **2004,** *108*, 8794.

15. Ericson, L. M.; Fan, H.; Peng, H.; Davis, V. A.; Zhou, W.; Sulpizio, J.; Wang, Y.; Booker, R.; Vavro, J.; Guthy, C.; Parra-Vasquez, A. N. G.; Kim, M.; Ramesh, S.; Saini, R. K.; Kittrell, C.; Lavin, G.; Schmidt, H. K.; Adams, W. W.; Billups, W. E.; Pasquali, M.; Hwang, W. F.; Hauge, R. H.; Fischer, J. E.; Smalley, R. E. *Science* **2004,** *305*, 1447.

16. Davis, V. A. *Phase Behavior and Rheology of Single-Walled Carbon Nanotubes (SWNTs) in Superacids with Application to Fiber Spinning*. PhD Thesis, Rice University, 2006.

17. Colvin, J.; Vignal, C.; Tissot, P. E.; Crowe, L. R. Resin Impregnated Substrate, Method of Manufacture and System Therefor. February 13, 2003.

18. Gruenwald, G. Method of Curing Vacuum Impregnated Coils. June 21, 1976.

19. Ghosh, M. K.; Mittal, K. L. *Polyimides: Fundamentals and Applications*. Marcel Dekker: New York, 1996.

20. Nikolaev, P.; Bronikowski, M. J.; Bradley, R. K.; Rohmund, F.; Colbert, D. T.; Smith, K. A.; Smalley, R. E. *Chem. Phys. Lett.* **1999,** *313*, 91.

21. Bronikowski, M. J.; Willis, P. A.; Colbert, D. T.; Smith, K. A.; Smalley, R. E. *J. Vac. Sci. Technol.* **2001,** *19*, 18000.

22. Price, B. K.; Lomeda, J. R.; Tour, J. M. *Chem. Mater.* **2009,** *21*, 3917-3923.

23. Hudson, J. L.; Casavant, M. J.; Tour, J. M. *J. Am. Chem. Soc.* **2004,** *126*, 11158.

Chapter 3

Diazonium Functionalization of Surfactant Wrapped Chemically Converted Graphene Sheets

3.1 Introduction

In this chapter, a method to functionalize chemically converted graphene sheets (CCG)[1,2] using diazonium salt is described. It focuses on the advantage of preparing and using using graphene oxide (GO)[3,4] that yields bulk quantities of single sheets of water-soluble graphene derivatives. CCG is obtained by reduction of GO with hydrazine followed by treatment with aryl diazonium salts. Although stable aqueous dispersions of CCG have been reported (Figure 3.1),[1,2,5] the direct use of CCGs is somewhat challenging because of the difficulty of redispersing the products in solvents after work-up and recovery, unless stabilized by surfactants or molecules that prevent reaggregation.

The oxidation of graphite to GO[3,4] allows for a high yielding route to exfoliated carbon nanosheets. The GO sheets disperse readily in water due to the presence of hydrophilic oxygen groups on the basal planes and edges,[6-8] although there may be variations depending on which oxidation method is used.[9] While the graphitic nature of the resulting nanosheets is highly compromised by the oxidation, leading to a loss of conductivity, reduction by chemical,[10] thermal,[11] or electrochemical[12] methods results in partial recovery of the graphitic character. That the sp^2 network is reestablished to a certain extent, can be determined by the conductivity of the films when these nanosheets

are deposited on different substrates,[13] by powder X-Ray diffraction data,[14] and electron diffraction pattern data.[15]

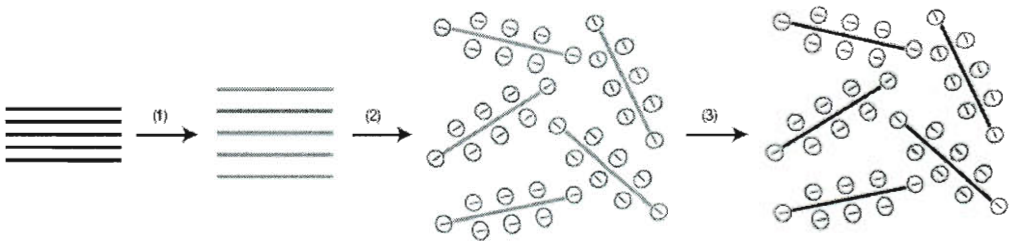

Figure 3.1 Scheme for preparation of stable aqueous dispersions of CCG by (1) oxidation of graphite to GO, (2) stabilization of GO sheets by electrostatic repulsion, and (3) hydrazine reduction to convert GO to CCG.[2]

Functionalized graphene sheets obtained from rapid thermal expansion of GO have been shown to yield individual sheets that disperse readily in a variety of solvents.[11] Furthermore, derivatization of GO via the oxygen groups[16-20] have rendered the initially hydrophilic sheets hydrophobic. Previous work in our group has shown that aryl diazonium salt treatment of single wall carbon nanotubes (SWCNTs)[21-26] produces functionalized SWCNTs; the diazonium chemistry gives us the capability of tailoring the functionalized materials by changing the addends. Functionalized SWCNTs have been shown to improve the dispersion and interfacial adhesion of the nano-reinforcing agent within the host matrix.[27] Likewise, substituted aryl groups can be readily anchored to other carbon surfaces such as graphite and glassy carbon by electrochemical reduction of diazonium salts.[28-31]

3.2 Results and Discussion

Owing to the high yield of individual sheets, the chemical oxidation of graphite to GO is one of the preferred methods to achieve nanosheets from graphite. The use of reducing agents such as hydroquinone, $NaBH_4$ and hydrazine have all been shown to be effective in removing most of the oxygen-containing groups[1,26,7] and to a certain extent restore the conductivity of the material, albeit several orders of magnitude lower (in S/cm) than that of graphene.[6,13,32]

The functionalization of CCG was accomplished by preparing surfactant-wrapped CCG (S-CCG) similar to the procedure employed for preparation of CNT decants (Scheme 3.1).[33] Prior to functionalization, the S-CCG sheets were analyzed in their solution environments by cryogenic transmission electron microscopy (cryo-TEM) to establish the existence of individual sheets and a few multiple sheet structures (Figure 3.2). Aqueous CCG dispersions without SDBS were also prepared based on the procedure reported by Li, et al.,[2] and treated with aryl diazonium salts and found out to react similarly in conjunction with the findings of Si, *et al.* yielding functionalized CCG (f-CCG).[34] However diazonium functionalization is maximized with the use of S-CCG decants due to a more concentrated nanosheet dispersion (1 mg/mL based on GO weight) compared to the nanosheets from aqueous CCG (0.25 mg/mL) .

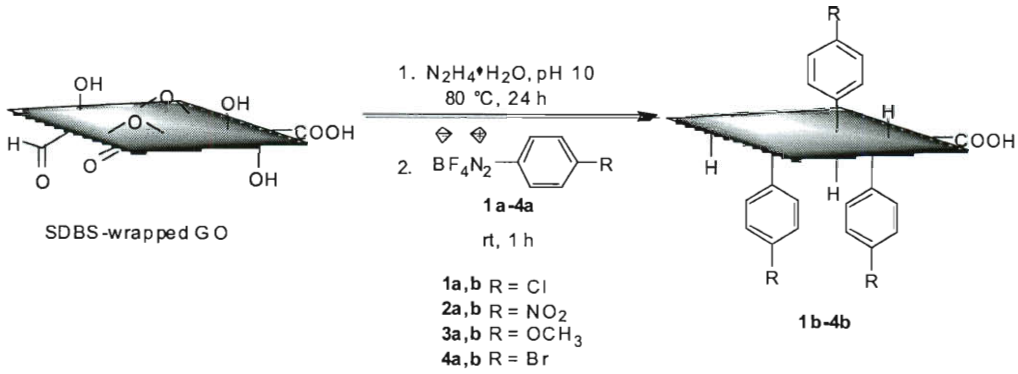

Scheme 3.1. Starting with SDBS-wrapped GO, reduction and functionalization of intermediate SDBS-wrapped CCG with diazonium salts.

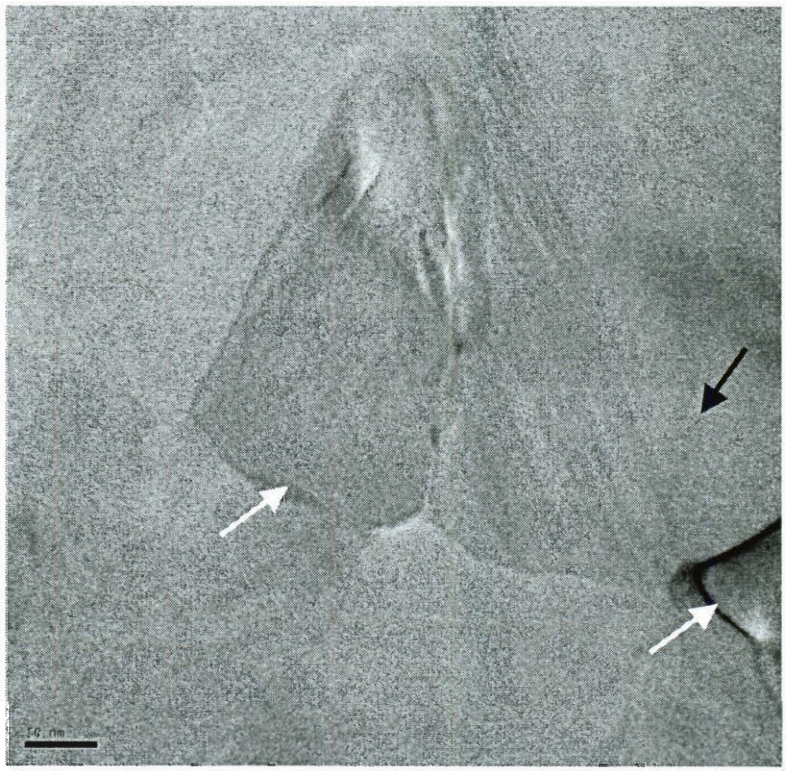

Figure 3.2. Cryo-TEM image of S-CCG (white arrows) and a crystal of ice situated beside the graphene sheet (black arrow). The scale bar is 50 nm.

Removal of a majority of the oxygen groups from GO by hydrazine has been verified using X-ray photoelectron spectroscopy (XPS) as has been reported by several groups.[1,2,13] The C1s spectrum of the CCG shows significant decrease of signals at 286-288 eV, which indicates loss of C-O and C=O functionalities (Figure 3.3). The surface oxygen groups in GO were estimated to be 32%, with little nitrogen (0.4%), while after treatment with hydrazine the percentage of oxygen decreased to 8.7% with 1.4% nitrogen. The small increase in nitrogen content can be attributed to the formation of hydrazones. Upon treatment with the appropriate aryl diazonium salts, a significant percentage of halogen marker (Cl or Br), was detected with very little accompanying nitrogen, which implies that the surface was successfully functionalized. High resolution XPS of **1b** and **4b** gave the following atomic percentages of halogens: (**1b**) 4.6% Cl and (**4b**) 3.2 % Br with ~1 % N. A control experiment was conducted by adding chlorobenzene to the S-CCG decant, followed by work-up and XPS analysis to rule out the possibility that the Cl was incorporated by physisorption and intercalation of chlorinated materials between the sheets rather than carbon-carbon bond formation. XPS analysis showed no Cl peak at 200 eV. Furthermore, GO was treated with **4a** showed no Br peak after work-up. Hence, the successful functionalization supports the assumption that partial rearomatization of the nanosheets under the hydrazine reduction conditions has occurred and thereby provided a surface for aryl grafting using the diazonium species.[35]

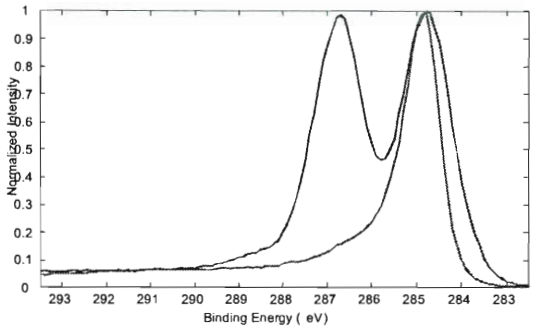

Figure 3.3. Core-level C1s XPS Spectra of GO (red) and CCG (blue) showing significant loss of C-O (286 eV) and C=O (287 eV) groups after reduction.

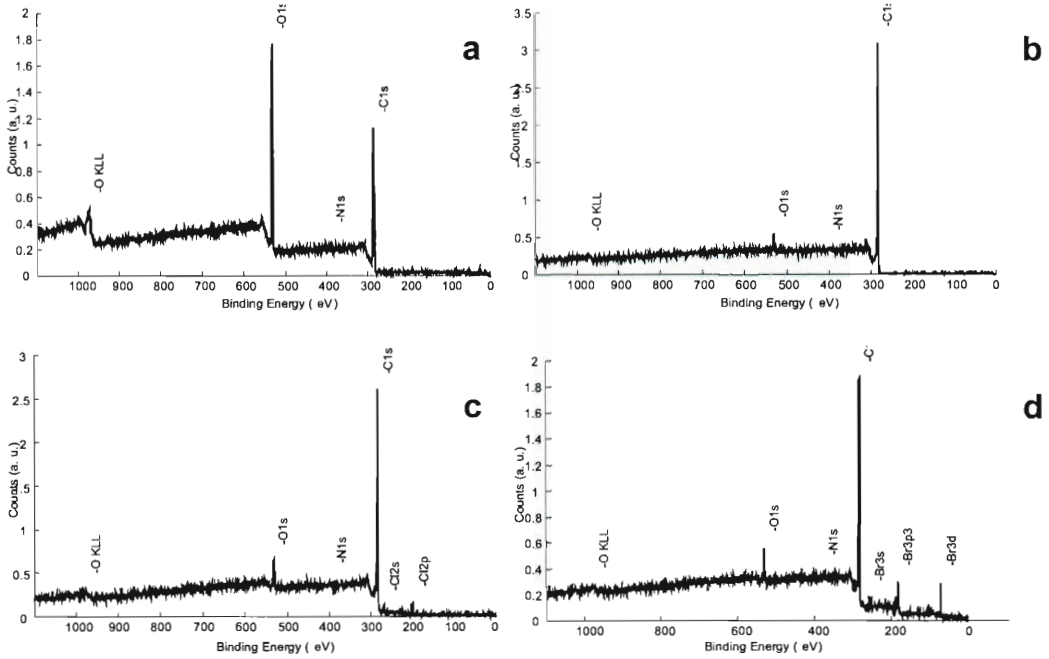

Figure 3.4. XPS Survey scan of (a) GO; (b) CCG; (c) **1b** showing Cl 2p peaks at ~ 200 eV; and (d) **4b** showing Br 3d peak at 70 eV.

The Raman spectrum of bulk CCG using 514 nm laser excitation shows a similar profile to that of GO, with a diamondoid (D) to graphitic (G) ratio close to 1, confirming the incomplete recovery of the graphene structure, similar to what was observed for thermally reduced graphene (Figure 3.5).[5,6] However, the 2D peak at ~2700 cm^{-1} is more pronounced on reduced samples compared to the parent GO, which is an indication of the sp^2 network being present within the sheets. After functionalization with diazonium salts as described here, the D to G ratios of the f-CCGs were similar to those of the S-CCG, therefore gauging the degree of functionalization was difficult using Raman spectroscopy. f-CCG samples heated in a thermogravimetric analysis (TGA) instrument to 850 °C under argon also showed some decrease in the intensity of the diamondoid peak, consistent with functionalization. Edge-defects may be responsible for the minimal change in the D/G ratios although larger CCG sheets (~ 2 μm) evaluated by Raman also gave the same profile.[32]

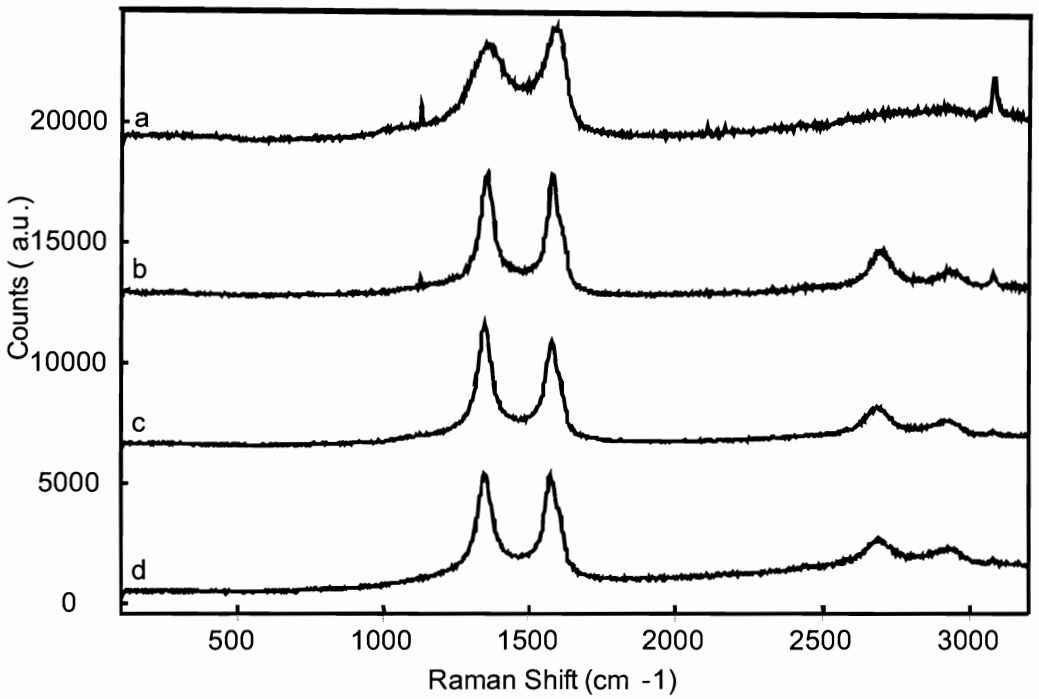

Figure 3.5. Raman spectra of (a) GO; (b) S-CCG (c) **1b** and (d) **1b** after heating under Ar to 850 °C.

The IR spectrum (Figure 3.6) of GO shows a C-O stretch at ~ 1200 cm^{-1} and O-H stretch at 3500 - 3300 cm^{-1}, as well as a C=O stretch at 1720 – 1690 cm^{-1}. The S-CCG (Figure 3.6b), however, is devoid of any informative signal and resembles that of bulk graphite. Figure 3.6c shows the ATR-IR spectrum of f-CCG **2b.** Asymmetric and symmetric stretches at 1513 cm^{-1} and 1343 cm^{-1}, respectively, are attributed to the NO_2 group, and the C-N stretch at 852 cm^{-1} and the aromatic stretch at 1586 cm^{-1} indicates the presence of nitrobenzene moieties on the f-CCG sheets.[28, 29] The presence of NO_2 was further confirmed by XPS analysis with a strong signal at 406 eV. Also, the absence of azo groups in the 1400 – 1500 cm^{-1} region in the spectra of the halogen-containing f-CCGs supports the assumption that a radical process is operating in the functionalization

with diazonium salts, similar to the process with SWCNTs, thereby generating the aryl radicals.[23,25,26]

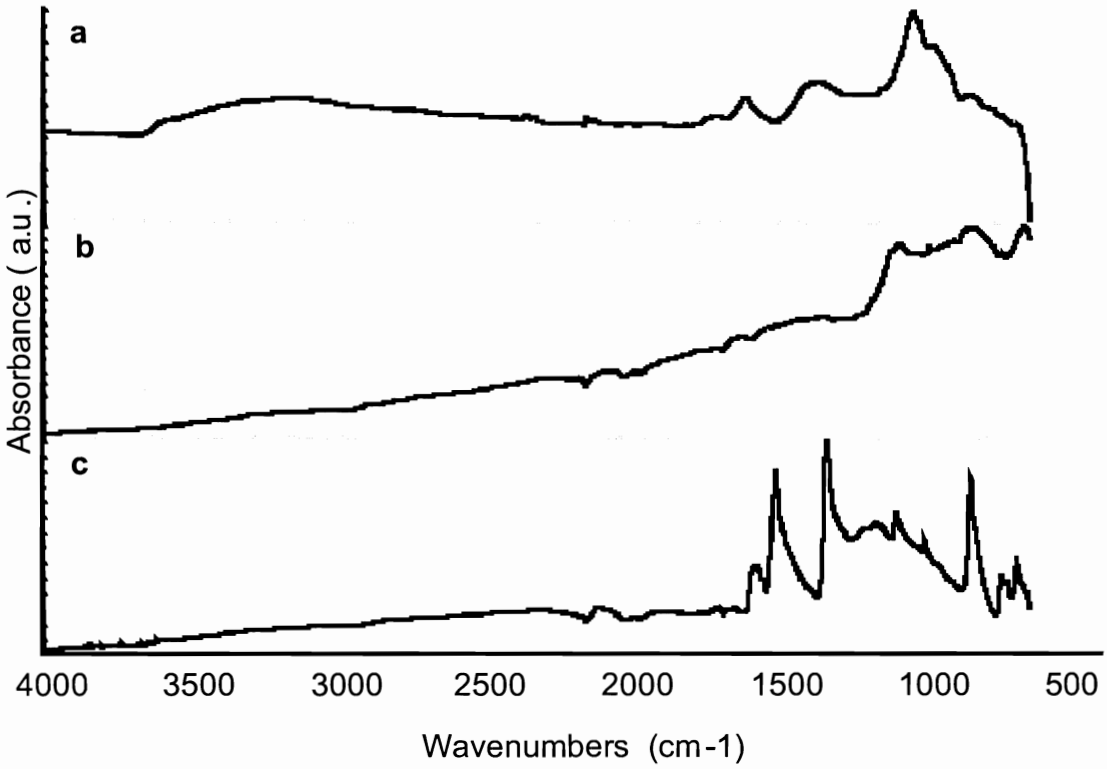

Figure 3.6. ATR-IR spectra of (a) GO; (b) S-CCG; and (c) f-CCG **2b**.

The f-CCGs can be readily dispersed in *N,N'*-dimethylformamide (DMF), *N,N'*-dimethylacetamide (DMAc) and *N*-methyl-2-pyrrolidinone (NMP) up to 1 mg/mL with minimal sedimentation (Figure 3.7). To further illustrate their respective solubilities in DMF, 3 mg of S-CCG or f-CCGs were dispersed in 3 mL DMF by using an ultrasonic cleaner (Cole-Parmer Model 08849-00) for 5 min followed by centrifugation in an Adams Analytical centrifuge (Model CT 3201) for 15 min at 3200 RPM, after which a 2

mL aliquot of each supernatant (Figure 3.7) was taken and precipitated in acetone, filtered and the filter cake was washed with acetone, dried and weighed. The supernatant of f-CCGs gave dark solutions with some sedimentation while nothing remained in the S-CCG supernatant; everything settled to the bottom and hence the solubility is taken as near zero. The solubilities of the f-CCGs are as follows: **1b,** 0.25 mg/mL; **2b,** 0.45 mg/mL; **3b,** 0.30 mg/mL and **4b,** 0.50 mg/mL.

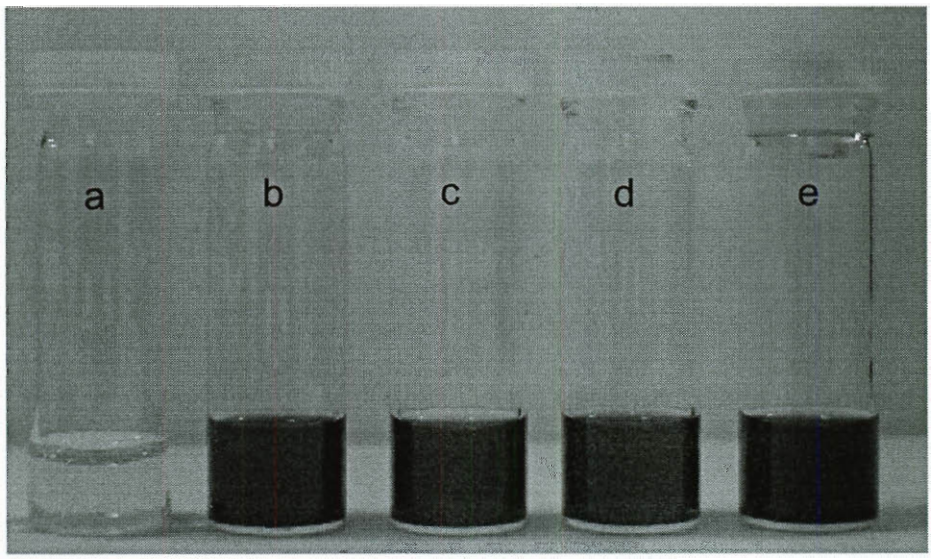

Figure 3.7. Photographs of supernatant solutions obtained from DMF dispersions of (a) CCG and (b) **4b** (c) **1b** (d) **2b** (e) **3b** after centrifugation for 15 min at 3200 RPM

Individual functionalized graphene sheets were imaged using tapping mode AFM. Figure 3.8 shows images of graphene sheets spin-coated onto a mica surface using a 0.1 mg/mL dispersion of **2b** in DMF. The theoretical height for a graphene sheet functionalized on both sides is ~2.2 nm, assuming that the height of the bare graphene

sheets is 1 nm[1,13] with the substituted aromatic groups contributing ~0.6 nm in height. On the average, the height of f-CCG sheets ranges from 1.8 – 2.2 nm. Overall, the nanosheets may be composed of single or bilayers of graphene sheets.

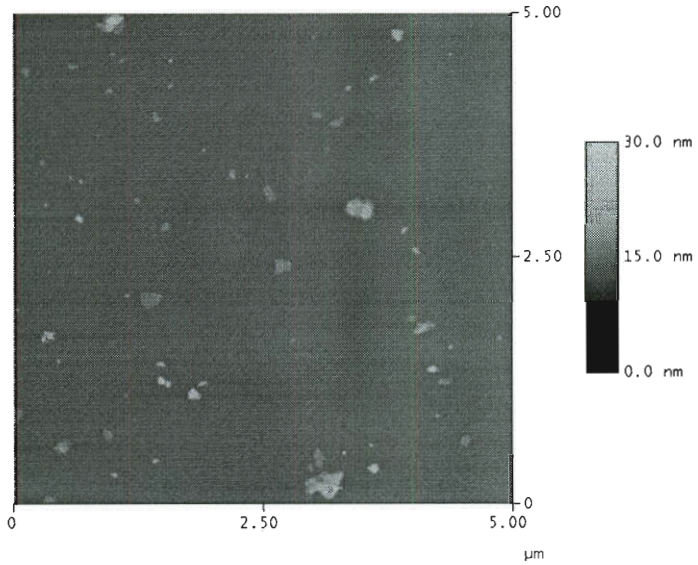

Figure 3.8. Atomic force micrographs by height of f-CCG **2b** spin coated from DMF dispersions onto a freshly cleaved mica surface showing single f-CCG sheets accompanied by bilayers to several layers.

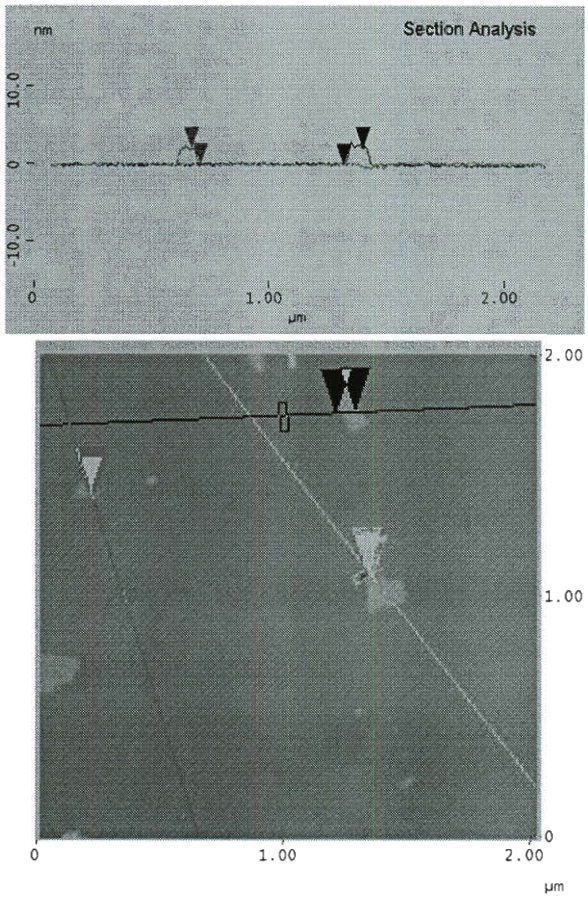

Figure 3.9. Section analysis of **2b** showing height ranges from 1.8 to 2.2 nm.

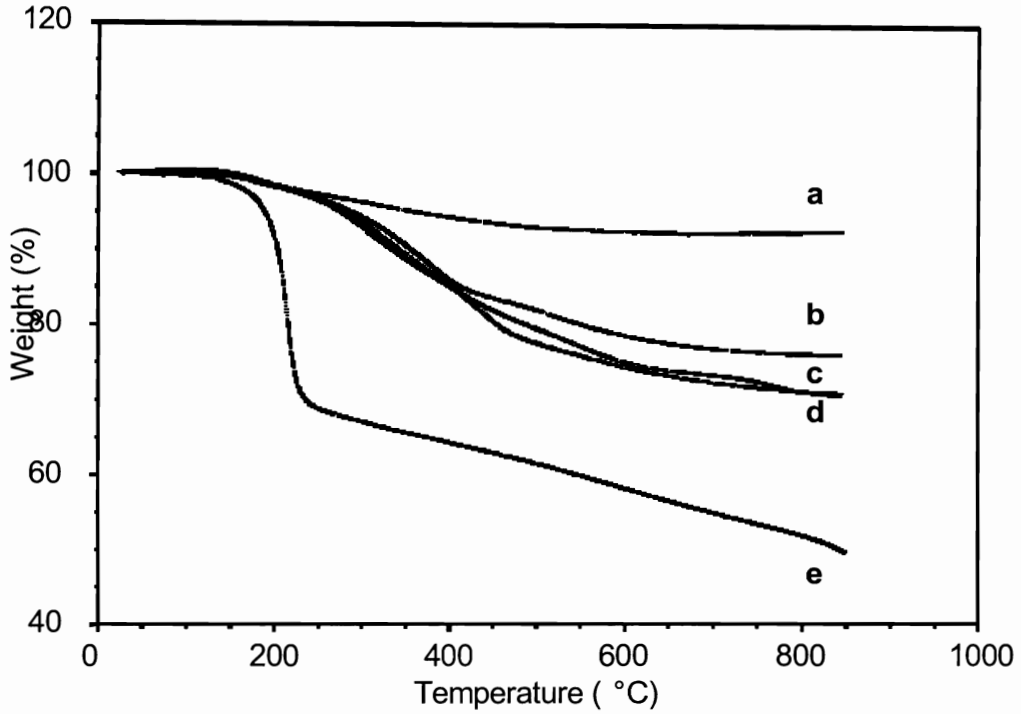

Figure 3.10. TGA thermograms of (a) CCG (b) **2b** (c) **3b** (d) **1b** and (e) GO.

The presence of functional groups on the graphene sheets was further analyzed using TGA by heating under an argon atmosphere to 850 °C at a rate of 10 °C/min (Figure 3.10).[26,28] The overall weight loss of S-CCG is ~7.4 %, which can be attributed to the loss of COOH groups that were not reduced by the hydrazine treatment; their presence is an indication of the incomplete rearomatization. On the other hand heating GO using the same heating program produced a weight loss of 50 %. The observed weight loss for the f-CCG sheets are as follows: (**1b**) 29 % (**2b**) 24 % (**3b**) 29 % (**4b**) 31 %. The degree of functionalization calculated from these weight losses is estimated to be ~1 functional group in 55 carbons. This underscores the efficacy of the functionalization method described here.

3.3 Experimental Section

3.3.1 Graphite Oxide. Graphite oxide was synthesized from expanded graphite obtained from SupraCarbonics, LLC using the Staudenmaier procedure.[4] Briefly, 5.00 g (416.7 mmol C) of expanded graphite was added in five portions into a stirred mixture of concentrated H_2SO_4 (87.5 mL) and fuming HNO_3 (45 mL) while cooling in an ice-water bath. To the mixture was added $KClO_3$ (55 g) in five separate portions over a period of 15 min. The reaction was conducted with sufficient venting using nitrogen gas to reduce the risk of explosion upon generation of chlorine dioxide gas. [Caution: protective equipment including lab coat, face shield, acid resistant gloves and blast shield must be used at all times.] The resulting slurry was stirred at room temperature for 96 h. The green slurry was poured into 4 L of ice water and the mixture was filtered and subsequently washed with 5 L of 5% HCl. The filter cake was then rinsed thoroughly with water until the filtrate was neutral. This was followed by rinsing the filter cake with methanol and diethyl ether, yielding 4.1 g of a fine brown powder of GO.

3.3.2 Diazonium Functionalization. The S-CCG sheets was prepared based on a procedure similar to that reported for SWCNT decant preparation.[33] GO (225 mg) was dispersed in 1 wt % aqueous sodium dodecylbenzenesulfonate (SDBS) surfactant (225 mL) and homogenized for 1 h using a Dremel tool (400 xpr) fitted with a standard-capacity rotor-stator generator (Cole-Parmer A-36904-52) followed by cup horn sonication (Cole-Parmer Ultrasonic Processor Model CP 750) at 80% power for 10 min. The pH was adjusted to 10 (measured with pH paper) using 1 M aqueous NaOH. The resulting GO dispersion was reduced with 60 % hydrazine hydrate (2.25 mL, 72.23

mmol) at 80 °C for 24 h,[1] followed by filtration using glass wool to remove large aggregates, yielding the S-CCG dispersion decant with a typical concentration of 1 mg/mL. In a typical functionalization procedure (Scheme 3.1), 20 mL of S-CCG dispersion was reacted with an aryl diazonium salt (0.33 mmol/mL S-CCG) for 1 h at room temperature. The mixture was then diluted with 100 mL of acetone and filtered through a 0.45 μm PTFE (Teflon®) membrane. The filter cake was washed with water and acetone (3 ×) and resuspended in DMF to remove SDBS and excess diazonium salt. This was followed by filtration and copiously washing the filter cake with acetone. The resulting solid was dried in a vacuum oven overnight at 70 °C with a yield of 22 – 24 mg of f-CCG.

3.4 Conclusion

A convenient procedure originally developed for functionalization of SCWNTs was successfully applied functionalize CCGs with high amounts of varying aryl addends, allowing these nanosheets to be solubilized in organic solvents. This development may prove to be useful in the area of composites, especially in the use of these 2-D structures as reinforcing agents where intimate interfacial bonding between the host and structural modifier is critical. Unlike the 1-D functionalized SWCNT composites, these 2-D structures should be of particular interest where gas diffusion or separation barriers are sought from the composite frameworks.

3.5 Experimental Contributions

My contribution to this work is the preparation of GO, CCG and S-CCG and functionalization with aryl diazonium salts. I also performed the characterizations of the f-CCGs including XPS, ATR-IR, and TGA. Condell D. Doyle prepared the aryl diazonium salts used in functionalization and AFM measurements. Dmitry V. Kosynkin provided advice and insights in the experimental design.

References

1. Stankovich, S.; Piner, R.; Chen, X.; Wu, N.; Nguyen, S. T.; Ruoff, R. S. *J. Mater. Chem.* **2006,** *16*, 155.
2. Li, D.; Mueller, M. B.; Gilje, S.; Kaner, R. B.; Wallace, G. G. *Nat. Nanotechnol.* **2008,** *3*, 101.
3. Hummers, W. S.; Offeman, R. E. *J. Am. Chem. Soc.* **1958,** *80*, 1339.
4. Staudenmaier, L. *Ber. Dtsch. Chem. Ges.* **1898,** *31*, 1481.
5. Tung, V. C.; Allen, M. J.; Yang, Y.; Kaner, R. B. *Nat. Nanotechnol.* **2009,** *4*, 25-29.
6. Lerf, A.; He, H.; Forster, M.; Klinowski, J. *J. Phys. Chem. B* **1998,** *102*, 4477-4482.
7. He, H. Y.; Riedl, T.; Lerf, A.; Klinowski, J. *J. Phys. Chem.* **1996,** *100*, 19954.
8. Szabo, T.; Berkesi, O.; Forgo, P.; Josepovits, K.; Sanakis, Y.; Petridis, D.; Dekany, I. *Chem. Mater.* **2006,** *18*, 2740-2749.
9. Boehm, H. P.; Scholtz, W. *Z. Anorg. Allg. Chem.* **1965,** *335*, 74.

10. Stankovich, S.; Dikin, D. A.; Piner, R.; Kohlhaas, K. M.; Kleinhammes, A.; Jia, Y.; Wu, Y.; Nguyen, S. T.; Ruoff, R. S. *Carbon* **2007,** *45*, 1558.

11. McAllister, M. J.; Li, J. L.; Adamson, D. H.; Schniepp, H. C.; AbdalaA, A.; Liu, J.; Herrera-Alonso, M.; Milius, D. L.; Car, R.; Prud'homme, R. K.; Aksay, I. A. *Chem. Mater.* **2007,** *19*, 4396.

12. Voloshin, A. G.; Kolesnikova, I. P. *Elektrokhimiya* **1980,** *16*, 270.

13. Gilje, S.; Han, S.; Wang, M.; Wang, K. L.; Kaner, R. B. *Nano Lett.* **2007,** *7*, 3394.

14. Bourlinos, A. B.; Gournis, D.; Petridis, D.; Szabo, T.; Szeri, A.; Dekany, I. *Langmuir* **2003,** *19*, 6050.

15. Stankovich, S.; Dikin, D. A.; Dommett, G. H. B.; Kohlhaas, K. M.; Zimney, E. J.; Stach, E. J.; Piner, R. D.; Nguyen, S. T.; Ruoff, R. S. *Nature* **2006,** *442*, 282.

16. Matsuo, Y.; Nishino, Y.; Fukutsuka, T.; Sugie, Y. *Carbon* **2007,** *45*, 1384.

17. Matsuo, Y.; Fukunaga, T.; Fukutsuka, T.; Sugie, Y. *Carbon* **2004,** *42*, 2117.

18. Matsuo, Y.; Tabata, T.; Fukunaga, T.; Fukutsuka, T.; Sugie, Y. *Carbon* **2005,** *43*, 2875.

19. Niyogi, S.; Bekyarova, E.; Itkis, M. E.; McWilliams, J. L.; Hamon, M. A.; Haddon, R. C. . *J. Am. Chem. Soc.* **2006,** *128*, 7720-7721.

20. Stankovich, S.; Piner, R. D.; Nguyen, S. T.; Ruoff, R. S. *Carbon* **2006,** *44*, 3342-3347.

21. Bahr, J. L.; Yang, J.; Kosynkin, D. V.; Bronikowski, M. J.; Smalley, R. E.; Tour, J. M. *J. Am. Chem. Soc.* **2001,** *123*, 6536.

22. Bahr, J. L.; Tour, J. M. *Chem. Mater.* **2001,** *13*, 3823.

23. Dyke, C. A.; Tour, J. M. *Nano Lett.* **2003,** *9*, 1215.

24. Dyke, C. A.; Stewart, M. P.; Maya, F.; Tour, J. M. *Synlett*. **2004**, 155.

25. Doyle, C. D.; Rocha, J. D. R.; Weisman, R. B.; Tour, J. M. *J. Am. Chem. Soc.* **2008,** *130*, 6795.

26. Price, B. K.; Tour, J. M. *J. Am. Chem. Soc.* **2006,** *128*, 12899.

27. Mitchell, C. A.; Bahr, J. L.; Arepalli, S.; Tour, J. M.; Krishnamoorti, R. *Macromolecules* **2002,** *35*, 8825.

28. Allongue, P.; Delamar, M.; Desbat, B.; Fagebaume, O.; Hitmi, R.; Pinson, J.; Saveant, J. M. *J. Am. Chem. Soc.* **1997,** *119*, 201.

29. Delamar, M.; Hitmi, R.; Pinson, J.; Saveant, J. M. *J. Am. Chem. Soc.* **1992,** *114*, 5883.

30. Kariuki, J. K.; McDermott, M. T. *Langmuir* **2001,** *17*, 5947.

31. Kariuki, J. K.; McDermott, M. T. *Langmuir* **1999,** *15*, 6534.

32. Gomez-Navarro, C.; Weitz, R. T.; Bittner, A. M.; Scolari, M.; Mews, A.; Burghard, M.; Kern, K. *Nano Lett.* **2007,** *7*, 3499-3503.

33. Moore, V. C.; Strano, M. S.; Haroz, E. H.; Hauge, R. H.; Smalley, R. E. *Nano Lett.* **2003,** *3*, 1379.

34. Si, Y.; Samulski, E. T. *Nano Lett.* **2008,** *8*, 1679.

Chapter 4

Reductive Alkylation of Graphite Oxide

4.1 Introduction

One of the most promising approaches towards high yield of graphene sheets is by employing graphite oxide (GO) that can be obtained by chemical exfoliation of graphite using strongly oxidizing agents.[1-3] GO is different than graphene and graphite due to its high fractions of sp^3-carbons and the presence of hydrophilic oxygen functionality, which makes GO even easily dispersible in water.[4-7] Employing reducing agents allow for partial restoration of the sp^2-network through deoxygenation of the oxygenated single carbon sheets yielding CCGs.[8-10] The reduction process, however, often leads to agglomeration of the CCG single sheets. This problem can be addressed by reduction in the presence of polymer to protect single sheets from agglomeration and in some cases, to achieve solubility in water by polymer wrapping.[11] An alternative procedure is presented in this chapter via reduction/in-situ functionalization process to deoxygenate and introduce the functional groups necessary for dispersing the sheets in polymer matrices as well as preventing the sheets from re-aggregation without the need of stabilizing reagents that can be a drawback in later processing.

The chemistry of fullerenes[12] and CNTs[13] has been well-developed, turning these carbon nanostructures into useful building blocks and fillers. Reductive alkylation has been successfully employed to CNTs for solubilization and use as nano-fillers (Figure

4.1).[14-16] Similar chemical methods have been employed on graphite and its derivatives as well.[17-19]

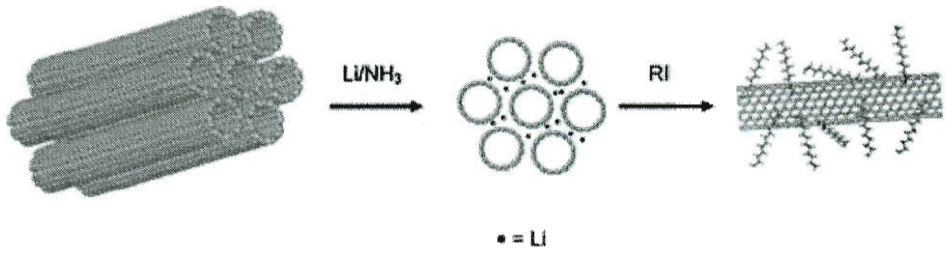

Figure 4.1. Scheme for reductive Alkylation of SWNT in Li/NH_3.[9]

This same protocol is employed to GO to obtain functionalized chemically converted graphene (f-CCG) starting from the corresponding GO, thereby permitting ready access to large amounts of functionalized graphene. In the reaction described here, GO sheets are functionalized which is the key in achieving highly solution-processable nanosheets since functionalization through only edge-COOH groups is insufficient for achieving high levels of solubility. With this method, we are able to obtain well-dispersed single graphene nanosheets without the need for additional surfactant stabilizers.[11] The nanosheets can be dispersed in various organic solvents such as chloroform or ortho-dichlorobenzene (ODCB) and are stable over several weeks, which makes them suitable for dispersion in polymer matrices primarily fluid phase processing.

4.2 Results and Discussion

Functionalization with concomitant reduction was achieved by dispersing GO in a lithium/liquid ammonia solution followed by addition of an aliphatic or aromatic iodide

(Scheme 4.1). The iodides that were used for functionalization were 1-iodooctane and 1-iodoteradecane to produce f-CCG with octyl groups (**1**) and tetradecyl functionalities (**2**). In an effort to obtain a water-soluble material, isophthalic acid groups were attached to the CCG sheets (**3**) using 5-iodoisophthalic acid.

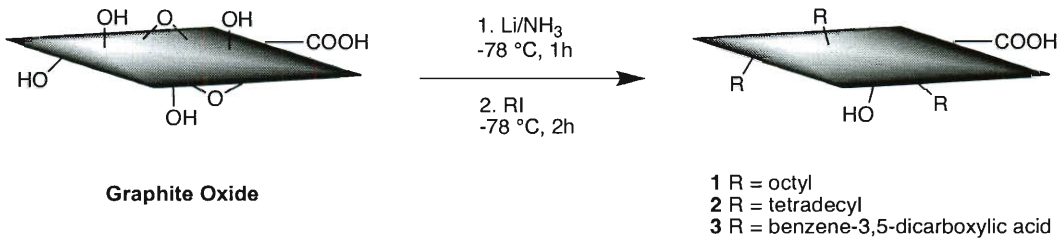

Scheme 4.1. Functionalization of GO with iodoalkanes and iodoisophthalic acid.

The functionalized graphene sheets **1** and **2** can be readily dispersed in organic solvents such as chloroform and ODCB. To estimate the solubility of these compounds, the dispersions were subject to centrifugation and the supernatant was collected. Figure 4.2 shows the supernatant of GO, CCG, **1** and **2** in chloroform. As expected, GO is insoluble and CCG shows minimal solubility, while the solubility of **1** and **2** is increased significantly as evidenced by the supernatants obtained. In the case of GO, all the nanosheets settled to the bottom. The concentration of **1** and **2** was estimated to be 0.35 mg/mL and 0.17 mg/mL, respectively by weighing the residues obtained on a pre-weighed PTFE membrane. Prior to filtration, acetone was added to the supernatant to flocculate the graphene sheets. The amount of CCG dispersed in chloroform was too low to be estimated since it was less than the uncertainty in the balance measurement (0.1 mg). The solubility of **3** was tested in water, 0.1 N NaOH and 0.1 N HCl. Unlike CCG, **3** disperses well in the basic solution, as well as neutral water. It disperses in acidic

solution, but precipitates faster compared to the solutions with higher pH values. However, after centrifugation, no significant amount of **3** was found in any of the supernatant solutions independent of the pH value indicating that after conversion to f-CCG, the –COOH are not effective in solubilizing the CCG. The lower solubility of **2** relative to **1** is likely the result of a higher degree of oxygen left on the structure as seen in the XPS.

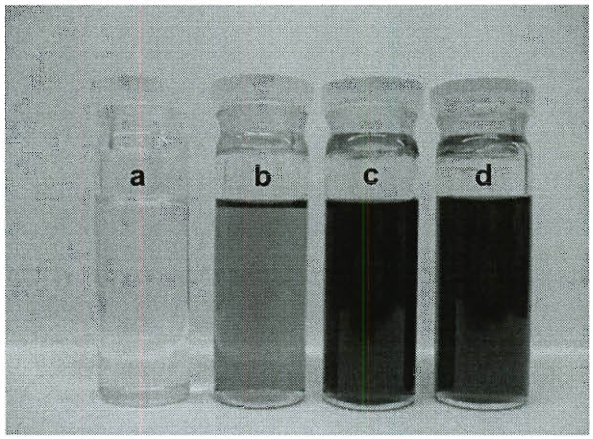

Figure 4.2. The supernatant chloroform solution after centrifugation of (a) GO; (b) CCG; (c) **1** and (d) **2**.

Covalent binding of addends characteristically affects the intensity ratio of the graphene Raman bands. Most important for functionalization is the increase of the D band relative to the G band. Thus the D:G ratio is a good indication of the relative degree of functionalization. The Raman spectrum of GO in Figure 4.3 shows a D:G ratio of 1.9, indicating a high degree of defects in the graphene sheets. As expected, for CCG, the ratio decreased to 1.4 (Figure 4.4), which is a sign of restoration of some of the sp^2 framework of the graphene sheets caused by reduction. Functionalization with 1-

iodooctane, however, increased the ratio to 1.7 (Figure 4.5). The same trend was observed for **2** and **3** with a D:G ratio of 1.5 for both.

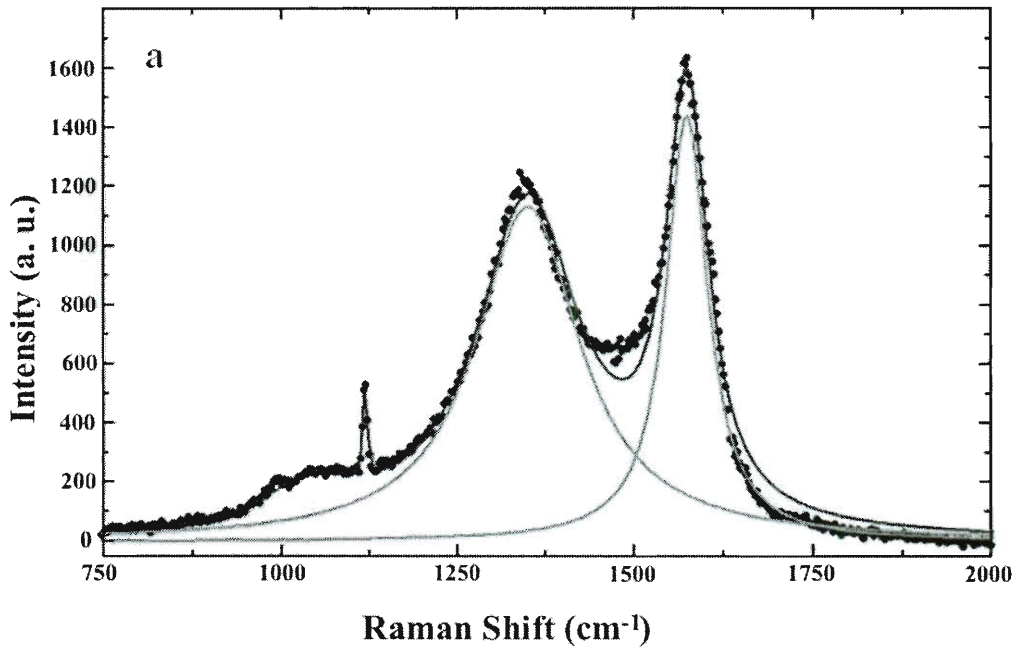

Figure 4.3. Raman spectrum of GO with a D:G ratio of 1.9:1.

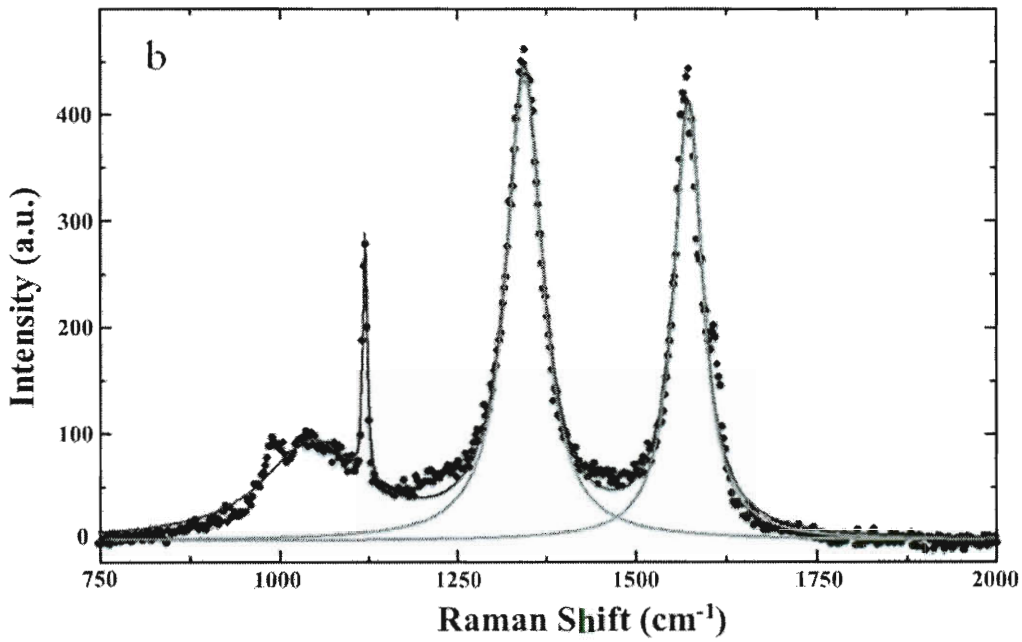

Figure 4.4. Raman spectrum of CCG with D:G ratio of 1.4:1.

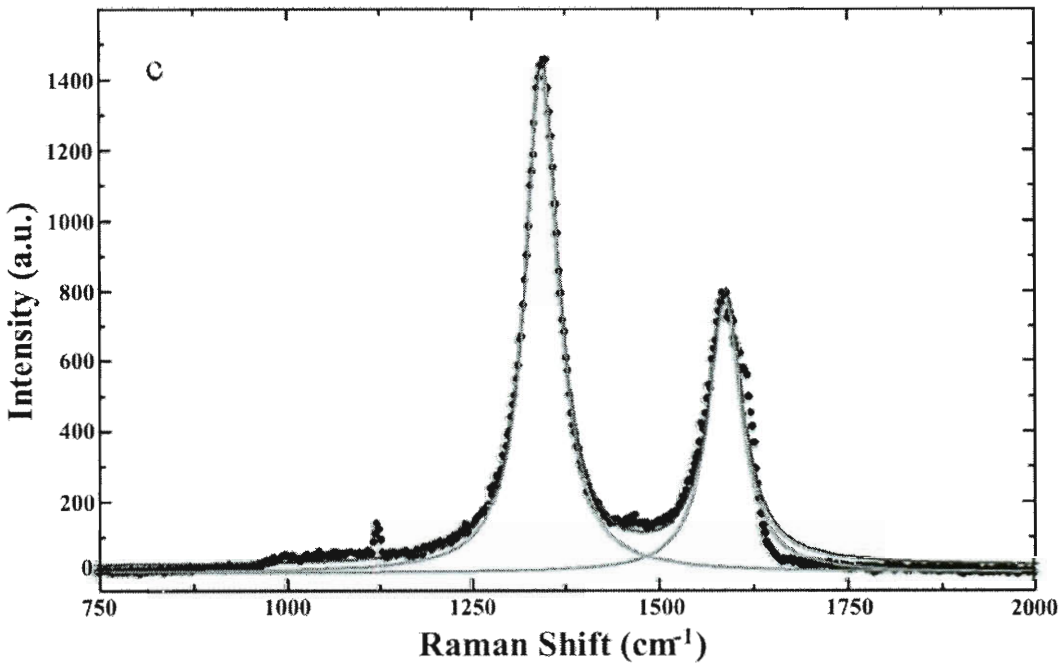

Figure 4.5. Raman spectrum of f-CCG **1** with D:G ratio of 1.7:1.

ATR-IR spectra were recorded and are shown in Figure 4.6. The spectrum of GO shows a strong and broad -COOH and O-H stretching vibration absorption at 3500 – 3300 cm^{-1}, as well as a C=O stretching vibration at 1720 – 1690 cm^{-1}, C-O stretching at 1200 cm^{-1}. The unfunctionalized CCG showed weak Csp^3-H stretching at 2920 cm^{-1} confirming the possibility of protonation upon quenching and the strong peak in O-H region primarily due COOH groups. The presence of alkyl groups in **1** and **2** was confirmed by increased intensities of the C-H stretch at 2840 - 2920 cm^{-1}. The IR spectrum of **3** exhibit carbonyl stretching at 1652 cm^{-1} attributed to the COOH groups of isophthalic acid and still possibly coupled to –COOH on the egdes of GO, an O-H stretching at around 3379 cm^{-1}. The C-H bending at 802 cm^{-1} and the C-O stretching vibration at 1063 cm^{-1} can be observed. Treatment with NaOH resulted in the disappearance of the signal at 1063 cm^{-1} and shift of the 1652 C=O cm^{-1} peak to 1571 cm^{-1} (asymmetrical $-COO^-$ stretching) and 1428 cm^{-1} (symmetrical C-O stretching),[20-21] further confirming the presence of the acidic addends. At 2920 – 2848 cm^{-1} the C-H stretch vibrations are also observed possibly arising from the protonation of the basal planes of CCG as well as protons on the aromatic rings which is common under Birch reduction conditions.

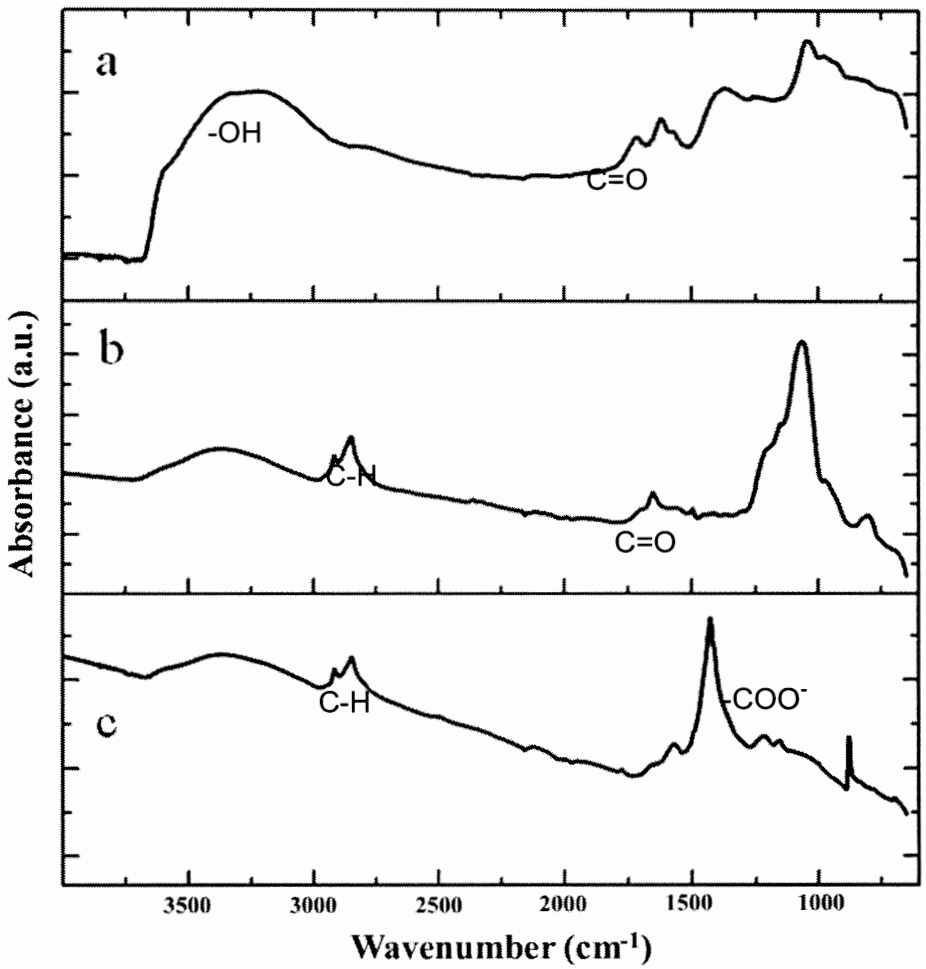

Figure 4.6. ATR-FTIR spectra of (a) GO, (b) f-CCG **3** treated with 10% HCl, and (c) f-CCG **3** treated with 0.1 N NaOH.

A 500 MHz ^{1}H NMR spectrum of a very dilute solution of **1** in $CDCl_3$ shows signals consistent with methyl (0.88 ppm) and methylene protons (1.26 ppm) from the octyl groups (Figure 4.7). The solution was too dilute to obtain any useful ^{13}C NMR data.

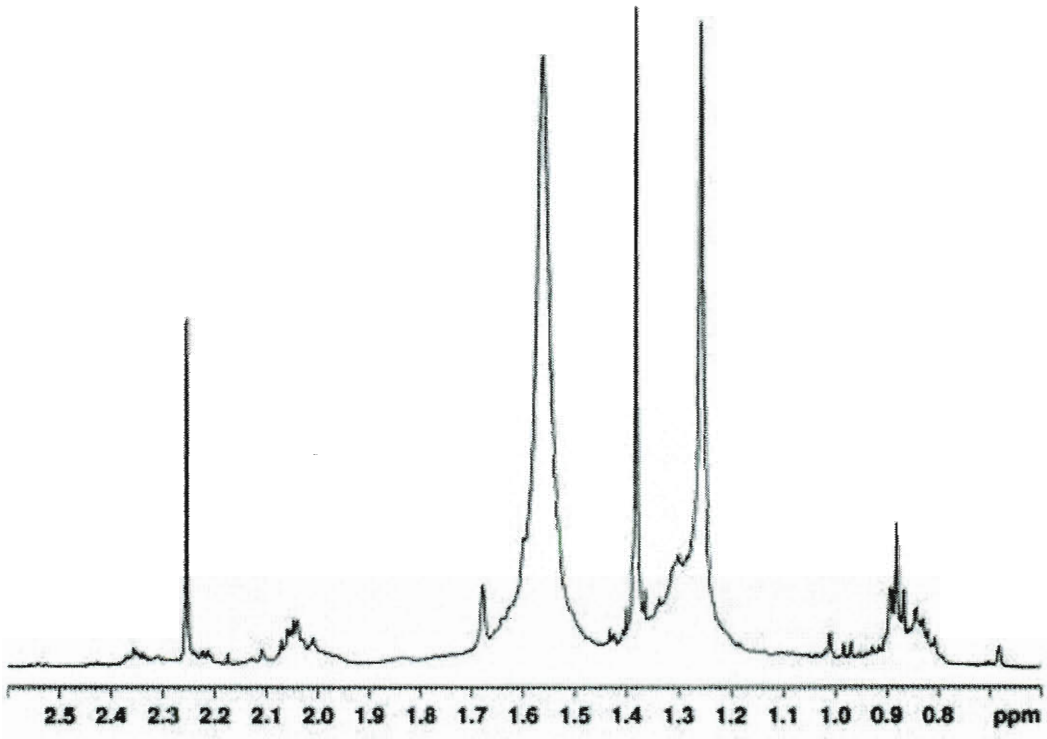

Figure 4.7. Solution 500 MHz ^{1}H NMR spectrum of **1** in $CDCl_3$. The signal at 1.56 ppm is due to water. The triplet at δ 0.88 ppm is consistent with the methyl groups in the octyl chains and the peak at δ 1.26 ppm with the methylene groups.

A ^{1}H-^{13}C cross polarization magic angle spinning (CPMAS) NMR spectrum of **2** shows its complex nature (Figure 4.8). A broad aliphatic carbon signal predominates, with a maximum at 29 ppm consistent with the internal (C-4 through C-11) methylene carbons of the tetradecyl groups. A much weaker signal centered at 73 ppm, consistent with aliphatic carbon bonded to oxygen, can result from tetradecylated hydroxyl groups or from alcohol or ether groups bonded to the graphene framework in the starting material. A broad aromatic carbon signal with a maximum at 123 ppm is evident for the

graphene carbons. A weak broad signal downfield of about 165 ppm is consistent with a variety of carbonyl carbon environments. A very weak downfield spinning sideband of the aliphatic signal might also contribute in this region; however, the corresponding upfield spinning sideband is not detectable.

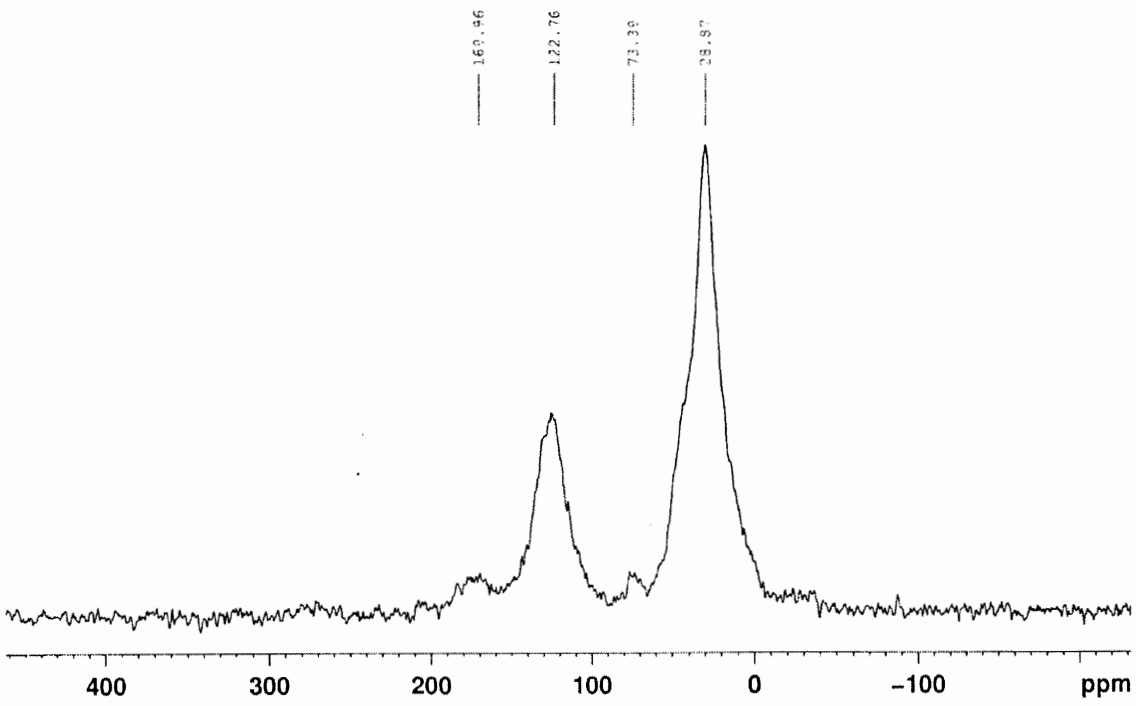

Figure 4.8. ^{1}H-^{13}C Cross polarization magic angle spinning (CPMAS) spectrum of **2**. The signal at δ 29 ppm originates from the aliphatic carbon atoms; the signal at δ 73 ppm from the alcohol and ether carbon atoms; the signal at δ 123 ppm are graphitic carbon atoms; the signal downfield at δ 170 ppm is attributed to various carbonyl groups.

Inserting a 50-μs dephasing interval between cross polarization and FID acquisition (Figure 4.9) severely attenuates the methylene carbon signals, as expected.[39] Unfortunately, no signal could be detected for the more slowly decaying quaternary aliphatic carbons

generated upon functionalization of the graphene sheets. The predominant signal results from the fully substituted, graphitic sp_2 carbons.

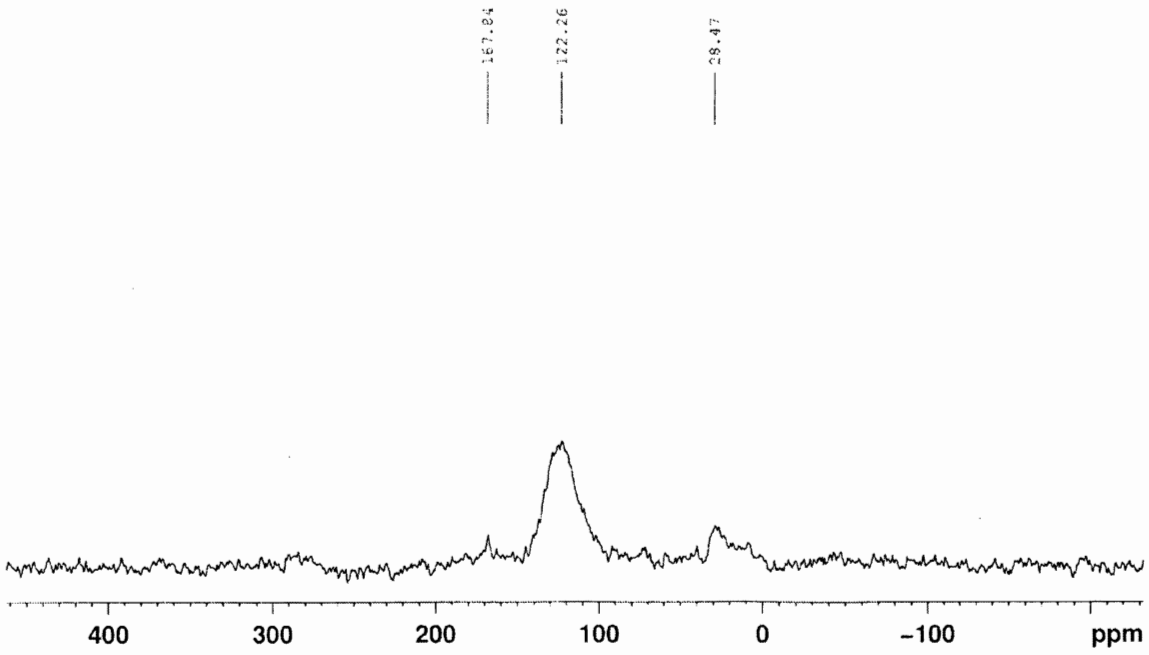

Figure 4.9. ^{1}H-^{13}C CPMAS NMR spectrum of **2** after insertion of a 50-μs dephasing interval between cross polarization and FID acquisition resulting in severe attenuation of the methylene signal at δ 29 ppm.

The direct ^{13}C pulse magic angle spinning (MAS) spectrum (Figure 4.10) differs significantly from the CPMAS spectrum. In the direct ^{13}C pulse spectrum, the signal from graphitic carbons is proportionately much stronger, and a strong, sharp carbonyl signal is present at 168 ppm. Clearly, many graphitic carbons are too far from protons to be cross polarized efficiently (or perhaps even at all), and similarly this specific type of carbonyl environment cannot be cross polarized. A sharp signal at 168 ppm that can be generated only in a direct ^{13}C pulse experiment and XPS data with a peak at 290 eV are consistent with the presence of carbonate groups. [41] The relative signal intensities are meaningful, as lengthening the relaxation delay from 10 s to 20 s results in no detectable change.

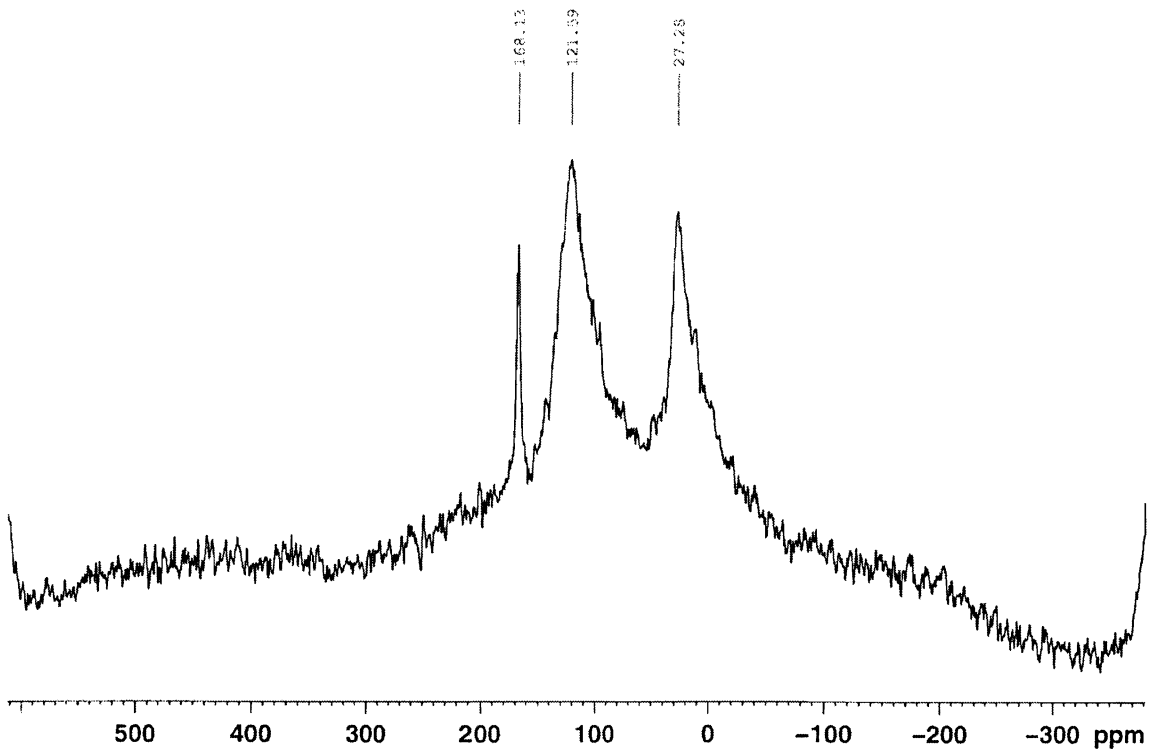

Figure 4.10. Direct ^{13}C pulse magic angle spinning (MAS) spectrum of **2**. The intensity of the aromatic C signal is proportionally greater than in the CPMAS spectrum. The sharp signal at δ 168 ppm is consistent with the presence of carbonate.

The reduction of GO to CCG was confirmed by XPS analysis. The oxygen content decreased from 32% in GO to 4.5% in CCG (4.7% in **1**, 15% in **2** and 18.7% in **3**; the high oxygen content in **2** was due to the presence of carbonate still left in the material that was also determined by NMR). The iodine and lithium content in the samples **1**, **2** and **3** was < 0.1% or not detectable, indicating that the reagents were successfully washed away in the workup procedure. The C1s XPS spectra shown in Figures 4.11 to 4.13

provide additional information about the change in the carbon framework of the graphene sheets. The GO spectrum (Figure 4.11) displays a peak at 284.8 eV and one at 286.7 eV. The higher C1s binding energy of 286.7 eV is due to the carbons bound to oxygen. Both signals are of the same intensity which is due to the highly oxidized sheets. After the treatment with lithium in liquid ammonia, the higher binding energy peak disappears, and one peak at 284.8 eV indicates a successful reduction (Figure 4.12). In Figure 4.13, the spectrum of compound **3**, small shoulders at 286.7 eV and 289 eV can be observed aside from the main peak at 284.8 eV. This is due to the carbonyl groups and COOH groups, respectively, of the isophthalic acid.

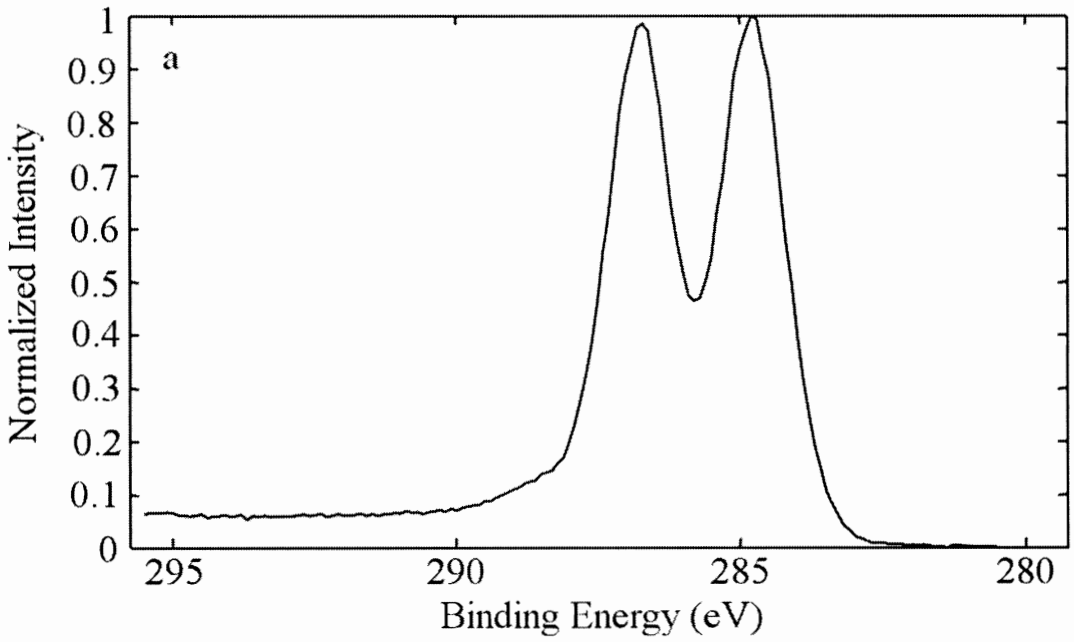

Figure 4.11. Core-level C1s XPS spectrum of GO.

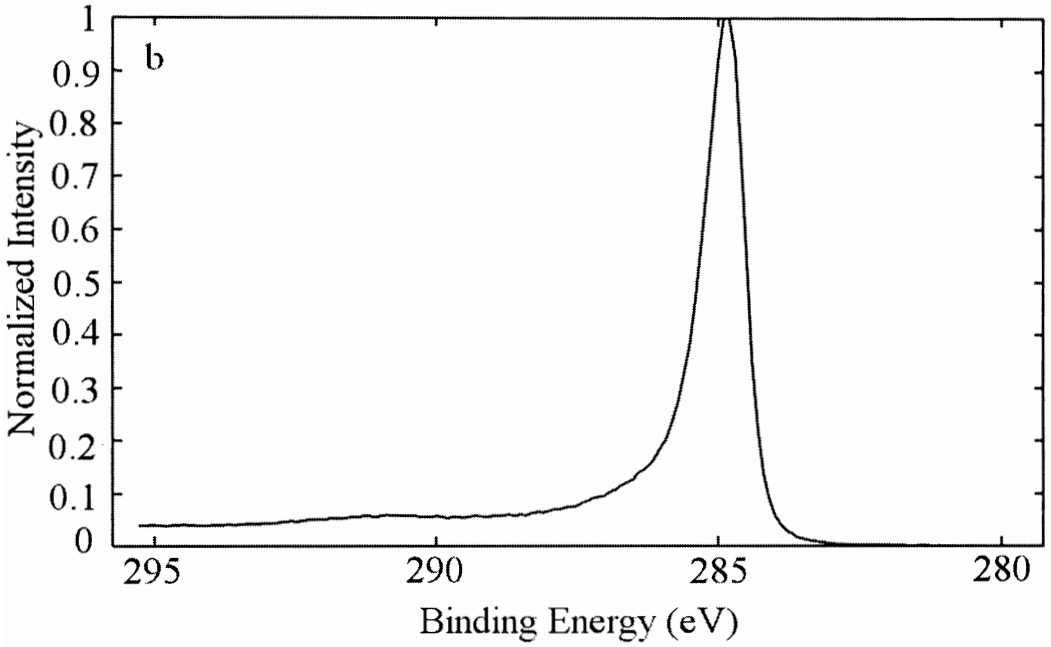

Figure 4.12. Core-level C1s XPS spectrum of CCG.

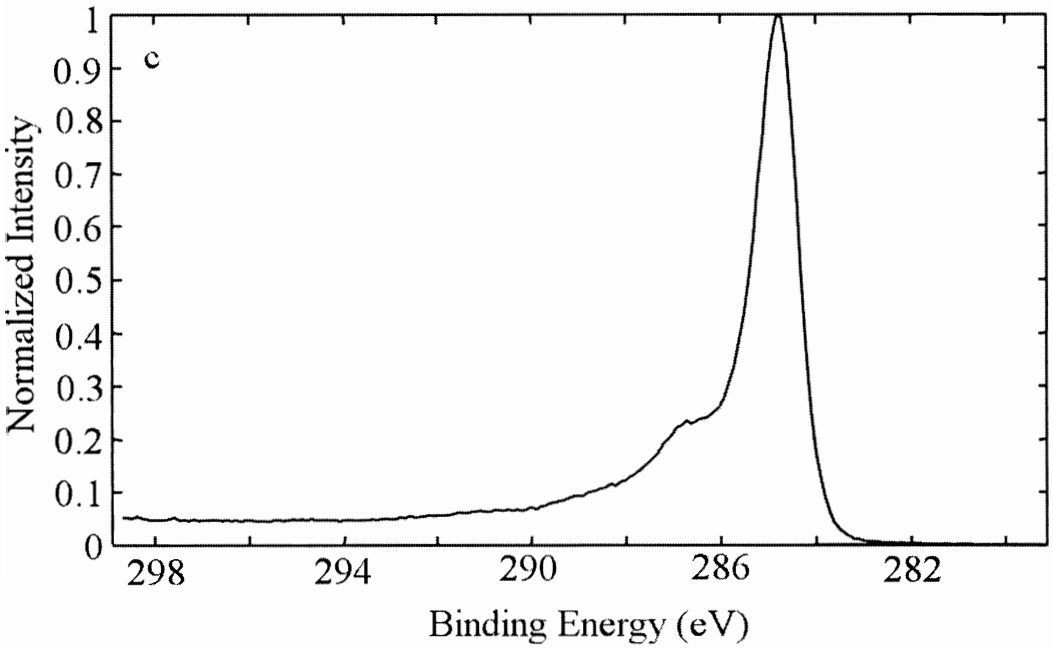

Figure 4.13. Core-level C1s XPS spectrum **3**.

The mass loss in TGA shown in Figure 4.14 was attributed to functional groups covalently attached to the graphene sheets. Using the mass loss relative to CCG and the molecular weight of the functional group fragment, the relative number of moles of functional group to graphitic carbon present was calculated. CCG showed 21% weight loss and GO 40%. The functionalized sheets exhibit a weight loss of 30% for **1**, which is due to one functional group on every 95 carbon atoms; and 47% for **2** which is one functional group every 47 carbon atoms. This heavier functionalization of **2** compared to **1** was also observed in the D:G ratios in the Raman spectra.

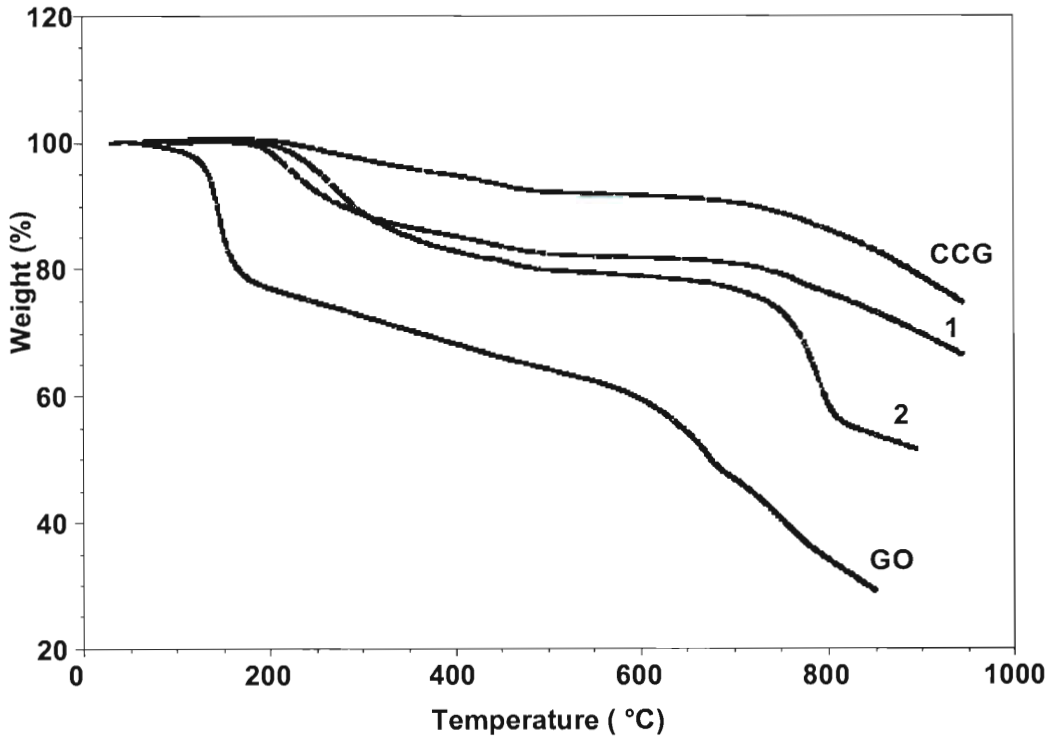

Figure 4.14. TGA thermograms of CCG, GO, **1**, and **2**.

AFM images taken of samples spin-coated onto a freshly cleaved mica surface confirmed the existence of single nanosheets as shown in Figure 4.15. The lateral dimension of the sheets normally ranges from about 50 to 500 nm aside from the presence of bigger flakes that can be a as large as 2 μm. The large flakes are most likely composed of several layers of CCG sheets. The height of the sheets range from 1.2 to 1.8 nm (Figures 4.16 and 4.17). The CCG sheets have heights of about 1 nm;[23] hence, the increase in height can be attributed to the alkyl addends on the sheets. With respect to the large flakes observed, the folding of the graphene sheets within itself as well as stacking is visible and the average height is estimated to be 3.5 nm.

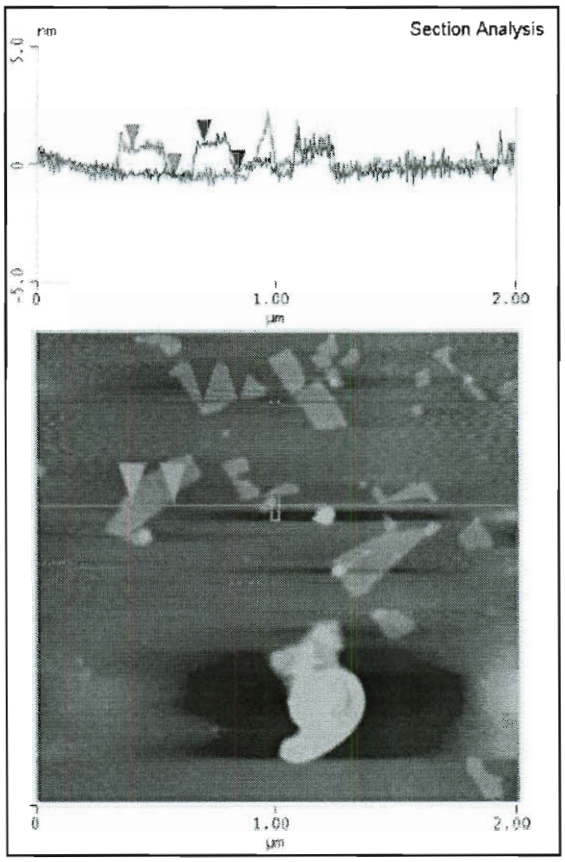

Figure 4.15. AFM micrograph of f-CCG **2** on a freshly cleaved mica surface. Section analysis of small flake **2** with heights ranging from 1.2 – 1.5 nm (top); height mode micrographs of **2** showing single sheets of graphene (bottom).

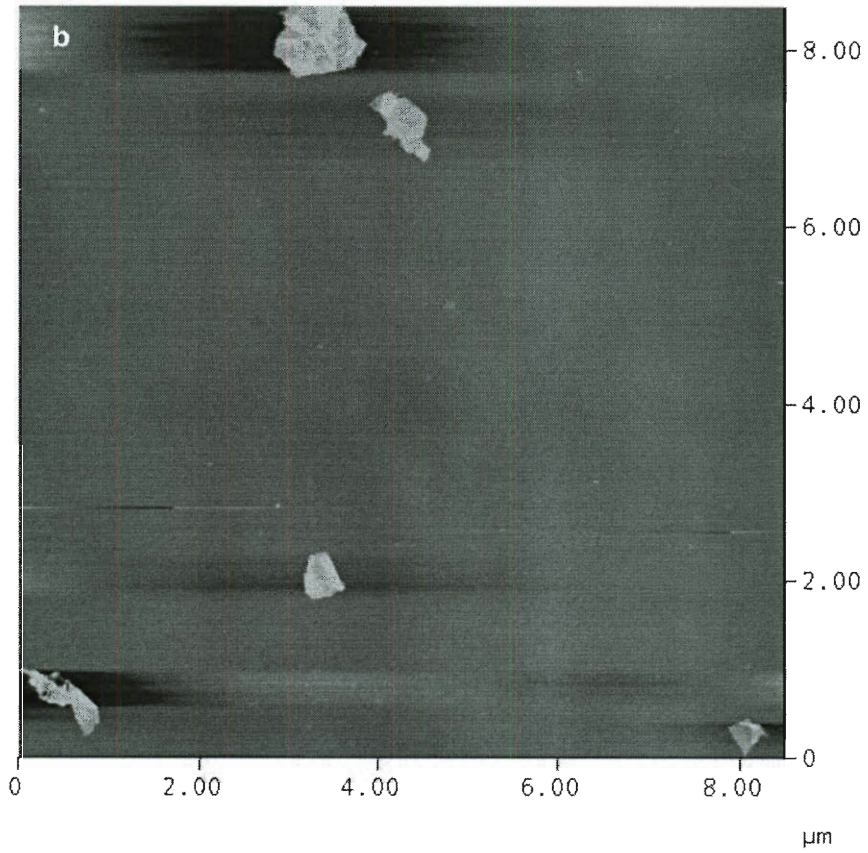

Figure 4.16. AFM micrograph of **1** in height mode consisting of several layers and exhibiting folding of sheets; average height: 1.8 – 3 nm.

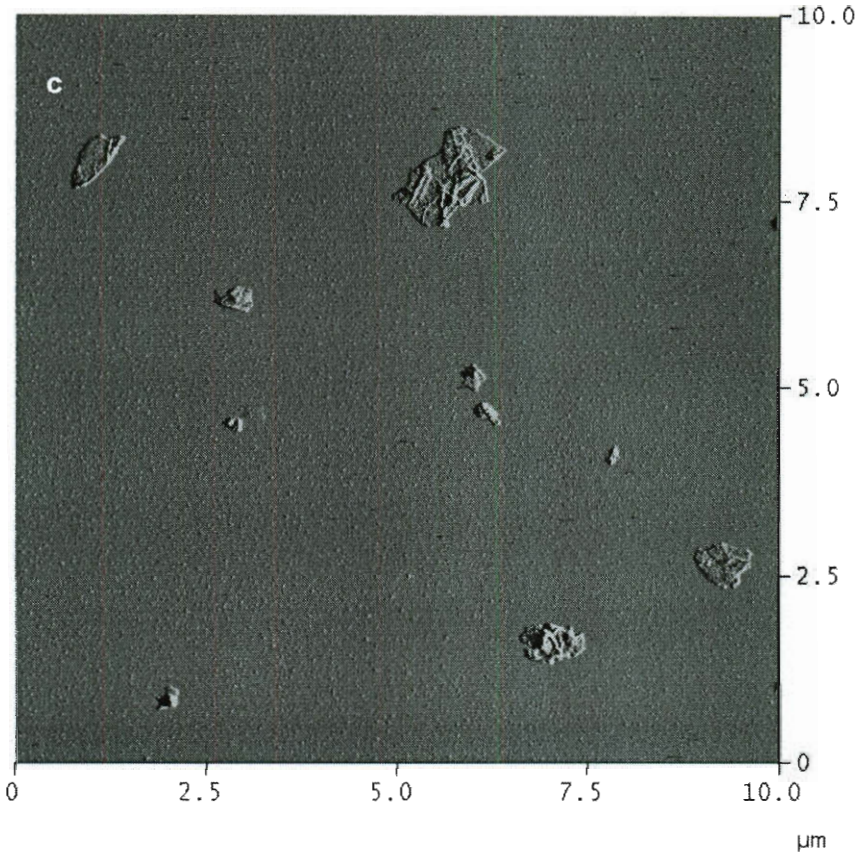

Figure 4.17. AFM micrograph of **2** in amplitude mode; height range: 2 – 3.5 nm.

4.3 Experimental Procedures

4.3.1 General Procedure for the Synthesis of Alkylated CCG. GO (50 mg), which was obtained using the Staudenmaier method[2] on the expanded graphite, was added to a 100 mL nitrogen-purged and heat-dried three-necked round bottom flask, equipped with two gas inlets, a homogenizer (IKA Ultra Turrax T25 fitted with IKA S-25N 10 G dispersing element), dry-ice condenser and bubbler. Dry ammonia (75 mL) was then condensed into the reaction vessel, and the mixture was homogenized at 11000 rpm for 15 min in a dry ice/acetone bath. To the mixture were added small pieces of

lithium metal (150 mg, 22 mmol), and the reaction mixture was homogenized for 1 h at -78 °C. The iodide (12 mmol) was added dropwise for the preparation of **1** and **2** and in small portions for **3** over a period of 15 min (Scheme 1), and the suspension was homogenized for an additional 2 h at -78 °C. After allowing the ammonia to evaporate at room temperature, the reaction mixture was quenched by the slow addition of absolute ethanol and then water. The mixture was acidified with 0.1 N HCl, and the product extracted into hexanes and washed several times with water. The hexane layer was then filtered through a 0.45 μm polytetrafluoroethylene (PTFE) membrane. The filter cake was washed with acetone and re-suspended in DMF, filtered again and the resulting filter cake was washed with acetone. The filter cake was re-suspended in chloroform, acetone was added to flocculate the solids, and the mixture was filtered and the solid was dried overnight in vacuo at 65 °C.

Octyl and tetradecyl f-CCG were produced using the general alkylation procedure. To produce CCG functionalized with 5-iodoisophthalic acid, for each acid group an additional lithium equivalent was added leading to an addition of 39 mmol of lithium per 15 mmol of isophthalic acid and 20 mg GO.

In addition, GO was treated with lithium in liquid ammonia as described above without adding an addend other than the proton from quenching, which led to unfunctionalized CCG that is chemically closer to the functionalized products and thus can act as a reference for our characterization. The workup procedure remained the same.

5.3.2 Characterization. Products were characterized by thermogravimetric analysis (TGA), Raman spectroscopy, FTIR spectroscopy, X-ray photoelectron

spectroscopy (XPS), nuclear magnetic resonance spectroscopy (NMR) and atomic force microscopy (AFM). The solubility of the f-CCG sheets in $CHCl_3$ and ODCB was determined for **1** and **2**. For **3**, the solubility in water with different pH values was investigated. For this purpose, 5 mg of material was dispersed in 8 mL of the solvent by sonication (Ultrasonic cleaner Cole-Parmer model 08849-00) for 10 min. The samples were then centrifuged for 1 h at 3200 rpm (Adams Analytical Centrifuge CT-3201); the supernatant was taken and the product was flocculated by the addition of acetone. The solids were filtered (0.45 μm PTFE membrane), dried and weighed to get the weight of the dissolved CCGs.

TGA was performed, after drying the sample at 150 °C for 45 min, from room temperature to 900 °C at 10 °C/min under argon. Raman spectra of powdered samples were recorded with a Renishaw Raman scope using a 514 nm argon laser. In order to verify functionalization of the CCG sheets, the ratio of the diamondoid peak (D) at 1350 cm^{-1} to the graphitic peak (G) at 1590 cm^{-1} band (D:G ratio) was calculated by applying a Lorentz fit to the spectrum after baseline correction and integrating the areas of the D and G bands. XPS was carried out on a PHI Quantera SXM Scanning X-ray Microprobe with a base pressure of 5 x 10^{-9} Torr. As X-ray source, an Al cathode at 100 W was used with a pass energy of 26.00 eV, 45° takeoff angle and a 100 μm beam size. Low resolution survey scans as well as high resolution scans of C, O, I and Li were taken. C1s spectra were normalized and shifted to standard positions. FTIR spectra were obtained with an attenuated total reflectance accessory. AFM samples were prepared by spin coating the sample from DMF onto a freshly cleaved mica surface. AFM images were obtained under tapping mode with a scan rate of 1 Hz. ^1H NMR was performed for **1** in $CDCl_3$ on a 500

MHz instrument and ^{13}C solid state NMR for **2** on a 200 MHz instrument as previously described.[39]

4.4 Conclusion

GO was successfully functionalized in a one-pot procedure involving a metal reduction and a subsequent alkylation or arylation to yield functionalized chemically converted graphene. The functionalized material shows higher solubility in organic solvents than GO or by metal-reduced CCG. The high degree of functionalization was confirmed by a combination of Raman spectral analysis, TGA, FTIR, NMR and AFM. The in situ reduction was confirmed by XPS and Raman spectroscopy. Restoration of the sp^2 framework and oxygen loss of the material provide evidence that the obtained material is suitable for further processing in polymer composites.

4.5 Experimental Contributions

My contribution to this work is the design and initial execution of the experiments, and characterization including AFM and ATR-IR. Sebastian Lacher continued and refined the reaction conditions performed characterizations such as Raman spectroscopy, XPS and TGA analyses. Lawrence B. Alemany performed the NMR analyses.

References

1. Brodie, B. *Ann. Chim. Phys.* **1855**, *45*, 351.
2. Staudenmaier, L. *Ber. Dtsch. Chem. Ges.* **1898**, *31*, 1481-1489.
3. Hummers, W. S.; Offeman, R., E. *J. Am. Chem. Soc.* **1958**, *80*, 1339.

4. Boehm, H.-P.; Diehl, E.; Heck, W.; Sappok, R. *Angew. Chem.* **1964**, *76*, 742-751.

5. Kohlschütter, V.; Haenni, P. *Z. Anorg. Allgem. Chem.* **1919**, *105*, 121-144.

6. Szabó, T.; Berkesi, O.; Forgó, P.; Josepovits, K.; Sanakis, Y.; Petridis, D.; Dékány, I. *Chem. Mater.* **2006**, *18*, 2740–2749.

7. Lerf, A.; He, H.; Forster, M.; Klinowski, J. *J. Phys. Chem. B* **1998**, *102*, 4477-4482. (e) He, H.; Klinowski, J.; Forster, M.; Lerf, A. *Chem. Phys. Lett.* **1998**, *287*, 53-56.

8. Gómez-Navarro, C.; Weitz, T. R.; Bittner, A. M.; Scolari, M.; Mews, A.; Burghard, M.; Kern, K. *Nano Lett.* **2007**, *7*, 3499-3503.

9. Li, D.; Müller, M. B.; Gilje, S.; Kaner, R. B.; Wallace, G. G. *Nat. Nanotechnol.* **2008**, *2*, 101-105.

10. Tung, V. C.; Allen, M., J.; Yang, Y.; Kaner, R. B. *Nat. Nanotechnol.* **2009**, *4*, 25-29.

11. Stankovich, S.; Piner, R. D.; Chen, X.; Wu, N.; Nguyen, S. T.; Ruoff, R. S. *J. Mater. Chem.* **2006**, *16*, 155-158.

12. Hirsch, A.; Brettreich, M. Fullerenes, *Chemistry and Reactions*, Wiley-VCH: Weinheim, 2005.

13. Tasis, D.; Tagmatarchis, N.; Bianco, A.; Prato, M. *Chem. Rev.* **2006,** *106*, 1105-1136.

14. Liang, F.; Sadana, A. K.; Peera, A.; Chattopadhyay, J.; Gu, Z.; Hauge, R. H.; Billups, W. E. *Nano Lett.* **2004**, *4*, 1257-1260.

15. Chattopadhyay, J.; Sadana, A. K.; Liang, F.; Beach, J. M.; Xiao, Y.; Hauge, R. H.; Billups, W. E. *Org. Lett.* **2005**, *7*, 4067-4069.

16. Stephenson, J. J.; Sadana, A. K.; Higginbotham, A. L.; Tour, J. M. *Chem. Mater.* **2006**, *18*, 4658-4661.

17. Chakraborty, S.; Chattopadhyay, J.; Guo, W.; Billups, W. E. *Angew. Chem. Int. Ed.* **2007**, *46*, 4486-4488.

18. Worsley, K. A.; Ramesh, P.; Mandal, S. K.; Niyogi, S.; Itkis, M. E.; Haddon, R. C. *Chem. Phys. Lett.* **2007**, *445*, 51-56.

19. Chakraborty, S.; Guo, W.; Hauge, R. H.; Billups, W. E. *Chem. Mater.* **2008**, *20*, 3134-3136.

20. Max, J-J.; Chapados, C. J. *J. Phys Chem. A* **2002**, *106*, 6452-6461.

21. Lambert, J. B.; Shurvell, H. F.; Lightner, D. A.; Cooks, R. G. *Organic Structural Spectroscopy*, Prentice-Hall, Inc.: New Jersey, 1998.

Chapter 5

Thermally Converted Graphene-Polyimide Composite Films

5.1 Introduction

Graphene, a 2-dimensional one atom thick network of sp^2 carbons, is a promising material for the fabrication of electronic devices and nanocomposites.[1,2] Graphene can be obtained by micromechanical cleavage of highly ordered pyrolytic graphite (HOPG),[3] CVD growth on metal substrates[4] and solution based exfoliation with the aid of ultrasound.[5] These techniques give good quality graphene but they are low yielding, hence the oxidation of graphite to graphene oxide (GO)[6] is still the preferred route for bulk processing of graphene sheets as it allows for a high yielding route to exfoliated sheets.[7] The graphitic nature of the resulting GO nanosheets is highly compromised due to the introduction of oxygen functionality and sp^3 hybridization within the basal planes, leading to loss of desirable electronic properties.[8] However, the presence of hydrophilic groups in GO impart it with water solubility and provides chemical handles that allow modification of the GO.[9]

Polyimides (PIs), such as Kapton®, belong to a class of polymers that have been used in aerospace and electronics applications primarily because of their excellent mechanical properties, solvent and radiation resistance, and low dielectric constant.[10] The key applications include pressure sensitive tapes, cable insulations and gas separation membranes. However, most polyimides suffer from high coefficients of thermal expansion and moisture absorption, often resulting in structural failures.[11] In addition

polyimide gossamer structures used in space exploration platforms require additives to mitigate their electrostatic charge build-up.[12] Modification of the chemical backbone is a common route taken to improve certain properties such as an increase in dielectric constant or a decrease in processing temperature. An alternative method to improve the matrix is by the incorporation of nanoparticles.

Nanocomposites are promising new materials that take advantage of the incorporation of nanoparticles, allowing multifunctionality that is not achievable with conventional polymers.[13] The addition of carbon nanomaterials such as CNTs result in enhancement of mechanical properties at low wt % loading.[12] Space durable carbon nanotubes (CNT)-polyimide composites have been fabricated and found to have sufficient electrostatic mitigation at 0.8 wt % loading.[13] Nanodiamonds have been successfully incorporated into polyimides resulting in an increase of ~30% in hardness at 1 wt % loading and an improvement in the thermal properties and adhesion.[14] Exfoliated layered silicates have also been shown to enhance the mechanical properties of polymers.[15] Similarly, work on graphene in a variety of matrices has been reported. Dispersion of graphene sheets and their derivatives, in polymers such as poly(acrylonitrile) (PAN),[16] poly(methyl methacrylate) (PMMA),[17] and polystyrene[2] (PS) has been shown to enhance mechanical properties and impart electrical conductivity. In this work, we produce a new nanocomposite by utilizing a polyimide matrix, the Kapton H variant, and incorporating GO. The GO is readily transformed to its conductive form, thermally converted graphene (TCG),[18] through thermolysis during thermal imidization step of the polymer precursor pyromellitic dianhydride-oxydianiline polyamic acid (PAA).

5.2 Results and Discussion

To take advantage of the desirable thermal and electrical properties of the graphene sheets, reduction of the GO in the polymer matrix has been conducted using chemical reducing agents such as hydrazine.[2] Conductive graphene-silica composite prepared by hydrazine reduction and thermal curing gave transparent conductive films.[20] It may be possible that the chemical reduction step is unnecessary as it has been shown that at temperatures ≥200 °C, thermal decomposition of GO occurs, resulting in deoxygenation and an increase in conductivity.[20,21] In this work reduction by hydrazine would be detrimental to the polyimide matrix as imide groups have been shown to be susceptible to ring opening and chain scission by hydrazine.[22] We therefore opted to blend GO vigorously with the PAA using the roto-stator and then take advantage of the thermal imidization and dehydration of the PAA to concomitantly convert GO into conductive TCG (Scheme 5.1). The ability of GO to improve composite properties can be compared to clays that also possess a similar plate-type structure.[16] Aside from imparting conductivity, graphene is an impermeable atomic membrane,[23] hence its incorporation into matrices might lead to gas selective permeation/restriction properties as well as minimize moisture absorption.

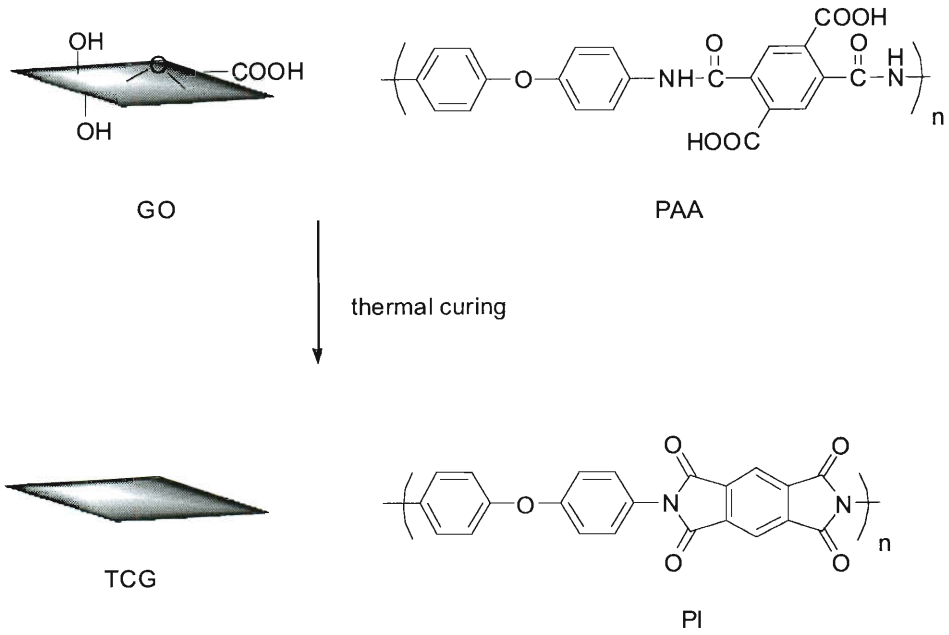

Scheme 5.1. Conversion of GO and PAA polyamic acid into TCG-PI composite film.

The GO used in this study was prepared using the Staudenmaier procedure.[6b] The resulting material showed significant oxidation based on ATR-IR, XPS and XRD results (see Supporting Information). Based on Raman analysis, the material showed a significant enhancement in the diamond peak (D-band, 1350 cm^{-1}), in comparison to the graphite starting material, signifying an increase in the fractions of sp^3 carbons.

The homogenized GO-PAA compositions were degassed prior to film casting. This step eliminates air bubbles incorporated during high shear mixing, thereby allowing for a more uniform film to be developed, especially during the 24 h vacuum step at 80 °C. The pre-composites were degassed by placing the beakers containing the mixtures inside a desiccator connected to an in-house vacuum line for 1 h. The dispersion of the nanosheets in the GO-PAA mixtures were then assessed using an optical microscope

(Figure 5.2). From the optical micrographs, some large plate-like structures are visible that may be attributed to incomplete exfoliation/oxidation of graphite.

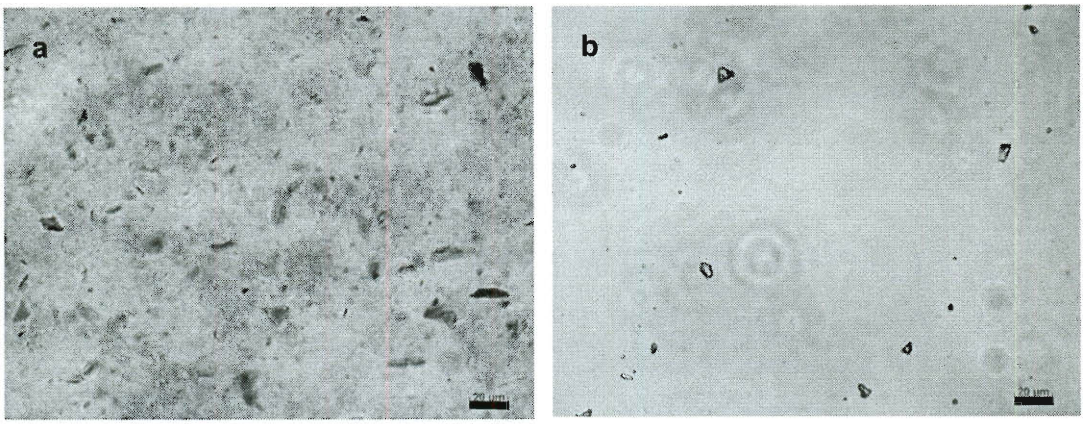

Figure 5.2. Optical micrographs of GO-PAA mixtures after degassing, (a) 2 wt % GO; (b) 1 wt % GO; scale bars are 20 μm.

Films were cast using a doctor blade with a gap set at 50 μm. Thermal curing of the films served two purposes in this study, namely: (1) imidization and cyclo-dehydration of the polyamic acid and (2) reduction of GO into TCG (see Supporting Information for curing protocol). The color development of the films containing GO showed darkening of the films as GO was converted to TCG with **PI-3** giving the darkest color (Figure 5.3). The resulting composite films were evaluated for conductivity. Samples **PI-1** and **PI-2** exhibited negligible improvement in conductivity in comparison to **PI-0**. The increase in GO loading from 1 % to 2 % resulted in a ~2 orders of magnitude increase in conductivity for **PI-3** with a value of 1.25 x 10^{-5} S/cm. Also, the

variation of current with respect to voltage over a relatively wide range of voltage from -20 to +20 V was linear for **PI-3** (Figure 5.4).

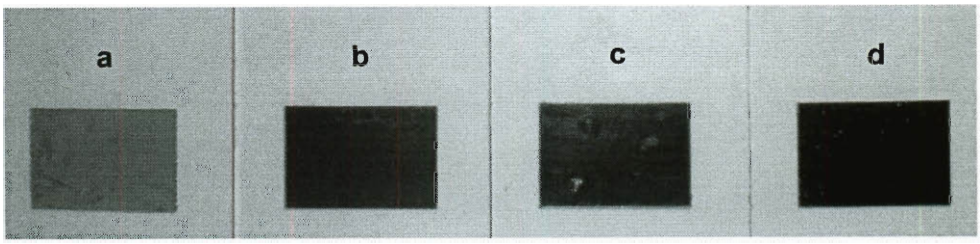

Figure 5.3. Optical micrographs of (a) **PI-0**; (b) **PI-1**; (c) **PI-2**; and (d) **PI-3** after imidization at 400 °C.

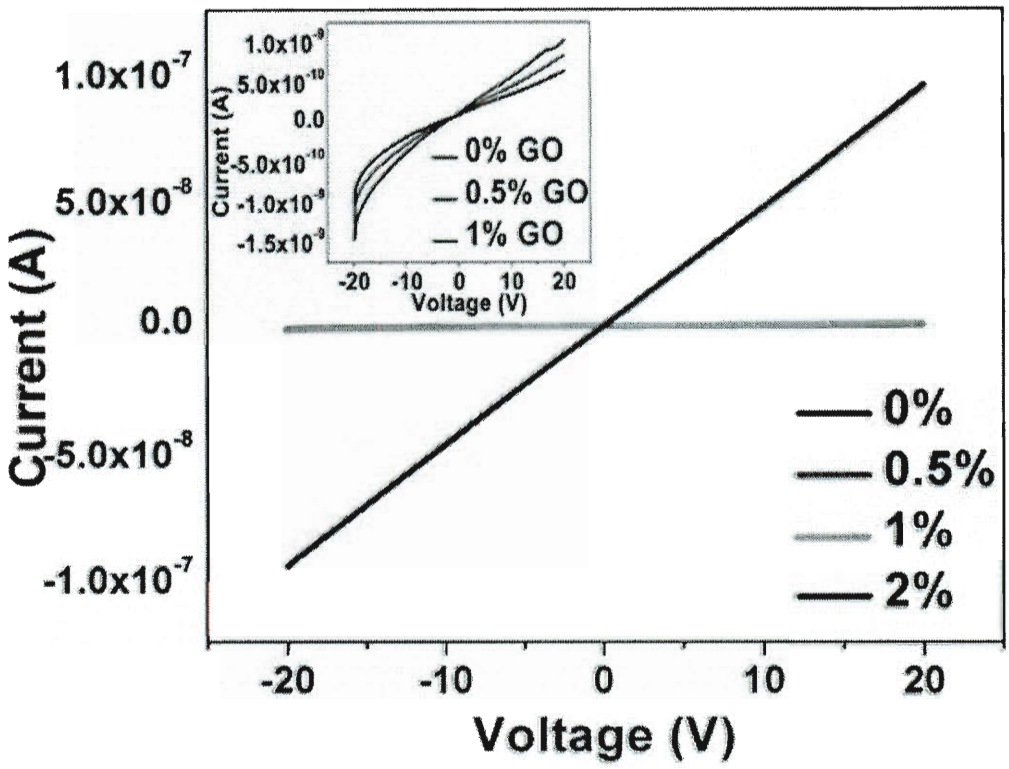

Figure 5.4. *I-V* curves of composite films with different GO concentrations. The horizontal line consists of coincided **PI-0**, **PI-1**, **PI-2** *I-V* data. Inset is the data set for **PI-0 to PI-2** at a more narrow current range.

The staged heating profile was evaluated and changes were monitored spectroscopically using ATR-IR and XPS to evaluate the effect of GO on the imidization process. In general, there are no significant variations observed in the film samples analyzed. Figure 5.5 shows the ATR-IR spectra of the samples **PI-0** and **PI-3** at different stages of curing. In both samples, upon curing at 225 °C, the carbonyl imide peak at ~1770 cm^{-1} appears to be pronounced along with the C-N vibration of the imide group at 1380 cm^{-1}. There are minimal variations between thespectra of filled and unfilled samples. Figure 5.6 shows the ATR-IR spectra of the imidized samples at different loadings of GO.

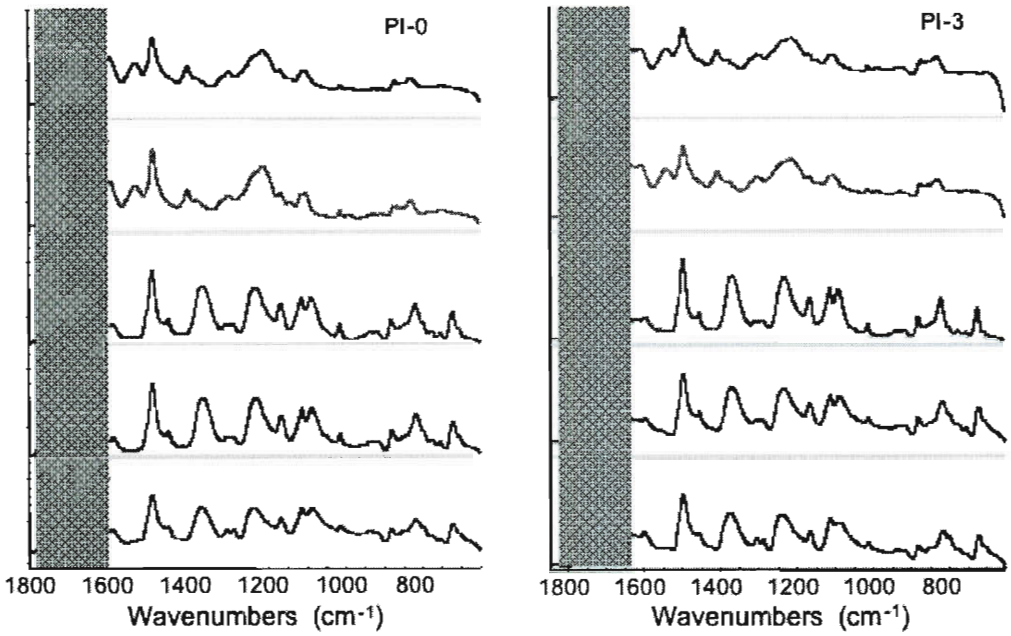

Figure 5.5. ATR-IR spectra of **PI-0** and **PI-3** at different stages of thermal imidization. All four film samples showed minimal variations.

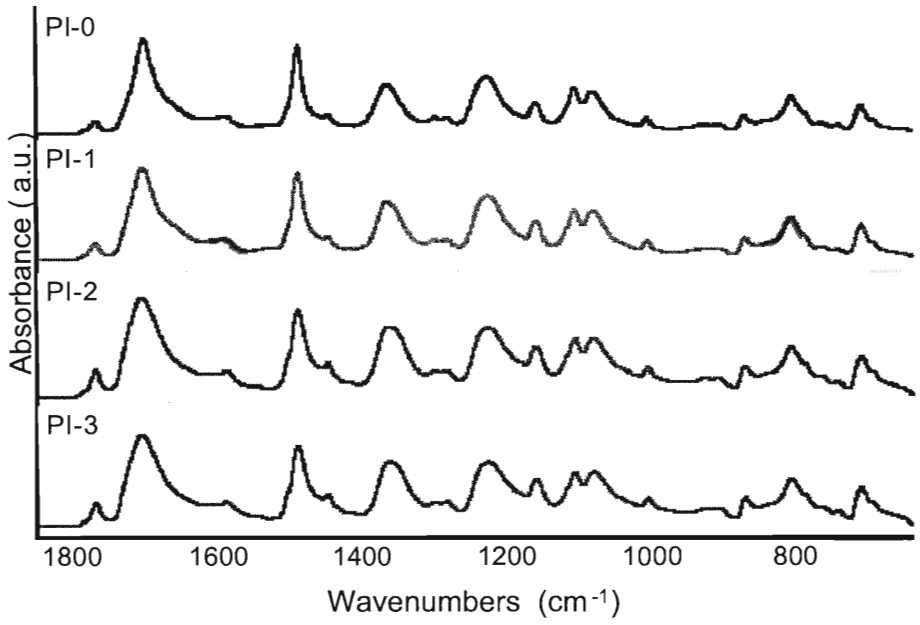

Figure 5.6. ATR-IR spectra of **PI-0**, **PI-1, PI-2** and **PI-3**. Note the absence of variation between the spectra.

XPS analysis showed minimal variations between the cured composites as well. Figures 5.6a and 5.6c show the C1s profile of pre-imidized films **PI-0** and **PI-3**. The deconvuluted peaks can be resolved into four different peaks, namely, C=C, C-H at 284.8 eV (dark blue); C-O at 286 eV (light blue); C-N amide peak (green) at 287 eV; and COOH at 289 eV (pink) prior to curing. After thermal imidization, the absence of the COOH peak at 289 eV is evidence that the carboxylic acid has been converted to the imide peak at 288 eV (pink).[23]

Wide angle X-ray diffraction analysis of the films was employed to evaluate the dispersion of TCG in the composite films (Figure 5.7). While the optical micrographs of GO-PAA mixtures show some sheets that are not completely exfoliated, the diffraction patterns obtained for the samples incorporated with GO closely resemble **PI-0**. The broad peak centered at $2\theta = 18.5°$ is attributed to the amorphous structure of the polyimide and the small peak $2\theta = 5.8°$ is assigned to repeat unit spacing.[27] Crystalline peaks from graphite ($2\theta = 26.6°$) and GO ($2\theta = 10.6°$) peaks are absent and the dominant peaks resemble that of the starting polyimide similar to results reported by Ramanathan *et. al.*[18] Hence, the majority of the GO and subsequently the TCG are molecularly dispersed in the matrix.

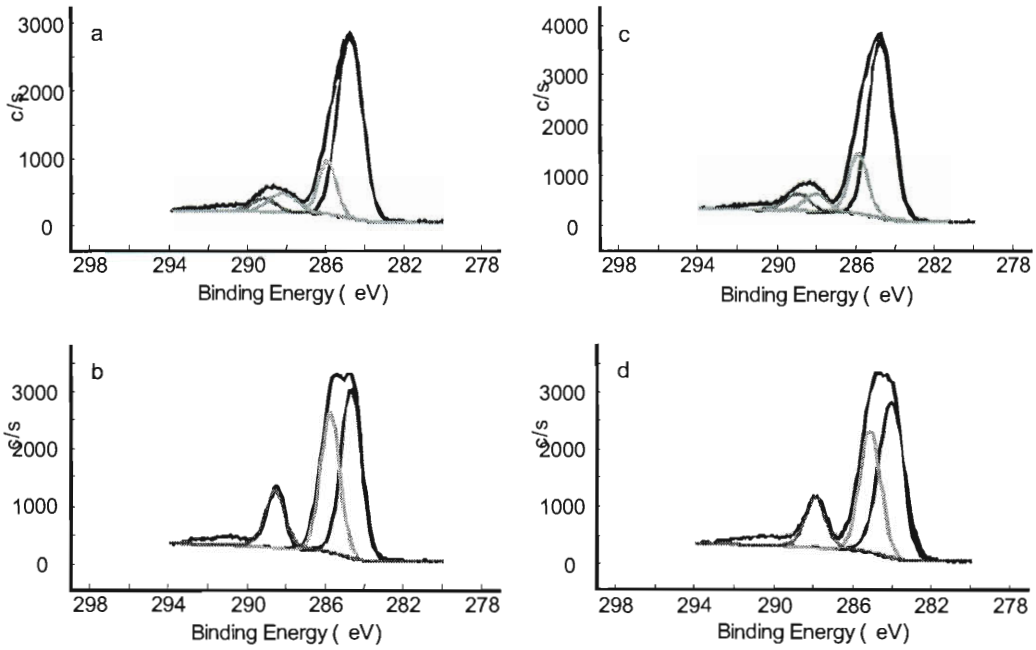

Figure 5.6. XPS C1s Spectra of **PI-0**: (a) after vacuum drying at 80 °C for 24 h; (b) after thermal imidization at 400 °C; and **PI-3**: (c) after vacuum drying at 80 °C for 24 h; (d) after thermal imidization at 400 °C. Note the presence of four different peaks in (a) and (c) assigned as: C=C, C-H at 284.8 eV (dark blue); C-O at 286 eV (light blue); C-N amide peak at 287 eV (green); and COOH at 289 eV. After imidization, (c) and (d), the COOH peak at 289 eV disappeared and replaced by the imide peak at 288 eV (pink).

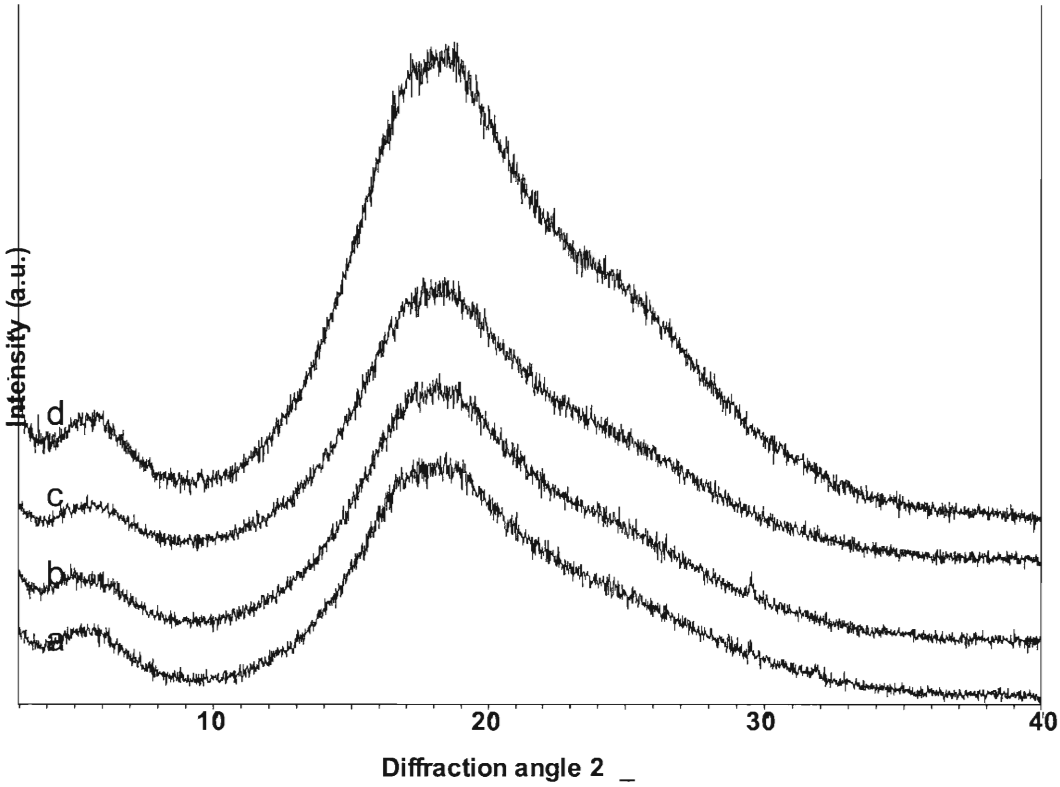

Figure 5.7. Wide angle XRD patterns of (a) **PI-0**; (b) **PI-1**; (c) **PI-2** and (d) **PI-3**. The GO and graphite peaks are not evident in the diffraction patterns obtained.

While there is minimal variation in the spectroscopic characterizations, a difference in the thermograms were observed between the PAA and GO-PAA mixtures by DSC (Figure 5.8). Samples for DSC were prepared by weighing approximately 25 mg of GO-PAA mixtures into Al pans and vacuum drying at 80 °C for 24 h. The resulting samples were analyzed with a heating rate of 10 °C/min under nitrogen atmosphere. From the DSC thermograms obtained (Figure 8), the transition starting at ~ 109 °C up to 200 °C is brought about by NMP evaporation and imidization.[28] There is a marked difference however at ~220 °C between **PI-0** and **PI-3** (Figure 8). The T_g for **PI-0** is

observed at ~ 420 °C but a much less defined T_g for **PI-3** is discernible. The GO transition however is clearly evident for the latter showing a peak at 221 °C, especially at rapid heating rates. GO has been known to show rapid evolution of water, CO and CO_2 due to pressure build-up brought about by the decomposition of thermally labile functionalities.[20] Upon imidization, however, the filled and unfilled samples showed insignificant variation in weight loss at 550 °C by TGA, thereby providing evidence that the deoxygenation of GO is close to completion after 400 °C. In addition, all four film specimens showed 10 % wt loss at 560 ± 2.5 °C.

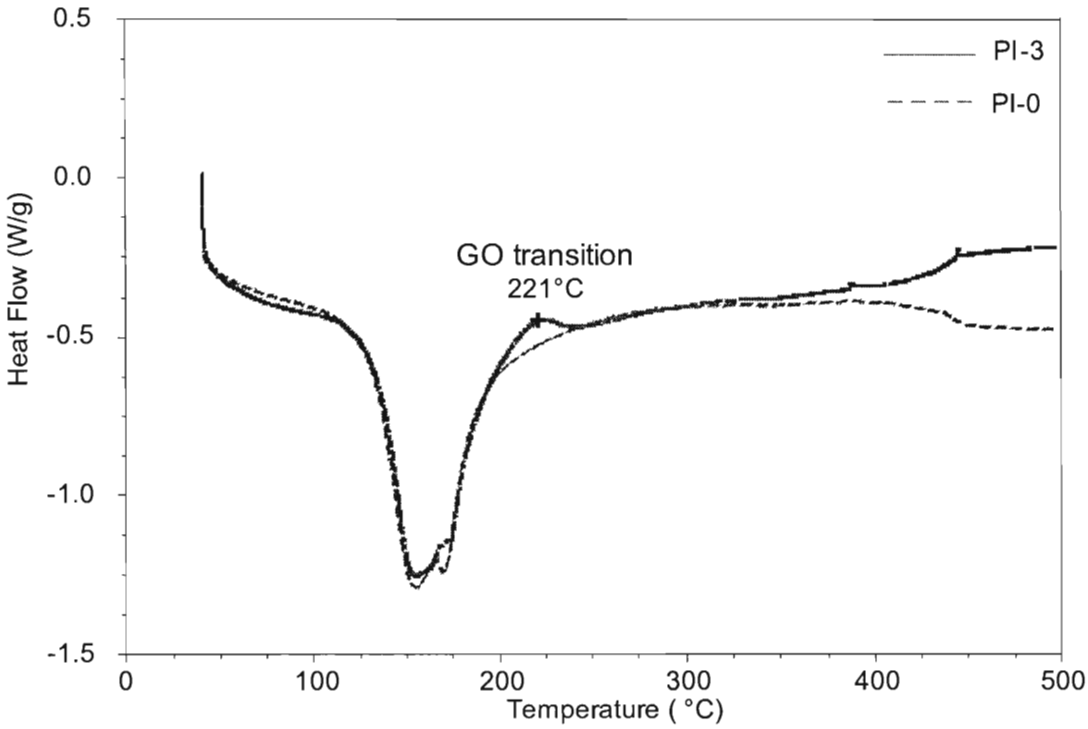

Figure 5.8. DSC thermogram of **PI-0** and **PI-3** showing the GO transition for GO filled samples.

The mechanical properties of the samples were evaluated using Instron electropuls 3000 and TA DMA Q800. Thin strips of the films were cut into 5 mm × 50 mm. sections and the film thickness varied between 0.015 to 0.023 mm as determined by a micrometer (Mitutoyo, Model 293-330). Tensile tests were performed at room temperature with a cross-head speed of 1 mm/min and a gauge length of 25 mm. To minimize slippage of the films from the clamps during testing, the samples were mounted to a paper holder and cemented with epoxy. The increase in modulus is observed to be as high as 75 % for TCG-filled samples but minimal change is this modulus increase was observed with respect to loading, i.e. from 0.5 wt % to 2 wt %. The tensile strength showed minimal decrease for **PI-1** and **PI-3** when compared to **PI-0**. Also the TCG-filled composite films exhibited lower elongations compared to the baseline **PI-0**. The results taken from an average of 5 samples for each formulation are summarized in Table 5.1.

DMA analysis was performed using a procedure reported by Thompson.[29] **PI-3** showed ~47% increase in storage modulus at room temperature compared to the reference material **PI-0**. The film microstructure was then analyzed by SEM from the fracture areas after tensile tests (Figure 5.9). The major difference observed is the surface roughness of the filled samples wherein there is observed flake type structures.

Table 5.1. Summary of the Mechanical Properties of Composite Films **PI-0** to **PI-3** after Imidization.

Sample	GO loading (wt %)	Young's Modulus (GPa)	Tensile Strength (MPa)	Elongation @ break (%)
PI-0	0	1.6	113	4.8
PI-1	0.5	2.7	95	2.9
PI-2	1	2.8	117	2.4
PI-3	2	2.7	103	2.8

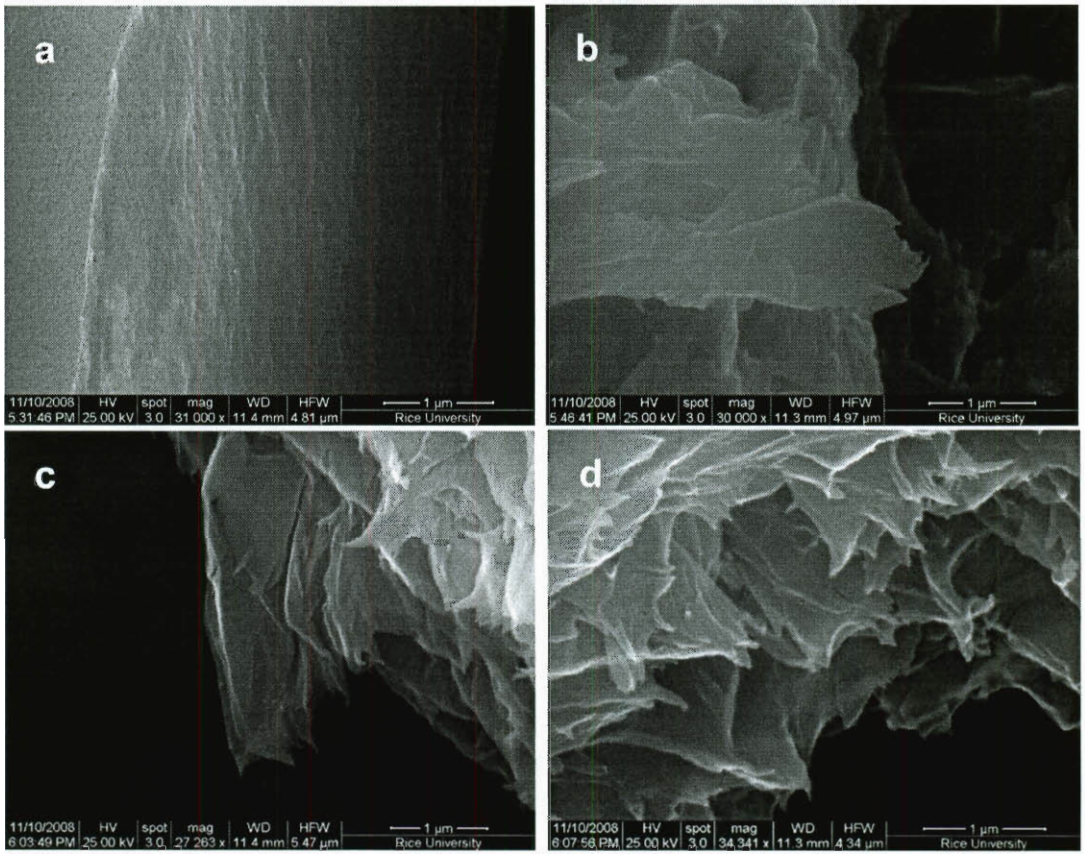

Figure 5.9. SEM images taken from the fracture surfaces of imidized film samples subjected to tensile tests: (a) **PI-0**; (b) **PI-1**; (c) **PI-2** and (d) **PI-3**.

The low moisture absorption of the films could be attributed to the presence of the nanosheets in the polyimide matrix. Using the same specimen size for tensile tests, moisture uptake tests were conducted based on ASTM D-5229. The baseline material (**PI-0**) gave 2.9 % while **PI-3** has 0.3 % moisture uptake. The results are summarized in Table 4.2

Table 5.2. Results of the Moisture Absorption Test Based on ASTM D-5229.

Sample	Dry Weight, mg	Wet Weight, mg	% Moisture Absorption
PI-0	2.9262	3.0111	2.9
PI-1	3.0447	3.0802	1.16
PI-2	3.0318	3.0466	0.4
PI-3	3.9347	3.9469	0.3

5.3 Experimental Section

5.3.1 Materials. PAA in *N*-methyl-2-pyrollidone (NMP) (15 wt %) and anhydrous *N,N'*-dimethylacetamide (DMAc) were purchased from Sigma-Aldrich. GO was prepared from expanded graphite obtained from Supracarbonic, LLC using the Staudenmaier procedure.[6b] (*Caution*: protective equipment including face shield, acid-resistant gloves, lab coat, apron, and blast shield must be used at all times during the preparation of GO by this procedure).

5.3.2 Solvent Blending. A representative example for the preparation of the GO-PAA mixtures is as follows: A dispersion of GO (30 mg) in DMAc (10.6 mL) was prepared by bath sonication (Cole-Parmer model 08849-00) for 1 h in a scintillation vial. The resulting dispersion was added to a beaker with pre-weighed 15 wt % PAA solution in NMP (20 g solution, 3 g PAA), lowering the concentration of solids to 10 wt % and yielding a 1:99 GO:PAA (**PI-2**) mixture in a mixed solvent of NMP and DMAc. A series of GO-PAA mixtures were prepared with increasing amount of GO. The loadings of GO with respect to PAA are as follows: 0 wt % GO (**PI-0**); 0.5 wt % (**PI-1**); 1.0 wt % (**PI-2**),

and 2.0 wt % (**PI-3**). The GO-polymer solution was homogenized for 1 h using IKA Ultra Turrax T25 fitted with an IKA S-25N 10 G dispersing element. The temperature was kept at 0-5 °C during the high shear mixing by immersing the beaker in a bath circulator (Forma Scientific, Model 2006) to minimize hydrolytic chain scission and anhydride formation.[19] The resulting mixture was allowed to stand for 30 min while keeping it at the same temperature and subsequently degassed in a desiccator using an in-house (~15 mm Hg) vacuum for 1 h prior to film application.

5.3.3 Film Casting. The GO-PAA mixture was cast into 50 μm thick films using a doctor blade (1117 Micrometer Adjustable Film Applicator, Sheen Instruments) onto clean glass plates and placed in a vacuum oven at 80 °C for 24 h. The resulting tack-free films were then thermally cured in four stages: 100 °C, 1 h; 225 °C, 1 h; 300 °C, 1 h; and 400 °C, 10 min, in air. After cooling, the film was etched from the glass substrates using 1 % HF and washed with copious amounts of deinoized water. The film samples were dried and kept in an oven at 100 °C under nitrogen for further testing.

5.3.4 Characterization. The fabricated composite film samples were characterized spectroscopically using a Nicolet FT-IR with a fitted attenuated total reflectance (ATR) attachment and Phi Quantera SXM Scanning X-Ray Microprobe with a pass energy of 26.00 eV, 45° takeoff angle and a 100 μm beam size. Raman spectroscopy was performed using Renishaw Raman scope using 633 nm He-Ne laser. X-ray diffraction was taken using Rigaku D/Max Ultima II using Cu Ka radiation source. The morphology of the films was analyzed using FEI Quanta 400 ESEM. Dispersions of GO in PAA were assessed using a Zeiss Axiovision Polarizing Optical Microscope. The

mechanical properties were measured using an Instron Electropuls 3000 Universal Testing Machine and Dynamic Mechanical Analyzer (DMA) Q800 (TA Instruments). Thermal analysis was performed using TA Differential Scanning Calorimeter (DSC) Q50 and Thermogravimetric Analyzer (TGA) Q100. Conductivity measurements were taken using a two probe station (Desert Cryogenics TT-probe 6 system) under atmospheric pressure. The *I–V* data was generated using an Agilent 4155C semiconductor parameter analyzer.

5.4 Conclusion

The incorporation of GO into PAA resulted in significant enhancement of the mechanical properties of polyimide. GO is transformed into TCG concomitantly with imidization and cyclodehydration of the PAA. In addition to mechanical reinforcement, the film samples exhibited conductivity at 2 wt % loading that might prove valuable for applications requiring electrostatic mitigation. Finally, a much lower moisture uptake material could be obtained by the GO addition, capitalizing on the excellent barrier properties of graphene.

5.5 Experimental Contributions

My contribution to this work is the synthesis of GO, preparation of GO-PAA mixtures and fabrication of films. I also performed characterization of the films such as ATR-IR, XPS, XRD, thermal analysis including DSC and TGA, and testing of mechanical properties. Zhengzong Sun assisted the in the preparation of GO-PAA mixtures and DSC experiments.

References

1. Geim, A. K.; Novoselov, K. S. *Nat. Mater.* **2007**, *6*, 183.

2. Stankovich, S.; Dikin, D. A.; Dommett, G. H. B.; Kohlhaas, K. M.; Zimney, E. J.; Stach, E. A.; Piner, R. D.; Nguyen, S. T.; Ruoff, R. S. *Nature* **2006**, *442*, 282-286.

3. Novoselov, K. S.; Geim, A. K.; Morozov, S. V.; Jiang, D.; Zhang, Y.; Dubonos, S. V.; Grigorieva, I. V.; Firsov, A. A. *Science* **2004**, *306*, 666.

4. (a) Kim, K. S.; Zhao, Y.; Jang, H.; Lee, S. Y.; Kim, J. M.; Kim, K. S.; Ahn, J.-H.; Kim, P.; Choi, J.-Y.; Hong, B. H. *Nature* **2009**, *457*, 706-710. (b) Li, X.; Cai, W.; An, J.; Kim, S.; Nah, J.; Yang, D.; Piner, R.; Velamakanni, A.; Jung, I.; Tutuc, E.; Banerjee, S. K.; Colombo, L.; Ruoff, R. S. *Science* **2009**, *324*, 1312-114. (c) Reina, A.; Jia, X.; Ho, J.; Nezich, D.; Son, H.; Bulovic, V.; Dresselhaus, M. S.; Kong, J. *Nano Lett.* **2008**, 9, 30-35.

5. (a) Blake, P.; Brimicombe, P. D.; Nair, R. R.; Booth, T. J.; Jiang, D.; Schedin, F.; Ponomarenko, L. A.; Morozov, S. V.; Gleeson, H. F.; Hill, E. W.; Geim, A. K.; Novoselov, K. S. *Nano Lett.* **2008**, *8*, 1704-1708. (b) Hernandez, Y.; Nicolosi, V.; Lotya, M.; Blighe, F. M.; Sun, Z.; De, S.; McGovern, I. T.; Holland, B.; Byrne, M.; Gun'Ko, Y. K.; Boland, J. J.; Niraj, P.; Duesberg, G.; Krishnamurthy, S.; Goodhue, R.; Hutchison, J.; Scardaci, V.; Ferrari, A. C.; Coleman, J. N. *Nat. Nanotechnol.* **2008**, *3*, 563-568. (c) Lotya, M.; Hernandez, Y.; King, P. J.; Smith, R. J.; Nicolosi, V.; Karlsson, L. S.; Blighe, F. M.; De, S.; Wang, Z.; McGovern, I. T.; Duesberg, G. S.; Coleman, J. N. *J. Am. Chem. Soc.* **2009**, *131*, 3611.

6. (a) Hummers, W. S.; Offeman, R. E. *J. Am. Chem. Soc.* **1958**, 80, 1339., (b) Staudenmaier, L. *Ber. Dtsch. Chem. Ges.* **1898**, *31*, 1481-1489.

7. Ruoff, R. *Nat. Nanotechnol.* **2008**, *3*, 10-11.

8. Lerf, A.; He, H.; Forster, M.; Klinowski, J. *J. Phys. Chem. B* **1998**, *102*, 4477-4482.

9. (a) Bourlinos, A. B.; Gournis, D.; Petridis, D.; Szabo, T.; Szeri, A.; Dekany, I. *Langmuir* **2003**, *19*, 6050-6055. (b) Boehm, H. P., Diehl, E., Heck, W., and Sappok, R. *Angew. Chem.* **1964**, *76*, 742-751.

10. Ghosh, M. K.; Mittal, K. L. *Polyimides: Fundamentals and Applications*; Marcel Dekker: New York, 1996.

11. (a) Paplham, W. P.; Brown, R. A.; Salin, I. M.; Seferis, J. C. *J. App. Polym. Sci.* **1995**, *57*, 133-137. (b) Campbell, F. J. *IEEE Trans.* **1985**, *EI-20*, 111-116.

12. Delozier, D. M.; Watson, K. A.; Smith, J. G.; Connell, J. W. *Comp. Sci. Technol.* **2005**, *65*, 749-755.

13. Thostenson, E. T.; Li, C.; Chou, T.-W. *Comp. Sci. Technol.* **2005**, *65*, 491-516.

14. (a) Kashiwagi, T.; Du, F.; Douglas, J. F.; Winey, K. I.; Harris, R. H.; Shields, J. R. *Nat Mater.* **2005**, *4*, 928-933. (b) Ruan, S. L.; Gao, P.; Yang, X. G.; Yu, T. X. *Polymer* **2003**, *44*, 5643–5654. (c) Chang, T. E.; Jensen, L. R.; Kisliuk, A.; Pipes, R. B.; Pyrz, R.; Sokolov, A. P. *Polymer* **2005**, *46*, 439-444. (d) Haggenmueller, R.; Guthy, C.; Lukes, J. R.; Fischer, J. E.; Winey, K. I. *Macromolecules* **2007**, *40*, 2417-2421. (e) Mitchell, C. A.; Bahr, J. L.; Arepalli, S.; Tour, J. M.; Krishnamoorti, R. *Macromolecules* **2002**, *35*, 8825-8830.

15. Smith, J. G.; Connell, J. W.; Delozier, D. M.; Lillehei, P. T.; Watson, K. A.; Lin, Y.; Zhou, B.; Sun, Y. P. *Polymer* **2004**, *45*, 825-836.

16. (a) Zhang, Q.; Naito, K.; Tanaka, Y.; Kagawa, Y. *Macromolecules* **2008**, *41*, 536-538. (b) Wang, D. H.; Tan, L.-S.; Huang, H.; Dai, L.; Osawa, E. *Macromolecules* **2008**, *42*, 114-124. (c) Shenderova, O.; Tyler, T.; Cunningham, G.; Ray, M.; Walsh, J.; Casulli, M.; Hens, S.; McGuire, G.; Kuznetsov, V.; Lipa, S. *Diamond Relat. Mater.* **2007**, *16*, 1213–1217.

17. (a) Yu, Z. Z.; Yang, M.; Zhang, Q.; Zhao, C.; Mai, Y. W. *J. Polym. Sci., Part B: Polym Phys.* **2003**, *41*, 1234–1243. (b) Alexandre, M.; Dubois, P. *Mater. Sci. Eng.* **2000**, *28*, 1–63. (c) Kazuhisa, Y.; Arimitsu, U.; Akane, O.; Toshio, K.; Osami, K. *J. Polym. Sci. Part A: Polym. Chem.* **1993**, *31*, 2493-2498.

18. RamanathanT; Abdala, A. A.; StankovichS; Dikin, D. A.; Herrera Alonso, M.; Piner, R. D.; Adamson, D. H.; Schniepp, H. C.; ChenX; Ruoff, R. S.; Nguyen, S. T.; Aksay, I. A.; Prud'Homme, R. K.; Brinson, L. C. *Nat. Nanotechnol.* **2008**, *3*, 327-331.

19. Zheng, W.; Wong, S. C. *Comp. Sci. Tech.* **2003**, *63*, 225-235.

20. Jung, I.; Dikin, D. A.; Piner, R. D.; Ruoff, R. S. *Nano Lett.* **2008**, *8*, 4283-4287.

21. Michael-Joachim, B.; Claudius, F. *J. Polym. Sci. Part A: Polym. Chem.* **1987**, *25*, 2479-2491.

22. McAllister, M. J.; Li, J.-L.; Adamson, D. H.; Schniepp, H. C.; Abdala, A. A.; Liu, J.; Herrera-Alonso, M.; Milius, D. L.; Car, R.; Prud'homme, R. K.; Aksay, I. A. *Chem. Mater.* **2007**, *19*, 4396-4404.

23. Jones, J. I. *J. Polym. Sci. Part C* **1969**, *22*, 773-784.

24. Bunch, J. S.; Verbridge, S. S.; Alden, J. S.; van der Zande, A. M.; Parpia, J. M.; Craighead, H. G.; McEuen, P. L. *Nano Lett.* **2008**, *8*, 2458-2462.

25. (a) Silverman, B. D.; Sanda, P. N.; Ho, P. S.; Rossi, A. R. *J. Polym. Sci. Part A: Polym. Chem.* **1986**, *24*, 3325-3333. (b) Wang, P. S.; Wittberg, T. N.; Wolf, J. D. *J. Mater. Sci.* **1988**, *23*, 3987-3991.

26. Ikeda, R. M. *J. Polym. Sci.* **1966**, *4*, 353. (b) Isoda, S.; Shimada, H.; Kochi, M.; Kmabe, H. *Polym. Sci.: Polym. Phys. Ed.* **1981**, *19*, 1293. (c) Jou, J.-H.; Huang, P.-T. *Polym. J.* **1990**, *22*, 909-918.

27. Kotera, M.; Nishino, T.; Nakame, K. *Polymer* **2000**, *41*, 3615-3619.

28. Thompson, C. M.; Herring, H. M.; Gates, T. S.; Connell, J. W. *Comp. Sci. Technol.* **2003**, *63*, 1591-1598.

Chapter 6

Graphene Dispersion at High Concentrations in Chlorosulfonic Acid

6.1 Introduction

This chapter describes a procedure to obtain few-layers and possibly single layers of graphene sheets without employing the harsh oxidizing conditions that are involved in the synthesis of graphite oxide (GO). By circumventing the oxidation process, the introduction of defects and oxygen groups that compromise many of graphene's desirable electrical and thermal properties are avoided.[1-4] The preferred route to obtain pristine graphene is by micromechanical cleavage of HOPG that normally entails sophisticated manipulation in a clean room.[5] To further advance the use of graphene in envisaged macroscopic applications, the development of new routes for effective graphite exfoliation and processing is required. Liquid phase dispersion of graphene can be attained by sonication in organic solvents such as NMP,[6] DMF,[7] and ODCB[8] without using chemical modification. Graphene has also been dispersed in aqueous solutions by sonication and stabilization using surfactants.[9] However, such liquid phase dispersions yield low concentrations (0.01 – 0.03 mg/mL).

The solubility of carbon nanomaterials in acids is known in the literature. Fullerenes are soluble in concentrated sulfuric acid.[10] However, when oleum is used, it oxidizes and functionalizes C_{60} because of the excess SO_3 resulting in polycyclosulfation.[11,12] CNTs exhibit similar behavior in strong acid environment such as oleum and chlorosulfonic acid and the solubilization process is governed by protonation of the aromatic rings acting as electron rich system capable of

accommodating the protons (Fig 6.1) in a base-acid equilibrium.[13-15] The dispersions are stabilized by the sulfuric acid or chlorosulfonic acid anions and thereby facilitates access to individualized SWCNT that have been exploited for functionalization.[16]

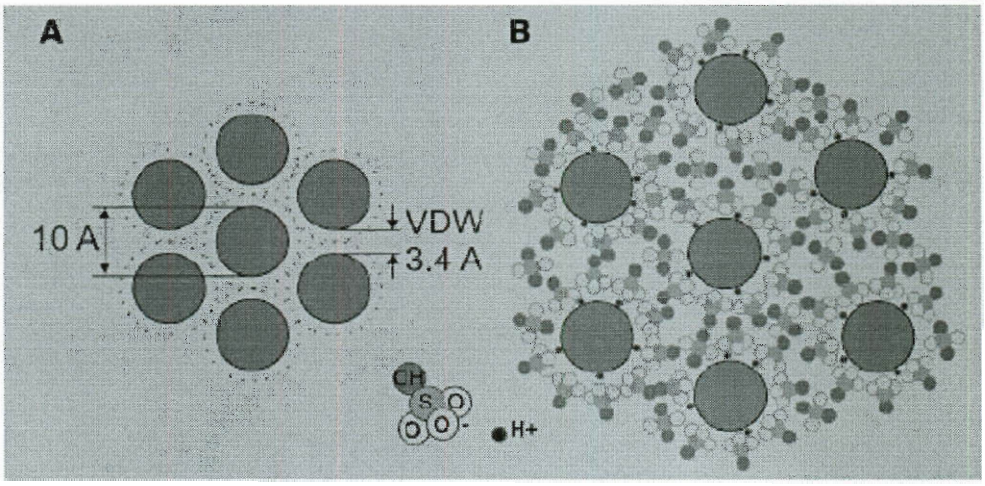

Figure 6.1. Proposed model for the swelling of SWNT bundle in oleum.[15]

Although the intercalation of graphite by strong acids, has been studied for decades,[17] there are no reports indicating that graphite is soluble in strong acids. A recent attempt to disperse graphene in oleum required pre-treatment such as grinding with an inorganic salt and intercalation with tetrabutylammonium hydroxide to completely exfoliate the graphene sheets.[18] In this work, pristine graphite is shown to spontaneously exfoliate into few layers of graphene in HSO_3Cl without the aid of sonication, forming isotropic solutions ten × more concentrated than those previously attained with organic solvents or surfactants in water. These high-concentration isotropic solutions were used in the fabrication of thin conductive films and possibly could be exploited for nanocomposites fabrication and functionalization of graphene.

6.2 Results and Discussion

To demonstrate the utility of dispersing graphene sheets in HSO_3Cl H, three sources of graphite were used: Graphoil (a commercial graphitic material used in seals), microcrystalline graphite, and HOPG. The concentration of the dispersed phase was determined gravimetrically by extracting the top isotropic phase after centrifugation and weighing the graphene residues after quenching the acid. The dispersions were further diluted and monitored by UV-vis-nIR spectroscopy to establish a Beer-Lambert correlation. Figure 6.2 shows that the acid-disperse graphene from various graphite sources at high concentrations without sonication.

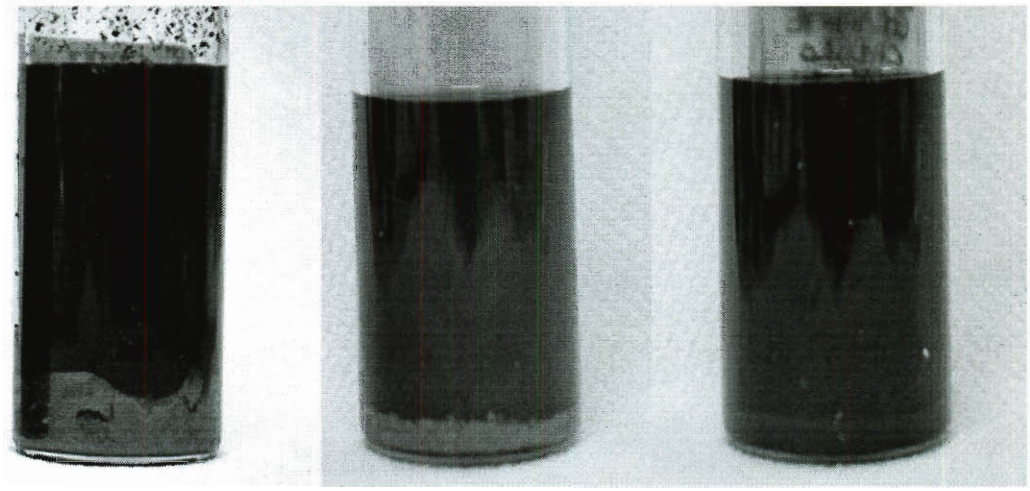

Figure 6.2. Photographs of different graphene dispersions in $ClSO_3H$ with a starting concentration of 25 mg/mL. The vials were centrifuged for 12 h at 5000 rpm and the supernatant was subjected to solubility determination. (a) Graphoil, (b) HOPG, (c) microcrystalline graphite.

The UV-vis-nIR spectrum is featureless as a function of wavenumber (Fig. 6.3), in accord with previous reports[6,9] The concentration of the top isotropic phase is a function of the initial dispersion concentration (Fig 6.4). The phase separation that occurs during centrifugation is not an equilibrium phase separation; instead, a given fraction of the original material goes into solution while the remainder is insoluble. This is similar to observations for surfactant and NMP dispersions.[6,9]

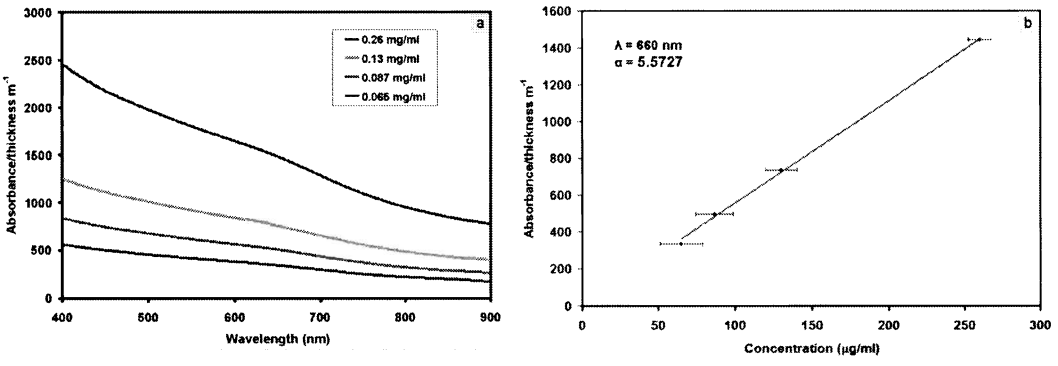

Figure 6.3. (**a**) UV-vis absorption spectra of the top phase from the vials after centrifugation. The dispersions were obtained from the Sigma graphite dispersion. The four different spectra represent different concentration (the top phase and three different dilutions). (**b**) Optical absorbance divided by the cell length as a function of different concentrations. The solution follows the Lambert-Beer law with an absorption coefficient of 5.6 mL $\mu g^{-1} m^{-1}$ at 660 nm. The error bar is a combination of instrument resolution for the UV-vis absorption, volume and mass measurement. The main contribution to the error bar is the determination graphene mass in the isotropic solution.

The dissolution efficiency was addressed using microcrystalline graphite obtained from Sigma Aldrich. When varying concentration of graphite are dissolved in chlorosulfonic acid, the concentration of the centrifuged upper phase increases as a

function of the initial concentration (Fig. 6.4). This means that there is just a fraction of the initial material that is soluble in acid, similar to what is observed for surfactant dispersions and NMP.

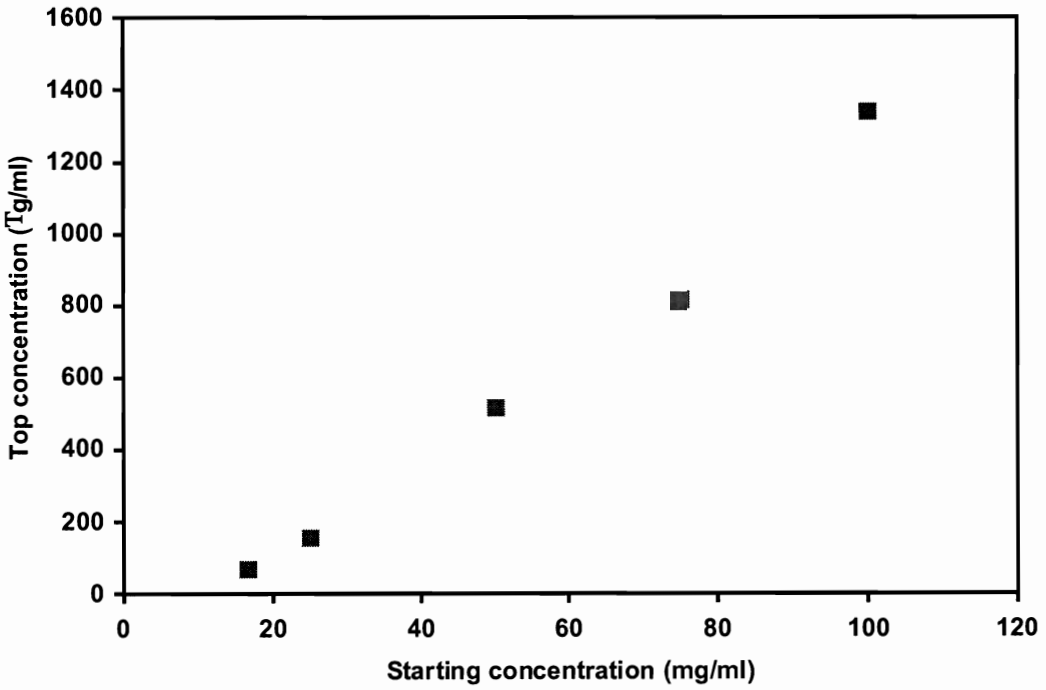

Figure 6.4. Effect of the initial dispersion concentration on the isotropic concentration. To calculate the top phase concentration, the initial dispersion was first centrifuged at 5000 rpm for 12 h. The UV-vis spectrum of the top phase was then measured and the concentration calculated by using the extinction coefficient previously calculated.

Acid strength affects the quality of dispersion. We control acid strength by mixing HSO_3Cl and concentrated (98%) H_2SO4 in varying proportions,[19] hereafter, mixed solvents are denoted by the concentration of HSO_3Cl. Figure 6.5 shows that

graphite solubility decreases markedly as the acidity is lowered to 80% HSO_3Cl; the solubility continues to drop as the acidity is further lowered. For comparison, we disperse the same material in NMP, an organic solvent previously reported for pristine graphene dissolution. Without sonication, the level of dispersion is negligible for NMP.

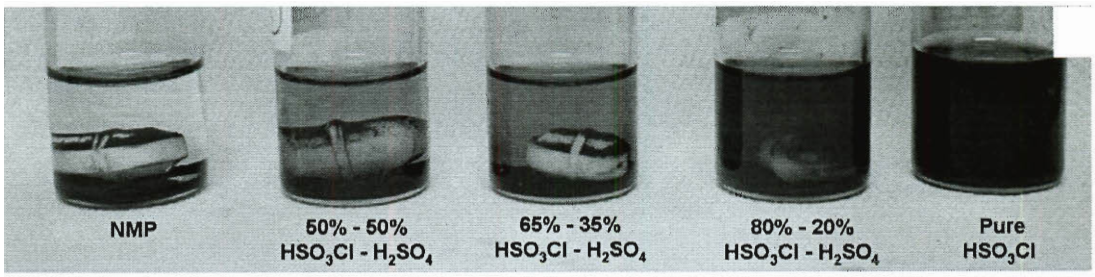

Figure 6.5. Qualitative comparison between graphite dissolution into different solvents showing graphite in vials with a Teflon-coated stir bar to promote dissolution. Starting from left, graphite in NMP, 50%, 65%, 80% vol. HSO_3Cl) in H_2SO_4 and pure HSO_3Cl. The dispersions were prepared at 10 mg/mL. The acid dispersions were then centrifuged at 5000 rpm for 12 h while the NMP dispersion was centrifuged for 3 h.

We next investigated the mechanism of graphene dissolution in superacids. Prior work with superacid/SWCNT solutions showed that the mechanism of dispersion is protonation of the SWCNT sidewalls, which causes electrostatic repulsion and debundling.[13,15,19] The degree of protonation in graphitic materials is evaluated from the magnitude of the acid-induced shift (dG) in the location of the G peak in the Raman spectra; dG is a measure of the positive charge per carbon caused by the acid.[13-15] Figure 6.6 reports dG for the various acid mixtures; the Raman shift dG drops with decreasing acidity, mirroring the decrease in solubility. Figure 6.7 shows the Raman spectra of a sample of graphite powder before and after acid dissolution, quenching in water, and drying. The spectrum is essentially unchanged (in particular, the D-band, characteristic

of sp^3 carbon content, remains low), hence acid dissolution does not introduce defects in the starting material. This indicates no damage or functionalization by the acid, the same behavior as seen in SWCNTs.[20] XPS data further support this conclusion (Fig 6.8). Compared to SWCNTs, graphene is less soluble in the same acid; SWNTs are soluble in weaker superacids, such as 102% sulfuric acid.

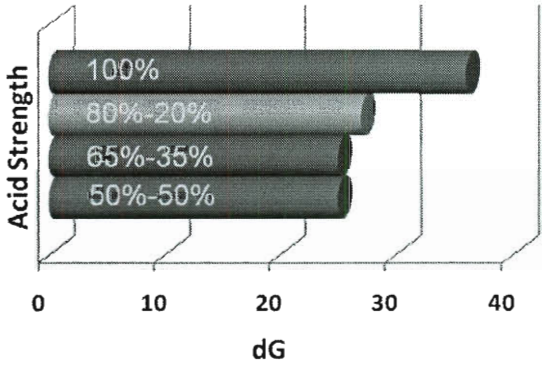

Figure 6.6. Comparison of acid-induced shifts in the liquid-phase Raman G-peak for graphite dispersed in the same mixtures of HSO_3CL in H_2SO_4. The G-peak shift, denoted as dG, is a quantitative measure of the degree of protonation.

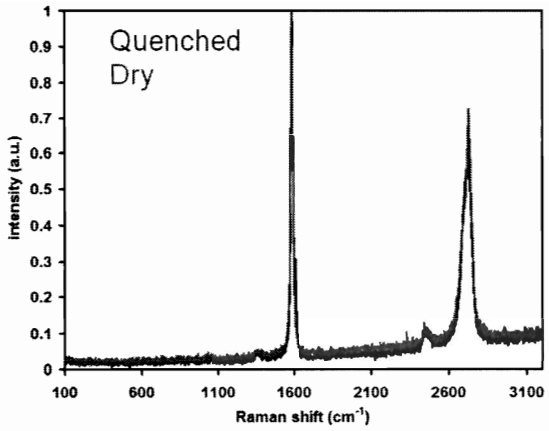

Figure 6.7. Solid-state Raman spectra of the initial graphite dry powder and the graphite quenched from the acid dispersion. The two spectra are virtually identical, indicating that protonation is reversible. Both the liquid and solid phase Raman spectra were taken with 514 nm excitation wavelengths and long working-distances on a 50x lens.

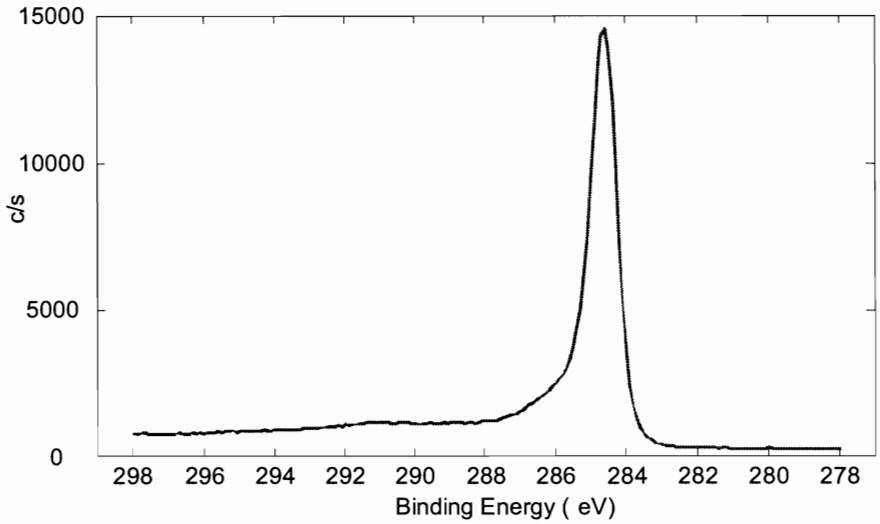

Figure 6.8. XPS from the dry material obtained upon quenching the isotropic phase from a centrifuged vial. The solution was centrifuged for 12 h at 5000 rpm.

High-resolution TEM (HR-TEM) was used to image graphene layers deposited from a HSO_3Cl solution directly onto a nickel grid. Some aggregation of the layers is expected from the deposition process; however, evidence of few-layer graphene was found. The edge of the structure in Figure 6.9 shows a representative region with low contrast relative to the vacuum; this region consists of few, possible single, layers protruding from a larger stack, defined by the change in contrast along the diagonal similar to the report by Meyer *et al,*[21] indicating that HSO_3Cl exfoliates graphite into few- or single-layered graphene.

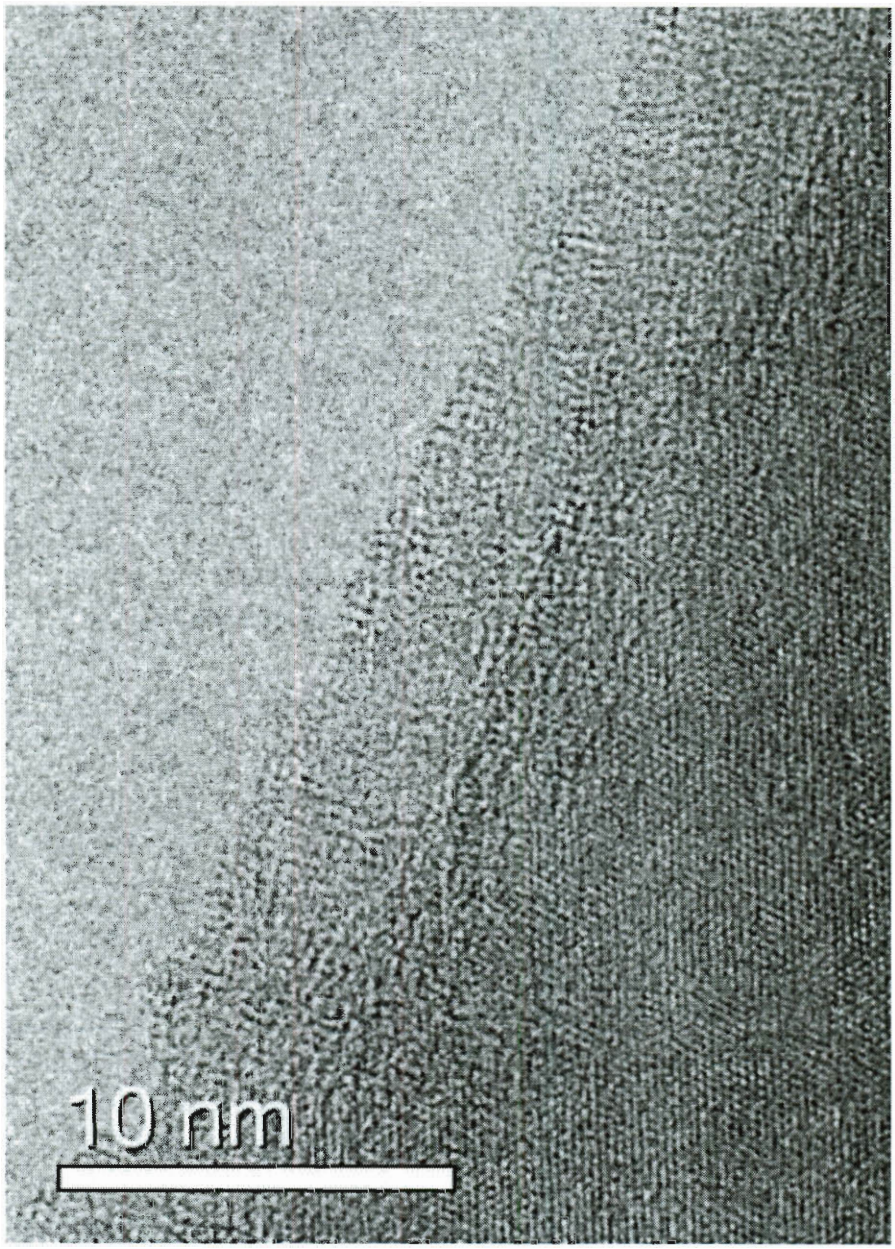

Figure 6.9. HR-TEM images of few-layer graphene deposited from a HSO_3Cl solution. The low-contrast region protruding near the edge of the structure indicates few (possibly single) layers of graphene.

We used cryo-TEM to visualize graphene in solution in HSO_3Cl as shown in several representative images depicted in Fig. 6.10, adapting a recent technique for imaging SWCNTs in HSO_3Cl.[20] A number of wrinkles, folds, and flat edges can be seen in the graphene flakes, particularly the larger flakes in Fig. 6.10c. These features are quite similar to TEM images of graphene [22] and graphene oxide sheets.[23] Moreover, similar wrinkles have previously been detected in AFM images of functionalized single graphene sheets.[24] The presence of wrinkles and folds indicates very few (possibly single) layers of graphene. Flake stiffness grows rapidly with the number of layers; thus, thick flakes could not form such features. No large (>1 μm) undissolved graphite aggregates were detected during imaging, providing further evidence of spontaneous dispersion of graphite into graphene. A set of experiments was performed to obtained AFM data; however, the results were inconclusive because of sample preparation difficulties associated with the superacid.

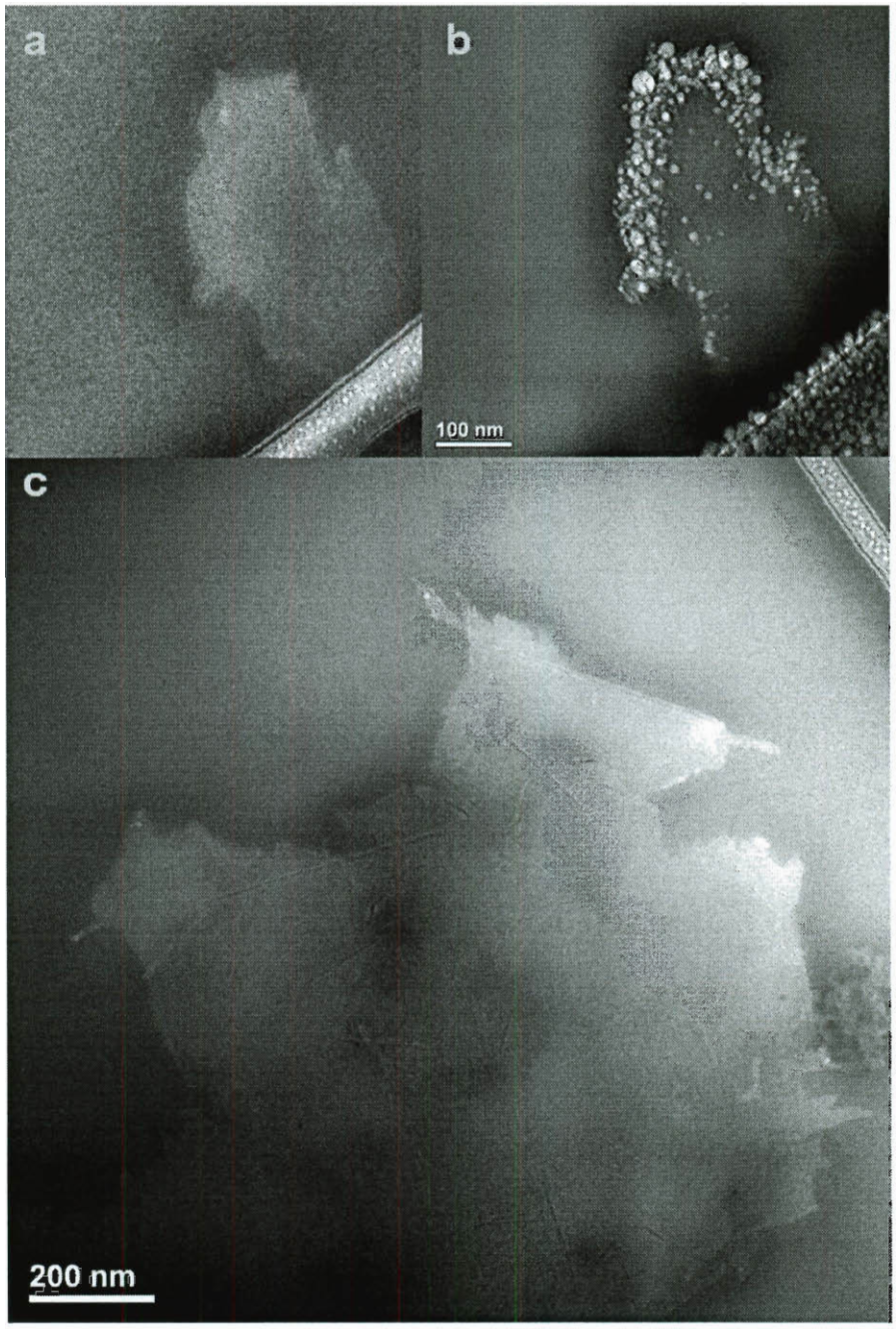

Figure 6.10. Cryogenic-temperature transmission electron microscopy (cryo-TEM) images of graphene flakes dispersed in $_{HSO3CL}$. A graphene flake (a) is shown nearby the TEM lacey carbon edge at very low imaging conditions (<10 electrons/Å^2). After some

irradiation from the electron beam of 50-80 electrons/Å^2, (b) the contrast between the graphene and acid is heightened nearby the graphene edges as acid is preferentially etched at these sites. In a large flake (c), a number of wrinkles, folds, and flat edges can be seen.

The ability to form thin free-standing films and the electrical properties of those films are highly dependent on the starting graphite; graphoil yields in better films on both counts compared with microcrystalline graphite. Twelve electronic devices based on thin (~10 nm thick) films exhibited similar conductivity values in 80,000-95,000 S/m range. We also measured sheet resistance of 1000 Ω/□ on an 80% transparent (at 550 nm) film (Fig. 6.11). These values are an order of magnitude better than other films produced from pristine graphene dispersions.[6,9]

Figure 6.11. 80% transparent (at 550 nm) film made by vacuum filtration of a 10 ppm isotropic Graphoil dispersion in chlorosulfonic acid. The measured sheet resistance was 1000 Ω/□.

6.3 Experimental Section

6.3.1 General Procedure for Preparation of Dispersions

We analyzed and characterized three different sources of graphite in this study: (1) Graphoil (Expanded graphite) from EGS Enterprises, Inc., (2) microcrystalline graphite from Sigma Aldrich (batch #08017EH), and (3) highly ordered pyrolytic graphite (HOPG) from SPI Supplies (Lot #1091028). HSO_3Cl from Sigma Aldrich (99%, batch #16096EJ) or a mixture of HSO_3Cl and H_2SO_4 acid (Fisher Chemical, certified ACS plus, lot #083290) are used as solvents.

The mixtures were prepared as follows: The initial powder was dried overnight in a vacuum oven at 100 °C to minimize moisture content. The vials were then transferred into a dry glove box and flushed with dry air for 12 h. The acid was then added via glass syringe, and the solution was mixed with a Teflon-coated magnetic stir-bar for a minimum of 2 d.

The vials were centrifuged on a Fisher Centrific Model 225 Benchtop centrifuge at 5100 rpm for 12 h, unless otherwise specified. The vials were then retransferred into the glove box, and the top phase was extracted by glass pipet. Approximately 50% of the top layer was extracted. This avoids the entrainment of the undispersed particles from the bottom during the extraction process. The top phase concentration was determined by quenching a portion of the top phase in water, filtering, and weighing the graphene. The top phase was then diluted, and the UV-vis-nIR spectra measured. A Shimadzu UV-3101PC spectrometer in 1 mm pathlength quartz Starna cells with Teflon closures was used for UV-vis absorption. The extinction coefficient was determined from the spectra of the various dilutions at a given wavelength.[6] The extinction coefficient was then used to measure concentration of the same graphite source in the same solvent.

6.3.2 Characterization

Raman spectroscopy was performed on a Renishaw Raman microscope using a 514 nm He-Ne laser. Samples for Raman spectroscopy were prepared in different ways depending on the type. Raman spectra of solid samples were taken by depositing the graphite on a glass slide with the aid of double sided tape. In order to measure the solid state Raman spectra of the top and bottom phase of a centrifuged sample, the sample was quenched through the addition of excess water (*Caution*: extreme care has to be taken during this operation due to the highly exothermic reaction of HSO_3Cl with water; dropwise addition of water into the acid is advised. The researcher also needs the appropriate protective equipment). Once the graphite precipitated, the mixture was filtered to yield a solid sample. To measure the Raman shift of the fluid, samples were prepared on glass slides in the glove box. A cover slip along with a sealant such as wax or tape was used to avoid moisture contact during the measurement. The same procedure was followed for the preparation of microscopy slides.

High-resolution TEM (HR-TEM) imaging and chemical analysis were done using a FEI Titan 80-300 S/TEM operated at 300 kV with a point-to-point resolution below 1Å. All samples were prepared by dropping a HSO_3Cl solution of graphene onto a 2000-mesh fine bar gilder nickel grid (Ernest F. Fullam, Inc.) in a fume hood. The grid was rinsed with chloroform followed by ether to remove excess acid. The grids were dried under vacuum at room temperature overnight prior to imaging.

The cryo-TEM techniques follow those by Davis *et al.*[20] The standard cryo-TEM procedure[25] was modified to account for the unique difficulties associated with working with superacids. Similar to the earlier procedure, soluble graphene was acquired by dispersing 250 mg of Graphoil in 10 mL of HSO_3Cl, centrifuging at 5000 rpm for 12 h,

removing the top phase simply by taking it up with a glass syringe, and quenching the top phase by slowly adding it to excess water This produced solid graphene that can be entirely redispersed in soluble in HSO_3Cl with no insoluble portion. Using this source, soluble graphene was dispersed in 97% reagent grade HSO_3Cl at concentrations of 0.042 mg/mL (50 ppm by mass). Dispersions were prepared and mixed for 1 d in a glove box (dew point -50 °C) in a nitrogen gas atmosphere to prevent contact with water and consequent evolution of gaseous hydrochloric acid. Small samples (2 mL) of either dispersion were transferred into a small vial and placed in the vitrification apparatus along with a glass filter paper and glass pipette. The entire set-up was placed in a glove bag and purged with ultra-pure nitrogen (99.9995%) for 30 min. A drop of the graphene dispersion was then placed on 200 copper mesh, lacey carbon grid (Ted Pella). The glass filter paper (not reactive with HSO_3Cl) was then used to blot the sample leaving a thin film of liquid. The grid was then quickly vitrified by dipping into liquid nitrogen (77 K) and was placed in a cryo-specimen holder for transfer into the TEM. Cryo-TEM imaging was carried out on an FEI T12 transmission electron microscope operated at 120 kV, using an Oxford CT3500 cooling holder, operated at about -180 °C.

XPS was performed on a PHI Quantera SXM Scanning X-ray Microprobe with a pass energy of 26.00 eV, 45° takeoff angle and a 100 μm beam size.

6.3.3 Fabrication and Testing of Thin Films

Thin films were prepared by vacuum filtration of isotropic graphene dispersions on alumina (Whatman anodisc, 47,mm, 0.02,μm pore size) as well as PTFE filters (Millipore – Omnipore membrane, 13 mm, 0.2 μm). Chloroform was then added to quench and remove residual acid; chloroform is miscible with HSO_3Cl and has a small

heat of mixing. In order to transfer films on an alumina filter to another substrate such as glass, the alumina is slowly placed in fluroware with DI water until the graphene films separated from the alumina mebrane.

The electrical transport properties of electronic devices were tested using a probe station (Desert Cryogenics TT-probe 6 system) under vacuum with chamber base pressure below 10^{-5} torr. The I-V data were collected by an Agilent 4155C semiconductor parameter analyzer.

Sheet resistance of the thin films samples were measured using a Alessi four-point probe fitted with custom-made film attachment with Pt leads. Measurements were taken in ambient conditions by securing and pressing the graphene thin films on glass substrate against the Pt leads.

AFM was attempted through a number of methods, including the following: spin coating on silica, Kevlar-coated silica, and APTES (aminopropyltriethoxysilane)-treated glass, as well as spray coating on heated silica. In all cases, the acid's wetting behavior, reactivity, and difficulty in evaporation cause aggregation of flakes during sample preparation. However, other methods indicate that HSO_3Cl does indeed disperse graphene at the few-to-single layer level.

6.4 Conclusion

We have shown that HSO_3Cl exfoliates graphite into isotropic graphene dispersions at concentrations one order of magnitude higher than any other known solvent or dispersant. The acid protonates the graphene to induce repulsion between layers; the protonation mechanism is similar to acid protonation of SWCNTs and does not damage or functionalize the material. A minimum degree of protonation is required

for dissolution at high concentrations. Moreover, HSO_3CL disperses new forms of graphene such as graphene nanoribbons. High-concentration dispersions of fully soluble material yield liquid-crystalline phases. The highly concentrated isotropic and liquid crystalline phases are promising for functionalization, and for scalable manufacturing of nanocomposites, films, coatings, and high performance fibers.

6.5 Experimental Contributions

My contribution to this work is the design and execution of the experiments including dispersion of graphene in HSO_3Cl, Raman spectroscopy measurements, film fabrication and measurement of sheet resistance, AFM sample preparation and analysis and XPS analysis. Natnael Behabtu executed graphene-chlorosulfonic acid dispersions performed Raman and UV-vis measurements and assisted in film preparation. Dr. Amanda L. Higginbotham and Professor Yeshayahu Talmon performed TEM analysis on graphene and graphene-HSO_3Cl dispersions. Dr. Alexander Sinitskii fabricated devices for conductivity measurements.

References

1. Boehm, H. P.; Clauss, A.; Fischer, G. O.; Hofmann, U. *Z. Anorg. Allg. Chem.* **1962**, *316*, 119.
2. Boehm, H. P.; Scholtz, W., *Z. Anorg. Allg. Chem.* **1965,** *335*, 74.
3. He, H. Y.; Riedl, T.; Lerf, A.; Klinowski, J. *J. Phys. Chem.* **1996**, *100,* 19954.
4. Lerf, A.; He, H.; Forster, M.; Klinowski, J. *J. Phys. Chem. B* **1998**, *102*, 4477-4482.

5. Novoselov, K. S.; Geim, A. K.; Morozov, S. V.; Jiang, D.; Zhang, Y.; Dubonos, S. V.; Grigorieva, I. V.; Firsov, A. A. *Science* **2004,** *306*, 666.

6. Hernandez, Y.; Nicolosi, V.; Lotya, M.; Blighe, F. M.; Sun, Z.; De, S.; McGovern, I. T.; Holland, B.; Byrne, M.; Gun'Ko, Y. K.; Boland, J. J.; Niraj, P.; Duesberg, G.; Krishnamurthy, S.; Goodhue, R.; Hutchinson, J.; Scardaci, V.; Ferrari, A. C.; Coleman, J. N. *Nat. Nanotechnol.* **2008**, *3*, 563.

7. Blake, P.; Brimicombe, P. D.; Nair, R. R.; Booth, T. J.; Jiang, D.; Schedin, F.; Ponomarenko, L. A.; Morozov, S. V.; Gleeson, H. F.; Hill, E. W.; Geim, A. K.; Novoselov, K. S. *Nano Lett.* **2008**, *8*, 1704-1708.

8. Hamilton, C. E.; Lomeda, J. R.; Sun, Z.; Tour, J. M.; Barron, A. R. *Nano Lett.* **2009**.

9. Lotya, M.; Hernandez, Y.; King, P. J.; Smith, R. J.; Nicolosi, V.; Karlsson, L. S.; Blighe, F. M.; De, S.; Wang, Z.; McGovern, I. T.; Duesberg, G. S.; Coleman, J. N. *J. Am. Chem. Soc.* **2009**, 131, 3611.

10. Rai, P. K.; Parra-Vasquez, A. N. G.; Peng, H.; Hauge, R. H.; Pasquali, M. *J. Phys. Chem. C* **2007**, *111*, 17966-17969.

11. Cataldo, F. *Spectrochim. Acta* **1995**, *51A*, 405.

12. Chiang, L. Y.; Wang, L. Y.; Swirczewski, J. W.; Solde, S.; Cameron, S. *J. Org. Chem.* **1994,** 59, 3960.

13. Davis, V. A.; Ericson, L. M.; Parra-Vasquez, A. N. G.; Fan, H.; Wang, Y. H.; Prieto, V.; Longoria, J. A.; Ramesh, S.; Saini, R. K.; Kittrell, C.; Billups, W. E.; Adams, W. W.; Hauge, R. H.; Smalley, R. E.; Pasquali, M. *Macromolecules* **2004**, *37*, 154-160.

14. Ramesh, S.; Ericson, L. M.; Davis, V. A.; Saini, R. K.; Kittrell, C.; Pasquali, M.; Billups, W. E.; Adams, W. W.; Hauge, R. H.; Smalley, R. E. *J. Phys. Chem. B* **2004**, *108*, 8794-8798.

15. Ericson, L. M.; Fan, H.; Peng, H.; Davis, V. A.; Zhou, W.; Sulpizio, J.; Wang, Y.; Booker, R.; Vavro, J.; Guthy, C.; Parra-Vasquez, A. N. G.; Kim, M.; Ramesh, S.; Saini, R. K.; Kittrell, C.; Lavin, G.; Schmidt, H. K.; Adams, W. W.; Billups, W. E.; Pasquali, M.; Hwang, W. F.; Hauge, R. H.; Fischer, J. E.; Smalley, R. E. *Science* **2004**, *305*, 1447.

16. Hudson, J. L.; Casavant, M. J.; Tour, J. M., *J. Am. Chem. Soc.* **2004**, *126*, 11158.

17. Melin, J.; Furdin, G.; Fuzellier, H.; Vasse, R.; Herold, A. *Mater. Sci. Eng.* **1977**, *31*, 61-65.

18. Li, X.; Zhang, G.; Bai, X.; Wang, X.; Wang, E.; Dai, H. *Nat. Nanotechnol.* **2008**, *3*, 538-542.

19. Rai, P. K.; Pinnick, R. A.; Parra-Vasquez, A. N. G.; Davis, V. A.; Schmidt, H. K.; Hauge, R. H.; Smalley, R. E.; Pasquali, M. *J. Am. Chem. Soc.* **2006**, *128*, 591-595.

20. Davis, V. A.; Parra -Vasquez, A. N. G.; Green, M. J.; Rai, P. K.; Behabtu, N.; Prieto, V.; Booker, R. D.; Schmidt, J.; Kesselman, E.; Zhou, W.; Fan, H.; Adams, W. W.; Hauge, R. H.; Fischer, J. E.; Cohen, Y.; Talmon, Y.; Smalley, R. E.; Pasquali, M. *Nat. Nanotechnol.* **2009**, accepted.

21. Meyer, J. C.; Geim, A. K.; Katsnelson, M. I.; Novoselov, K. S.; Booth, T. J.; Roth, S. *Nature* **2007**, *446*, 60-63.

22. Dato, A.; Radmilovic, V.; Lee, Z. H.; Phillips, J.; Frenklach, M. *Nano Lett.* **2008**, *8*, 2012-2016.

23. OuYang, F. P.; Huang, B.; Li, Z. Y.; Xiao, J.; Wang, H. Y.; Xu, H. *J. Phys. Chem. C* **2008**, *112*, 12003-12007.

24. McAllister, M. J.; Li, J. L.; Adamson, D. H.; Schniepp, H. C.; Abdala, A. A.; Liu, J.; Herrera-Alonso, M.; Milius, D. L.; Car, R.; Prud'homme, R. K.; Aksay, I. A. *Chem. Mater.* **2007**, *19*, 4396-4404.

25. Talmon, Y. *Berichte Der Bunsen-Gesellschaft-Phys. Chem. Chem. Phys.* **1996**, *100*, 364-372.

Chapter 7

Layer-by-Layer Assembly of Chemically Converted Graphene-Polyimide Composite Films

7.1 Introduction

Layer-by-layer (LbL) assembly is a simple technique that allows for fabrication of thin coatings and macroscopic films by taking advantage of specific interactions facilitating self- assembly.[1] Precise deposition of components can be achieved at the nanometer scale using alternate dipping in polyanionic and polycationic solutions.[2,3] The success of this technique lies in the versatility of the nanomaterials employable in the process, ranging from inorganic nanoparticles to nanosheets and nanowires.[1] The combination of polymeric and nanoparticle species allows for the production of multifunctional materials in small volumes. The hierarchical architecture arising from these protocols is reminiscent of some of the toughest minerals such as nacre produced by mollusks that possess layered structures.[4] LbL also allows for fabrication of macroscopic articles, both flat and non-planar. Hence, this is another approach to the fabrication of composites that allows control of the architecture, transparency and thickness compared to bulk composites.[2] In addition to alternate dipping, spin coating,[5] spraying,[6] and dewetting[7] can also yield layered structures.

Nanocomposites are promising new materials that can have unique properties. Compared to a bulk fabrication technique such as blending, incorporation of nanoparticles results in superior mechanical properties.[8] The addition of carbon

nanomaterials such as carbon nanotubes (CNTs) results in enhancement of mechanical properties at low wt % loading. Polyvinyl alcohol (PVA)-single walled carbon nanotube (SWCNT) composites prepared by LbL showed properties up to 10× better than a comparative system prepared in bulk.[9] The multifunctional materials have superior properties due to better interfacial adhesion to and dispersion in the host matrices.[10]

Graphene, a 2-dimensional one-atom-thick network of sp^2 carbons, is a promising material for the fabrication of electronic devices and nanocomposites.[11,12] The reported solution phase exfoliation of these nanosheets in a variety of solvents such as polar aprotic solvents,[13,14] surfactant solutions,[15] *ortho*-dichlorobenzene (ODCB)[16] and superacids allows access to pristine graphene sheets. Oxidation of graphite to graphene oxide (GO) is also a very practical approach to achieve that water-soluble graphene derivative.[17,18] While the properties of GO are different compared to graphene, thermal and chemical reduction allow for partial recovery of the sp^2 graphitic structure yielding chemically converted graphene (CCG), and stable solutions of CCG have also been prepared.[19-23] Such solution based exfoliation can then be exploited in a manner similar to that employed for clays and silicates for LbL assembly, and that process is disclosed here for the formation of functionalized CCG (f-CCG) composite materials.

7.2 Results and Discussion

Graphene oxide-polyelectrolyte LbL assembled films was first reported by Kotov.[25] Self-assembly of poly(diallylmethylammonium chloride) (PDDA) and GO was driven by the polycationic character of the PDDA and the polyanionic nature of the GO. The approach using GO allowed for incorporation of graphite in ultra-thin films.

Reduction of the samples was accomplished by either hydrazine, HCl and Zn, or electrochemically, rendering conductive sandwich structures. Along this same line of thought, the fabrication of thin films comprised of f-CCG and polyimide (PI) were investigated here. Graphene has been shown to be an impermeable membrane even to helium and capable of withstanding high pressures.[26] This could further enhance the barrier and gas selective properties of polyimides,[27-29] in addition to improving structural reinforcement and conductivity. To take advantage of the desirable thermal and electrical properties of the graphene sheets, in-situ reduction of GO within the polymer matrix is normally employed.[30] For polyimides however, the use of GO and its subsequent reduction would have deleterious effects for PAA and the polyimide. PAA is susceptible to hydrolytic chain scission and PI is vulnerable to ring opening by hydrazine.[31] To circumvent this problem, f-CCG was employed in order to have a reduced form of graphene sheets without the need for chemical reduction. Also, due to the thin-film nature, the dehydration of GO[32] during imidization might produce too much water, leading to oligomerization of the PAA. Since clays have a plate-type structure that can improve composite properties,[16] GO, with a similar structure, may be as good or better than clays in producing composites with good properties. But the reduced, GO, CCG, is not soluble by itself and the driving force for assembly less controllable by itself, thus we carried out their aryl functionalizations.

The functionalization was achieved by treating surfactant wrapped CCG with an aryl diazonium salt.[22] Two possible routes were considered in the functionalization: (1) treatment with nitrobenzene diazonium salt followed by reduction of the $-NO_2$ to an $-NH_2$ group with elemental sulfur (Scheme 7.1) and (2) treatment with anilinium diazonium

salt. However, the second protocol did not yield significant functionalization based on IR and XPS analyses, hence the first one was pursued.

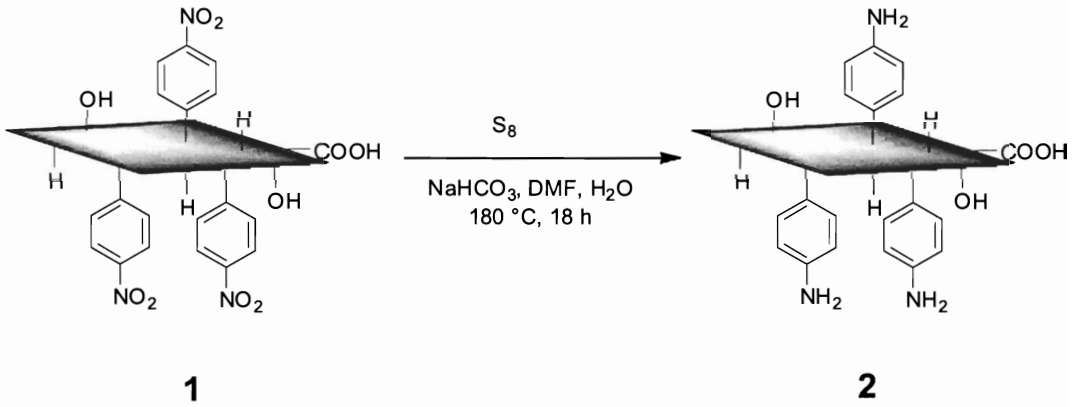

1 **2**

Scheme 7.1. Reduction of nitrophenyl-f-CCG (**1**) to aniline-f-CCG (**2**) using elemental sulfur.

ATR-IR and XPS spectroscopic analyses of f-CCG are shown in Figure 1. Asymmetric and symmetric stretches at 1513 cm^{-1} and 1343 cm^{-1}, respectively, are assigned to the -NO_2 group (Figure 7.1a). After reduction, a broad peak due to minimal H-bonding in the solid at 3200 – 3300 cm^{-1} is assigned as -NH stretch, and the weak peak at 1590 cm^{-1} is assigned as -NH_2 deformation (Figure 7.1b). High resolution XPS scans of the N1s core-level, which showed that the nitrogen binding energy shifted from 406 eV (-NO_2 group) to 400 eV (-NH_2 group) further supports this functional group conversion (Figure 7.1c).

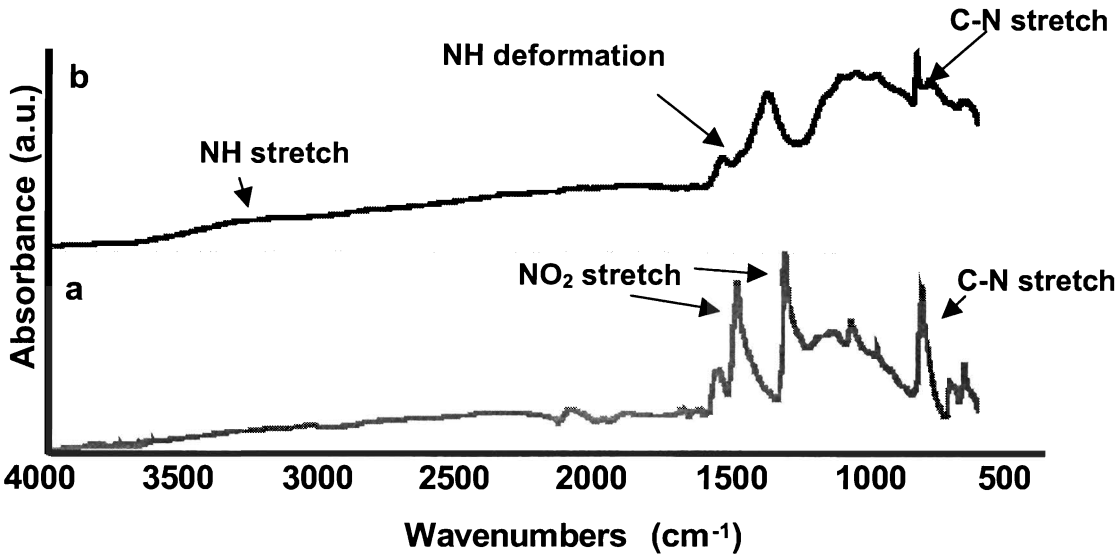
C-N stretch
NH deformation
b
NH stretch
Absorbance (a.u.)
a
NO2 stretch
C-N stretch
4000
3500
3000
2500
2000
1500
1000
500
Wavenumbers (cm-1)

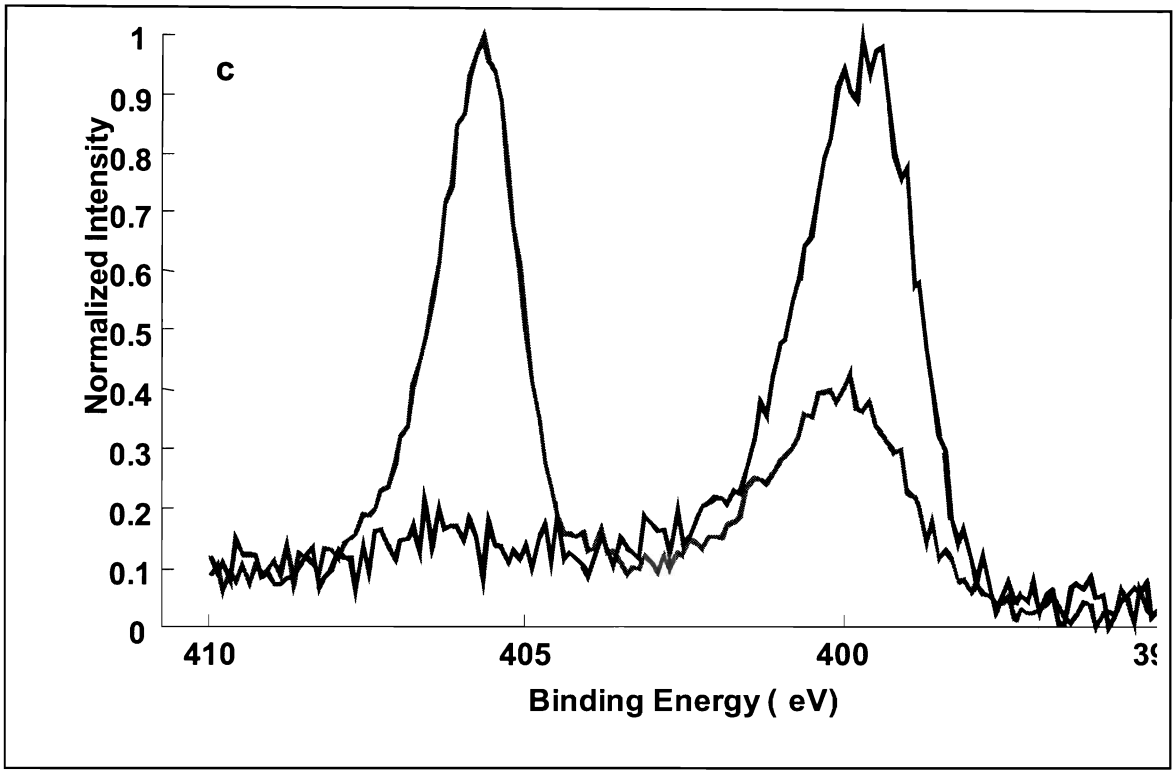

Figure 7.1. ATR-IR spectra (a) **1**, (b) **2**, and (c) core-level N1s spectra of **1** (red) showing the NO_2 peak at 406 eV and after reduction to **2** (blue) indicating the reduction to NH_2 (400 eV).

The initial assembly of layers was monitored by XPS after adsorption of each layer on a 200-nm SiO_2 coated silicon wafer. Figure 7.2 shows the survey scans obtained on a Si substrate after (a) piranha treatment (b) APTES functionalization (c) deposition of PAA and (d) deposition of CCG. There is significant increase in the nitrogen content after APTES and PAA assembly. For Figure 7.2b and 7.2c, the carbon/nitrogen ratio is estimated to ~ 6.8. After the deposition of graphene however, the ratio increase to 71 due to the increase in carbon fraction from the graphene framework (Figure 7.2d).

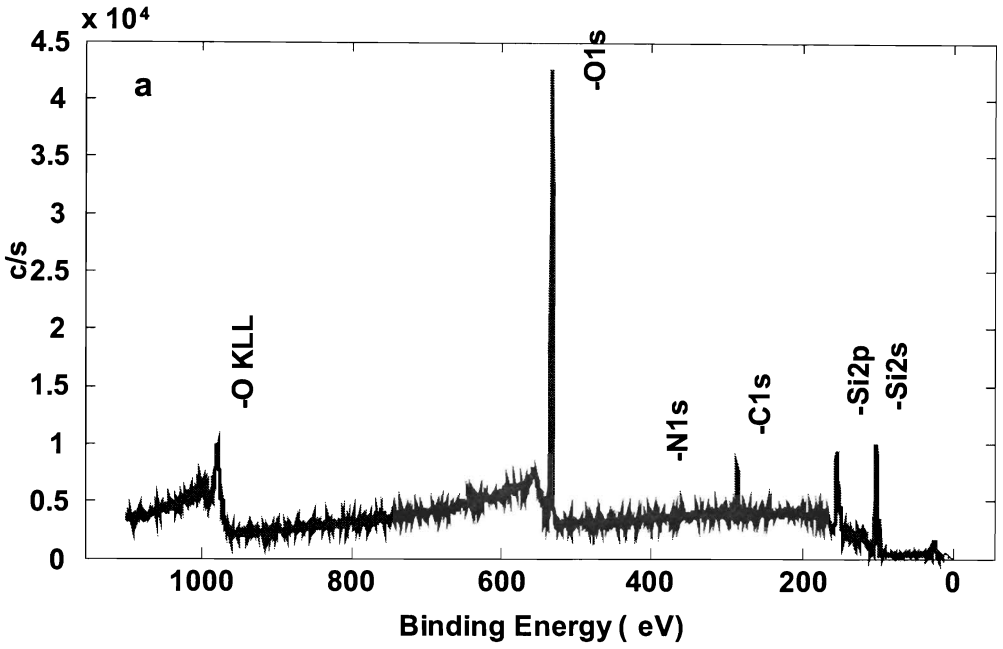
x 10⁴
4.5
4
3.5
3
2.5
2
1.5
1
0.5
0
c/s
a
-O1s
-O KLL
-N1s
-C1s
-Si2p
-Si2s
1000
800
600
400
200
0
Binding Energy (eV)

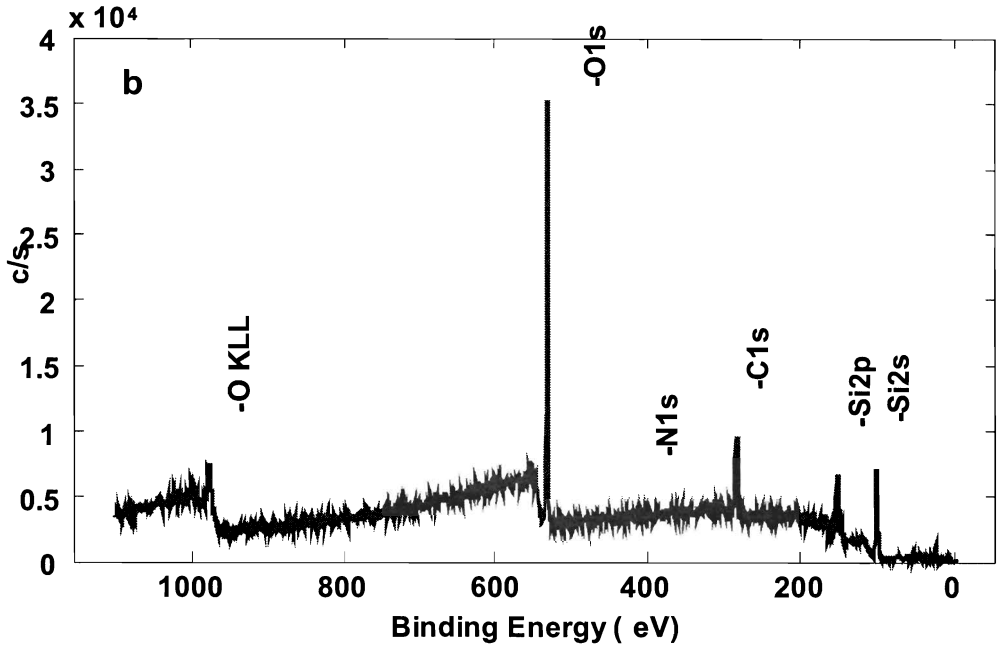
x 10⁴
4
3.5
3
2.5
2
1.5
1
0.5
0
c/s
b
-O1s
-O KLL
-N1s
-C1s
-Si2p
-Si2s
1000
800
600
400
200
0
Binding Energy (eV)

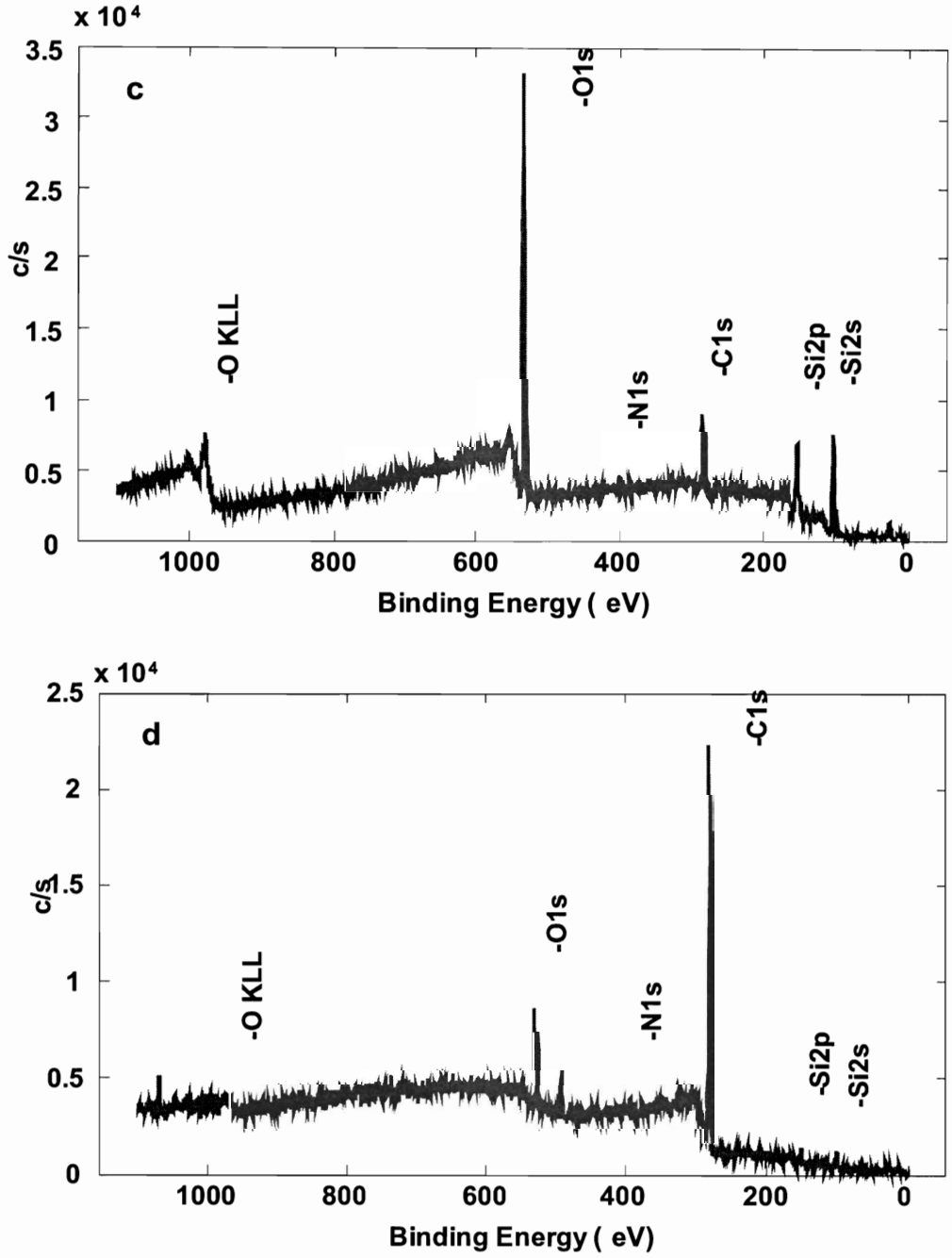

Figure 7.2. XPS survey scans on Si substrate after (a) piranha treatment, (b) APTES assembly, (c) PAA deposition, and (d) f-CCG (**2**) deposition. Note the increase in carbon fraction in (d).

Raman analysis of the 40 - bilayer film (Figure 7.3) showed imide peaks in agreement with the results reported by Pethe.[33] The imidized thin films showed the following Raman bands: 1200 – 1300 cm^{-1} (C-O-C stretch), 1397 cm^{-1} (imide C-N stretch), 1660 cm^{-1} (imine C=N stretch) and 1790 cm^{-1} (symmetric C=O imide stretch). The narrow peak at 1350 cm^{-1} is assigned to the diamondoid peak (D-peak) of the f-CCG while the graphitic peak (G-peak) is not evident as it overlaps with the imine C=N stretch (shoulder). The spectrum was collected with the pinhole engaged to minimize the fluorescence starting at 1500 cm^{-1} and extending to 3300 cm^{-1}.

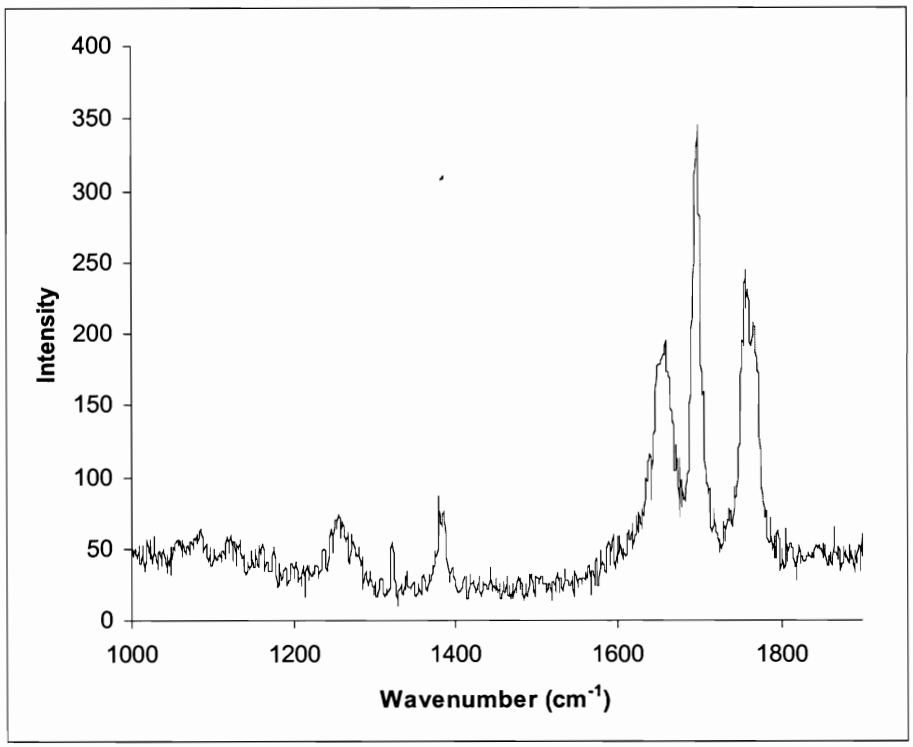

Figure 7.3. Raman spectrum of 40 - bilayer film taken using 633 nm laser.

XPS analysis of the film showed that the imidiazation at 225 °C is complete with the C1s core-level spectrum resembling that of bulk polyimides (Figure 7.4). The peak assignments are as follows: 284.8 eV (C=C, C-H); 286 eV (C-O) and 288 eV (imide peak).

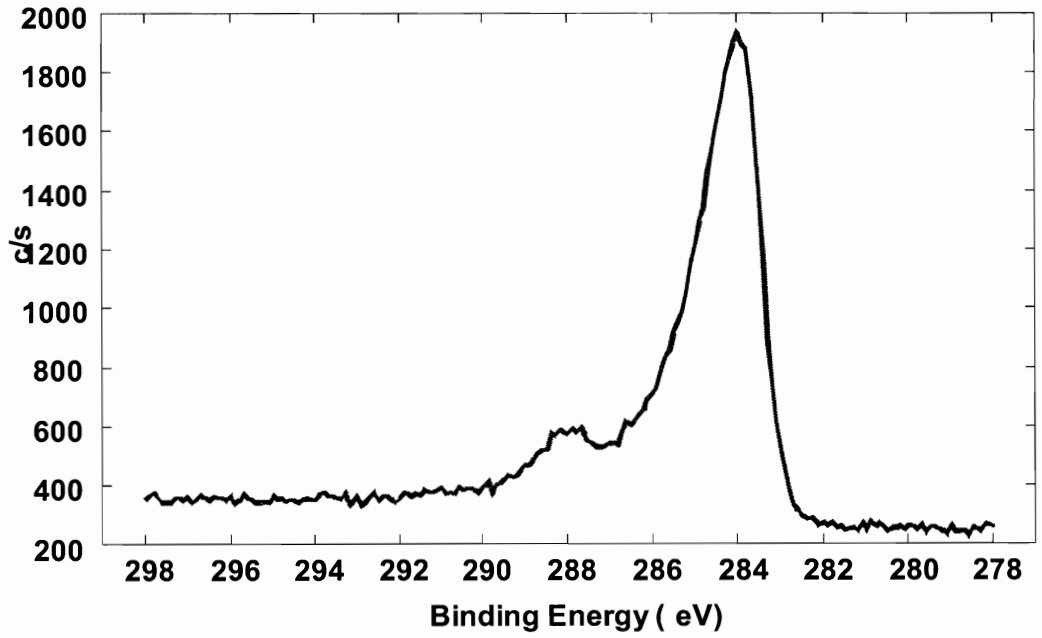

Figure 7.4. Core-level C1s spectrum of 40 - bilayer film.

The driving force most utilized in LbL assembly has been the attractive complementary charges of polyelectroyte systems. But the technique has now been extended for other driving forces such as charge transfer, hydrogen bonding, biological recognition, and hydrophobic interactions.[1,10] An attractive feature of the process arising from these interactions is that the rinsing steps remove the excess layers due to non-interaction or repulsion. The interactions exploited in this work are the acid-base

interaction between the aniline group of the f-CCG **2** and the carboxyl functionality of the PAA chains similar to the work by Song.[3]

AFM analysis was performed on the thin film after the 40 - bilayer depositions (Figure 7.5). After piranha treatment and APTES functionalization, the glass substrate shows a rough morphology, (Figure 7.5a). The thickness of APTES deposited during silanization, based on ellipsometry, was estimated to be ~5 nm. The in-plane structure of LbL film after 40 - bilayer depositions is shown in Figure 7.5b. The mean roughness measured is about 2.7 nm, although some aggregated flakes are visible. Section analysis (Figure 7.5c) showed that the large flakes have heights reaching up to ~9 nm and the coverage of graphene sheets is not very uniform.

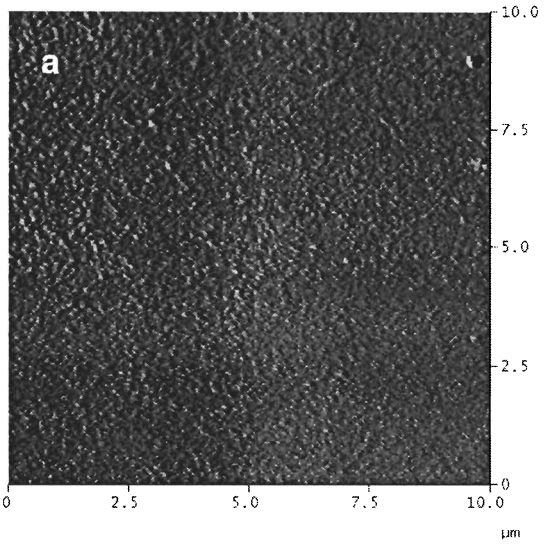
a
10.0
7.5
5.0
2.5
0
0
2.5
5.0
7.5
10.0
µm

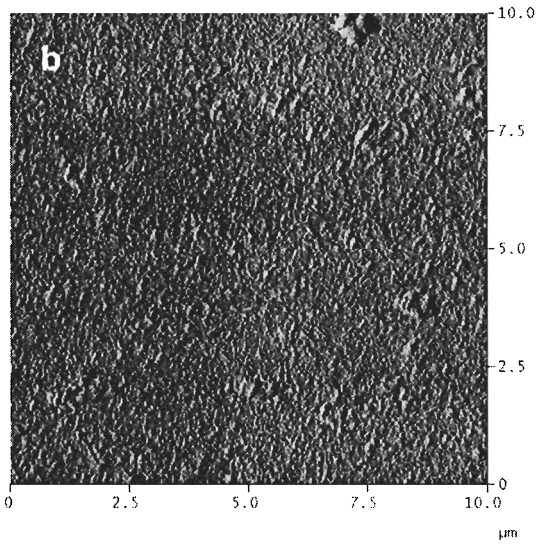
b
10.0
7.5
5.0
2.5
0
0
2.5
5.0
7.5
10.0
µm

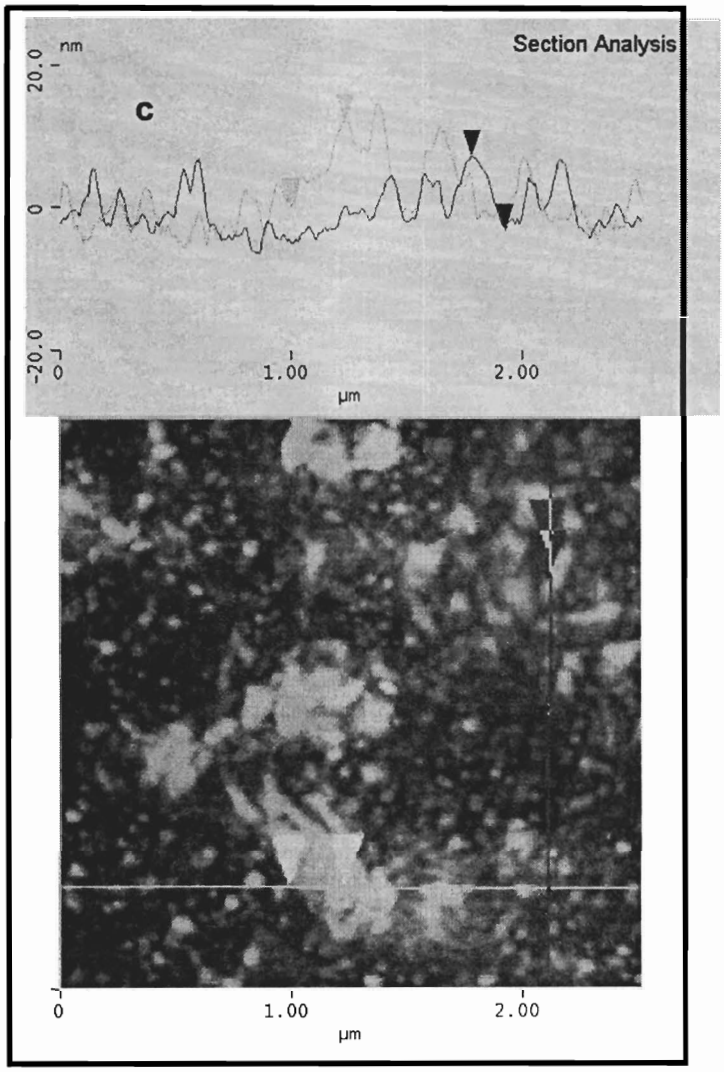

Figure 7.5. AFM micrographs of (a) APTES treated glass slide (phase mode), (b) in-plane morphology of 40 - bilayer LbL assembled films, and (c) section analysis of the 40 - bilayer film.

The inhomogeneity of the film surface is also evident on the SEM micrographs obtained. Figure 7.6 shows a representative example of the surface obtained after 40

depositions. Based on the section analysis of the deposited films, the estimated thickness is about 28 nm (Figure 7.6b). The layered structure, however, is not very evident.

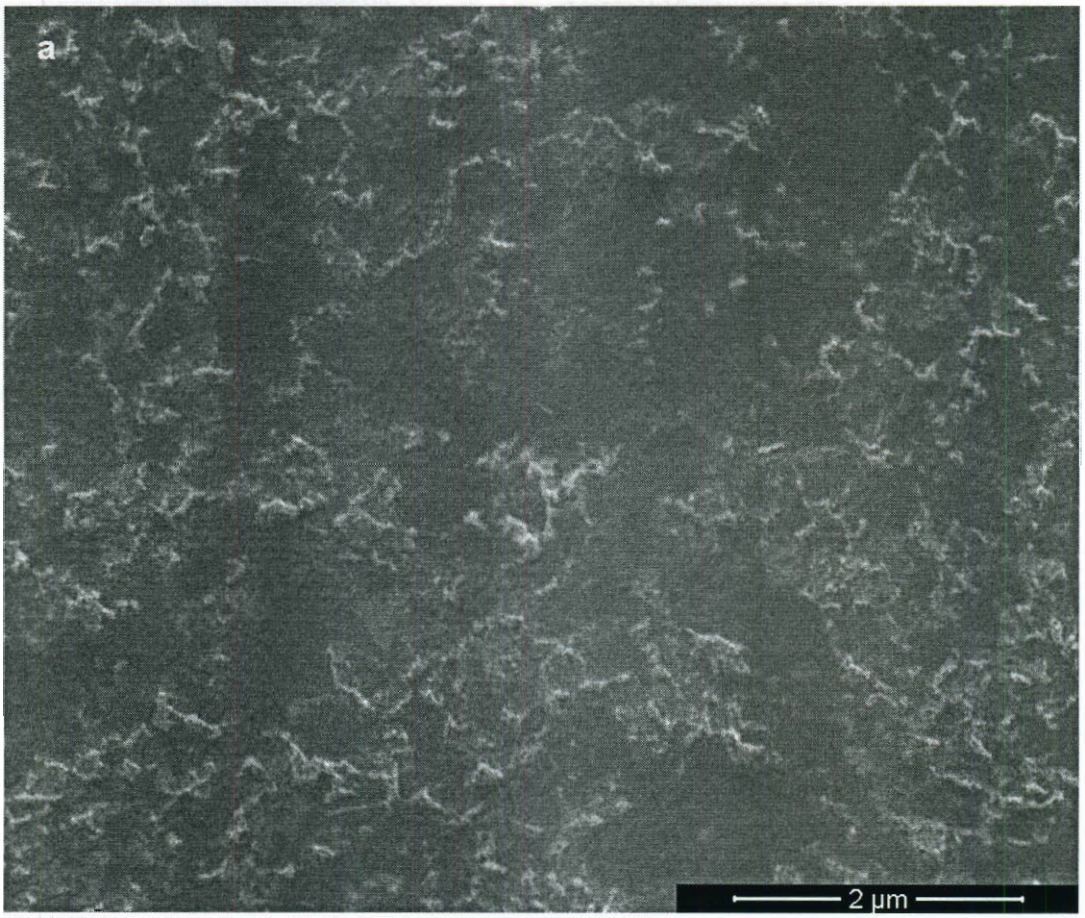

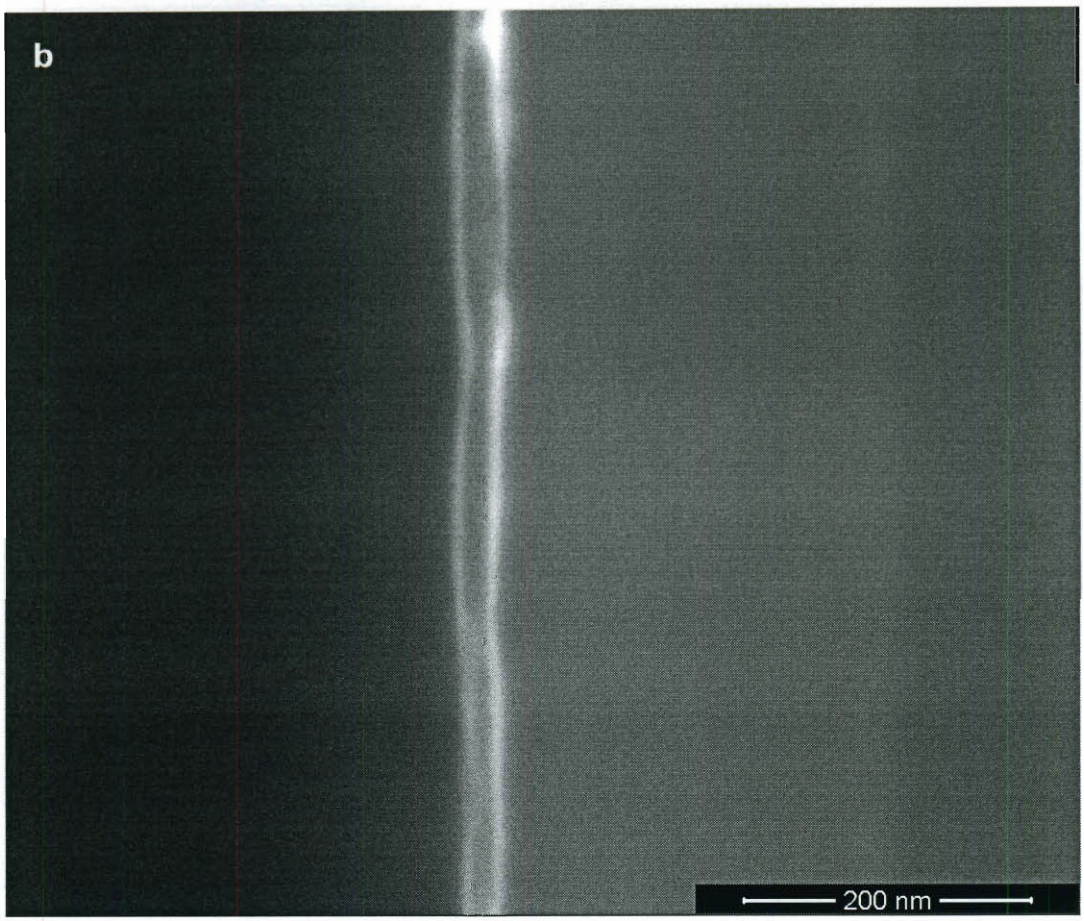

Figure 7.6. SEM micrographs of 40 - bilayer film (a) in-plane structure showing rough morphology and (b) cross-section image.

7.3 Experimental Section

7.3.1 Materials. Pyromellitic dianhydride-oxydianiline polyamic acid (PAA) in *N*-methyl-2-pyrollidone (NMP) (15 wt %), NMP and *N,N'*-dimethylformamide (DMF) were purchased from Sigma-Aldrich. The PAA solution was diluted with NMP to 1 wt % prior to LbL assembly. GO was prepared from expanded graphite obtained from Supracarbonic, LLC using the Staudenmaier procedure.[18] (*Caution*: protective equipment including face shield, acid-resistant gloves, lab coat, apron, and blast shield must be used

at all times during the preparation of GO by this procedure.) Functionalized chemically converted graphene (f-CCG) was prepared using nitrobenzene diazonium salt treatment of surfactant wrapped CCG[22] and reduced with elemental sulfur in the presence of $NaHCO_3$ (Scheme 1).[24] A 0.1 wt % solution of f-CCG in DMF was used for the LbL assembly.

7.3.2 LbL Assembly. Microscope slides (25mm × 75mm × 1 mm, Premiere) and 200-nm SiO_2 coated Si substrates were cleaned with piranha (30:70 v/v H_2O_2:H_2SO_4) solution and functionalized by 3-aminopropyl triethoxysilane (APTES) by immersing in a 1:9 (v/v) APTES:toluene solution for 1 h at 23 °C. After 1 h, the substrate was rinsed with freshly distilled toluene, sonicated in toluene for 10 m and rinsed with MeOH followed by drying with N_2 gas. PAA-f-CCG composite films were prepared by alternate dipping of the substrate into PAA and f-CCG solutions. The APTES functionalized microscope slide was immersed in a 1 wt % solution of PAA for 1 h (step a) (Scheme 2). The slide was rinsed with copious amounts of NMP to remove the excess PAA (step b) followed by drying with N_2. Step b was followed by immersion in a 0.1 wt % f-CCG solution in DMF (step c). And finally, the slide was rinsed with DMF (step d), followed by drying wth N_2. Steps a-d comprise the deposition cycle resulting in a bilayer deposited on the substrate after each round. The manual LBL assembly was performed for 10 cycles.

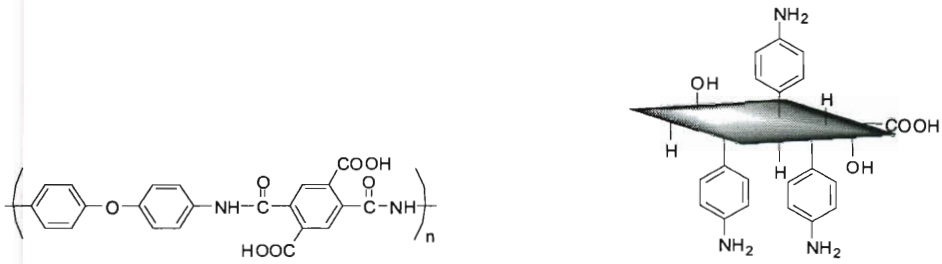

Scheme 7.2. Scheme for LbL deposition using PAA and f-CCG.

To fabricate thick films, a modified Asymtek printing machine (Asymtek Model d-583) was fitted with a clamp for glass slide attachment. The layers were assembled by immersing the APTES-functionalized glass slides in a 1 % PAA solution for 10 min followed by rinsing for 2 min in a beaker with NMP (3×), and flush drying with N_2 gas. This is then followed by immersion into the f-CCG solution and subsequent rinsing. The whole assembly was repeated 40×.

7.3.3 Thermal Imidization. The imidization of the LbL assembled films was conducted in a Linberg/Blue M gravity oven at 100 °C (1 h) followed by heating at 225 °C (1 h).

7.3.4 Characterization. The fabricated composite film samples were characterized by X-ray photoelectron spectroscopy (XPS) using a Phi Quantera SXM Scanning X-Ray Microprobe with a pass energy of 26.00 eV, 45° takeoff angle and a 100 μm beam size. Raman spectroscopy was performed using Renishaw Raman scope using 633 nm He-Ne laser. FT-IR analysis was performed using a Nicolet FT-IR fitted with

attenuated total reflectance (ATR) attachment. Atomic force microscopy (AFM) images were obtained using Digital Instrument Nanoscope III in tapping mode.

7.4 Conclusion

We have successfully fabricated thin films comprised CCG and polyimide using LbL assembly. The assembly is largely driven by acid-base interaction of the aniline moiety on the f-CCG and the carboxylic acid groups on PAA. The use of f-CCG circumvented the use of reducing agents such as in-situ hydrazine. This could to applications such as piezo-electric devices and coatings for gas selective permeation.

7.5 Experimental Contributions

My contribution to this work is as follows: (1) synthesis of f-CCG and execution of LbL experiments. Shinchiro Kohama performed SEM analysis. Zhengzong Sun and Paris J. Cox assisted in the preparation of solutions and programming of the Asymtek printer. Prabir K. Patra provided suggestions for the dipping experiments.

References

1. Srivastava, S.; Kotov, N. A. *Acct. Chem. Res.* **2008,** *41*, 1831-1841.
2. Decher, G. *Science* **1997,** *277*, 1232-1237.
3. Song, N.; Wang, Z. Y. *Macromolecules* **2003,** *36*, 5885-5890.
4. Tang, Z. Y.; Kotov, N. A.; Magonov, S.; Ozturk, B. *Nat. Mater.* **2003,** *2*, 413.
5. Cho, J.; Char, K.; Hong, J. D.; Lee, K. B. *Adv. Mater.* **2001,** *13*, 1076.

6. Izquierdo, A.; Ono, S. S.; Voegel, J. C.; Schaaf, P.; Decher, G. *Langmuir* **2005,** *21*, 7558.

7. Shim, B. S.; Podsiadlo, P.; Lilly, D. G.; Agarwal, A.; Lee, J.; Tang, Z.; Ho, S.; Ingle, P.; Paterson, D.; Lu, W., *Nano Lett.* **2007,** *7*, 3266.

8. Podsiadlo, P.; Arruda, E. M.; Kheng, E.; Waas, A. M.; Lee, J.; Critchley, K.; Qin, M.; Chuang, E.; Kaushik, A. K.; Kim, H.-S.; Qi, Y.; Noh, S.-T.; Kotov, N. A. *ACS Nano* **2009,** *3*, 1564-1572.

9. Shim, B. S.; Zhu, J.; Jan, E.; Critchley, K.; Ho, S.; Podsiadlo, P.; Sun, K.; Kotov, N. A. *ACS Nano* **2009,** *3*, 1711-1722.

10. Hammond, P. T. *Adv. Mater.* **2004,** *16*, 1271-1293.

11. Novoselov, K. S.; Geim, A. K.; Morozov, S. V.; Jiang, D.; Zhang, Y.; Dubonos, S. V.; Grigorieva, I. V.; Firsov, A. A. *Science* **2004,** *306*, 666.

12. Ruoff, R. S. *Nat. Nanotechnol.* **2008,** 3, 10.

13. Hernandez, Y.; Nicolosi, V.; Lotya, M.; Blighe, F. M.; Sun, Z. Y.; De, S.; McGovern, I. T.; Holland, B.; Byrne, M.; Gun'ko, Y. K.; Boland, J. J.; Niraj, P.; Duesberg, G.; Krishnamurthy, S.; Goodhue, R.; Hutchison, J.; Scardaci, V.; Ferrari, A. C.; Coleman, J. N. *Nat. Nanotechnol.* **2008,** *3*, 563-568.

14. Nair, R. R.; Blake, P.; Grigorenko, A. N.; Novoselov, K. S.; Booth, T. J.; Stauber, T.; Peres, N. M. R.; Geim, A. K. *Science* **2008**, *320*, 1308.

15. Lotya, M.; Hernandez, Y.; King, P. J.; Smith, R. J.; Nicolosi, V.; Karlsson, L. S.; Blighe, F. M.; De, S.; Wang, Z. M.; McGovern, I. T.; Duesberg, G. S.; Coleman, J. N. *J. Am. Chem. Soc.* **2009,** *131*, 3611-3620.

16. Hamilton, C. E.; Lomeda, J. R.; Sun, Z.; Tour, J. M.; Barron, A. R. *Nano Lett.* **2009**.

17. Hummers, W. S.; Offeman, R. E. *J. Am. Chem. Soc.* **1958,** *80*, 1339.

18. Staudenmaier, L., *Ber. Dtsch. Chem. Ges.* **1898,** *31*, 1481.

19. McAllister, M. J.; Li, J.-L.; Adamson, D. H.; Schniepp, H. C.; Abdala, A. A.; Liu, J.; Herrera-Alonso, M.; Milius, D. L.; Car, R.; Prud'homme, R. K.; Aksay, I. A. *Chem. Mater.* **2007**, *19*, 4396-4404.

20. Stankovich, S. *J. Mater. Chem.* **2006,** *16*, 155-158.

21. Li, D.; Muller, M. B.; Gilje, S.; Kaner, R. B.; Wallace, G. G. *Nat Nanotechnol.* **2008**, *3*, 101-105.

22. Lomeda, J. R.; Doyle, C. D.; Kosynkin, D. V.; Hwang, W.-F.; Tour, J. M. *J. Am. Chem. Soc.* **2008**, *130*, 16201-16206.

23. Si, Y.; Samulski, E. T. *Nano Lett.* **2008**, *8*, 1679-1682.

24. McLaughlin, M. A.; Barnes, D. M. *Tetrahedron Lett.* **2006,** *47*, 9095-9097.

25. Kotov, N. A.; Dekany, I.; Fendler, J. H. *Adv. Mater.* **1996,** 8, 637-641.

26. Bunch, J. S.; Verbridge, S. S.; Alden, J. S.; van der Zande, A. M.; Parpia, J. M.; Craighead, H. G.; McEuen, P. L. *Nano Lett.* **2008,** *8*, 2458-2462.

27. Ding, Y.; Bikson, B.; Nelson, J. K. *Macromolecules* **2001,** *35*, 905-911.

28. Ding, Y.; Bikson, B.; Nelson, J. K. *Macromolecules* **2001,** *35*, 912-916.

29. Bikson, B.; Nelson, J. K.; Muruganandam, N., *J. Membr. Sci.* **1994,** *94*, 313.

30. Stankovich, S.; Dikin, D. A.; Dommett, G. H. B.; Kohlhaas, K. M.; Zimney, E. J.; Stach, E. J.; Piner, R. D.; Nguyen, S. T.; Ruoff, R. S. *Nature* **2006,** *442*, 282.

31. Dine-Hart, R. A.; Parker, D. B. V.; Wright, W. W. *Br. Polym. J.* **1971**, *3*, 226-234.

32. Schniepp, H. C.; Li, J. L.; McAllister, M. J.; Sai, H.; Herrera-Alonso, M.; Adamson, D. H.; Prud'homme, R. K.; Car, R.; Saville, D. A.; Aksay, I. A. *J. Phys. Chem. B* **2006,** *110*, 8535.

33. Pethe, R. G.; Cralin, C. M.; Patterson, H. H.; Unertl, W. N. *J. Mater. Res.* **1993,** *8*, 3218-3228.

Chapter 8

Edge Selective Functionalization for Low Resistivity of Soluble Graphene

8.1 Introduction

The production of chemically converted graphene from graphene oxide is a convenient method to obtain large amounts of graphene,[1-3] however, even with efficient reducing agents such as hydrazine or H_2, and annealing at high temperature, the original crystalline structure of graphene is not restored. Graphene oxide is heavily functionalized with many permanent chemical defects, such as holes introduced into the basal plane. These holes are not readily healed even upon annealing.

Micromechanically cleaved graphene affords crystalline single sheets of graphene using highly ordered pyrolytic graphite and adhesive tape.[4] While this method opened an avenue for many fundamental studies, it is likely impossible to scale and thereby produce larger quantities.

The exfoliation of graphene in the liquid phase, by continuously sonicating graphite in a high surface-tension organic solvent,[5,6] is another route to obtain mono- or few-layered sheets of graphene that are suspended in a dark mixture. However, the suspended graphene sheets tend to aggregate due to the absence of stabilizing groups such as surfactants or polymers to reduce interlayer attractions.[7] Because of significant π-π interactions, unlike graphene oxide and chemically converted graphene, liquid phase exfoliated graphene can not be stabilized as a concentrated mixture.

Chemical vapor deposition techniques have been used to grow thin and highly crystalline graphitic layers atop catalysts.[8,9] At elevated temperatures, methane or other volatile carbon precursors are decomposed on metal catalysts, such as Ni or Cu, in a reductive atmosphere to produce graphene.[10] Epitaxial growth by annealing SiC at temperatures as high as 2000 °C produces graphene that is deposited directly on the SiC wafer.[11-13] This method is referred to as chemical solid deposition since the precursor is solid rather than a gas. While these growth methods, coupled with patterning, will likely be among the dominant growth methods for future high performance graphene electronics, generating bulk scales of few-layered graphene for other materials applications will be problematic using the chemical vapor deposition and chemical solid deposition approaches.

Recently, chemically converted graphene was successfully functionalized using diazonium salts and the product showed improved solubility in polar aprotic organic solvents compared to chemically converted graphene.[14] In this paper, thermally expanded graphite was predominantly edge-functionalized with 4-bromophenyl groups using in situ formation of the corresponding diazonium salt from 4-bromoaniline. Mild sonication in *N,N'*-dimethylformamide (DMF) then exfoliated thin chemically-assisted exfoliated graphene (CEG) sheets from the bulk functionalized graphite. CEG was more soluble than pristine graphene in DMF. In addition, without any surfactant or polymer stabilizers, CEG exhibited far lower sheet resistance than chemically converted graphene. By taking advantage of the edge-selective functionalization, and low basal plane disruption, a bulk preparation of soluble yet far more conductive graphene has been demonstrated.

8.2. Results and Discussions

8.2.1 Protocol for Chemical-Assisted Exfoliation

Scheme 8.1. Production of Chemically-Assisted Exfoliated Graphene (CEG)

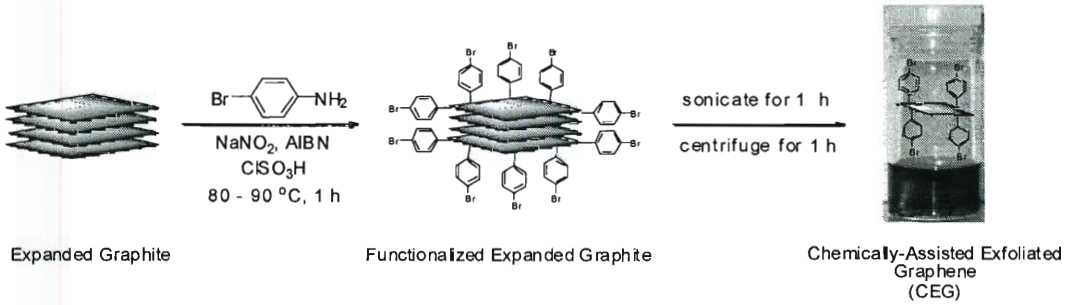

Scheme 8.1 shows the experimental procedure for making CEG. Expanded graphite was first dispersed in chlorosulfonic acid, showing a relatively high solubility of 0.97 mg/mL. The diazonium salt was formed in situ from 4-bromoaniline in the presence of sodium nitrite and catalytic azobis(isobutyronitrile) (AIBN) and 4-bromophenyl groups were grafted mainly on the exposed edges of the expanded graphite flakes to produce functionalized expanded graphite. Because the diazonium salt of 4-bromoaniline is a relatively bulky molecule, it does not penetrate and react to the same degree with all of the graphene surfaces. In addition, the edges of the expanded graphite are more accessible than the interior basal plane surfaces that are stacked with strong π-π interactions. After mild sonication of the functionalized expended graphite flakes, CEG was produced. The functionalized CEG was much more soluble in DMF than the expanded graphite, as shown in Scheme 8.1.

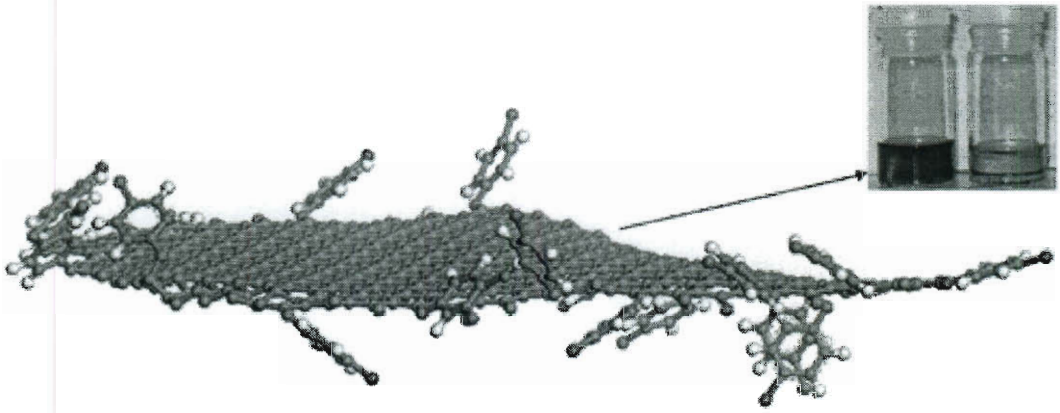

Figure 8.1. Simulated CEG structure (gray: C atoms; red: Br atoms; white: H atoms). The inset shows the expanded graphite control supernatant (right vial) and the CEG supernatant (left vial) after both had been treated with sonication and centrifugation in DMF.

As shown in the Figure 8.1 inset, expanded graphite and CEG were sonicated (Ultrasonic cleaner Cole-Parmer model 08849-00) for 1 h in DMF, followed by centrifugation for 1 h at 3200 rpm (Adams Analytical Centrifuge CT-3201) and the supernatant was decanted from the solid. The supernatant on the right in the Figure 1 inset is the expanded graphite control while the vial on the left holds the CEG supernatant; it has a much darker color and has remained stable for more than 3 months, indicating that the CEG is soluble in DMF while expanded graphite is poorly if at all soluble. The presumed CEG structure is shown in Figure 8.1 with functional groups around the edges.

8.2.2. Functionality and Quality of Graphene Films.

The CEG was analyzed by X-ray photoelectron spectroscopy (XPS) as shown in Figure 8.2. The XPS spectrum had a Br3d peak at 71 eV; unlike 4-bromophenyl diazonium functionalized chemically converted graphite (3.2% Br),[14] much less bromine was detected in the CEG (0.4%). Also, the sharp and symmetric C1s peak at 285 eV confirmed the presence of a graphitic structure with minimal oxidation, indicating that a large number of crystalline domains remained after the reaction. Energy dispersive X-ray spectroscopy (EDX) was used as a supplemental technique to investigate the Br concentration on single-sheet CEG flakes. The Br concentration varied from 0.56% to 0.67%, comparable to the XPS result.

The crystalline structure of the CEG was confirmed by selected area electron diffraction (SAED) in the transmission electron microscope, as shown in Figure 8.3. Figure 8.3a shows a clear hexagonal electron diffraction pattern from single layer CEG. The SAED of two stacked CEG layers with a twist angle between the layers is shown in Figure 8.3b.

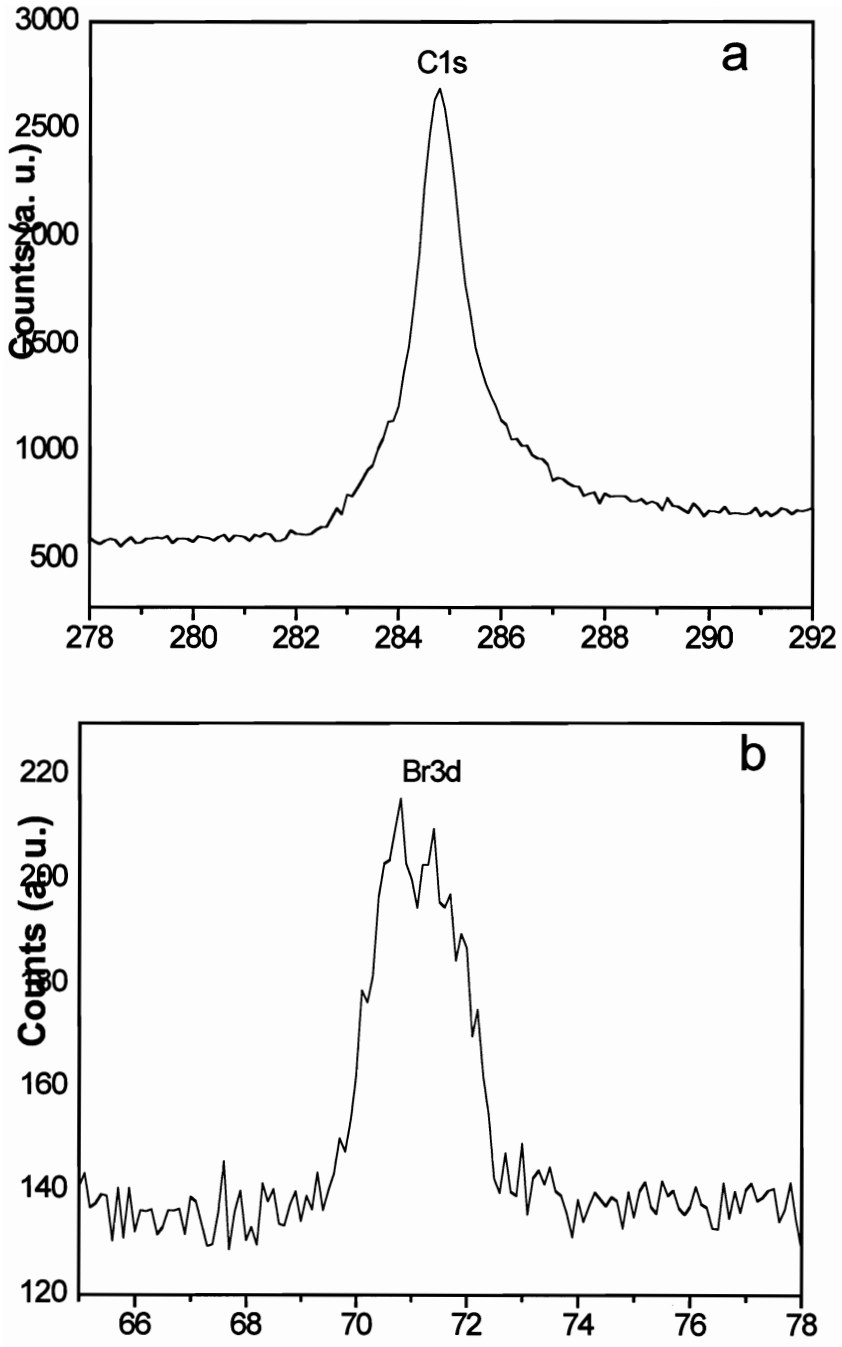

Figure 8.2. XPS analysis of CEG. (a) C1s peak (b) Br3d peak.

High resolution transmission electron microscopy (HRTEM, JEOL 2100F Field Emission Gun Transmission Electron Microscope) was used to estimate the thickness of the CEG by focusing the HRTEM on the edge of the sheets. In Figure 8.4, the samples have fewer than 10 layers, which is consistent with the definition of graphene.[15] Single-layer graphene must be imaged carefully since electron irradiation can easily generate defects (sp^3 C) in the graphene sheet.[16] The treated fast Fourier transform (FFT) HRTEM image (Figure 8.4e) displays the lattice structure of a four-layer CEG overlaid with a polycyclic aromatic hydrocarbon model. CEG has fewer defects than graphene oxide and chemically converted graphene,[17] thus the polycyclic aromatic hydrocarbon model is a viable simulation of the structure. Crystalline graphene edges can be assigned as having either zigzag or armchair configurations.[18,19] Energetically, zigzag edges are more stable than armchair edges.[18] Therefore, the reactivity sequence of edge C atoms should be: dangling C > armchair C > zigzag C. The edge structure was also simulated and overlaid on the image. As shown in Figure 8.4e, the white and black lines represent zigzag and armchair directions, respectively. The real edges are marked with red and green lines. However, based on the HRTEM results, the CEG edges analyzed are neither zigzag nor armchair, except for a few small zigzag fragments.

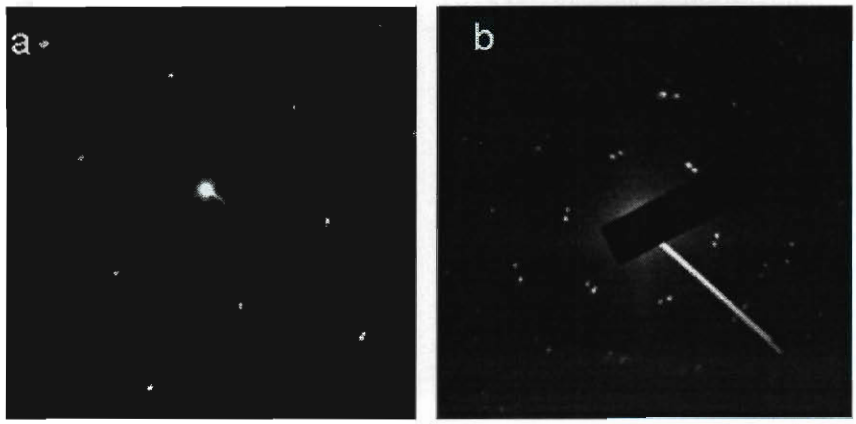

Figure 8.3. SAED of (a) a single layer of CEG, (b) two layers of CEG with a slight twist angle between the layers.

There are several reasons for problems with the graphene edge simulation. First, the simulated edge may not be the real edge of the CEG, since functional groups and heteroatoms attached directly to the edges would blur the graphene boundary. It is difficult to differentiate functional groups from the graphene backbone by regular HRTEM. Secondly, defects and functional groups on graphene determine its surface profile. Vacancies and sp^3 bonds interrupt the conjugation and make the graphene surface buckle over short ranges. This is different from long-range roughness due to the intrinsic flexibility of single graphene sheets,[20] which can be overcome by tilting and focusing in a small area. Lastly, short-range surface fluctuation, especially curvature around the edge, will change the direction of the edge line and make its edge structure unpredictable. Single- and few-layer graphene sheets are sensitive to their chemical and physical environment, and form ripples on the nm scale. However, the simulated model is ideally flat and does not take into account the effects of rippling on the edge configuration. As

shown in Figure 8.4e, the edge of the graphene sheet is pointing out of the plane and appears to be rippled.

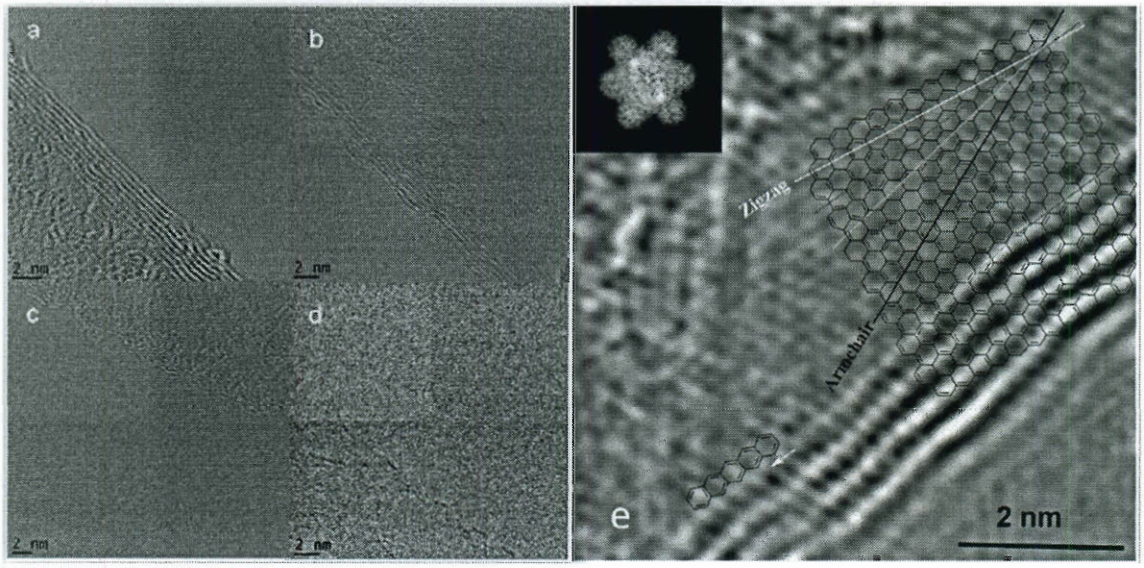

Figure 8.4. HRTEM of the edges of various samples. (a) Eight- layer CEG; (b) six-layer CEG; (c) three-layer CEG; (d) single-layer CEG; (e) simulated four-layer CEG edge (inset is the FFT) overlaid on an HRTEM; the white line is the zigzag direction while the black line shows the armchair direction. The red and green lines indicate the direction of real edges. The sectioning of pictures in a-d is a result of the CCD design.

The Raman spectrum of the expanded graphite, as shown in Figure 8.5a, has a minor D band around 1375 cm^{-1} and relatively strong G and 2D bands at 1585 and 2700 cm^{-1}, respectively. The D band could be ascribed to defects induced by thermal expansion and edge effects.[21] After the diazonium reaction, the G and 2D peaks in the spectrum of CEG (Figure 8.5b) kept their intensity and shape, which indicates that the quality of graphene was largely preserved. The D band increased slightly in size,

presumably because the CEG contained more functional groups than the expanded graphite. Compared to graphene oxide or chemically converted graphene, which have a larger D/G ratio,[14] the CEG has a relatively small D/G ratio ~ 0.1. This data agrees with the XPS results in that the CEG was lightly functionalized.

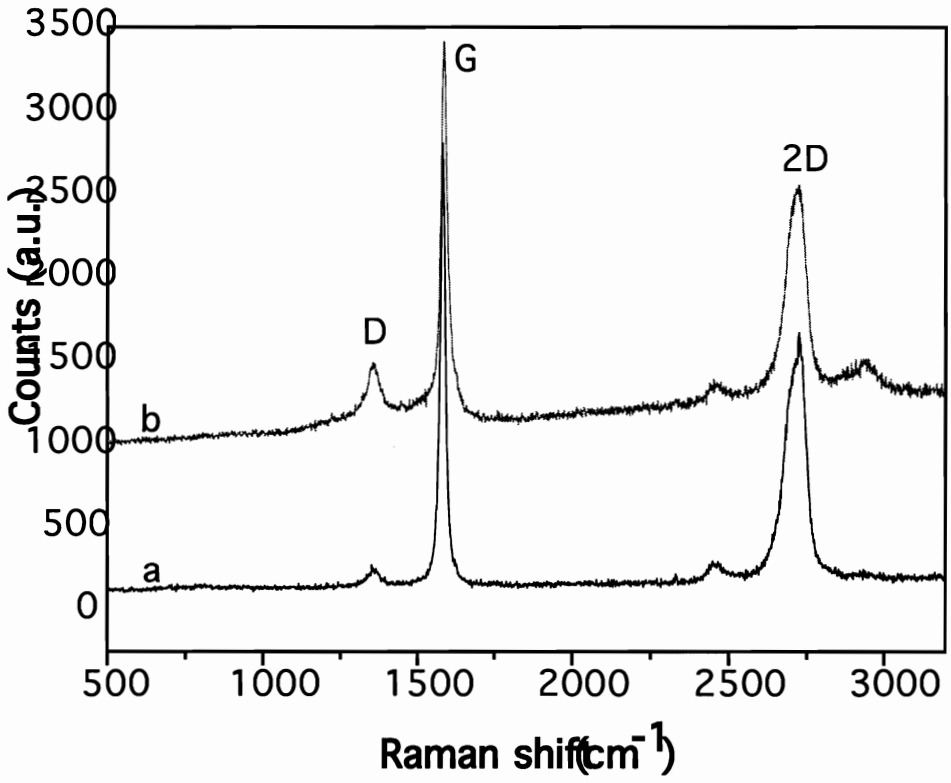

Figure 8.5. (a) Raman spectrum of the expanded graphite before functionalization; (b) Raman spectrum of CEG after functionalization. Spectra were obtained on a Renishaw Raman Scope at 514 nm Ar ion laser excitation at a laser power of 5% on a dry solid sample.

8.2.3 Edge Selectivity of Functional Groups

One multi-layered expanded graphite flake has only two exposed faces. Except for their edges, functionalization of the faces of the inner sheets would be retarded since the reagents cannot gain access to the spaces between the sheets. That the CEG sheets have more functional groups around their edges can be confirmed by electron energy loss spectroscopy (EELS); using elemental mapping under energy filtered TEM (EFTEM), the distribution of Br substituents can be obtained directly from the TEM image. Figure 6a shows the zero loss TEM image of CEG. Figure 8.6b and 8.6c are the mapping of the C (K edge at 284 eV) and Br (M_{45} edge at 69 eV) elements present in the CEG flake. Therefore, based on the EFTEM images, the 4-bromophenyl functional groups are bonded in greater proportion within ~70 nm of the edges of the CEG. It is this region that produces most of the Raman D signal.[22] Because the thermal expansion process opens the expanded graphite edges to a certain extent, the functionalization reagents penetrate into that limited depth and graft on those near-edge planes. The edge selectivity is directly related to the degree of exposure of the interior basal planes to the functionalization reagent.

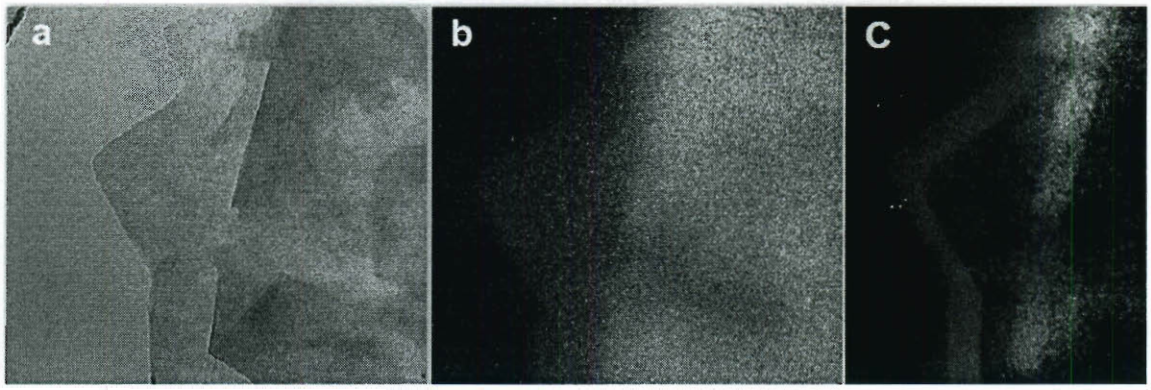

Figure 8.6. EFTEM of CEG flakes: (a) zero loss image, (b) C mapping (K edge at 284 eV), and (c) Br mapping (M_{45} edge at 69 eV). Scale bars are 100 nm. Note the elemental highlights near the edges. Br is only observed within ~70 nm of the edge.

8.2.4 Electrical Properties

The electrical properties were measured on a CEG device built by e-beam lithography (GEOL 6500) using a Pt 2-probe method. The sheet resistance was about 5.6 $\times 10^2$ Ω/sq (see Figure S1), comparable with CVD graphene, which is about 7 – 10 $\times 10^2$ Ω/sq.[8] From Table 1, although graphene oxide has the best solubility in DMF (1 mg/mL), it is an insulator with a sheet resistance up to 4 $\times 10^{10}$ Ω/sq. Even after the graphene oxide reduction, the chemically converted graphene sheet resistance is still 10,000 times higher than the CEG sheet resistance due to the formers high number of defects.[24] A concentration of 0.015 mg/mL in DMF for expanded graphite can be achieved only when excess stabilizer tetrabutylammonium hydroxide (TBAH) is added.[26] The sheet resistance of the stabilized expanded graphite is about 10 times higher than the resistance of CEG. Moreover, CEG, with functional mainly on the edges, can achieve a concentration similar to that of stabilized expanded graphite.

Table 8.1. Solubility and Sheet Resistance Comparison of Graphene Materials.

Material	Solvent	Concentration (mg/mL)	Sheet resistance (Ω/sq)
Graphene Oxide[23,24]	DMF	1	4×10^{10} (2-probe)
CCG[24,25]	0.5% NH_4OH	< 0.5	4×10^{6} (2-probe)
Expanded Graphite[26]	DMF/TBAH	0.015 - 0.020	$8 - 150 \times 10^{3}$
CVD-Graphene[8]	-	-	$7 - 10 \times 10^{2}$ (4-probe)
CEG	DMF	0.010 - 0.020	5.6×10^{2} (2-probe)

8.2.3 Morphology of CEG

The CEG sample was deposited directly on a lacey carbon TEM grid for SEM analysis. According to the SEM data (Figure 8.7), the CEG flakes usually have a size around 1 μm. Some larger flakes could be visualized under an optical microscope on a 300 nm-thick layer of SiO_2 atop a Si wafer. These flakes were noted in the final solution even after centrifugation. They are likely to have more functional groups that stabilize them in the DMF. The thickness of CEG flakes was measured by atomic force microscopy (AFM, Digital Instruments Nanoscope III A, in tapping mode). Figure 8.8 shows a height mode scan from a CEG solution spin-coated on mica. With a height of 1.7 nm in Figure 8.8a and 1.4 nm in Figure 8.8b, the CEG shows a thickness of 1 to 2 layers, which corresponds well to the TEM measurements.

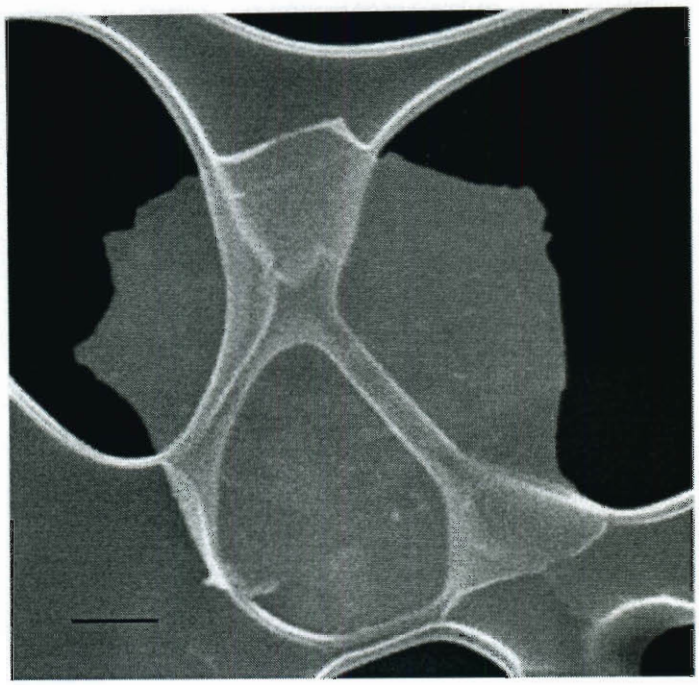

Figure 8.7. SEM image of CEG flake atop a lacey carbon grid. Scale bar is 250 nm.

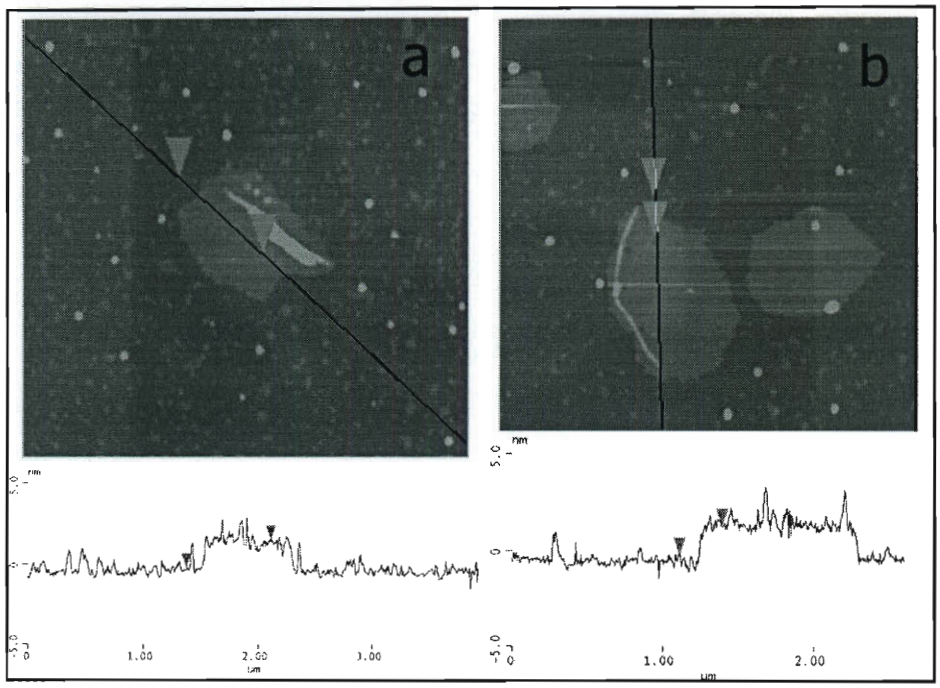

Figure 8.8. AFM of CEG on mica. (a) The edge of the image is 4 µm and the vertical distance (bottom) marked is 1.7 nm; (b) the edge of the image is 2.5 µm and the vertical distance (bottom) is 1.4 nm.

8.3 Experimental Section

8.3.1 Thermal expansion of acid intercalated graphite

Acid intercalated graphite was annealed at 1000 °C in the furnace under nitrogen for 1 h. The solution was bath sonicated overnight, then it was centrifuged for 1 h at 3200 rpm. Although some portion of the graphite precipitated after centrifugation, most of the material was well dispersed in chlorosulfonic acid even after centrifugation. The top portion was separated by decanting and used for functionalization. The well dispersed graphite had a solubility of 0.97 mg/mL.

8.3.2 Functionalization of the thermally expanded graphite in $ClSO_3H$

The well dispersed graphite in $ClSO_3H$ was used for functionalization. The typical functionalization reaction were as follows. A 16 mL $ClSO_3H$ acid solution, in which thermally expanded graphite (15.52 g) had been well dispersed, was heated under nitrogen at 80 °C for 1 h. 4-Bromoaniline (2.22 g, 12.9 mmol) was added followed by sodium nitrite (0.89 g, 12.9 mmol) and AIBN (0.11 g, 0.65 mmol). The mixture was stirred at 80 °C for 1 h. The solution was allowed to cool to room temperature, and then was added dropwise into 250 mL ice water. The suspension was filtered through a 0.45 μm Teflon membrane. The filter cake was washed with water, acetone, and DMF, and then dried in vacuum at 80 °C.

8.3.3 Exfoliation of graphene from functionalized graphite in DMF

The functionalized graphite (10 mg) was dispersed into DMF and bath sonicated for 1 h. The top organic layer (35 mL) was collected after 1 h centrifugation at 3200 rpm.

The CEG can be directly storedin DMF solution or collected by filtration with 0.45 μm Teflon membrane and vacuum drying at 80 °C. The well dispersed CEG had a solubility of 0.01~0.02 mg/mL in DMF.

8.3.4 Characterization

The CEG sheet was characterized spectroscopically using a Phi Quantera SXM Scanning X-ray Microprobe with a pass energy of 26.00 eV, 45 ° takeoff angle and 100 μm beam size. Raman spectra were obtained using a Renishaw Raman scope using a 514 nm argon laser. The SEM image was taken using FEI Quanta 400 ESEM. HRTEM images and EFTEM analysis were acquired using JEOL 2100F Field Emission Gun Transmission Electron Microscope. AFM analysis was performed using Digital Instruments Nanoscope IIIA, in tapping mode.

8.4 Conclusions

Expanded graphite can be converted via functionalization to CEG that is stable in DMF solvent without any added stabilizer. These CEG sheets have functional groups predominantly bonded within 70 nm of the edges and retain the pristine graphene structure in the interior basal planes. Because of CEG's unique structure, its solubility is higher than pure graphene without a surfactant and the sheet resistance is considerably lower than those of graphene oxide and chemically converted graphene. In addition, CEG is easier to prepare than the multi-step method for preparing graphene oxide followed by reduction to chemically converted graphene. The process for preparing CEG

is a promising method to achieve soluble graphenes that have nearly the same sheet resistance as CVD-generated graphenes.

8.5 Experimental Contributions

My contribution to this work is the design and initial execution of the experiments including development of dispersion and in-situ diazonium functionalization in $ClSO_3H$. Shinichiro Kohama assisted in the functionalization experiments. Zhengzong Sun performed the TEM characterization. Zengxing Zhang performed device fabrication and electrical measurements.

References

1. Ruoff, R. *Nature Nanotech.* **2008**, *3*, 10-11.
2. Stankovich, S.; Dikin, D. A.; Piner, R. D.; Kohlhaas, K. A.; Kleinhammes, A.; Jia, Y.; Wu, Y.; Nguyen, S. T.; Ruoff, R. S. *Carbon.* **2007**, *45*, 1558-1565.
3. Wang, H.; Robinson, J. T.; Li, X.; Dai, H. *J. Am. Chem. Soc.* **2009,** 131, 9910-9911.
4. Novoselov, K. S.; Geim, A. K.; Morozov, S. V.; Jiang, D.; Zhang, Y.; Dubonos, S. V.; Grigorieva, I. V.; Firsov, A. A. *Science.* **2004**, *306*, 666-669.
5. Hamilton, C. E.; Lomeda, J. R.; Sun, Z. Z.; Tour, J. M.; Barron, A. R. *Nano Lett.* **2009**, *ASAP*.
6. Hernandez, Y.; et al. *Nature Nanotech.* **2008**, *3*, 563-568.
7. Lotya, M.; Hernandez, Y.; King, P. J.; Smith, R. J.; Nicolosi, V.; Karlsson, L. S.; Blighe, F. M.; De, S.; Wang, Z.; McGovern, I. T.; Duesberg, G. S.; Coleman, J. N., *J. Am. Chem. Soc.* **2009,** 131, 3611-3620

8. Reina, A.; Jia, X. T.; Ho, J.; Nezich, D.; Son, H. B.; Bulovic, V.; Dresselhaus, M. S.; Kong, J. *Nano Lett.* **2009**, *9*, 30-35.

9. Jia, X. T.; Hofmann, M.; Meunier, V.; Sumpter, B. G.; Campos-Delgado, J.; Romo-Herrera, J. M.; Son, H. B.; Hsieh, Y. P.; Reina, A.; Kong, J.; Terrones, M.; Dresselhaus, M. S. *Science*. **2009**, *323*, 1701-1705.

10. Li, X. S.; Cai, W. W.; An, J. H.; Kim, S.; Nah, J.; Yang, D. X.; Piner, R.; Velamakanni, A.; Jung, I.; Tutuc, E.; Banerjee, S. K.; Colombo, L.; Ruoff, R. S. *Science*. **2009**, 324, 1312-1314.

11. Robinson, J. A.; Puls, C. P.; Staley, N. E.; Stitt, J. P.; Fanton, M. A.; Emtsev, K. V.; Seyller, T.; Liu, Y. *Nano Lett.* **2009**, *9*, 964-968.

12. Ni, Z. H.; Chen, W.; Fan, X. F.; Kuo, J. L.; Yu, T.; Wee, A. T. S.; Shen, Z. X. *Phys. Rev. B*. **2008**, *77*.

13. Rohrl, J.; Hundhausen, M.; Emtsev, K. V.; Seyller, T.; Graupner, R.; Ley, L. *App. Phys. Lett.* **2008**, *92*.

14. Lomeda, J. R.; Doyle, C. D.; Kosynkin, D. V.; Hwang, W. F.; Tour, J. M. *J. Am. Chem. Soc*. **2008**, *130*, 16201-16206.

15. Geim, A. K.; Novoselov, K. S. *Nature Mater*. **2007**, *6*, 183-191.

16. Teweldebrhan, D.; Balandin, A. A. *App. Phys. Lett*. **2009**, *94*, 3.

17. Mkhoyan, K. A.; Contryman, A. W.; Silcox, J.; Stewart, D. A.; Eda, G.; Mattevi, C.; Miller, S.; Chhowalla, M. *Nano Lett*. **2009**, *9*, 1058-1063.

18. Girit, C. O.; Meyer, J. C.; Erni, R.; Rossell, M. D.; Kisielowski, C.; Yang, L.; Park, C. H.; Crommie, M. F.; Cohen, M. L.; Louie, S. G.; Zettl, A. *Science* **2009**, *323*, 1705-1708.

19. Liu, Z.; Suenaga, K.; Harris, P. J. F.; Iijima, S. *Phys. Rev. Lett.* **2009**, *102*.

20. Barnard, A. S.; Snook, I. K. *J. Chem. Phys.* **2008**, *128*, 094707.

21. Pimenta, M. A.; Dresselhaus, G.; Dresselhaus, M. S.; Cancado, L. G.; Jorio, A.; Saito, R. *Phys. Chem. Chem. Phys.***2007**, *9*, 1276-1291.

22. Gupta, A. K.; Russin, T. J.; Gutierrez, H. R.; Eklund, P. C. *ACS Nano* **2009**, *3*, 45-52.

23. Stankovich, S.; Piner, R. D.; Nguyen, S. T.; Ruoff, R. S. *Carbon* **2006**, *44*, 3342-3347.

24. Gilje, S.; Han, S.; Wang, M.; Wang, K. L.; Kaner, R. B. *Nano Lett.* **2007**, *7*, 3394-3398.

25. Li, D.; Muller, M. B.; Gilje, S.; Kaner, R. B.; Wallace, G. G. *Nature Nanotech.* **2008**, *3*, 101-105.

26. Li, X. L.; Zhang, G. Y.; Bai, X. D.; Sun, X. M.; Wang, X. R.; Wang, E.; Dai, H. J. *Nature Nanotech.* **2008**, *3*, 538-542.